Grant Agreement Number 608553

IMAGE
Integrated Methods for Advanced Geothermal Exploration
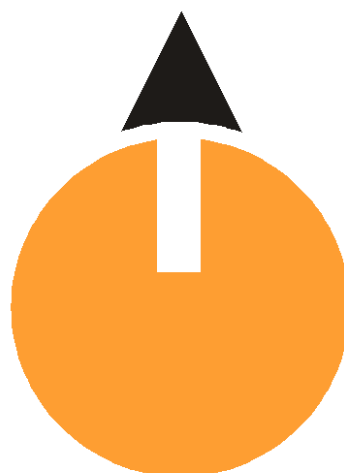
IMAGE-D6.03:
Interacting processes

Responsible author	Jan Diederik van Wees (TNO)
Responsible WP-leader	Judith Sippel (GFZ)
Contributions by:	Jan ter Heege (TNO)
	Maarten Pluymaekers (TNO)
	Tantiana Goldberg (TNO)
	Lilya Ghazaryan (TNO)
	Stefan Carpentier (TNO)
	Hans Veldkamp (TNO)
	Lindsay Lipsey (UU)
	Sierd Cloetingh (UU)
	Katrien van Oversteeg (UU)
	Théophile Guillon (BRGM)
	Mariane Peter-Borie (BRGM)
	Sylvie Gentier (BRGM)
	Arnold Blaisonneau (BRGM)
	Moritz Ziegler (GFZ)
	Oliver Heidbach (GFZ)
	Magdalena Scheck-Wenderoth (GFZ)
	Mohammad Moein (ETHZ)
	Benoit Valley (ETHZ/UniNe)
	Keith Evans (ETHZ)

Table of Content

1 Introduction and Summary

The objective of IMAGE is to develop reliable exploration methods for site characterization and well-siting, to meet targets for extension of the resource base for electricity production and cogeneration of heat. Goals of IMAGE include

- To improve model theory and concepts (diagnostic analysis, theoretical models, physics interaction, natural laboratories) for geological, geochemical and geophysical process-interactions underlying the geothermal system and validate these on appropriate selected datasets across Europe and selected sites of industry participants
- To develop and demonstrate integrated and multidisciplinary approach for site-characterization, based on the conceptual advances, improved models/parameters and exploration techniques of IMAGE
- To improve parameterisation catalogues for site models and exploration techniques, based on compilation studies and laboratory determination of basic physical and chemical parameters

This deliverable reports the IMAGE results with respect to the above goals for basement/sedimentary reservoirs, with a particular focus towards fractured systems.

This deliverable extends on D6.01 which provides an outline of reference physics-based models, and underlying properties, compositional reference models, boundary conditions and observational data constraints at EU scale for thermal and mechanical characterization. At the EU scale (but also more local scales) we use a lithological interpretation approach to drive properties. This means we derive first in a layered geometry the lithological composition (or lithofacies) and from there derive the relevant properties for that particular lithology based on databases and catalogues which hold in general for that particular lithology. For this reason we defined in D6.01 jointly with the modelling approach, in what way a lithological interpretation can be translated to relevant properties that characterize a geometrically well-defined model unit.

Evidently the multi-physics approach at EU scale, is – in principle – not different from simulating processes active at regional to site scale. There are three challenges which relate to site application:
- Local model refinement is generally targeted at improving robustness through more detail in the modelled processes as well as better constraints in model parameters and properties. Conceptual advancement in linkage of processes and properties or novel solution techniques are key to delivering more detail;
- Furthermore, a major challenge is to optimally use direct measurements of physical properties from different scales, which may exist from within the area of interest or outside it. In this case, it is advisable to use this direct information together with sophisticated (multiscale physical and empirical) laws to populate accordingly the local model;
- Finally the proposed methods require validation in site studies and have practical value for industry workflows

This deliverable addresses the above challenges with a particular focus towards predicting stress, interrelationship between stress and faults/fractures, permeability and fractures and asscoiated thermal anomalies. In chapter 2 we present approaches to perform multiscale stress models capable to achieve both targets in increased stress resolution constrained by local data as well as capability to constrain the models with regional and large scale tectonic boundary conditions. In chapter 3 we present a novel method to predict complex stress/fault interactions caused by tectonic faulting and fault rheology, as a function of full 3D structural complexity of sedimentary basins. Chapter 4 is focussed towards conceptual understanding of the relationship between

scaling laws occurring in natural fracture networks and stress heterogeneities with practical implication for characterising attributes of the fracture network based on well log data sets. Subsequently, chapter 5 presents methods to assess bulk permeability tensor from different approaches in fracture characterization, which can be easily adopted in industrial workflows. Chapter 6 assesses the interrelationship of 3D reservoir fracture permeability distributions and its potential effect on the occurrence of thermal anomalies. Finally, chapter 7 gives a synthesis of the results and provides recommendations for use in industrial workflows

2 Multistage Stress Modelling

Moritz Ziegler, Oliver Heidbach, Magdalena Scheck-Wenderoth

This chapter summarized work published by Ziegler et al., 2016, which has been included as Appendix A.

2.1 Introduction

The contemporary stress field in the upper crust is of key importance for safe and sustainable subsurface operations and reservoir engineering such as required for geothermal operations (Gaucher et al., 2015, Cornet, 2015). The stress state is amongst other factors used to determine the criticality of faults within reservoirs and hence knowledge of the stress state is an important component for the research of potential for induced seismicity (Hornbach et al., 2015, Zoback et al., 1985, Kohl & Mégel, 2007, Morris et al., 1996, Connolly & Cosgrove, 1999).

The 3-D in situ stress state can be described with a symmetric tensor of second degree with six independent components (Jaeger et al., 2007). Assuming that the vertical stress Sv is one of the principal stresses in the upper crust, the number of independent unknowns reduces to four (Zoback, 2010). In the principal axis system these are the orientation of one of the two principal horizontal stresses, i.e. the maximum and minimum horizontal stress, SHmax and Shmin , as well as the magnitudes Sv, SHmax and Shmin (Zoback, 2010, Schmitt et al., 2012). Thus, the orientation of this so-called reduced-stress tensor is described by the SHmax orientation, which is systematically compiled by the World Stress Map (WSM) project (Heidbach et al., 2016, Heidbach et al., 2010, Heidbach et al., 2008, Sperner et al., 2003, Zoback et al., 1989).

Even though the orientation of the reduced stress tensor is relatively well known, the provided information is from point data records and hence only a snapshot of the real stress field (Heidbach et al., 2010). Furthermore, information on the stress magnitudes is even less densely available than information on the orientation (Heidbach et al., 2016). Therefore 3D geomechanical numerical modelling is essential for estimation of the full stress tensor in the volume from the sparsely distributed available orientation and magnitude data records (Hergert et al., 2015, Reiter & Heidbach, 2014, Fischer & Henk, 2013). The widely scattered distribution of stress data records (both magnitude and orientation) requires a large-scale regional model to simulate the stress state in the volume. Yet, the simulated stress state is meant for a local application in a reservoir sized area. However, usually no stress data records are available within the area of the reservoir previous to any exploration activity. Hence the only available stress data are most likely in a large distance to the actual area of interest.

A strategy to overcome this scale-gap with a multistage geomechanical modelling is the subject of the open access publication (Ziegler et al., 2016) which is one of the results of this workpackage. The entire manuscript is supplemented in the appendix of this deliverable and a short summary of the work is presented in the following.

2.2 Multistage-Modelling approach

The multistage approach relies on two or more different models of different extent. Here the approach is exemplified with two calibrated models in the Bavarian Molasse basin. A regional scale 70x70km² model which is called root model and a local reservoir sized (10x10 km²) branch model (Fig 3.1).

The root model includes a low resolution first order geologic model and according material properties. Within the model area sufficient stress orientation and magnitude data records are available to achieve a satisfactory calibration of the model. The smaller branch model of a potential generic reservoir consists of a higher resolution geologic model which is e.g. based on a 3D seismic survey. It is entirely

situated within the root model area. The branch model is as well populated with according material properties. Yet, within its perimeter there are no data records for calibration available.

The calibration of the root model closely follows the procedure described in detail by (Hergert et al., 2015, Reiter & Heidbach, 2014). It is realised with the application of different Dirichlet boundary conditions on three test models. At the locations of the available data records the model stress state is compared to the actual stress state provided by the data records. A linear regression then provides the optimal boundary conditions for the root model (Fig. 3.2 a-d). With the application of these boundary conditions a model is computed which represents the stress state in the entire volume of the root model. This is called the best-fit root model.
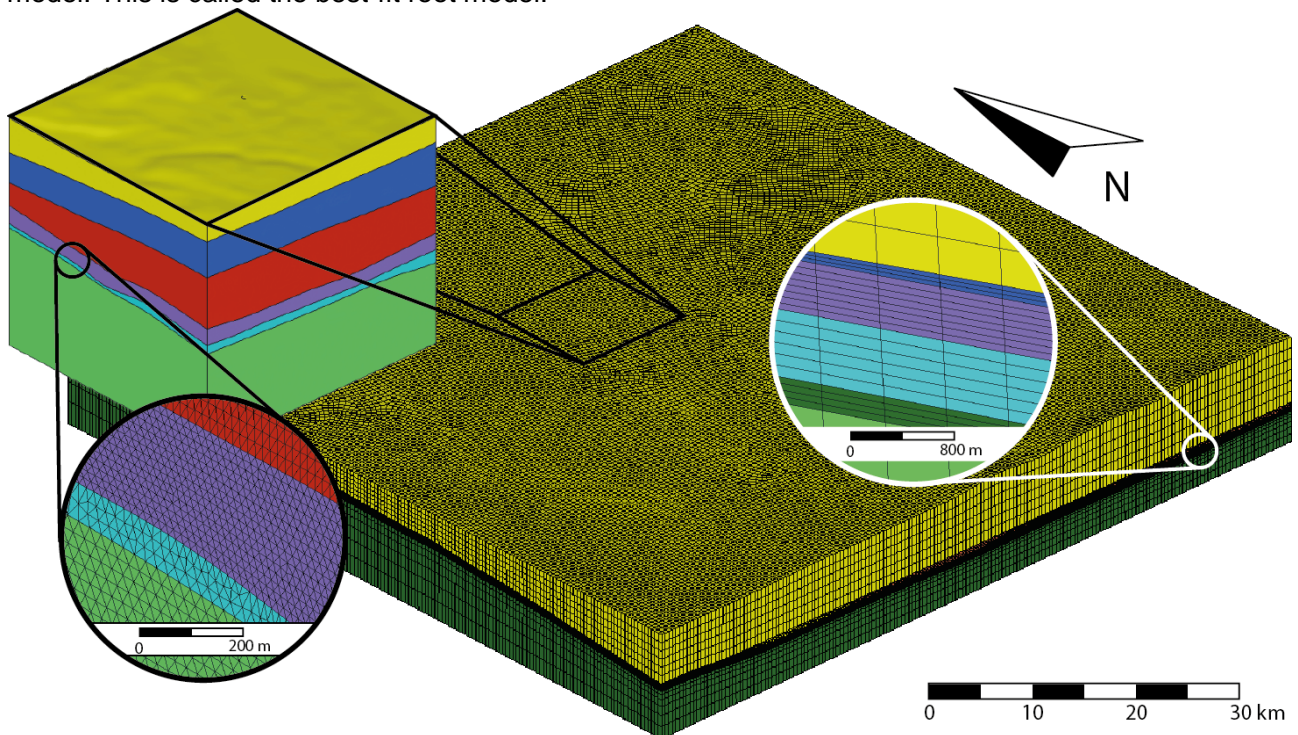

Figure 3.1 The root and branch model discretised with 10^6 hexahedral and $21*10^6$ tetrahedral elements respectively. Please note that to improve visibility the discretisation of the branch model is only displayed within the magnified inset.

The branch model is calibrated in a similar way with the difference that no stress data records are available for calibration. Instead the modelled stress state from the root model is used for the calibration of the branch model. In three test branch models with different Dirichlet boundary conditions the simulated test stress state in the branch models is compared to the stress state in the same location in the best-fit root model. Again a linear regression provides the Dirichlet boundary conditions required to compute the best-fit branch model (Fig. 3.2 e-h).

The resulting best-fit branch model simulates all six independent components of the stress tensor within the volume of the branch model. Hence it can be applied to estimate scalar values on the criticality of the volume and/or pre-existing faults and thereby estimate the potential for induced seismicity and the amount of fluid necessary to improve permeability (Fig. 3.3) (Morris et al., 1996, Connolly & Cosgrove, 1999).

Furthermore, the stress state in the branch model can be used as initial stress conditions for thermo-hydro-mechanical (THM) reservoir modelling which are useful to estimate the anthropogenic stress changes induced by longterm production and/or injection (Altmann et al., 2014, Tingay et al., 2008, Jeanne et al., 2015). Such models can be used as a predictive method to estimate the potential for induced seismic events even before any injection or production started.

a)

b)

c)

$\Delta S_{Hmax} = S_{Hmax\ root} - S_{Hmax\ field\ data}$
$\Delta S_{hmin} = S_{hmin\ root} - S_{hmin\ field\ data}$

d)

Push North–South [m]

$\Delta S_{Hmax} = 0\ MPa$

$\Delta S_{hmin} = 0\ MPa$

Pull East–West [m]

Boundary conditions

for „best-fit" root model

e)

f)

g)

$\Delta S_{Hmax} = S_{Hmax\ branch} - S_{Hmax\ root}$
$\Delta S_{hmin} = S_{hmin\ branch} - S_{hmin\ root}$

h)

Push North–South [m]

$\Delta S_{hmin} = 0\ MPa$

$\Delta S_{Hmax} = 0\ MPa$

Pull East–West [m]

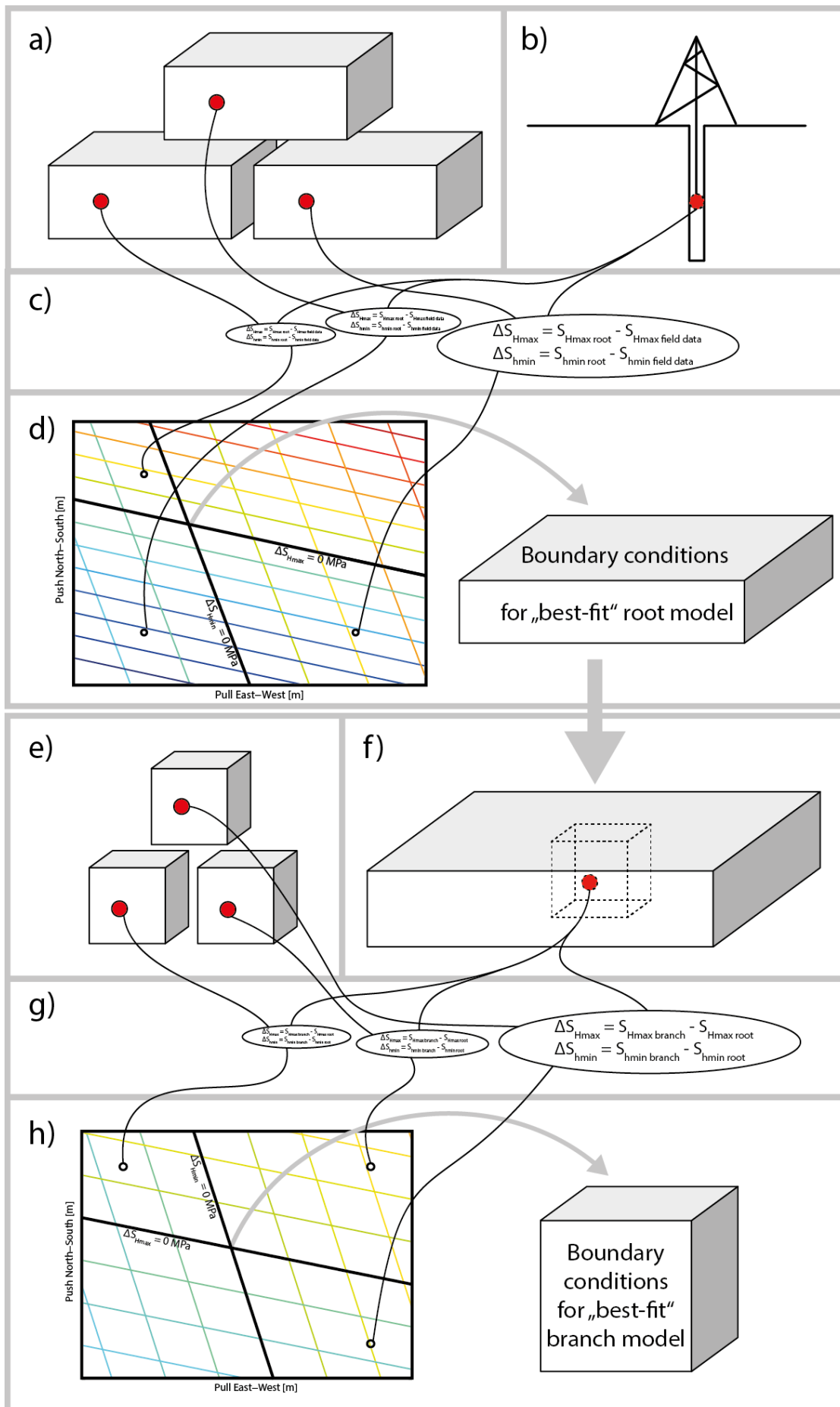Boundary conditions for „best-fit" branch model

Figure 3.2 (previous page) The calibration workflow for the root and branch model. (a) Three models with different Dirichlet boundary conditions provide stress data comparison values for a calibration with (b) observed magnitude stress data. The deviation of the modelled from theobserved stress state of each of the three scenarios (c) is used in a linear regression to derive the boundary conditions to compute the "best-fit" root model (d). (e) Three different branch models provide stress data comparison values for a calibration with magnitude data from the "best-fit" root model (f). The deviation of the modelled stress state to that provided from the root model for each of the three scenarios (g) is used in a linear regression to derive the boundary conditions required to compute the "best-fit" branch model (h).

Figure 3.3 For For the generic branch model the model results are shown by means of slip tendency (ST) values (Morris et al., 1996) mapped on generic faults in the Chattian, Purbeck, and Malm units and by means of the Fracture Potential (FP) (Connolly & Cosgrove, 1999) displayed for the model volume of the basement. Both values vary from zero to one indicating low and high criticality, respectively. Note, that the colour map of these values is non-linear. The results clearly indicate that the generic faults are far away from failure with the largest value of ST of 0.3. The low FP values (max. 0.38) e.g. give an estimate on how much fluid pressure would be needed to fracture the intact rock in a stimulation experiment to enhance the permeability.

2.3 Conclusion

The research conducted in this part of the workpackage shows the benefits and challenges related to geomechanical numerical modelling. We present a multi-stage 3-D geomechanical–numerical modelling approach, which provides a costefficient, reliable, and fast way to generate and evaluate the criticality of the stress state in a small target area where, in general, no stress data for model calibration are available. The approach uses a large-scale root model which is calibrated on available stress data and a small-scale branch model which is calibrated on the root model. We exemplify this in a two-stage approach in the German Molasse Basin around the municipality of Munich.

Furthermore, the discussion of reliability of the model results clearly shows (1) that variations are large and (2) that they are mainly introduced by the uncertain material properties and missing SHmax magnitude data. At this stage, the model's quality depends on the amount and quality of available input data and not on the modelling technique itself. Any further improvements in the model's resolution and applied techniques will not lead to an increase in reliability. This can only be achieved by more high-quality data for calibration.

2.4 References

Altmann, JB, Müller, BIR, Müller, TM, Heidbach, O, Tingay, M, & Weißhardt, A. 2014. Pore pressure stress coupling in 3D and consequences for reservoir stress states and fault reactivation. *Geothermics*, **52**(October), 195–204.

Connolly, Peter, & Cosgrove, John. 1999. Prediction of static and dynamic fluid pathways within and around dilational jogs. *Geological Society, London, Special Publications*, **155**(1), 105–121.

Cornet, François Henri. 2015. *Elements of Crustal Geomechanics*. Cambridge University Press.

Fischer, K., & Henk, A. 2013. A workflow for building and calibrating 3-D geomechanical models - a case study for a gas reservoir in the North German Basin. *Solid Earth*, **4**(2), 347–355.

Gaucher, Emmanuel, Schoenball, Martin, Heidbach, Oliver, Zang, Arno, Fokker, Peter A, van Wees, Jan-Diederik, & Kohl, Thomas. 2015. Induced seismicity in geothermal reservoirs: A review of forecasting approaches. *Renewable and Sustainable Energy Reviews*, **52**, 1473–1490.

Heidbach, O., Tingay, M., Barth, A., Reinecker, J., Kurfeß, D., & Müller, B. 2008. *The 2008 release of the World Stress Map*.

Heidbach, Oliver, Tingay, Mark, Barth, Andreas, Reinecker, John, Kurfeß, Daniel, & Müller, Birgit. 2010. Global crustal stress pattern based on the World Stress Map database release 2008. *Tectonophysics*, **482**(1-4), 3–15.

Heidbach, Oliver, Rajabi, Mojtaba, Reiter, Karsten, Ziegler, Moritz, & WSM Team. 2016. *World Stress Map Database Release 2016*.

Hergert, T., Heidbach, O., Reiter, K., Giger, S. B., & Marschall, P. 2015. Stress field sensitivity analysis in a sedimentary sequence of the Alpine foreland, northern Switzerland. *Solid Earth*, **6**(2), 533–552.

Hornbach, Matthew J, DeShon, Heather R, Ellsworth, William L, Stump, Brian W, Hayward, Chris, Frohlich, Cliff, Oldham, Harrison R, Olson, Jon E, Magnani, M Beatrice, Brokaw, Casey, & Luetgert, James H. 2015. Causal factors for seismicity near Azle, Texas. *Nature communications*, **6**(jan), 6728.

Jaeger, J.C., Cook, N.G.W., & Zimmerman, R.W. 2007. *Fundamentals of Rock Mechanics*. 4th edn. Malden Oxford Carlton: Blackwell Publishing Ltd.

Jeanne, Pierre, Rutqvist, Jonny, Dobson, Patrick F, Garcia, Julio, Walters, Mark, Hartline, Craig, & Borgia, Andrea. 2015. Geomechanical simulation of the stress tensor rotation caused by injection of cold water in a deep geothermal reservoir. *Journal of Geophysical Research: Solid Earth*, **120**(12), 8422–8438.

Kohl, T, & Mégel, T. 2007. Predictive modeling of reservoir response to hydraulic stimulations at the European EGS site Soultz-sous-Forêts. *International Journal of Rock Mechanics and Mining Sciences*, **44**(8), 1118–1131.

Morris, A., Ferrill, D. A., & Henderson, D. B. 1996. Slip-tendency analysis and fault reactivation. *Geology*, **24**(3), 275.

Reiter, K., & Heidbach, O. 2014. 3-D geomechanical-numerical model of the contemporary crustal stress state in the Alberta Basin (Canada). *Solid Earth*, **5**(2), 1123–1149.

Schmitt, Douglas R, Currie, Claire A, & Zhang, Lei. 2012. Crustal stress determination from boreholes and rock cores: Fundamental principles. *Tectonophysics*, **580**, 1–26.

Sperner, B., Muller, B., Heidbach, O., Delvaux, D., Reinecker, J., & Fuchs, K. 2003. Tectonic stress in the Earth's crust: advances in the World Stress Map project. *Geological Society, London, Special Publications*, **212**(1), 101–116.

Tingay, Mark, Heidbach, Oliver, Davies, Richard, & Swarbrick, Richard. 2008. Triggering of the Lusi mud eruption: Earthquake versus drilling initiation. *Geology*, **36**(8), 639–642.

Ziegler, Moritz O., Heidbach, Oliver, Reinecker, John, Przybycin, Anna M., & Scheck-Wenderoth, Magdalena. 2016. A multi-stage 3-D stress field modelling approach exemplified in the Bavarian Molasse Basin. *Solid Earth*, **7**(5), 1365–1382.

Zoback, Mark D, Moos, Daniel, Mastin, Larry, & Anderson, Roger N. 1985. Well bore breakouts and in situ stress. *Journal of Geophysical Research: Solid Earth*, **90**(B7), 5523–5530.

Zoback, Mary Lou, Zoback, Mark D., Adams, J, Assumpção, M., Bell, S., Bergman, E. A., Blümling, P., Brereton, N. R., Denham, D., Ding, J., Fuchs, K., Gay, N., Gregersen, S., Gupta, H. K., Gvishiani, A., Jacob, K., Klein, R., Knoll, P., Magee, M., Mercier, J. L., Müller, B. C., Paquin, C., Rajendran, K., Stephansson, O., Suarez, G., Suter, M., Udias, A., Xu, Z. H., & Zhizhin, M. 1989. Global patterns of tectonic stress. *Nature*, **341**(6240), 291–298.

Zoback, M.D. 2010. *Reservoir Geomechanics*. Cambridge: Cambridge University Press.

3 Geomechanic based techniques to evaluate the regional stress field: BRGM models based on the Distinct Element Method

Théophile Guillon, Mariane Peter-Borie, Sylvie Gentier, Arnold Blaisonneau

This chapter includes work, that has been published as Guillon et al., 2016 at the European Geothermal congress.

3.1 The Distinct Element Method: motivation and principle

Modelling of regional stresses deals with large dimensions (hundreds to tens of thousands of square kilometres at surface per tens to hundreds of kilometres height). When such large scales are considered, the modelled rock masses are cut by major fault zones that affect the overall mechanical behaviour. Fault zones must be taken into account in the modelling, especially if numerous ones are encountered in the studied region (Yale, 2003). Besides, fault zones (FZs) themselves are affected by the tectonic regime, and studying their mechanical response might be of interest depending on the context of the study (flow-paths creation, seismogenic potential …). Among the various numerical methods used in geomechanics, the Distinct Element Method offers a relevant tool to handle mechanically active discontinuities. With the DEM, deformable blocks interact one with another through joints (Itasca, 2013). The DEM thus offers the possibility to:
-   explicitly account for discontinuities and their impact on blocks,
-   use complex mechanical laws for the joints, and thus study their response to tectonic efforts.

The solving phase of the DEM is almost-similar to that of any continuous numerical method: at each time step, the solver runs until mechanical equilibrium is achieved within the system. For the deformable blocks, the problem unknowns are the displacements $\underline{u}$ [m] at mesh gridpoints. $\underline{u}$ is computed by solving the balance equation Eq. 3.1.

$$\int_{\Omega} div(\underline{\underline{\sigma}})dV + \underline{F}_{ext} + m\underline{g} = m\frac{\partial^2 \underline{u}}{\partial t^2} \tag{3.1}$$

Where $\Omega\ [m^3]$ and $m\ [kg]$ are the volume and mass for the considered block, $\underline{\underline{\sigma}}\ [Pa]$ the stress tensor, $\underline{F}_{ext}\ [N]$ is the sum of external forces other than gravity forces, $\underline{g}\ [N.kg^{-1}]$ the gravity vector, and $t\ [s]$ is time.

With the DEM, the external forces $\underline{F}_{ext}$ account for the interaction with the contiguous blocks. These interaction forces are obtained through the joint constitutive equations which, given a prescribed displacement, return the resulting forces. That is, in addition to the constitutive equations $\underline{\underline{\sigma}} = f(\underline{u})$ that must be given for continuous methods, the DEM also requires joint constitutive equations to solve Eq. 3.1. The complete solving scheme at each time-step is then achieved by balancing the displacements resulting from blocks deformation with the forces resulting from blocks interactions (Figure 3.4).
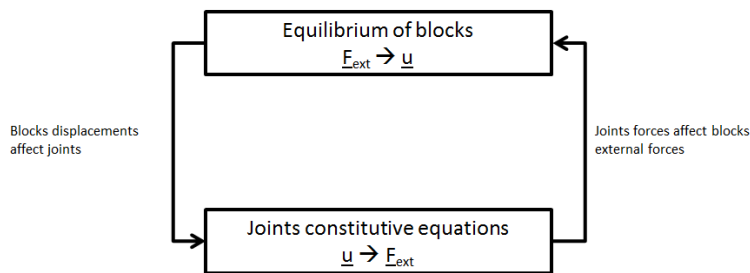
Figure 3.4. DEM solving scheme at each time-step: solver loops until $\underline{u}$ and $\underline{F}_{ext}$ are balanced.

In the following, we first present how a DEM model can be built (paragraph 3.2). Then, some considerations are given on the mechanical behaviour both for the blocks and the joints (paragraph 3.3). In paragraph 3.4, we briefly discuss the issues for the initial state and boundary conditions. Finally, a non-exhaustive overview of model results is illustrated in paragraph 3.5, before skipping to conclusions (paragraph 3.6). All computations results are obtained with Itasca's commercial code 3DEC^{TM} (Itasca, 2013).

3.2 Geometry building

The model geometry must result from a structural analysis of the region of interest. Based on geological and mechanical arguments, the main structures must be hierarchized prior to any geometry construction. Indeed, regional models usually deal with several geological layers exhibiting different mechanical behaviours, numerous fault zones, and an uneven surface topography. Due to limits in meshing algorithms and solvers robustness, all these heterogeneities can rarely be taken into account at once, and must be sorted in the first place. For example, despite studying similar geological configurations (i.e., sedimentary basins with no or few fault zones), Gunzburger and Magnenet (2014) decided to neglect the effect of surface topography compared to that of the contrasts in layers stiffnesses (eastern Paris basin) while Hergert et al. (2015) took both surface topography and stiffnesses contrasts into account (Alpine foreland).

With the DEM, additional attention must be given to the fault zone network. All fault zones cannot be taken into account, and must be selected in terms of:
- Importance in the regional response of the structural blocks they delineate,
- Assumed behaviour (stiff or compliant),
- Possible impact on regional fluid circulations.

Based on literature review, geophysical data and region-specific geological knowledge, a fault network can be identified for the model. An example is given in the Upper Rhine Graben, where the analysis of seismic reflection results (GeORG team 2013) and structural results (Edel 2006) combined with a Riedel structural model lead to the network presented in Figure 3.5.
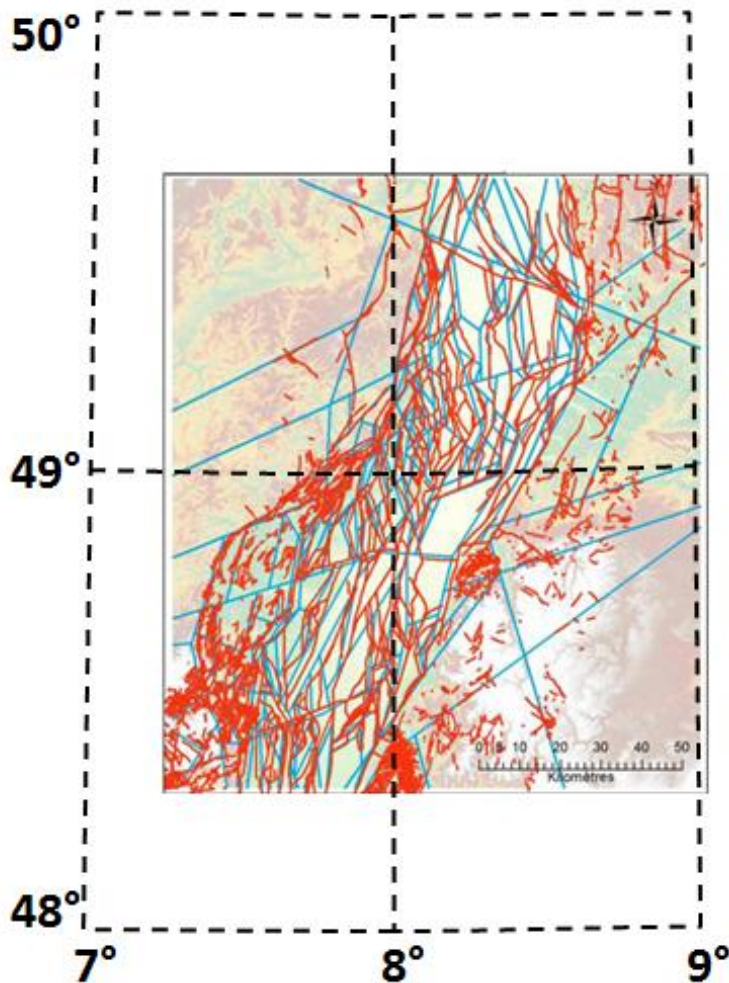
Figure 3.5. Fault network identified at the top of the crystalline basement in the Upper Rhine Graben. Red: seismic reflection results (GeORG team 2013), and blue: modelled network (after Dezayes et al 2014).

In addition, in 3DEC^{TM} software, discontinuities are persistent within the rock mass, i.e., a fault zone must stop on another one or on a boundary, and cannot stop in the middle of a block. This topological aspect requires additional criteria for fault zone creation (e.g., criterion on fault zone chronology). Whenever the geometry must incorporate fault zones stopping within blocks, heterogeneous joint parameters can be used along a same joint (very stiff parameters mimicking rock mass continuity). The final geometry obtained in 3DEC^{TM} according to the network in Figure 3.5 is depicted in Figure 3.6.

Figure 3.6. An example of highly-segmented geometry obtained for the Upper Rhine Graben. The white dot highlights Soultz-sous-Forêts wellheads. A portion of the model is not depicted to highlight its 3D extent.

3.3 Mechanical behaviour

The constitutive equations condition how the model responds to a solicitation. As far as the rock mass is considered, the const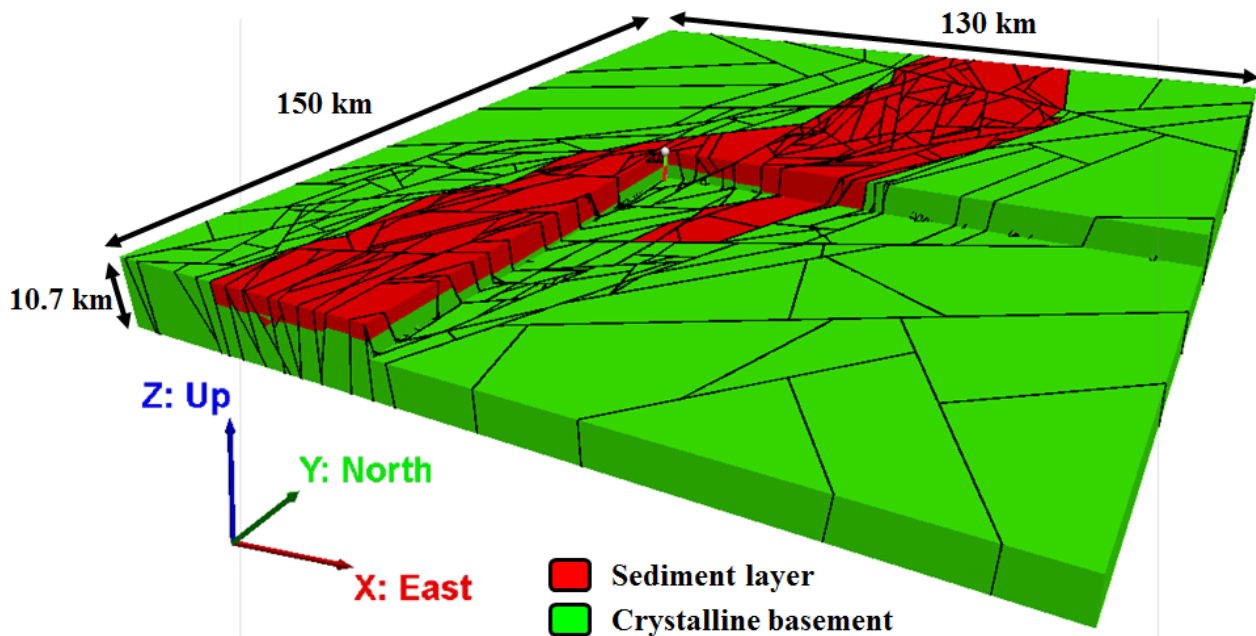itutive equations relate the stress tensor with the strain tensor (or similarly, with the displacements) and can be abbreviated as $\underline{\underline{\sigma}} = f(\underline{u})$. These equations must be chosen as an optimal ratio of the accuracy regarding addressed physics over complexity regarding number and "assessability" of parameters and numerical robustness. When regional models are considered, additional difficulties arise because of the large dimensions involved: material spatial heterogeneities and scale effect (i.e., impact of smaller scales heterogeneities and fractures not explicitly accounted for in the model) make it difficult to extrapolate regional behaviours and parameters from laboratory tests. Two kinds of behaviour are frequently used for the rock mass at this scale: elastoplastic (Hergert et al 2015) and viscoelastic (Buchmann and Connolly 2007, Petricca et al 2013), which respectively enable to account for the irreversible and relaxation-related aspects of mechanical behaviours. When highly segmented models are considered, geometry itself can play a major role on stress redistributions, and elastic properties can be used as a first approximation in order to reduce computation times.

For the FZs, constitutive equations relate the forces with the displacements. At the regional scale, FZs are simplified as surfaces, and their behaviour are given along normal and shear components. The same difficulties as for the rock mass arise for the FZs constitutive equations:
- spatial behaviour and parameter heterogeneities due to the various mechanisms creating the FZs and the diverse material they cut,
- scale effect since FZs are actually 3D objects with internal heterogeneities and fractures (Chester et al 1993) which are embedded in the macroscopic, 2D-simplified behaviour.

Some FEM codes incorporate 2D elements to account for the FZs, but only purely frictional behaviour seem to be considered (see, e.g., Buchmann and Connolly 2007 or Hergert et al 2015). The DEM enables to consider more complex behaviours (peak-residual laws) and to incorporate dilation which has an impact on the creation of flow-paths. Dilation reproduces the opening of FZs under shearing due to their irregular aspects. Figure 3.7 illustrates a Mohr-Coulomb behaviour for the shear component, where irreversible displacements occur under constant stress once the onset of plasticity is exceeded. During the plastic phase, dilation occurs, i.e., opening under

shearing. Normal stress impacts the behaviour: when increased, it delays the onset of plasticity and reduces the dilation.
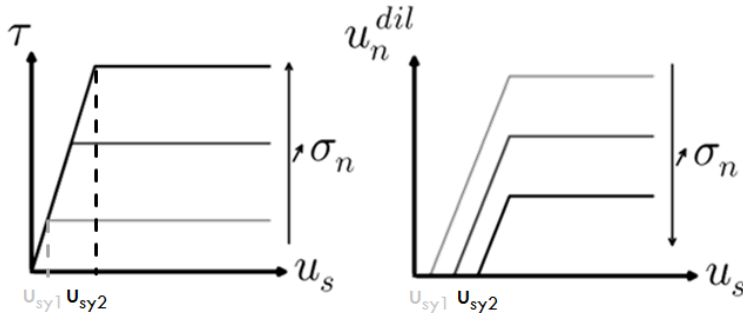

Figure 3.7. Mohr-Coulomb shear behaviour (left) with dilation during plastic phase (right)

3.4 Initial state and boundary conditions

Given the large space and time scales considered, the initial state and boundary conditions are difficult to apprehend. Ideally, a complete geodynamic model should incorporate all the successive tectonic events and corresponding changes in geometry that lead to the present-day stress regime. Such a complete model is nearly impossible to build since the boundary conditions of the past events cannot be inferred from contemporary observations. Instead, the present-day stress field is usually built by setting an initial state for the model, then applying the present-day far-field stresses or displacements to its boundaries.

Setting an initial state that accounts for the residual stresses resulting from the past events is called the pre-stressing method. Several pre-stressing methods exist, and should be adapted depending on the tectonic history of the modelled region: uniaxial stress condition (see Eq. 3.2), Sheorey model (Buchmann and Connolly 2007, Reiter and Heidbach 2014), or Over Consolidation Ratio-dependant models (Hergert et al 2015) can be found in the literature.

$$
\begin{cases}
S_V(z) = \int_0^z \rho g \, dz \\
S_H(z) = S_h(z) = \int_0^z \frac{\nu}{1-\nu} dS_V(z) = \int_0^z \frac{\rho g \nu}{1-\nu} dz
\end{cases}
\tag{3.2}
$$

Where S_V, S_H and S_h $[Pa]$ are the vertical, maximum horizontal and minimum horizontal principal stresses, z $[m]$ is the depth, g $[N.kg^{-1}]$ the gravity vector magnitude, and ν $[-]$ the Poisson ratio.

Once the initial state has been set up, the present-day tectonic conditions can be applied to the model boundaries. Depending on the studied region, the boundary conditions can be difficult to estimate from in situ measurements since:
- Stress measurements are affected by local perturbations (material heterogeneities, FZs, anthropic activities) and can rarely be extrapolated to obtain the far-field conditions.
- GPS measurements give information on motion of tectonic plates, but the estimated values can fall in the range of measurement errors (Fuhrmann et al 2013).

As a result, several authors consider the model boundary conditions as a model parameter rather than as a model input, and fit them by minimizing the model results with in situ stress measurements (Buchmann and Connolly 2007, Gunzburger and Magnenet 2014). With the DEM, using such an approach might be irrelevant. Indeed, the FZs geometry and parameters have a greater impact on local stress redistributions than the far-field conditions. In situ data should thus be used to constrain the uncertainties on the model geometry and behaviour rather than the uncertainty on the boundary conditions.

An alternative might be to use larger numerical models to constrain the boundary conditions. This is done by Guillon et al (2016), where the model is embedded in a larger one from Buchmann and Connolly (2007) (Figure 3.8).
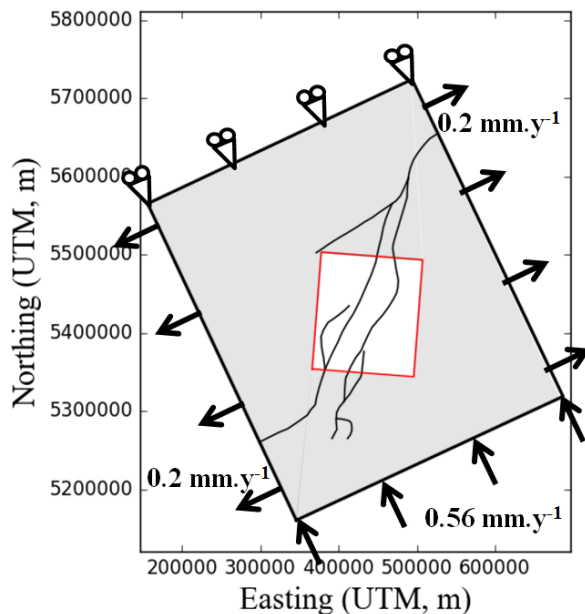
Figure 3.8. An example of numerically derivated boundary conditions: boundary conditions on the black square are estimated by Buchmann and Connolly (2007). The boundary conditions on the red square are obtained by embedding it in the larger, black model. The red square outlines the contour of the model presented in Figure 3.6.

3.5 Result examples

The examined results depend on the context of the study. Here, we present only a non-exhaustive couple of results that cannot be obtained with continuous numerical results.

- Horizontal stress redistributions

The distribution of S_H at 4750 meters depth in the geometry presented in Figure 3.6 is plotted in . The results are obtained after 10,000 years under the boundary conditions depicted in Figure 3.8.
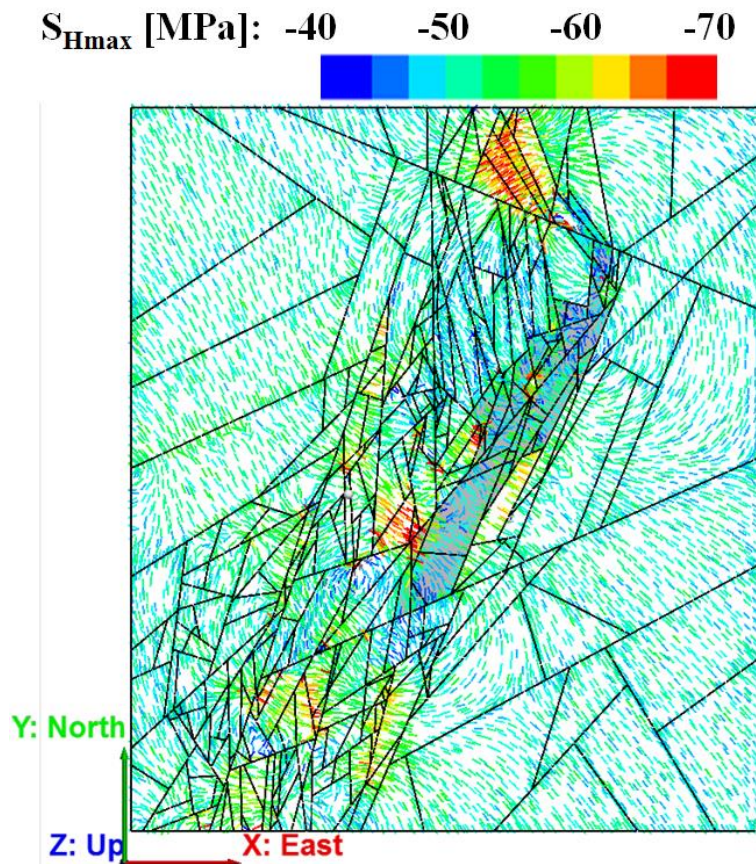
Figure 3.9. Distribution of maximum horizontal stress at 4750m depth within modelled region.

The results highlight the strong influence of the fault network on stress redistributions, to the point where some areas exhibit a S_H oriented perpendicular to the direction of maximum compression (~SE-NW). Also, the geometry has an impact on the stress intensity, highlighting areas of greater or lesser compression.

- Slip tendency (ST) heterogeneity

The ST is commonly used to evaluate how critically stressed a FZ is (Cloetingh et al 2010). The ST is given by the ratio of shear to normal stress acting on the FZ:

$$ST = \frac{\left\| \underline{\underline{\sigma}}.\underline{n} - \underline{n}.\underline{\underline{\sigma}}.\underline{n} \right\|}{\left\| \underline{n}.\underline{\underline{\sigma}}.\underline{n} \right\|} \qquad (3.3)$$

Where $\underline{n}$ $[-]$ is the unit vector normal to the considered FZ.

From Eq. 3.3, it can be seen that the ST is influenced by both the local stress state ($\underline{\underline{\sigma}}$ varies in space, see Figure 3.9) and the FZ shape ($\underline{n}$). Usually, the ST is computed using the far-field stresses, estimated according to in situ measurements, and the stress tensor considered in Eq. 3.3 is thus uniform. With the DEM, the impact of the highly redistributed stresses is taken into account, and the stress tensor considered in Eq. 3.3 is heterogeneous through space. As a result, and despite the planar nature of the joints (constant $\underline{n}$), the ST along a FZ will exhibit regions with a more or less high ST (Figure 3.10).
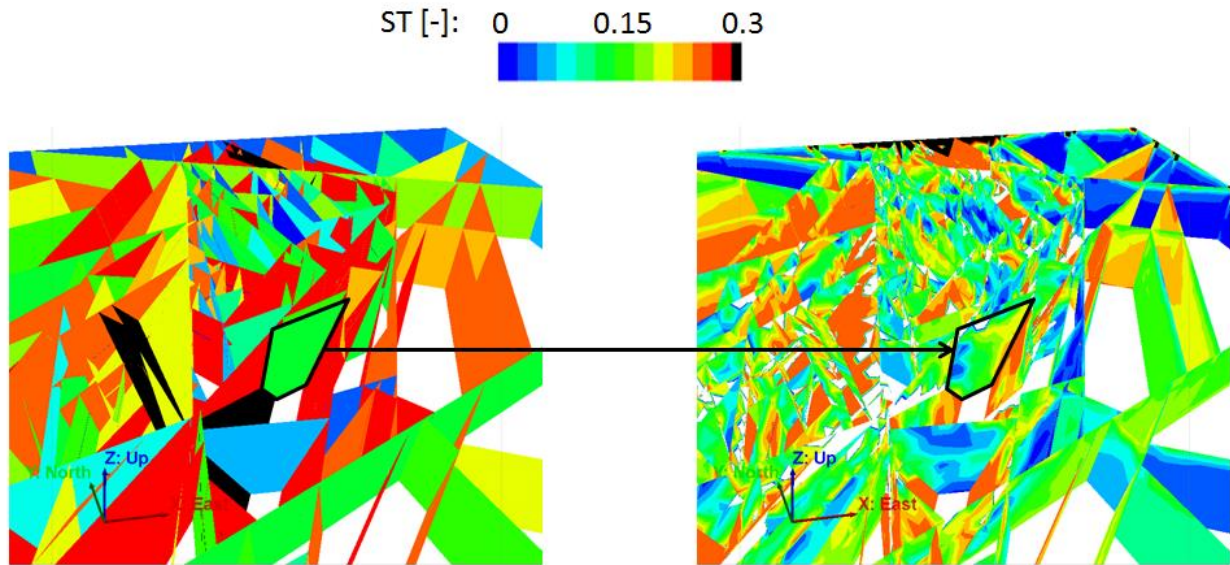
Figure 3.10. Contrasts in ST results when considering a uniform stress tensor for the whole model (left) and the local stress tensor (right). In this example, the same FZ (outlined in black) exhibits regions with greater and lesser ST values compared to the uniform case.

- Fault zones dilational opening

As mentioned in paragraph **3.3 Mechanical behaviour**, the joints' constitutive equation can account for the dilatant nature of FZs. In Figure 3.11 the shear and normal displacements of FZs at 4750 meters depth are presented. Again, the results are obtained for the geometry depicted in Figure 3.6 after 10,000 years under the BC in Figure 3.8. These results highlight that under the local stress redistributions, FZs not favourably oriented towards far-field stresses (i.e., orthogonal to direction of maximum compression) can shear. Opening then occurs due to FZs dilation, and could favour the creation of a flow-path in the SW-NE direction.

a   b
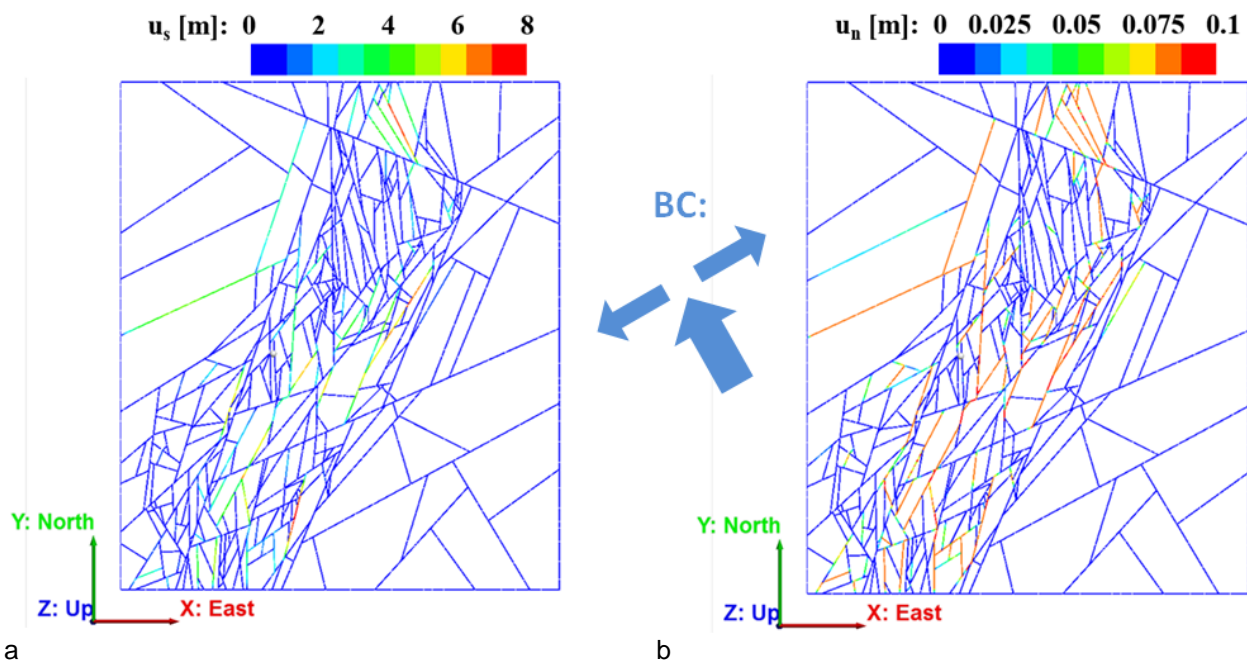
Figure 3.11. Fault zones' (a) shear displacements and (b) normal opening at 4750 m depth within modelled region.

3.6 Summary

In this section, we present the models used at BRGM to compute regional stress redistributions. These models are based on the Distinct Element Method, which explicitly handles mechanically active discontinuities. These joints are used to model the regional fault zones cutting through the rock mass. Considerations on the model creation, including geometry, physical laws, initial state and boundary conditions, are exposed. Some emblematic results are also given, which cannot be obtained with more widespread continuous methods.

3.7 References

Buchman, T. and Connolly, P. 2007. Contemporary kinematics of the Upper Rhine Graben: A 3D finite element approach, Global and Planetary Change 58, 287-309.

Chester, F.M., Evans, J.P. and Biegel, R.L. 1993. Internal structure and weakening mechanisms of the San Andreas fault, Journal of Geophysical Research 98, 771-786

Cloetingh, S., van Wees, J.D., Ziegler, P.A., Lenkey, L., Beekman, F., Tesauro, M., Förster, A., Norden, B., Kaban, M., Hardebol, N., Bonté, D., Genter, A., Guillou-Frottier, L., Ter Voorde, M., Sokoutis, D., Willingshofer, E., Cornu, T. and Worum, G. 2010. Lithosphere tectonics and thermo-mechanical properties: An integrated modelling approach for Enhanced Geothermal Systems exploration in Europe, Earth-Science Reviews 102, 159-206.

Dezayes, C., Lerouge, C., Sanjuan, B., Gentier, S., Guillon, T., Peter, M., Brach, M., Bailly, L. Fléhoc, C., Innocent, C., Wille, G, Ramboz, C. and Gurenko A. 2014. Relations tectonique et anomalies thermiques : le rôle des circulations fluides dans le Fossé Rhénan, TECITUR project final report BRGM/RP-63928-FR, in French

Edel, J.B., Whitechurch, H. and Diraison, M. 2006. Seismicity wedge beneath the Upper Rhine Graben due to backwards Alpine push?, Tectonophysics 428, 49-64.

Fuhrmann, T., Heck, B., Knöpfler, A., Masson, F., Mayer, M., Ulrich, P., Westerhaus, M. and Zippelt, K. 2013. Recent surface displacements in the Upper Rhine Graben – Preliminary results from geodetic networks, Tectonophysics 602, 300-315.

GeORG team 2013. Geopotentials of the deep Upper Rhine Graben. Interreg Project GeORG scientific and technical report, online PDF (http://www.geopotenziale.eu), 1-4.

Guillon, T., Peter-Borie, M., Gentier, S. and Blaisonneau, A. 2016. Regional stress distribution to help with locating exploration areas, Proceedings of the European Geothermal Congress, ID 138, 8 pp

Gunzburger, Y. and Magnenet, V. 2014. Stress inversion and basement-cover stress transmission across weak layers in the Paris basin, France, Tectonophysics 617, 44-57.

Hergert, T., Heidbach, O., Reiter, K., Giger, S.B and Marschall, P. 2015. Stress field sensitivity analysis in a sedimentary sequence of the Alpine foreland, northern Switzerland, Solid Earth 6, 533-552.

Itasca Consulting Group, Inc. 2013. 3DEC – Three-Dimensional Distinct Element Code, Ver. 5.0., Itasca, Minneapolis

Peters, G. 2007. Active tectonics in the Upper Rhine Graben – Integration of paleoseismology, geomorphology and geomechanical modeling, Vrije Universiteit, Amsterdam

Petricca, P., Carafa, M., Barba, S., and Carminati, E. 2013. Local, regional, and plate scale sources for the stress field in the Adriatic and Periadriatic region, Marine and Petroleum Geology 42, 160-181.

Reiter, K. and Heidbach, O. 2014. 3-D geomechanical–numerical model of the contemporary crustal stress state in the Alberta Basin (Canada), Solid Earth 5, 1123-1149.

Yale, D. 2003. Fault and stress magnitude controls on variations in the orientation of in situ stress, Geological Society Special Publications 209, 55-64.

4 Physical linkage between power-law scaling relations for fractures inferred for observed stress heterogeneity, b-value of induced seismicity and fracture scaling using data-constrained models

Benoît Valley, Mohammad Moein, Keith F. Evans

4.1 Objectives and context

Enhanced Geothermal Systems (EGSs) aims to extract the heat from the earth by circulating fluid (e.g. water) through flow paths within a reservoir that extends between injection and production boreholes at sufficient depth that the temperatures are of commercial interest. Such systems aim to extract heat from deep, low-porosity basement rocks, and hence the flow occurs primarily within a fracture network, which increases the complexity of the reservoirs (Genter et al. 2010). In order to allow flow rates that are economical viable, hydraulic stimulation (massive fluid injection) is applied to increase the permeability of the natural fracture system. The injections are believed to increase the permeability of the reservoir through fracture dilation arising from shearing of rough surfaces, although the generation of new fractures is also possible. The process of stimulation is accompanied by micro-seismicity and sometimes felt earthquakes, such as observed during the stimulation of the Basel EGS project in Switzerland, which led to its abandonment (Häring et al. 2008). Such reservoirs are complex and the stimulation process is not well understood. Therefore, research on developing techniques in reducing the risks and forecasting EGS reservoir behavior in different scenarios is currently ongoing. Developing efficient techniques to characterize the deep reservoirs is part of the risk reduction strategy.

In order to design and assess the performance of Enhanced Geothermal Systems (EGS), a geological model of the target rock mass is required. This geological model should be representative of the whole reservoir with a realistic distribution of geological features such as fractures. Power law scaling has been widely utilized to characterize Discrete Fracture Network (DFN) attributes such as length, spatial distribution, aperture etc. (Velde et al. 1990; Power and Tullis 1991; Barton and Zoback 1992; Boadu and Long 1994). The scale invariance of power law distributions facilitates the construction of a geological model at different scales. In addition to DFNs, stress heterogeneities (Valley and Evans 2007; Valley and Evans 2009) and induced seismicity (Smalley et al. 1987; Enescu and Ito 2001; Hainzl 2004) have been observed to follow well-defined scaling relationships. The possible relation among these three scaling relationships might enable us to improve the way we characterize fracture network and to better anticipate the occurrence of induced seismicity during the reservoir stimulation and exploitation.

Although fracture image logs allow the fractures crossing the borehole to be identified, they provide no information about the fractures that are remote from the borehole. Therefore we can only quantify the self-similarity and clustering degree of the fracture intersections with the borehole. Assuming the fractal behavior of fracture attributes such as spatial distribution and length (equivalent radius of fracture planes), prevails in the reservoir, it is possible to create a three dimensional Discrete Fracture Network (DFN) with the spatial distribution observed in the borehole. Since the length distribution is not known, the hypothesis is to use the relationship among stress heterogeneities and network properties to constrain the fracture length.

In order to enable the practical outcomes of this research (such as length distributions and induced seismicity in terms magnitude and spatial distribution), there should be 1) a fundamental understanding of scaling relationships amongst the stress heterogeneities, DFNs and induced micro-seismicity and 2) a clarification of the methodologies applied to characterize the above-mentioned scaling relationships. At the moment, the focus of the research is largely on methodologies applied to stress heterogeneities and DFNs. Induced seismicity is not developed yet and will be included in future development of this work. We apply these methodologies to the Basel EGS reservoir as a case study and we may include other sites in future. In this report, we present the work performed in DFN and stress heterogeneities characterization.

4.2 Scaling of fracture networks

Fractal geometry has been widely utilized to quantify the scale invariant pattern of DFNs. Since our data from a deep geothermal reservoir is restricted to the data obtained from the borehole, we have to characterize the available data to create a reliable geologic model. We need to extend the 1-D line sample of the spatial distribution of fractures from the borehole to a three dimensional model. Therefore, this model must incorporate valid stereological relationships for mapping from one dimension up to three dimensions. According to the literature, the only model with such a stereological relationships is a first-order fractal model of fracture length and density proposed by Davy et al. (2010). This model is based on a double power-law in the form of equation 4.1,

$$n(l,L) = c\,L^D l^{-a} \tag{4.1}$$

where, $n(l,L)dl$ is the number of fractures whose length is in the range $[l, l + dl]$ and whose center belongs to a volume in three dimensions of size L, c is a constant, D is the correlation dimension of fracture centers and a is the length exponent. Bour et al. (2002) have applied this statistical model to scale the fracture geometry on multiscale fracture maps taken from outcrop in Hornelen basin in Norway. If equation 4.1 governs the spatial distribution of fracture centers and length distributions, we would be able to construct a three dimensional probabilistic geological model from borehole observations, according to stereological relationships established by Darcel et al. (2003a). At the moment, the research is focused on performing a critical analysis of such stereological relationships in one and two dimensions, and will be extended to three dimensions in the future. Some of the initial outputs from this analysis will be presented in section 4.2.2.4.

4.2.1 Generating synthetic fracture networks

In order to develop methodologies to assess scaling relationships of fracture network with sampling in one dimension (e.g. along a borehole), two and three dimensions, it is required to be able to reliably generate DFNs of known scaling characteristics. Later on, such DFNs will be used with geomechanical modeling tools to study the scaling relationship between fracture network and stress heterogeneities.

Various methodologies have been evaluated to generate DNFs of known fractal dimension, including an approach based on the Levy flight procedure that is implemented in the commercial package Fracman. The conclusion of our evaluation is that the most reliable approach is to use a network generation methodology based on a Multiplicative Cascade process, the details of which can be found in a paper by Darcel et al. (2003b). We have developed a two dimensional implementation of this method in Matlab and the three dimensional code will be developed in future.

In order to generate the fracture networks using a Multiplicative Cascade process, it is necessary to specify the fracture density exponent, D, which is the correlation dimension of fracture centers, the length exponent, a, and c, which sets the number of fractures and does not affect the self-similarity of the DFN. The number of fracture families and the statistical distribution of their orientation can also be specified. A two dimensional example of a fracture network with random orientations generated in a 100 x 100 m area is shown in Fig. 4.12. The minimum length of the fractures is set to 1 m. Such DFNs can be used to test approaches that permit the assessment of the scaling characteristics of natural fracture datasets.
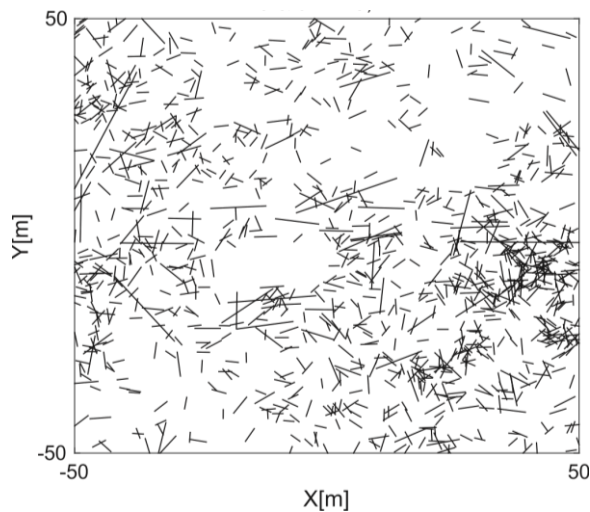
Figure 4.12. A typical synthetic fracture network including 1121 fractures (*n*) created by Multiplicative Cascade Process with a correlation dimension $D = 1.6$ a length exponent $a = 2.5$ and minimum length of 1m.

4.2.2 Evaluation of one dimensional approaches to determine fractal dimension on two dimensional networks

Various methods have been developed to assess the fractal dimension of fracture attributes in a network. For a comprehensive review of the existing methods, we refer to Bonnet et al. (2001). We will focus here on one dimensional methods, since our data stems from 1D borehole datasets. We will apply three methods called the box counting technique, the cumulative distribution of fracture spacing and the correlation function analysis. We first explain the principle of the methods in Section 4.2.2.1, 4.2.2.2 and 4.2.2.3 and then we will test them on two dimensional synthetic DFN of known fractal dimension. This will also permit to test the stereological relationships developed by Darcel et al. (2003a). Stereological relationships capture the change in fractal dimension when changing the number of spatial dimension, as for example when studying a 2D facture network with a 1D sampling line (e.g. a borehole). Finally, we apply the introduced methods to the Basel dataset in Section 4.2.3.

4.2.2.1 Box counting analysis

The box counting technique consists of dividing the data space in to boxes of equal sizes and to determine how many boxes contains data, i.e. the number boxes covering the entire fracture dataset. In a 1D analyses, for example along a borehole, these boxes will be actually intervals and we will count the number of interval containing an intersection between a fracture and the borehole. The division of the data space is repeated sequentially, generating smaller boxes at each iteration. If the distribution of fracture intersections follows a fractal behavior, the following equation will be valid for all r:

$$N(r) = c \cdot r^{-D} \tag{4.2}$$

where $N(r)$ is the number of boxes that cover all of the fractures in equally spaced divisions of length r, D is the fractal dimension, and c is a constant. The fractal dimension is then evaluated by measuring the local slope of the number of boxes containing data vs. the box size in a log-log plot. This slope will not be constant over the entire range and different regimes develop. When there is a small number of large boxes, all boxes will contain data and the local slope will essentially be -1. On the other hand, when boxes have sizes smaller the minimum data spacing, the number of boxes containing data will become a constant equal to the number of data points and the slope on the log-log plot will tend to zero. In between these two extreme cases, a regime with a constant slope should develop if the data set is truly fractal, and this constant slope is an estimator of the fractal dimension of the data set.

From this method, it is quite intuitive to understand the meaning of the fractal dimension: a data set with its elements uniformly distributed over the entire data space will have a fractal dimension close to 1 (for 1D dataset), because data will be present in many intervals even when the intervals become numerous. On the

other hand, a highly clustered data set will have a small fractal dimension since data will be present in only a few intervals, when increasing the number of intervals.

4.2.2.2 Cumulative distribution method

The intersection of fractures with a borehole generates a dataset of fracture spacing. Spacing is defined as the depth difference between two consecutive intersections. An approach to estimate the fractal dimension of the intersection of factures with the borehole is to evaluate the cumulative spacing distributions. The cummulative spacing distribution is the plot of the number of spacings greater or equal to specific spacing (S). When displayed in a log-log space, one can estimate the fractal dimension by fitting a line in the linear section with a power law exponent m. The equivalent fractal dimension would be obtained by adding one the slope ($D=1+m$). Examples of these plots can be found in Section 4.2.3.3. Valley (2007) has applied this method to study the spacing distributions in Soultz-sous-Forêts data set.

4.2.2.3 Correlation function analysis

According to Vicesk (1992), the most efficient way to assign a fractal dimension to a natural system is by calculating the so-called density-density $C_2(r)$ or pair correlation function. This method consists of the calculation of $C_2(r)$ as the in equation 4.3,

$$C_2(r) = \frac{2N_p(r)}{n(n-1)} \tag{4.3}$$

where, $N_p(r)$ is the number of pairs of points whose distance is less than r and n is the total number of points. $C_2(r)$ is expected to scale with r such as r^{Dc}, with Dc the correlation dimension equal to the fractal dimension of fracture centers applied in synthetic network generations as discussed in Section 4.2.1.

Correlation dimension has been applied to characterize the spatial distribution of micro-earthquakes observed in hydraulic stimulation of EGS. Using the correlation dimension of hypocenters of earthquake clusters, Tafti et al. (2013) have tried to determine the structure of fracture network in Geysers geothermal field.

4.2.2.4 Evaluation of fractal dimension on synthetic fracture networks

The stereological relationships presented by Darcel et al. (2003a) are based on the first order model presented in equation 4.1. These relationships have been derived analytically and verified in synthetic fracture networks by Darcel et al. (2003a). Here we present these stereological rules and try to verify them using the developed DFN generator as presented in Section 4.2.1. According to the set of equation 4.4, 4.5, 4.6, the correlation dimension along a 1D sampling line (e.g. a scanline or a borehole), D_{1-D}, in a 2D domain, is dependent on the two dimensional correlation dimension, D_{2-D}, and the length exponent of fractures, a_{2-D}. Depending on the length exponents, three different relations are derived:

$$D_{1-D} = D_{2-D} - 1 \qquad\qquad a_{2-D} \geq 2 \tag{4.4}$$
$$D_{1-D} = D_{2-D} - a_{2-D} + 1 \qquad\qquad D_{2-D} \leq a_{2-D} \leq 2 \tag{4.5}$$
$$D_{2-D} = 1 \qquad\qquad a_{2-D} \leq D_{2-D} \tag{4.6}$$

These relationships are tested using the synthetic discrete fracture network presented in Fig. 4.13, with a fractal dimension of fracture centers of $D=1.7$ and the length exponent of $a=3$. With such a length exponent, small fracture are relatively more numerous than large fractures. A minimum fracture length of two metres was also imposed in this model. The DFN was generated using Multiplicative Cascade process as explained in Section 4.2.1. The number of fractures are chosen to be high enough to have statistically meaningful correlation dimensions in the case of one dimensional sampling. In order to get a sufficient number of fractures, the parameter c is set to 30 and the number of generated fractures are 17106. It is important to note that, the increase in c does not affect the self-similarity of the network. The DFN domain is 100x100m.

A vertical scan line is placed through the center of the model (X=0). The fracture intersecting the scanline are presented in Fig. 4.13 (right). An analysis of correlation dimension was done over two orders of magnitude (one to hundred meters) and is presented in Fig. 4.14.
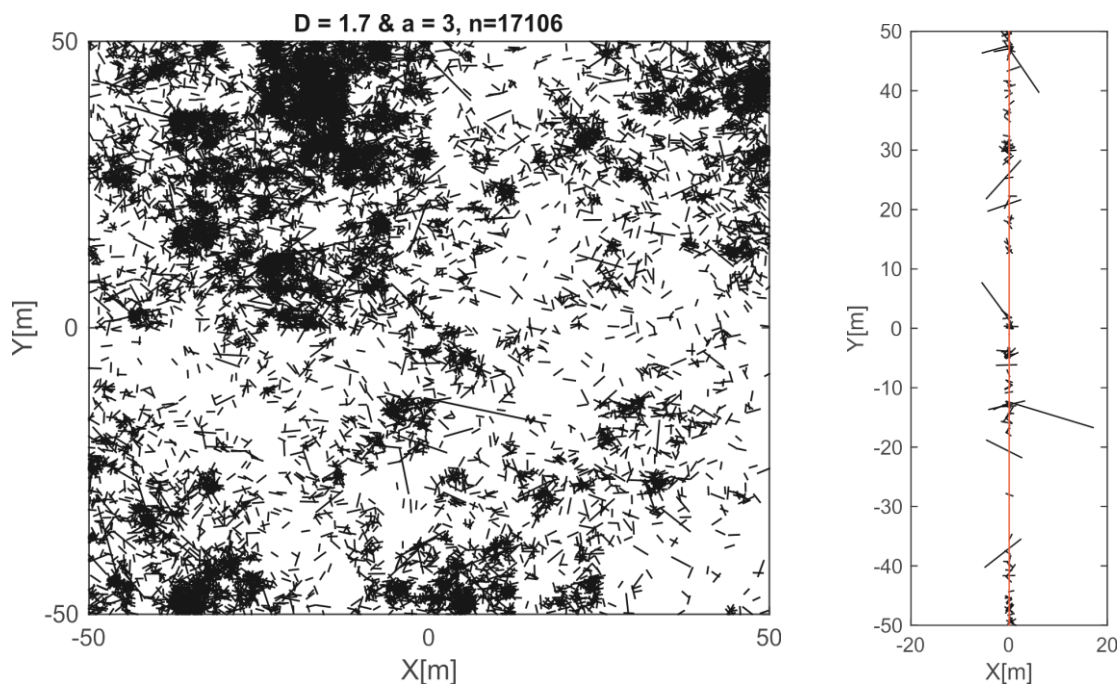
Figure 4.13. (left) A typical synthetic fracture network including 17106 fractures (n) created by Multiplicative Cascade Process with a correlation dimension $D = 1.7$ a length exponent $a = 3$ and minimum length of 2m. (right) The representation of a scanline in X=0 intersecting the fracture network

Figure 4.14. Correlation function of the fracture intersections with the scanline at X=0 (black), the local slope of the correlation function (red), the calculated correlation dimension in more than 1.5 orders of magnitude (blue) and the fitted correlation function in the linear section (green). The local slope of the curve is calculated for by linear fit through data windows with a width of 1/40 of the complete studied range.

The obtained correlation dimension from the scanline is 0.76 which is slightly higher than $D_{1-D} = 0.7$ expected from equation 4.4. This analysis has been repeated for scanline placed at other location (X=-45, -30, 15 or 35) of the DFN of Fig. 4.13. The correlation functions of these scanlines are shown in Fig. 4.15. The computed one dimensional correlation dimensions are 0.78, 0.73, 0.82 and 0.75. All values are slightly higher than the expected fractal dimension of 0.7. Work is on-going to assess if this overestimation is systematic. Further work will also evaluate the determination of the fractal estimation methods, not only the correlation analyses but also the other methods presented above, for fracture networks with different characteristics.
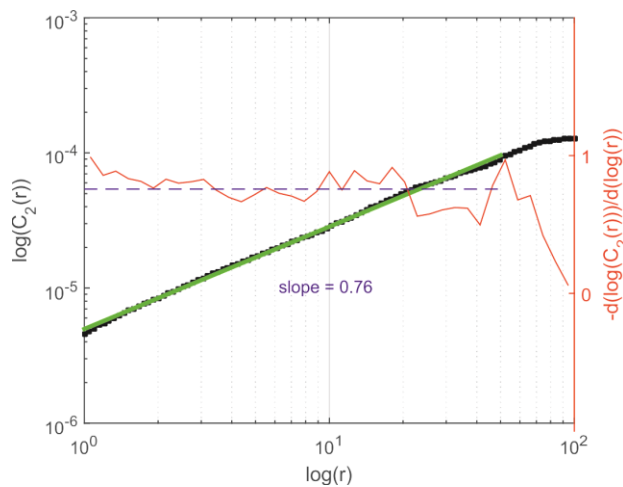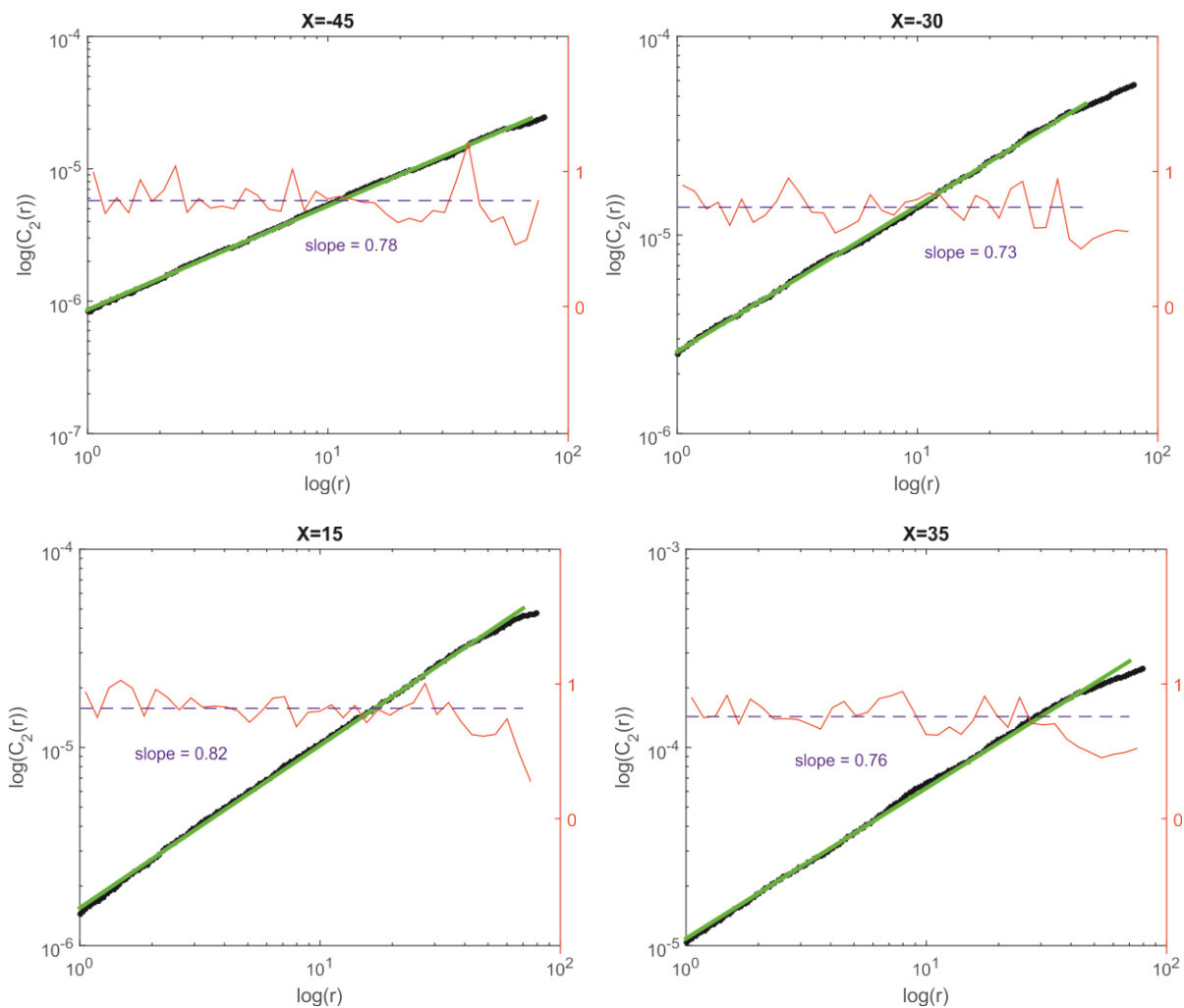
Figure 4.15. Correlation function of the fracture intersections with the scanline at X=-45, -30, 15, 35 (black), the local slope of the correlation function (red), the calculated correlation dimension in more than 1.5 orders of magnitude (blue) and the fitted correlation function in the linear section (green)

4.2.3 Estimated fractal parameters of existing fracture networks with application to Basel-1 well

We apply here three methods to quantify the self-similarity of fracture intersections in the Basel-1 well: the Box-counting method (Section 4.2.2.1), the cumulative distribution methods (Section 4.2.2.2) and the pair-density correlation function (Section 4.2.2.3). The objective is to assess the suitability of the methods when applied to real data sets and to assess if the fracture data from Basel are actually fractal.

4.2.3.1 Basel fracturing data set

We performed an estimation of the fractal dimension of the fracture intersections observed in the Basel-1 well. A comprehensive study of the characterization of the fractures has been performed by Ziegler et al. (2015) and is presented in Fig. 4.16. These data are the basis of our fracture network scaling analyses.

The crystalline section below Basel was penetrated by the Basel-1 well between 2507m and 5000m measured along hole from the rotary table. The dataset consists of 1164 natural fractures (including both certain and uncertain identifications) in the logged interval between 2600m and 5000m. Of these, 1035 fractures were grouped into six possible sets based on their orientation. Some of the sets may be conjugate pairs. In this study we do not take the uncertainty rating into account and studied all fractures that were grouped into the largest sets 1–4.

Number of fractures along Basel-1 in 10 m bins
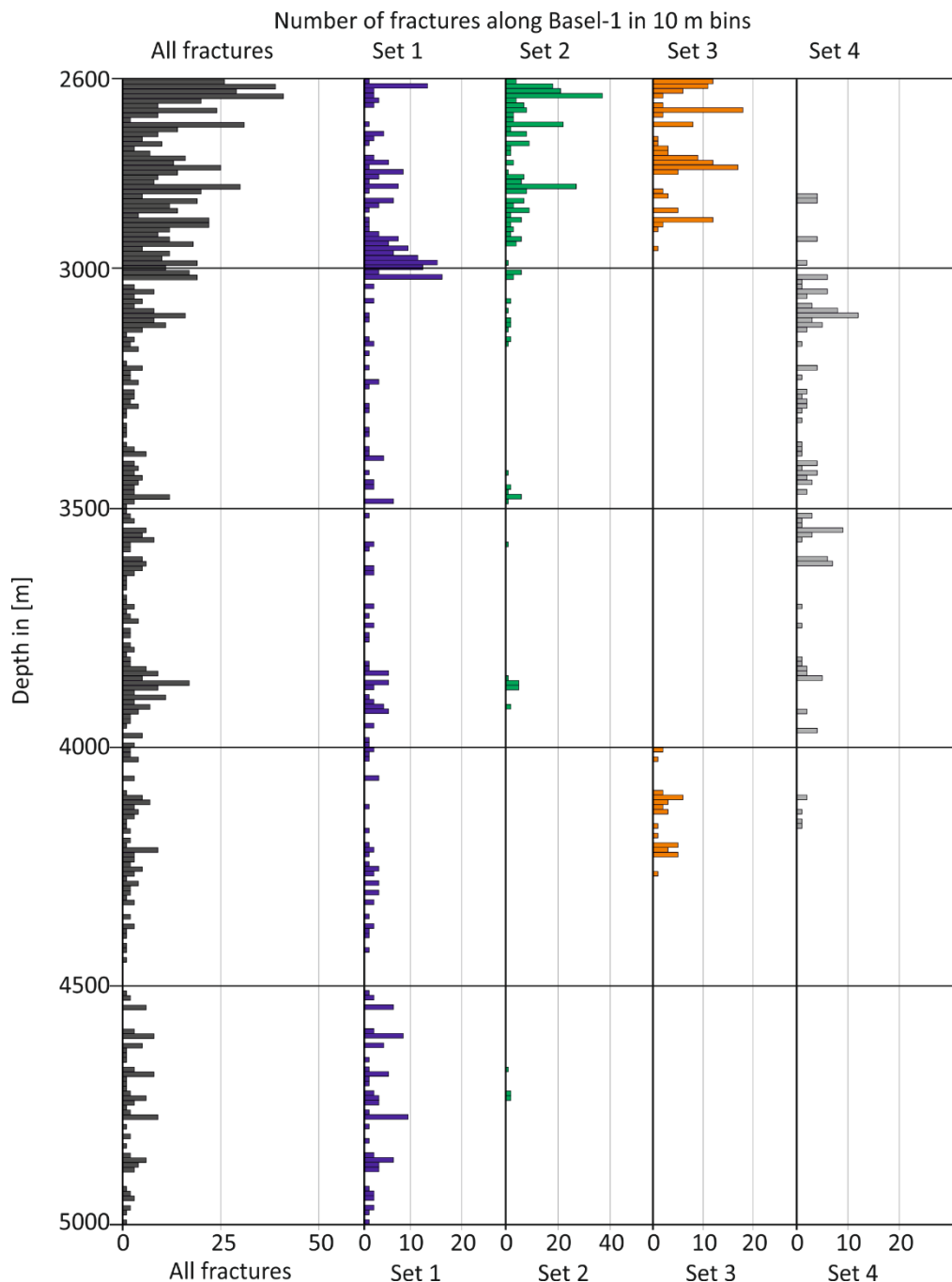
Figure 4.16. Histograms of all fractures (1164 fractures) and set 1–4 vs. depth in 10 m bins.

4.2.3.2 Box counting analyses

A box counting analysis has been performed on the three main fracture sets independently as well as on all fractures intersecting the BS1 well. The results of these analyses are presented in Fig. 4.17 and 4.18 and summarized in Table 4.1. In addition to the box counting curve, a local slope calculation is presented in red in Fig. 4.17 and 4.18. This local slope is calculated over intervals of 1/40 of the total box size range in logarithmic scale. The local slope curve help in assessing if a sufficiently linear section exist: it will show up as a plateau over at least one decade on the local slope curve.

For set 1 (Fig. 4.17) such a plateau do not truly exist and the estimated slope of -0.31 is just added as an indication but should not be considered as reliable. For set 2, a constant slope of -0.52 is observed over more than one decade indicating that this data set is fractal with a box counting dimension of 0.52. A reasonable plateau is also observed for set 3 indicating a box counting dimension of 0.48. For set 4, no real plateau is obtained and the -0.24 value indicated is likely not reliable. Taken on face value, this analyses

indicates that only set 2 and 3 have fractal characteristics with a box dimension of about 0.5. The graphs for set 1 and 4 are not sufficiently linear to be considered as fractal. The latter is also true when considering the intersection with all fractures encountered along the crystalline section of BS1 borehole (see Fig. 4.18). The box counting graph shows a curved function with a progressively decreasing slope with decreasing box size without any indication of a plateau. This phenomenon is also observed in two dimensional fracture networks and Bour et al. (2002) have reported the failure of box-counting in assigning a box dimension to Hornelen basin in Norway. They explained such limitation by the fact that box-counting technique is highly affected by finite size effects. They have proposed two point correlation function of fracture centers to assign a reliable fractal dimension to facture networks.
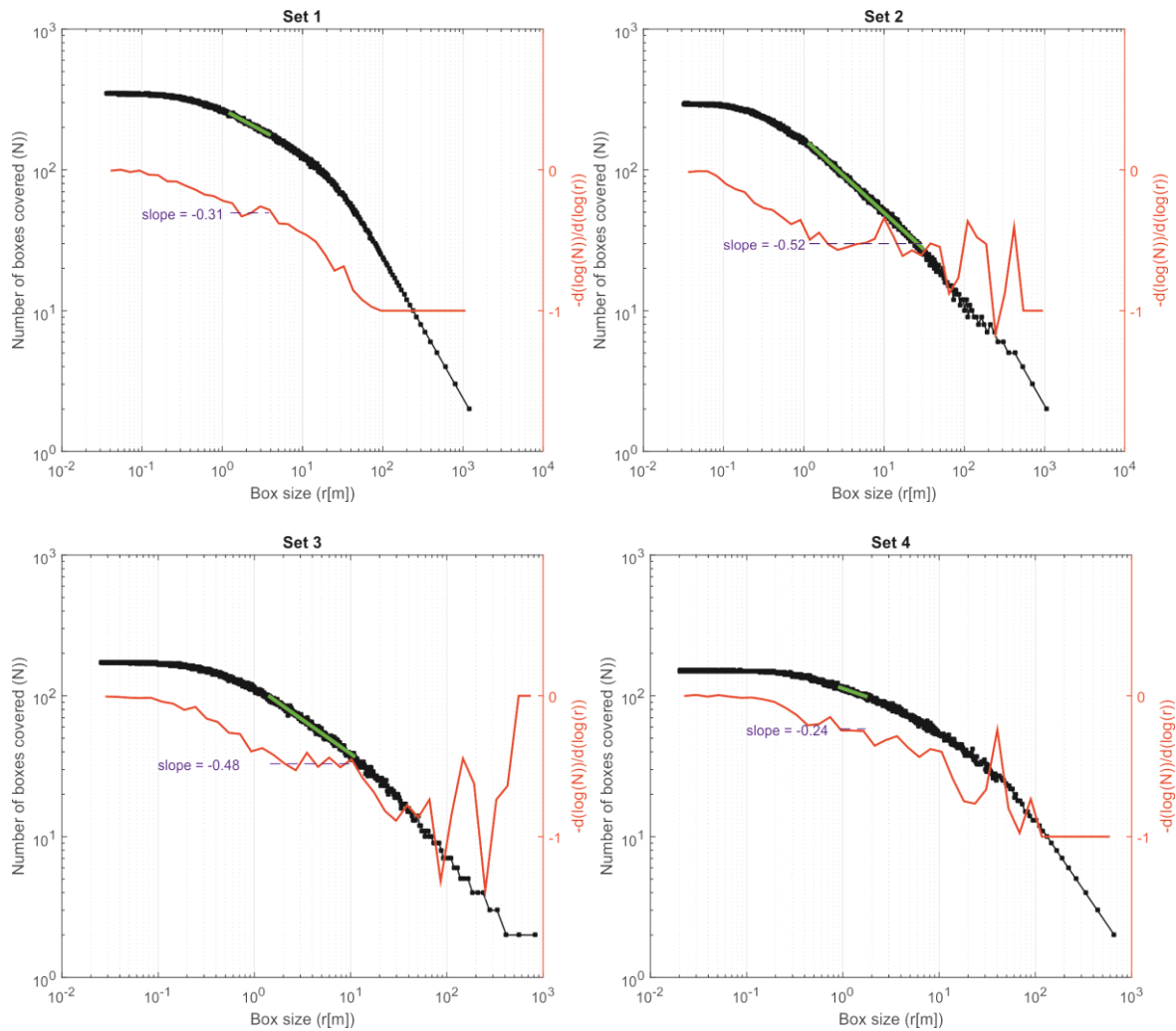
Figure 4.17. Box dimension analysis for set 1, set 2, set 3 and set 4. The black line with square symbol is the output of the box counting method. The local slope of the box counting curve is displayed in red and is calculated by linear fit through data windows with a width of 1/40 of the complete ruler size range. An estimation of a constant slope regime in the middle of the box counting curve is given in blue and the fitted section on the box counting curve is traced in green.
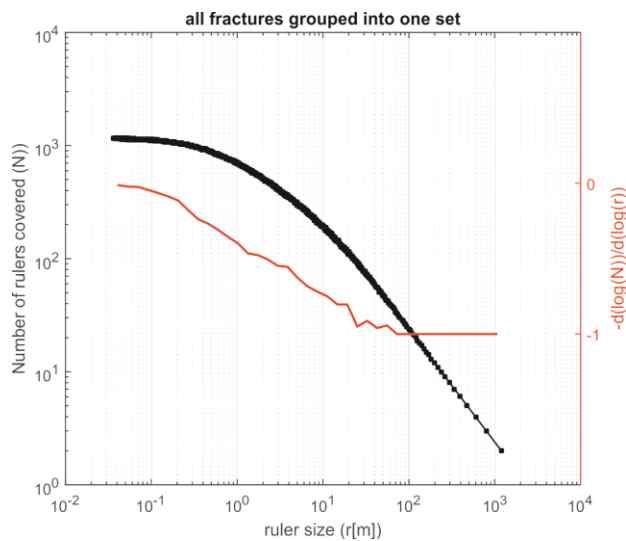
Figure 4.18. Box dimension analysis of all fractures grouped into one set showing no linear slope in the transition zone from -1 to zero.

4.2.3.3 Cumulative spacing analyses

We calculated the cumulative spacing distribution, i.e. the number of spacing greater or equal to a specific spacing of S as a function of S, for four different fracture sets and display it in a log-log space (see Fig. 4.19). The local slope of the obtained plot is calculated for by linear fit through data windows with a width of 1/40 of the complete study size range.

Set 1 shows a range where the local slope stays relatively constant. The local slope is -0.4, which gives a power-law exponent of 0.6. For set 2, an exponent of -0.6 was observed for more than two decade, also very large local slope variations are observed. This exponent must then considered uncertain and would lead to an equivalent fractal dimension of 0.4. For set 3, we obtained an equivalent fractal dimension of 0.46 with large deviations from the constant slope range. For set 4, the equivalent fractal dimension of 0.71 with large deviations from the constant slope was assigned. Generally, for all sets it is difficult to assess what part of the spacing distribution should be considered as sufficiently linear and to assess its slope.

We performed also an analyses of the spacing with all fractures without sorting them by sets. The result of this analysis is presented in Fig. 4.20. The cumulative distribution has a continuously curved shape and deciding for a constant slope is highly subjective. We identified a slope of -0.79 over less than one decade that yields an equivalent fractal dimension of 0.21.
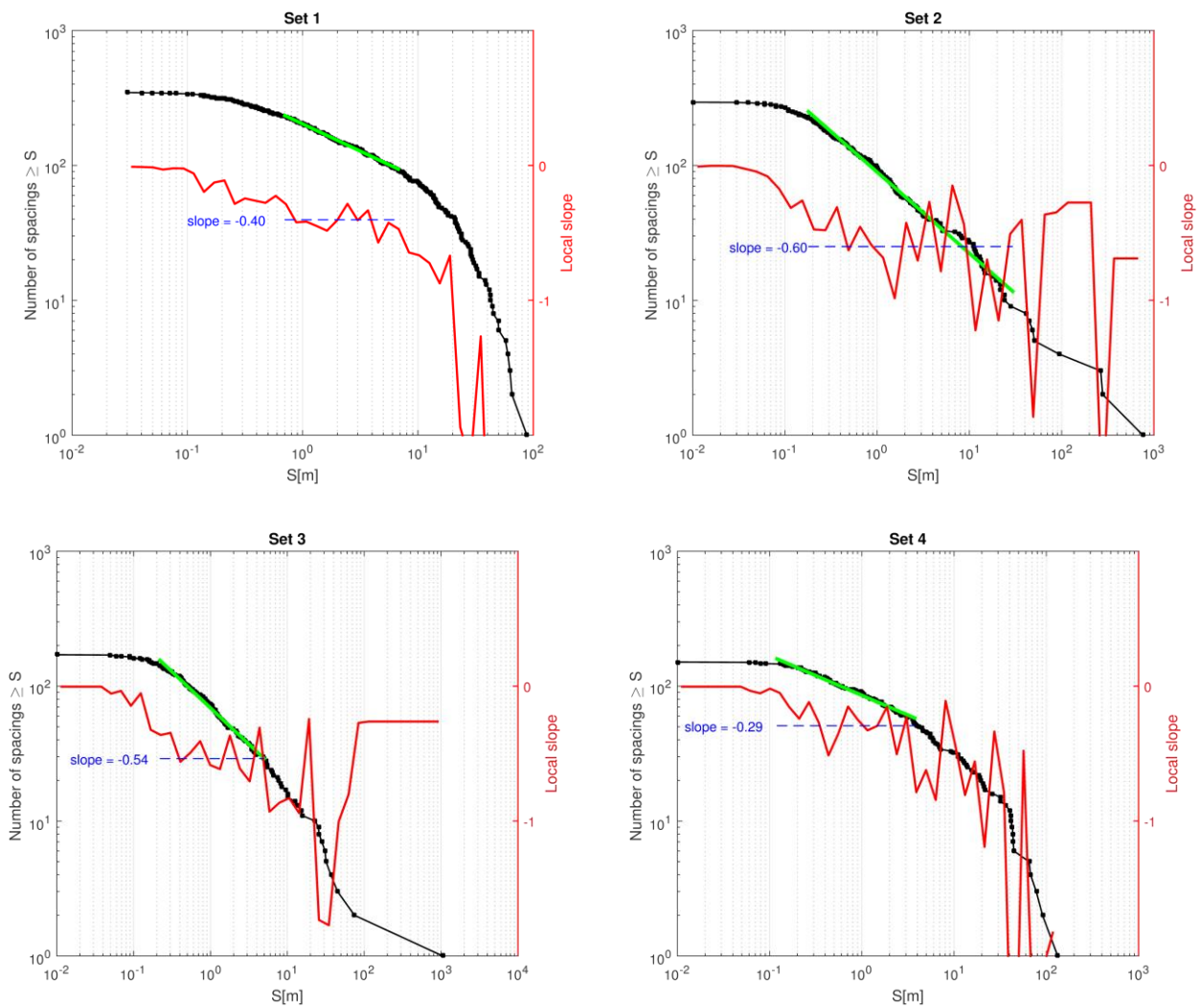
Figure 4.19. Apparent spacing distributions four fracture sets present in Basel (black) and the local slope of the box counting curve is displayed in red and is calculated for by linear fit through data windows with a width of 1/40 of the complete study size range.
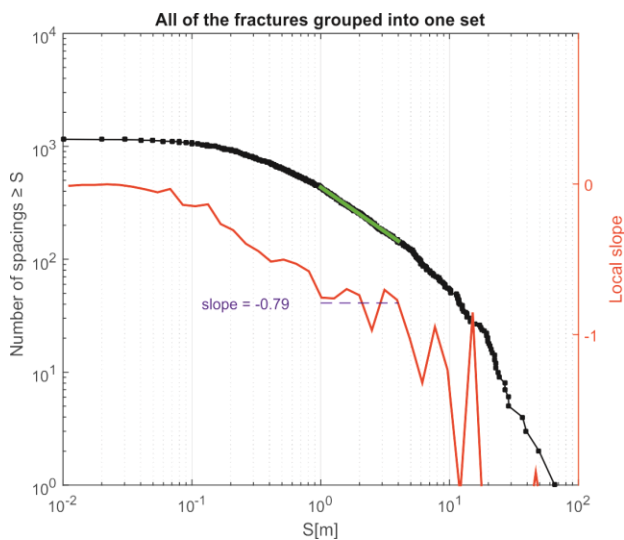
Figure 4.20. Apparent spacing distributions all of the fractures grouped into one set in Basel (black) and the local slope of the black curve (red)

4.2.3.4 Correlation function analysis

Correlation function of different fracture sets in BS1 are calculated using equation 4.3. The correlation function is calculated for logarithmically spaced distance r over four orders of magnitude from 0.1 to 10^3 m. The local slope of the correlation dimensions are calculated using the methodologies we applied for box-counting and cumulative spacing distributions. For all sets, we observe a plateau in the correlation dimension over more than two orders of magnitudes (see Fig. 4.21). The correlation dimensions are 0.74, 0.69, 0.64 and 0.68 for set 1, set 2, set 3 and set 4 respectively. If we group all of the fractures into one set, a clear plateau with little variations (see Fig. 4.22) is also observed and the correlation dimension 0.86.

Figure 4.21. Pair density correlation function of four fracture sets present in Basel (black) and the local slope of the correlation function curve is displayed in red and is calculated for by linear fit through data windows with a width of 1/40 of the complete study size range.
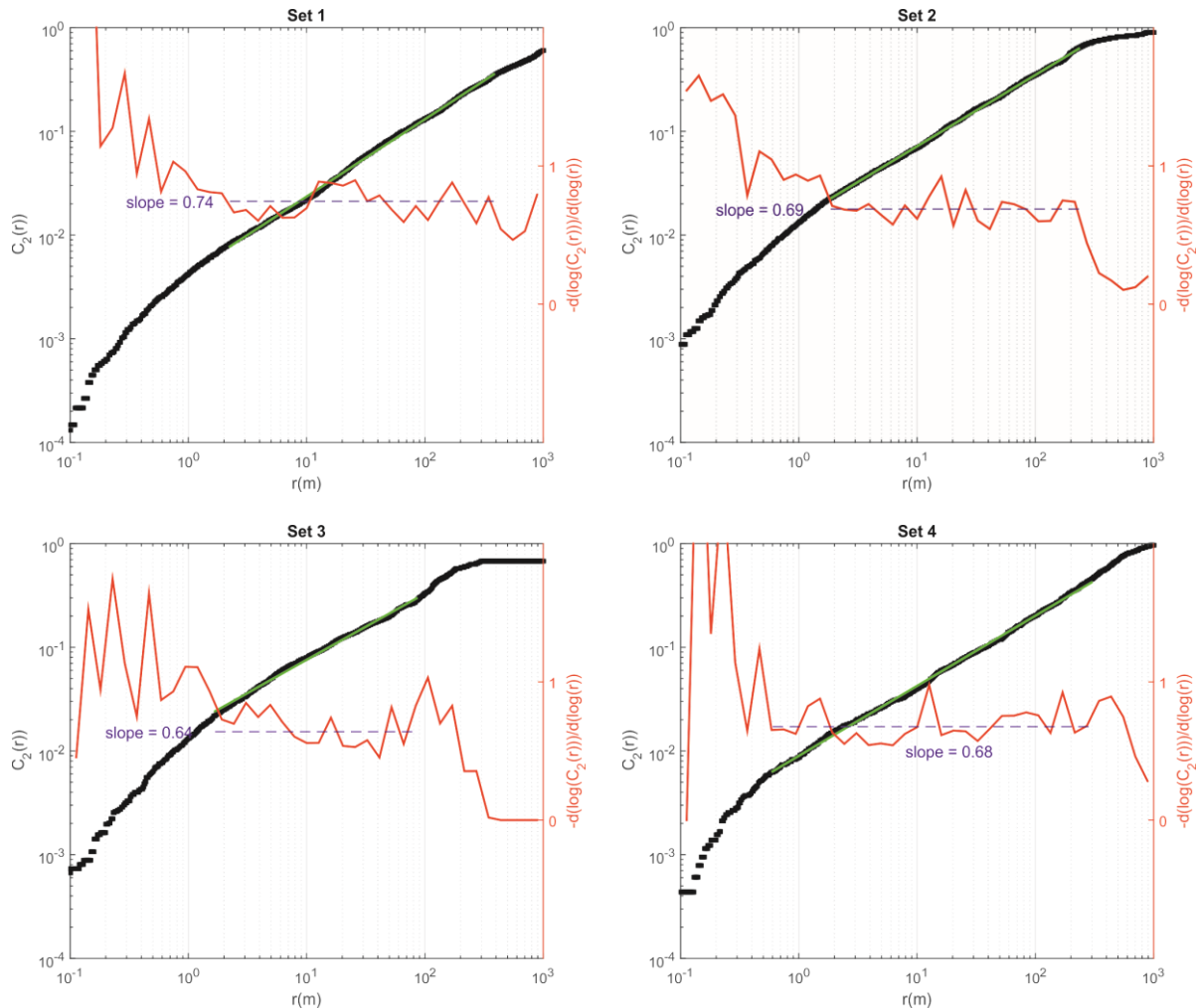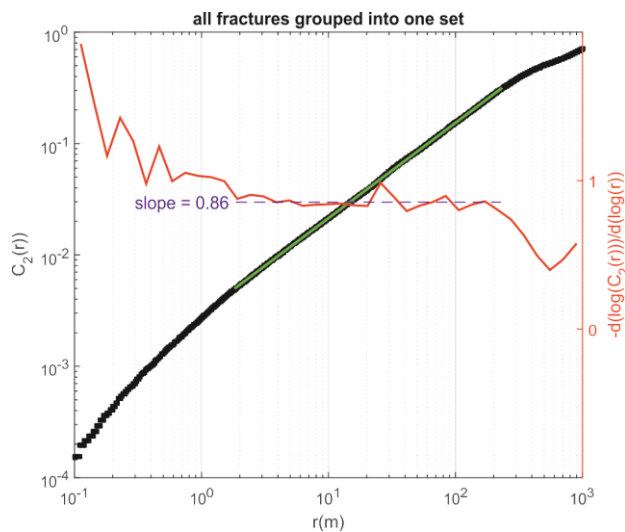
Figure 4.22. Pair density correlation function of all fracture present in Basel (black) grouped into one set and the local slope

4.2.3.5 Discussion

We performed a detailed fractal analysis spacing (spatial distribution) of the fractures from Basel-1 using three different methods: Box-counting technique, cumulative spacing distribution and correlation function. The summary of the obtained fractal dimensions using different methods are presented in Table 4.1.

For the box dimension and power-law exponent of cumulative spacing distribution, the linearity of the graph are almost always disputable and deriving a constant slope and the equivalent fractal dimension is somewhat arbitrary. Such limitation is not present using the correlation dimension method, for which defining a constant slope was much more objective. For the box-counting analysis this is likely due to the bias introduced by the finite size effects (Bour et al. 2002). Therefore, the box-dimensions is not considered as a reliable for estimating the fractal dimension. Nevertheless the large discrepancy between the methods illustrated in Table 4.1 remain unexplained and are under investigation.

In our current knowledge, we consider the correlation dimension method as the most reliable because we can observe a plateau on the local slope over more than two orders of magnitude and thus the determination of the fractal dimension is the least subjective. Bour et al. (2002) have concluded the correlation function characterizes the fracture centers and clustering degree of two dimensional fracture network in Hornelen basin, better than box-counting technique. Our current results suggest that this is also true for one dimensional observations.

Table 4.1. The properties of fractures sets in Basel-1 well and obtained box-dimension

Fracture set	Number of fractures	Box dimension [-]	Power-law exponent of spacing distributions	Correlation dimension [-]
1	348	0.31 *	0.60 *	0.74
2	297	0.52	0.40 *	0.69
3	173	0.48	0.46 *	0.64
4	152	0.24 *	0.71 *	0.68
All sets	1164	-	0.21 *	0.87
* Indicative slopes that are not reliable since linearity was not observed over a sufficient range.				

4.3 Scaling of stress heterogenities

As noted in section 4.1, there are indications that in-situ stress variations, like other geological phenomena, might follow self-affine scaling (Turcotte and Huang 1995). It is hypothesized that such scaling characteristics for stress variations are intimately related to the scaling characteristics of the fracture network and earthquake magnitude-frequency statistics (Day-Lewis et al. 2010). If this were the case, then the measurable variations in stress orientation could be used to constrain statistical attributes of the fracture network that are otherwise difficult to estimate, and to anticipate the seismic response of a rock mass to hydraulic injections.

In order to be of practical value, the scaling characteristics of stress variability must be reliably determined. This contribution evaluates various methods for estimating the scaling characteristics of stress variations by applying them to synthetic series of known fractal dimension. We also evaluate the ability of the methods to deal with gaps in the record and measurement inaccuracy, which is common for borehole failure data. Finally, the various methods are applied to real datasets from three 5 km deep boreholes at Soultz-sous-Forêts and Basel to compare the estimates of fractal dimension of the stress series.

This section builds mostly on a conference paper on the topic (Valley and Evans 2014) with some improvements. The main modification is the selection of another synthetic fractal data generator as explained in Section 4.3.2.

4.3.1 Fractal dimension of 1-D signal

Fractal mathematical models are useful to describe geometries that have no characteristic size or length scale. Statistical fractals are objects that are not exactly identical when changing scale but that conserve their statistical attributes. In this paper we will deal with a one-dimensional series $V(x)$ (e.g. a quantity that varies with time or distance). Fractal distributions are parameterized by the fractal dimension D that specifies how details in a pattern change with the observation scale. Fractal dimension is also a measure of the space-filling capacity. That is, the fractal dimension of a one-dimensional function may vary from $D = 1$, for which the graph is a straight line, to $D = 2$, which is a highly variable quantity whose graph will be a very rough line and which will fill the function space. The distinction between self-similarity and self-affinity is related to the conservation of statistical properties upon magnification of a profile (e.g. Brown 1995). Self-similar shapes repeat them-selves (exactly or statistically) under a magnification with equal scaling for both axis x and $V(x)$ axis. Self-affine shapes, however, require different (but constant) scaling factors to conserve their properties.

4.3.2 Generation of synthetic fractal data

We use fractional Brownian motion (fBm) series of known fractal dimension in order to test various approaches to the estimation of fractal dimension. The Hurst exponent, H, controls the scaling behavior of fractional Brownian motion by the simple scaling law $\Delta V \propto \Delta x^H$. The Hurst exponent takes value in the range $0 < H < 1$. For one dimensional signal, it is related to the fractal dimension by:

$$D = 2 - H \tag{4.7}$$

Pure Brownian motion series can be generated by integrating white noise, (i.e. successive random draws from a normal distribution). Such a series will have a fractal dimension $D = 1.5$. Fractional Brownian motion with other fractal dimensions can be generated using various algorithms summarized by Saupe (1988).

Initially in the work presented in Valley and Evans (2014), we used a frequency domain method developed by Davies and Harte (1987) with a modification from Percival (1992) and Wood and Chan (1994). This algorithm has been implemented in FORTRAN (code called 'fgp', which stands for fractional Gaussian process) by the Physiom project at the National Simulation Resource Center for Bioengineering at the University of Washington (Physiom Project, http://www.physiome.org/software/fractal/). However, it turned out that series produced with the implemented algorithm did not have the specified fractal dimension when D was close to 2 ($H = 0$). Thus, the for the following, the analyses are performed using another fractal signal generator based upon the spectral synthesis methods of Peitgen and Saupe (1988). This code is also implemented in FORTRAN by the Physiom project (http://www.physiome.org/software/fractal/) and is called ssm for spectral synthesis method. Examples of series generated with this algorithm with fractal dimension varying from 1.05 to 1.95 are shown in Fig. 4.23.
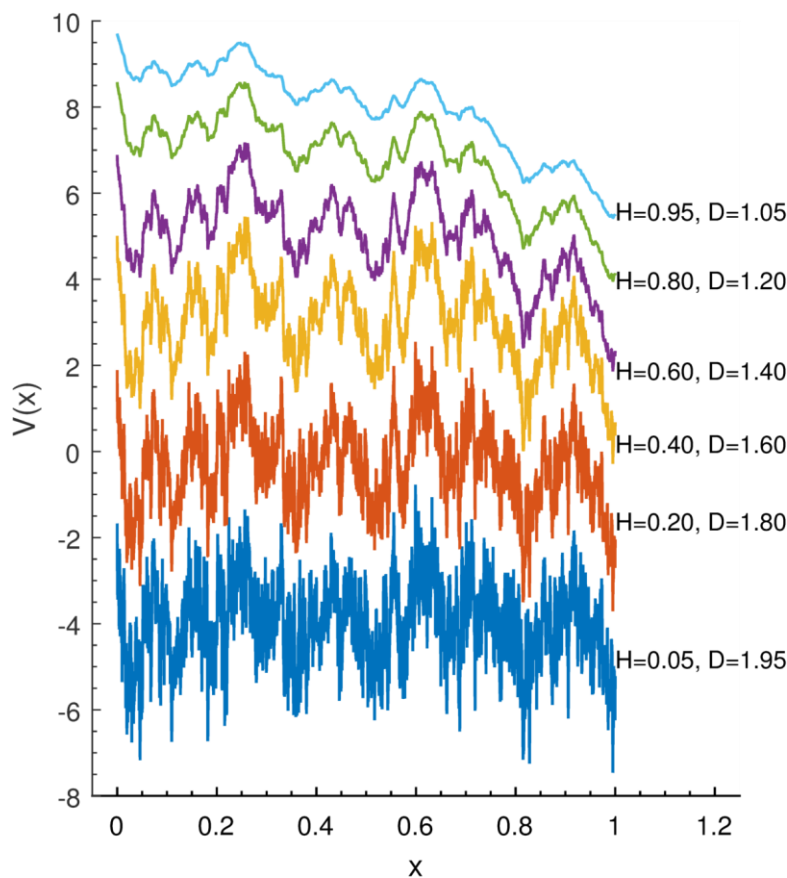
Figure 4.23: Signal generated with a range of Hurst coefficients using the ssm algorithm (see http://www.physiome.org/software/fractal/), but with generating a signal 8 times too long and keeping only the middle part with the target signal size. Here the signals are 2048 (2^11) data point long. The signals have been also centered (mean = 0) and normalized (std dev. = 1). For the figure, the signals have been offset to avoid overlap.

4.3.3 Methods for estimating fractal dimension

Three types of method were tested: divider and box counting methods, windowed variance methods and power spectrum methods. These methods are introduced in the following sections.

4.3.3.1 Divider and box counting methods

Divider and box counting methods are perhaps closest to the original definition of the fractal dimension. Brown (1995) presents improved divider and counting box methods to determine the fractal dimension of self-affine fractals. The divider method is performed conceptually by opening a pair of dividers to some distance r and walking them along the curve of the series to measure its total length λ (Brown 1995). The slope of the total measured length λ vs. r in a log-log plot gives an estimate of the fractal dimension using the following relation:

$$\lambda \propto r^{1-D} \tag{4.8}$$

As noted by Brown (1995), the method breaks down if the divider length r is not much smaller than the series amplitude variations. This can be remedied by iteratively multiplying the series, an operation which does not affect the fractal dimension, until r is small compared to the series variations and a stable determination of D with increasing magnification is achieved.

For the box counting method, the fractal dimension is estimated by laying a grid with n^2 cells over the curve and counting the number of cells $N(n)$ covering the signal. For self-affine series, the aspect ratio of the cells used can introduce bias in the determination of D. To prevent such bias, Brown (1995) suggests using an aspect ratio for the cells of $\lambda_o/6\sigma_o$, where λ_o is the nominal length of the signal, i.e. its length along the x-axis, σ_o is its standard deviation. With this approach, the fractal dimension is estimated by determining the slope of the relation $N(n)$ vs. n on a log-log plot with the following formula:

$$N(n) \propto n^D \tag{4.9}$$

4.3.3.2 Windowed variance methods

Cannon et al. (1997) introduced the scaled windowed variance (SWV) methods for estimating the Hurst exponent *H* of fractional Brownian motion series. The principle is to repeatedly divide the series into sets of windows of length *s*-points, and compute the mean of the standard deviations of each set of windows SD, $\overline{}(s)$ as a function of *s*. The Hurst exponent is estimated on a log-log plot of SD, $\overline{}(s)$ vs. *s* by the following relation:

$$SD, \overline{}(s) \propto s^H \tag{4.10}$$

Implementation of the method without detrending the series in each window will be referred to here as the standard SWV approach. Cannon et al. (1997) also proposed two variations where the series in each window was detrended before computing the standard deviation in order to reduce bias and variability in the estimate of *H.* Detrending is achieve by subtracting a linear regression line for each interval (denoted here as LD-SWV) or a bridge (i.e. straight line from first and last point) over the interval (BD-SWV). Details of the implementation are given in Cannon et al. (1997). The algorithms were implemented in FORTRAN by the Physiom Project.

4.3.3.3 Power density spectrum methods

The power spectral density (PSD), $Sv(f)$, where *f* is the frequency, for a series $V(x)$ is an estimate of the mean square fluctuation of the series at frequency *f*. For a fractal series, the PSD spectrum has a slope of $1/f^\beta$, and thus declines linearly with frequency with a slope of $-\beta$ in a log $Sv(f)$ vs. log *f* plot. The slope β is referred as the spectral index. For a one-dimensional fractal signal, β lies in the range $1 < \beta < 3$, and is related to the fractal dimension by:

Error! (4.11)

The options to determine *D* using PSD methods are thus distinguished by the approach used to determine the power density spectrum. We use an approach based on a fast Fourier transform with pre-filtering of the data using a Hanning window (FFT). In order to reduce the noise on the obtained spectrum we used section averaging, which averages the spectra obtained on segments of the complete signal. The noise reduction is obtained at the expense of frequency resolution. In our analyses we split the signal in 15 segments with a 50% overlap (i.e. Welch's method). The method is implemented in MATLAB[TM]. The fast Fourier transform and Hanning window function are part of commercial MATLAB[TM] distributions.

4.3.4 Evaluation on synthetic data

The methods of estimating the fractal dimension, *D*, are evaluated and compared by applying them to synthetic series of known fractal dimension. It is assumed that the true fractal dimensions of the generated series correspond to the expected values. Although we cannot be sure of this, some small deviation can be tolerated since the primary objective is to compare the *D*-estimates from the different methods rather than the absolute value of *D*. The processing is applied first on clean synthetic data and then on series degraded by adding noise or gaps.

4.3.4.1 Clean continuous data

A comparison of the *D*-estimates obtained by applying each method to clean data series of known fractal dimension in the range *D* = 1.0 to 2.0 is presented on Fig. 4.24. Each estimate was made over 100 randomly generated fractal series with 2048 data points (similar to the series shown in Fig. 4.23). The median, lower- and upper-quartile values of *D* obtained for the 100 realizations is displayed as a function of the expected fractal dimension of the generated series. A perfect estimation of *D* would plot on the 1:1 lines that are drawn for convenience (note that the curves have been offset to facilitate readability).
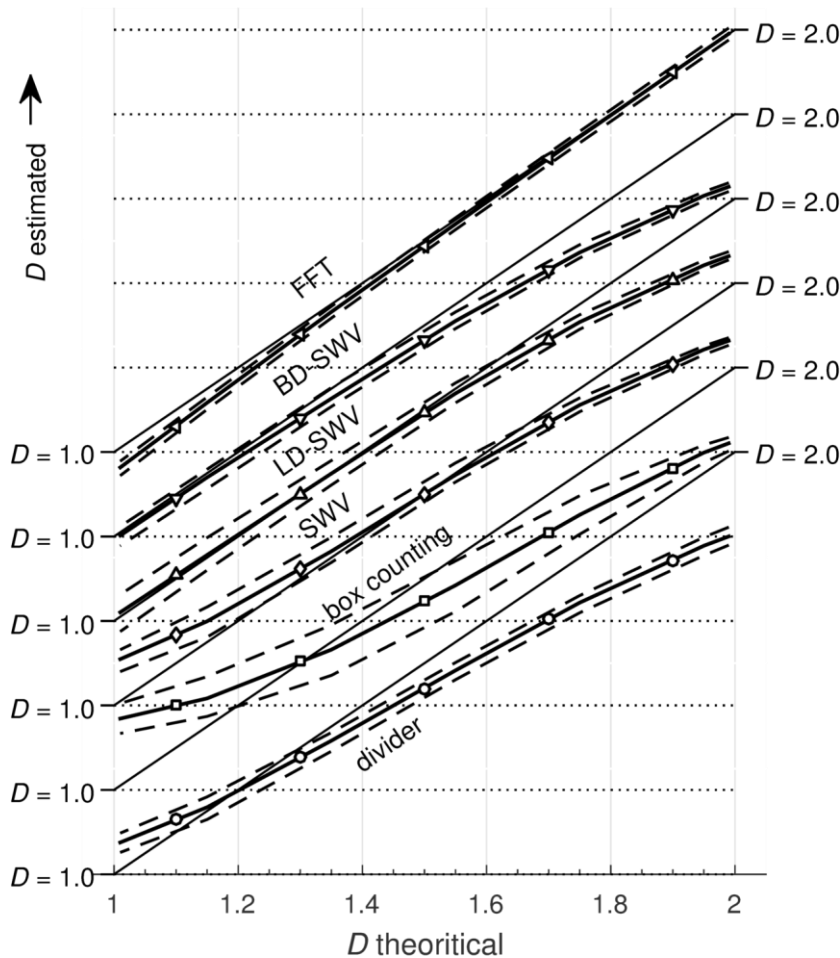
Figure 4.24: Evaluation of the accuracy of methods for estimating D of synthetically-generated series whose D-value is known and ranges between 1.0 and 2.0. The series have 2048 data points. The solid and bounding dashed lines denote median and lower and upper quartiles of estimate distributions computed over 100 randomly generated series.

Fig. 4.24 suggests that the FFT methods generally yield the best estimations of D over the range considered. The estimates are slightly low for low values of D, but the medians are always within 0.05 and the quartiles within 0.07 of the expected value for the series. With this approach, the interquartile range is very tight, 0.035 at most. The next best estimates are obtained from the windowed variance methods. However, these methods progressively underestimate the value of D for expected D values higher than 1.5. In addition, the SWV method also overestimates the value of D for small D. The interquartile range is also larger, up to 0.09, in comparison with the results obtained from the FFT method.

The divider method gives results that are qualitatively comparable to the one obtained with the SWV. The box counting method shows the largest most pronounced discrepancy and the largest interquartile range.

The impact of series length on the accuracy of the fractal dimension estimates was evaluated for series with expected fractal dimension $D = 1.2$, 1.5 and 1.8 by varying the length of the series from 128 to 8192 data points (see Fig. 4.25). Generally, the interquartile range of the estimates increased with decreasing series length. For example, for the DIVIDER method, the interquartile range of the estimate of D for expected $D = 1.5$ increases from 0.02 for a series length of 8192 points to 0.12 for a series length of 128 points. For the DIVIDER, SWV and LD-SWV, the median of the estimates is not too strongly affected by decreasing series length, whereas for other methods it increases the discrepancy between the estimated median and expected value of D. For all methods, lengthening the series beyond 1024 data points does not significantly improve the median of the estimates of D, except for the FFT method for low D-values where the estimates continue to improve and become almost exact for series of 8192 or more.
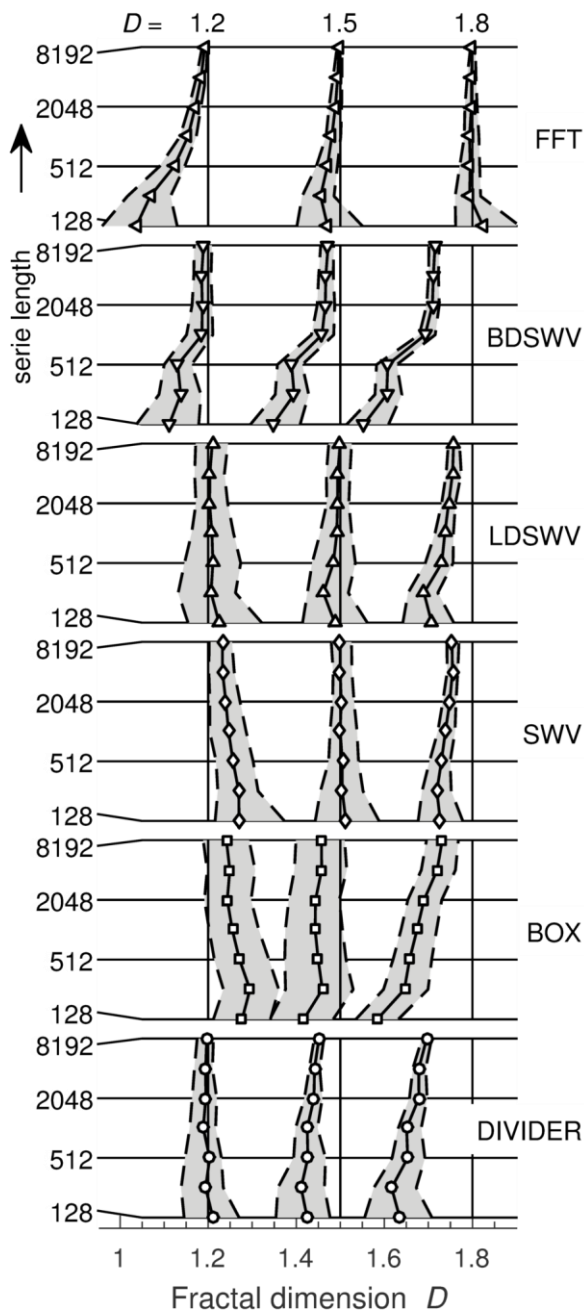
Figure 4.25: Impact of the number of data points in the source series on the accuracy of the estimates of *D* for the methods considered. This evaluation was performed for D = 1.2, 1.5 and 1.8 and for series lengths from 128 (2^7) to 8192 (2^{13}) data points. Solid line lines are medians and dash line are lower and upper quartile computed over 100 randomly generated signal. Greyed area is the interquartile range.

4.3.4.2 Data with noise

Noise is invariably present in a series describing the measured variation of any physical variable. For the case of interest, that of profiles of the orientation of the maximum horizontal stress, SHmax, from say borehole breakouts, the uncertainty in determining the center point of the breakout will add some noise to the SHmax-orientation estimates. The impact of such random noise on the estimates of fractal dimension of the synthetic fractal series is evaluated by adding Gaussian noise to the data. The results shown Fig. 4.27, correspond to the case where the standard deviation of the added Gaussian noise is 1/60 of the total range covered by the series. Examples of the data series with the added noise are shown of Fig. 4.26 (to be compared with Fig. 4.23). This scaling is necessary because the range of series of different fractal dimension generated by the algorithm varied over several orders of magnitude. Normalizing by a fraction of the range thus simulates the case of adding constant amplitude noise to series of the same range (such as

those shown in Fig. 4.23). Series of 2048 data points length were used. For all methods, the impact of the noise is to give progressively greater overestimates of D for series whose theoretical D less than 1.5. The method that is most resistant to the added noise is the box counting method. The maximum discrepancy between estimated and expected D occurs for $D = 1$ and is about 0.34. For the divider and windowed variance methods, this difference reaches 0.9 and for the FFT method it reaches excessive values suggesting the signal may not be considered as fractal anymore.

Generally, random noise added to the data will have a severe impact on the determination of the fractal dimension when $D < 1.6$. If the underlying signal has a fractal dimension smaller then 1.6, it is very likely that the determined fractal dimension will be severely overestimated.
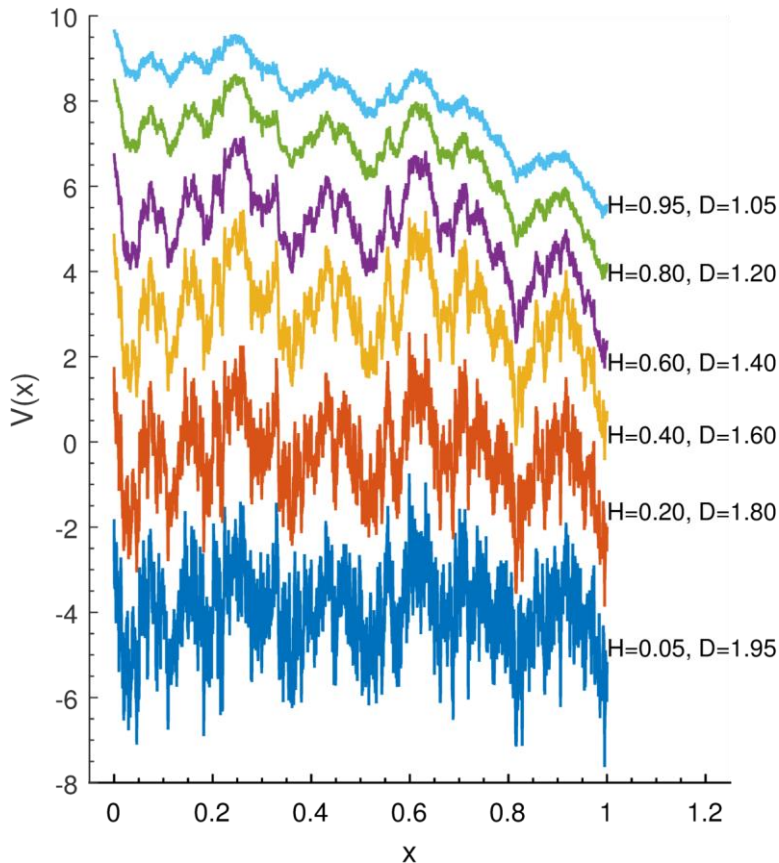
Figure 4.26: Examples of data series with added noise. Compare these series with the noise-free data series of Fig. 4.23.
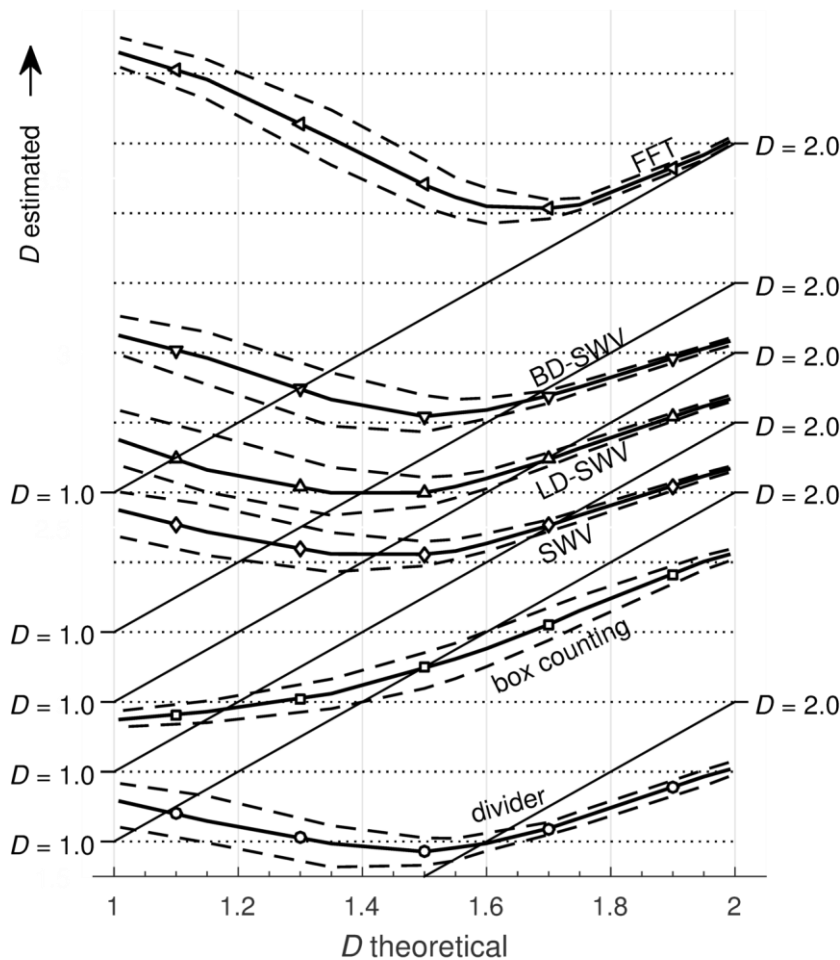
Figure 4.27: Evaluation of the accuracy of methods for estimating D when random noise is added to the fractal series. Gaussian noise with a standard deviation of 1/60 of the range of the fractal series is added. The series length is 2048 data points.

4.3.4.3 Data with gaps

   Typically, wellbore failure is not continuous, and thus the series describing the variation of a stress attribute along the borehole will include gaps. The effect of gaps in the data on the estimates of D is evaluated by randomly adding gaps to the synthetic fractal series. Two parameters were used to control the application of gaps to the data: 1) the percentage of missing data, which can vary between 0% for continuous data to 100% for no data, and 2) the number of gaps. For the same percentage of missing data, if the number of gaps is higher, the gaps will generally be shorter. However, the actual size and location of the gaps is random.

   In all methods, the gaps were filled by straight lines (i.e. linear interpolation) prior to the analysis. Fig. 4.28 shows a comparison of the D-estimates for the case where 35% of the data are missing, distributed over 40 gaps. In this case, the estimates for the FFT method are the least affected by the presence of gaps, the estimates being about 0.04 too low over the entire range of D. For the box counting, standard SWV, and LD-SWV methods, the underestimate is up to 0.1, and for the divider and BD-SWV methods it is slightly larger. The bias generally becomes more pronounced when the percentage of missing data increases. This is illustrated in Fig. 4.29 for the FFT method. The degradation of the estimate becomes even more pronounced if the missing data are distributed over many gaps. When there are 30 gaps, the underestimation of D is always less than 0.1 even with 85% of the data missing.
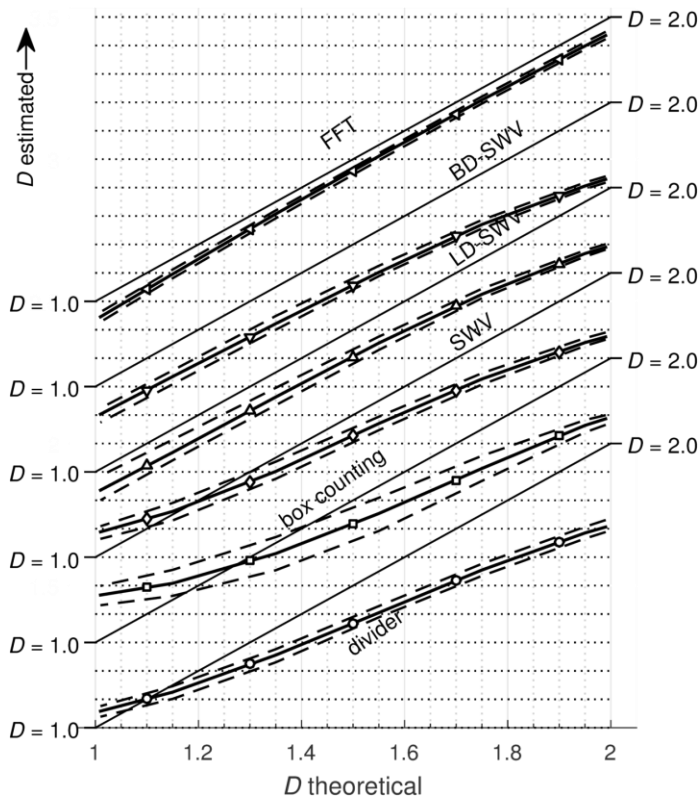
Figure 4.28: Evaluation of the impact of gap on the estimates of *D*. In this example, 35% of the data were removed distributed over 40 gaps.
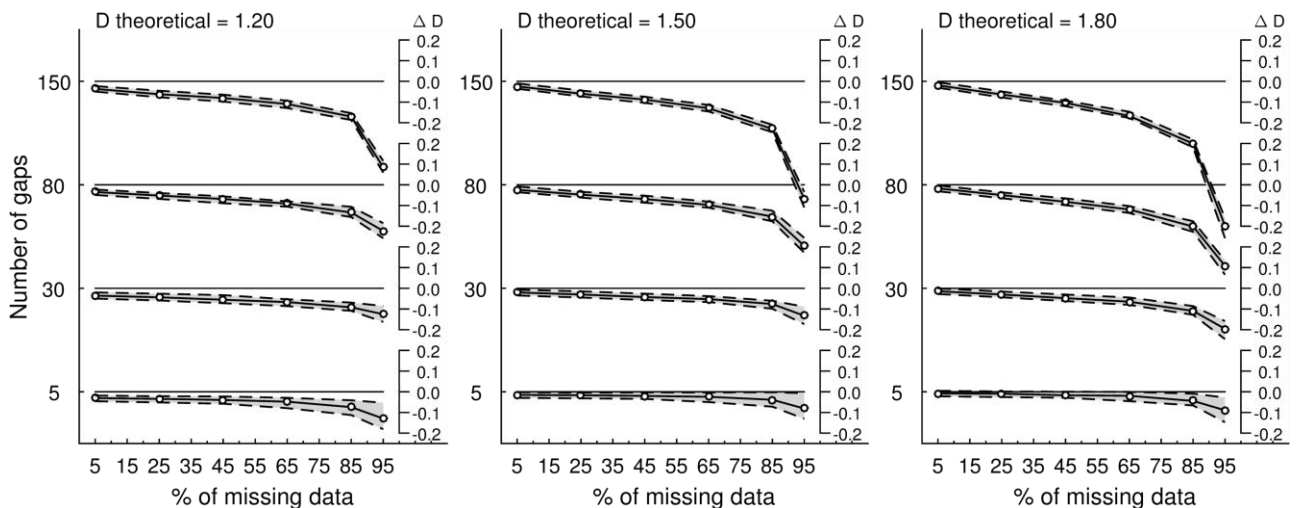
Figure 4.29: Evaluation of the impact on percentage of missing data (from 5 to 95%) and number of gaps (for the case 5, 30 80 and 150) using the FFT method. Calculation are performed for theoretical *D* of 1.2 (left), 1.5 (middle) and 1.8 (right). ΔD, the difference between the estimated *D* and theoretical *D* is displayed. For each case, 100 realization are computed and the median is displayed (solid line with circle symbols) with the interquartile range (grey area limited by dashed lines).

4.3.5 Application to real stress data

In this section, the various methods of determining fractal dimension are applied to real borehole failure data. The datasets stem from three deep boreholes: GPK3 and GPK4 located at the Soultz-sous-Forêts EGS site in France, and borehole BS1 at Basel in Switzerland. The original data for Soultz-sous-Forêts are presented in Valley and Evans (2010) and for Basel in Valley and Evans (2009). The data sets consist of profiles of SHmax-orientation derived from wellbore failure indicators.

In the case of the Soultz-sous-Forêts data, the orientation of the features were determined over successive 0.5 m windows, whereas for the Basel data, the orientation of the features were determined every 0.4 m. For each well, the mean SHmax-orientation was subtracted from the data in order to keep only the variation from the mean. The data were prepared for the analyses by resampling at a uniform spacing of 0.1 m. Only subsections of the datasets where the SHmax-orientation estimates are relatively continuous are considered for the analyses performed in this paper.

The prepared datasets are presented in Fig. 4.30, and a summary of their key characteristics is given in Table 4.2. For the GPK3 and GPK4 datasets, the SHmax-estimates in the selected intervals are derived largely from drilling induced tension fractures, whereas for BS1 data. the estimates stem principally from borehole breakouts.
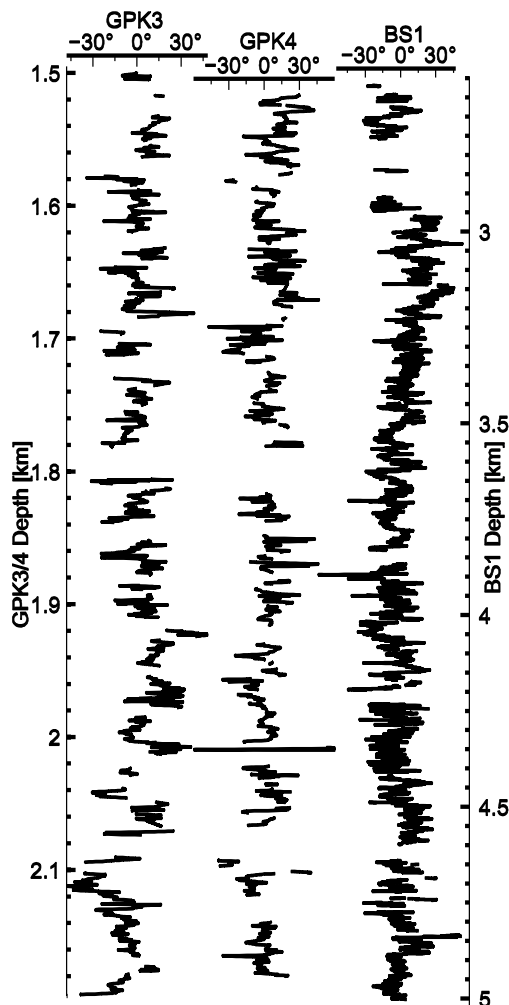
Figure 4.30: Sections of the GPK3, GPK4 and BS1 data sets used in this paper.

Table 4.2: Summary of key characteristics of the prepared data

Hole	GPK3	GPK4	BS1
Interval	1495 – 2195 m	1511 – 2186 m	2618 – 5000 m
Length	700 m	675 m	2382 m
Number of data point	7001	6751	23820
% of missing data	36%	35%	19%
Number of gaps	41	43	115
Longest continuous data section	63 m	44 m	99 m
Longest gap	24 m	35 m	80 m

The fractal dimension estimates obtained by applying the six methods to each of the three data sets are summarized in Fig. 4.31. The interpretation of the results is not trivial since large variability between the estimates derived from the different methods for a given borehole is evident. The FFT method yielded the most reliable results across the entire range of *D*-values in the study with synthetic data. The low values obtained from the DIVIDER and BD-SWV methods probably reflect the effect of the gaps. The study on synthetic data indicated these methods more strongly underestimate *D* in the presence of gaps, and the discrepancy with the other methods is not so marked for the BS-1 data, which contains far fewer gaps. If this is accepted, then the best estimate of *D* for GPK4 is 1.75 and for BS1 it is 1.74, whilst for GPK3 it is 1.68. The important conclusion is that there is more similarity in the range of *D*-estimates between GPK4 and BS1 than there is between GPK3 and 4, despite the fact that the latter two sample essentially the same rock volume.
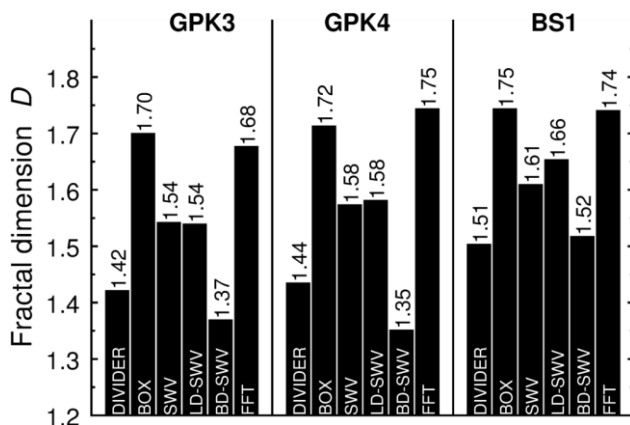
Figure 4.31: Fractal dimension estimate for the three data sets investigated using the six methods presented above.

A more detailed analyses of the BS1 dataset was performed using the FFT approach in order to clarify the form of the power spectrum at long wavelengths. Power Spectral Density (PSD) estimates were derived in a similar manner than explained in Section 4.3.3.3 but with 20-30% overlap of adjacent series segments. The results are presented in Fig. 4.32 for two analyses in which gaps in the original series shorter than 15 m and 41 m were filled with linear trends. Including longer filled gaps in the analysis serves to increase the length of continuous sections, thereby allowing PSD estimates to be derived for longer wavelength variations. Filling all gaps with length less than 41 m yielded 4 sections of 650 m length to be formed with 27% overlap.
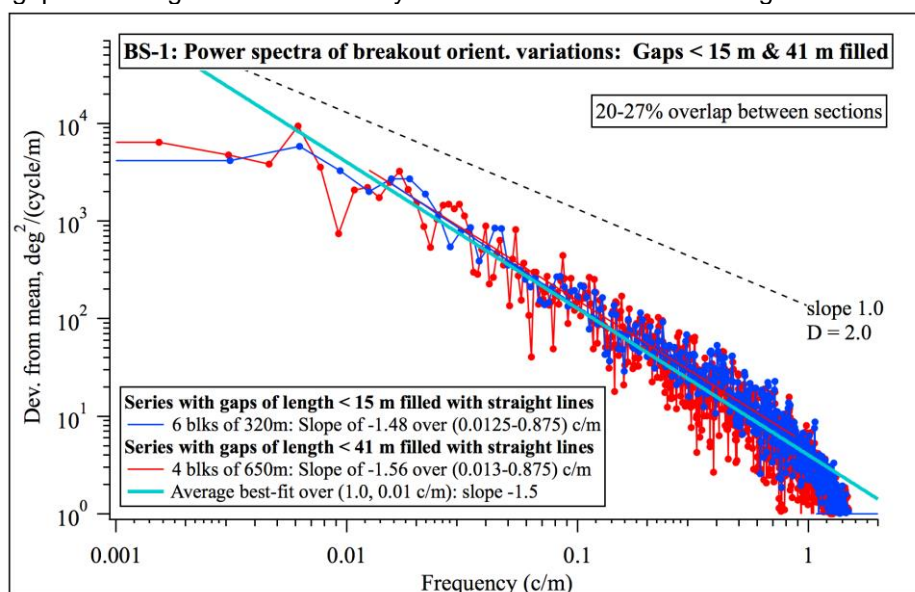
Figure 4.32: PSD functions derived from the BS-1 data for two series which differ in the maximum gap length that was filled with linear trends. Both curves define a slope of about -1.5 extending from 1 c/m to 0.01 c/m, and become flat at frequencies less than 0.01 c/m.

The analysis yielded the following results:

- The log-log plot of PSD vs frequency is linear between 1 and 0.006 c/m (wavelengths of 1 and 166 m) and has a slope of -1.5, implying a fractal dimension D = 1.75. This is in agreement with the results presented above using the FFT method.
- At frequencies above 1 c/m, the power decreases faster than for the linear trend. Fluctuations at such short wavelengths are expected to be small, and approach the scale of the borehole itself.
- At frequencies lower than 0.006 c/m (wavelengths longer than 166 m), the spectra becomes flat and remains so out to the longest wavelength of 650 m at which PSD could be estimated. This flattening is also evident in the spectra from the higher-quality series with gaps up to 15 m filled, for which the 6 sections of length 320 m could be formed. Consequently, it is possibly real and not an artifact of the uncertainty in the spectra at the longest wavelengths resolved.

4.3.6 Conclusion

The determination of fractal dimension from borehole failure data is not a trivial exercise. Biases can occur because the data contain noise and gaps.

The assessment performed in this study used synthetic series of known fractal dimension to tests the various methods for estimating D. The effect of gaps and noise in the data on the estimates was evaluated. The FFT method was found to yield the best estimates of D when gaps were present, as is often the case with stress profiles from wellbore failure data. The various methods were then applied to real data sets from Soultz-sous-Forêts and Basel. Significantly different estimates of D were found for different methods applied to the same dataset which are best explained as reflecting the impact of gaps in the data. Analysis of the BS-1 dataset using the FFT approach suggests a change in scaling may occur at wavelengths longer than 100 m

4.4 Estimating fracture length

As stated in the introduction, the practical implications of the work presented in Sections 4.2 and 4.3 is to provide methodologies to better characterize the rock mass targeted by deep EGS, particularly with regard to the properties of the fracture network and stress variability. The methodologies presented in Sections 4.2 and 4.3 are based on statistical approaches with the concept of scaling invariance as the basic assumption on which the work is developed. In the following, we investigate another venue with the same objective of characterizing fracture network properties but using a more direct and deterministic approach. This work was initially presented at the DFNE conference in Vancouver (Valley et al. 2014).

4.4.1 Introduction

The starting point of the work presented in this section is to use this potential relationship between the natural fracture network and stress variability to constrain characteristics of the natural fracture network that are otherwise not determinable. Specifically, we present and evaluate the practicality of a possible approach for the determination of fracture lengths constrained by the observation of stress variability.

The fundamental concepts are developed in two dimensions and tested using a synthetic data set generated from stress models. The simple case of a stress perturbation due to a single fracture is examined first. This is used to evaluate parameter sensitivity by solving the forward problem (i.e., determining the stress profile knowing all the fracture characteristics). Then, the inverse problem is solved (i.e., determining the geometrical characteristics of the fracture knowing the stress profile) using an optimization routine that iteratively adjusts the fracture geometrical characteristics and computes the stress perturbations induced by the natural fractures until a satisfactory match between the modelled and observed stress perturbation is obtained. The method is first applied to the single fracture case and then to the case of a fracture network.

4.4.2 Constraining fracture and stress at the borehole

The primary source of information for characterizing fracturing in deep boreholes are datasets stemming from borehole wall imaging sondes. Both natural and stress induced features can be distinguished on these images. The location and orientation of natural fractures can be directly measured. However, it is not

possible to determine fracture length or connectivity. Stress induced features like axial drilling-induced tension fractures (ADITFs), en-echelon drilling-induced tension fractures (EDITFs) and borehole breakouts can also be identified. These features provide an estimate of the orientation of the principal stresses in the plane perpendicular to the borehole axis and provide some constraints on their magnitude.

The variation of the attributes of stress along the borehole seem to be influenced by natural fractures that intersect the borehole (Valley and Evans 2010). A plausible interpretation of this observation is that the observed stress perturbations reflect the accommodation of past or current tectonic deformation by slippage on the fracture planes. If that is the case, the characteristics of the stress perturbation should capture some geometrical and mechanical characteristics of the fractures. In this study, we focus on evaluating the degree to which constraints on fracture length can be derived from the characteristics of the stress perturbation. We perform this evaluation by assessing the sensitivity of the stress perturbation induced by slip on a fracture to the fracture length using a numerical modeling approach.

4.4.3 Modelling the stress perturbation induced by fractures

4.4.3.1 Modelling assumptions

In order to keep the sensitivity analyses tractable, we will treat the problem as a 2D, plain strain problem. This implies assumptions on the shape of the fracture, i.e. we will only consider straight fracture traces of variable length in the modeling plane while the out-of-plane fracture length is assumed to be infinite. The rock mass is represented as an isotropic, homogeneous elastic medium subjected to far-field principal stresses and the fractures as elasto-plastic Mohr-Coulomb frictional interfaces.

After applying initial stress conditions, the fracture is allowed to slip and the resulting stress field around the fractures computed using the displacement discontinuity method (DDM) from Crouch (1976). In our solution, we solve for both the normal and shear relative displacement at the fracture plane, allowing for mobilizing the fractures both in shear and opening. The model parameters describing the problem are listed in Table 4.3.

Table 4.3. Listing of inputs parameters required for the DDM approach and values used for the base case in the parameter study.

Description	Parameters	Base case values
Fracture geometry	l, α and i:length, angle from vertical and intersection ratio	l = 15 m α = 30° i = 0.5
Far-field stress	σ_{xx} , σ_{yy} , σ_{xy}	σ_{xx} = 20 MPa σ_{yy} = 38 MPa σ_{xy} = 0 MPa
Rock properties	E, ν: the Young's modulus and Poisson's ratio	E = 60 GPa ν = 0.25
Fracture properties	K_n , K_s , c, ϕ: the shear and normal stiffness, the cohesion and the angle of friction	K_n = 1e5 MPa/m K_s = 1e4 MPa/m c = 0 MPa ϕ = 10°

4.4.3.2 Stress Perturbation of a Single Fracture

We performed a parameter study on the model inputs listed in Table 4.3 with the objective of identifying the parameters that had the most influence on our estimation of fracture length for the observed stress perturbation. We limited this study to parameters that cannot be constrained independently.

The key parameters for our analyses are the ones related to the fracture geometry. Our analyses are restricted to 2D geometries and we considered the case of a fracture intersected by a vertical hole. Within these assumptions, the fracture geometry can be determined using three parameters: fracture length, l; fracture angle from vertical, α, varying from 0° to 180°; and an intersection ratio, i, as defined in Fig. 4.33,

which is the ratio of the distance of the borehole intersection point from the tip with the smallest x-coordinate to the length of the fracture (i.e. it takes a value of 0.5 when the hole intersects the center and 1.0 at the tip with the largest x-coordinate). The angle α can be directly measured on borehole images and will not be considered as a variable in our analyses.
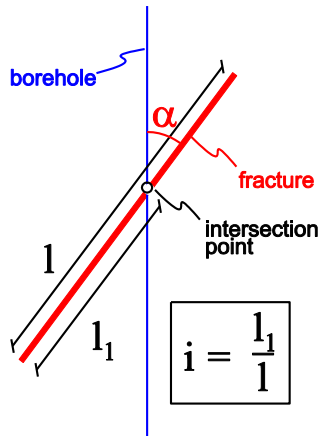
Figure 4.33: Definition of the parameters defining the fracture geometry. l is the fracture length and i is the intersection ratio.

The far-field stress state at a site is typically approximated by averaging stress estimates, and/or by deriving a first order characterization typically in the form of linear depth trends for the principal stress magnitudes. The more difficult question, however, is to decide what far-field stress is relevant for the formation of a stress perturbation around a fracture. Typically, a rock mass is subjected to a succession of changing stress regimes over geological history. The final stress perturbation around a fracture may, thus, reflect the effect of multiple, successive slips on the fracture plane.

The reconstruction of the stress history from the final slip state would be very challenging, to say the least. In our analyses we adopt the working hypothesis that the stress perturbation has developed entirely within the current stress field to render the problem tractable.

The impact of fracture length on the vertical profile of β is illustrated in Fig. 4.34. Fig. 4.34a shows the case when the fracture is intersected at its center. The pattern of variation of β is symmetric about the fracture center and scales linearly with fracture length. When the fracture is not intersected at its center, the pattern is asymmetric with a sharp discontinuity across the fracture plane. However, the pattern of variation of β also scales linearly with fracture length.
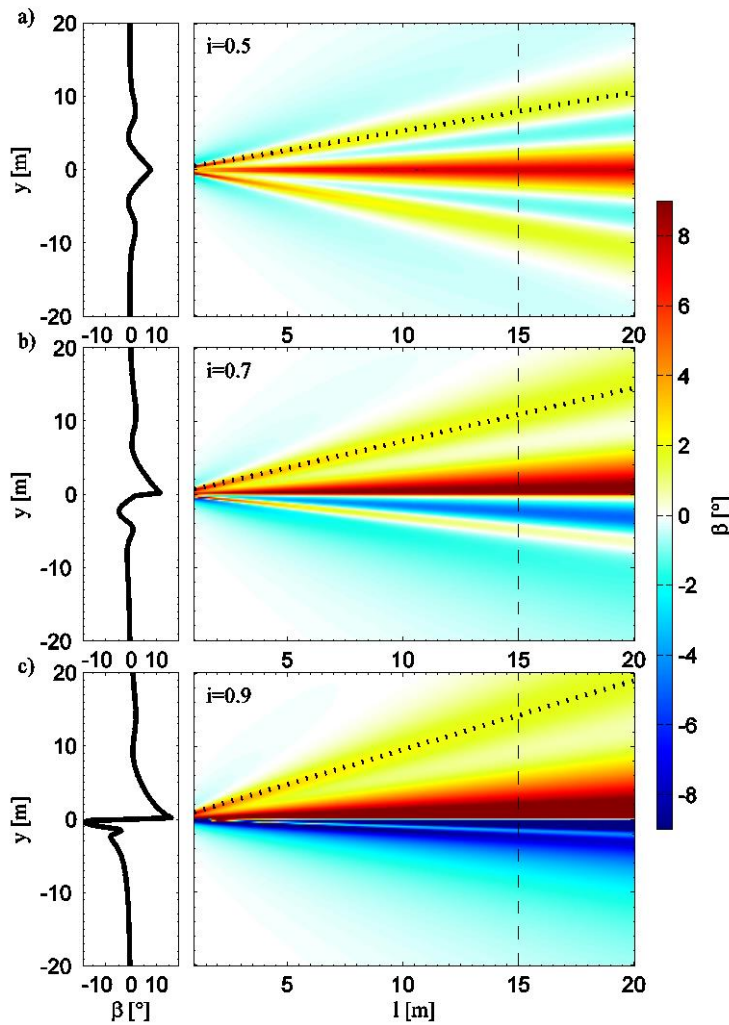
Figure 4.34: Effect of fracture length on the vertical profile of β. At y = 0, the vertical profile intersects the fracture [a) for i = 0.5, b) for i = 0.7 and c) for i = 0.9]. All input parameters are listed in Table 4.3. On the left hand side, the profiles of β for a fracture length l = 15 m are shown (the profile locations are highlighted by the dotted lines on the right hand figures). The dotted lines highlight the direct linear dependency of the β profile pattern on fracture length.

The exact pattern of β variation is controlled primarily by the intersection ratio (i.e., the parameter i). This is shown in Fig. 4.35 where the profiles of β are mapped for i varying from 0 to 1 and all other parameters are as listed in Table 4.3. The profile of β becomes more asymmetric the further the intersection point is away from the fracture centre (i = 0.5).
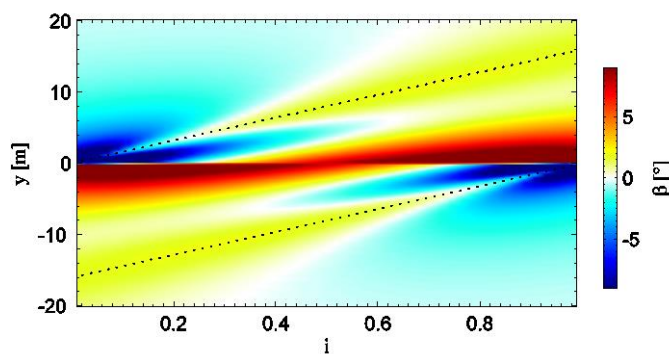
Figure 4.35: Effect of the fracture intersection point (i) on the profile of β. All input parameters are listed in Table 4.3. This is the case for l = 15 m and α = 30°.

In summary, the parameters that have the largest influence on the stress perturbation pattern are the intersection ratio (i) and the fracture orientation (α), although the latter can be determined on borehole wall image. Strength parameters and principal stress ratio have limited impact on the pattern of the perturbation, although they influence the intensity of the stress perturbation. The only parameter that impacts the scaling of the perturbation along the borehole (i.e. the range of influence) is the fracture length.

4.4.3.3 Stress Perturbation of a Fracture Network

When multiple fractures are present, the stress situation is much more complex, as illustrated in Fig. 4.36a. In this model, a fracture network with two fracture sets was generated and the stress perturbation induced by the fractures was computed.

Vertical profiles at x = 0 m of both stress orientation (β) and stress magnitude (σ_1) are presented in Fig. 4.36b. Profiles at x = 0 m intersect 8 fractures. The relation between the pattern of the stress perturbation and the fracture intersections is not obvious. This is due to the effect of fracture interactions and the influence of the stress perturbation induced by fractures that do not intersect the profile. In the following, we will investigate the practicality of an inverse approach to relate the observed, complex stress profile to geometrical characteristics of fractures.
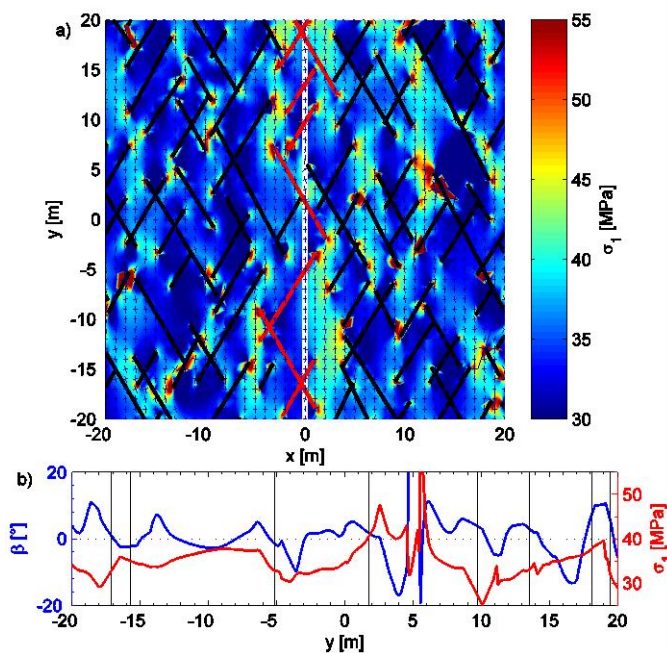
Fig. 4.36: a) a synthetic fracture network with two fracture sets and the corresponding computed stress perturbation. All stress and mechanical properties used are from Table 4.3. Fracture lengths follow log-normal distribution and fracture orientations a Von Mises distribution. Set 1 has a mean α of 30° and a mean length of 6 m while set 2 has a mean α of 150° and a mean length of 13 m. The fractures in red intersect a vertical profile at x = 0. b) stress along a vertical profile at x = 0. The vertical black lines indicate the locations of fracture intersections along the profile.

4.4.4 Inverse approach to extract fracture geometrical characteristics from a stress profile

The inverse problem consists of determining fracture geometrical characteristics, specifically fracture length, when the stress profile along the borehole is known. The approach proposed here uses an optimization routine that iteratively adjusts the fracture geometrical characteristics, computes the induced stress profile, and compares it with the observed stress profile until a satisfactory match is obtained. The approach is illustrated first for the case of a single fracture and then for a fracture network.

4.4.4.1 Determining Geometrical Characteristics of a Single Fracture

Based on the sensitivity analyses presented in Section 4.4.3.2, we will consider the fracture length, l, and the fracture intersection point, i, as the unknown parameters. Having only two unknown parameters has the advantage of allowing us to easily visualize the solution space. The fracture angle, α, can be measured at the borehole wall and is considered as a known parameter. The stress perturbation (as before, we will consider here only the deviation from vertical of the σ_1 direction, β) is the primary input to the inverse problem. All other parameters listed in Table 4.3, i.e., the stress and strength parameters, are considered to be known exactly.

We use the base case, i = 0.5 and l = 15 m from Table 4.3 to illustrate our approach. We compute the stress profile along a borehole penetrating the fracture in its center: this will be referred to as the observed stress profile, $\beta^{obs.}$. We compute the stress profiles, $\beta^{comp.}$, caused by the fractures having a range of combinations of intersection ratio, i, and length, l (all fractures intersect the profile at y = 0 and have an angle $\alpha = 30°$). We evaluate the similarity of the computed profile with the observed profile using a least square estimation as follows:

$$\phi = \Sigma \ (\beta^{comp.} - \beta^{obs.})^2 \tag{4.12}$$

If the observed profile and the computed profile are identical, ϕ will be equal to 0. An increasing value of ϕ implies increasing dissimilarity between the profiles.

The result of this analysis is presented in Figure 4.37. Over the range of i and l considered, the solution space is continuous with a single global minimum (Figure 4.37a). This minimum is well defined, unique, and fits exactly with the expected outcome (i = 0.5 and l = 15 m). The value of ϕ is generally very sensitive to i (Figure 4.37b) but less sensitive to the value of l (Figure 4.37c). Issues are encountered for small values of l, when the fracture length is of similar size than the sampling rate of the stress profile. In such case, the perturbation induced by a fracture is captured by only a few data points and thus is not well defined. Associated with this problem, another aspect of the solution space to be noted is the presence of a local minimum for small l values (Figure 4.37c).

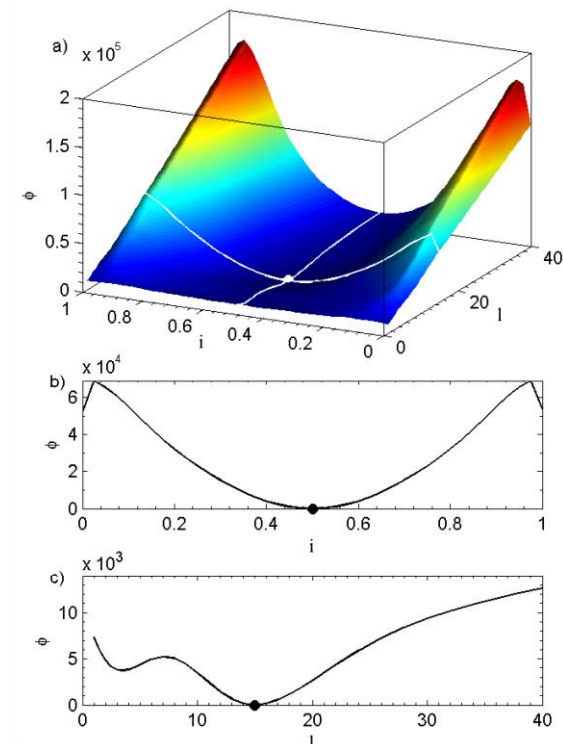Fig. 4.37: Illustration of the inverse approach to compute fracture geometrical characteristics for the case of a single fracture. The observed data are for the base case presented in Table 4.3 (i = 0.5, l = 15 m). a) Solution space of similarity ϕ, for i values ranging from 0 to 1 and l values ranging from 1 m to 40 m. b) and c) sections through the solution space at l = 15 m and i = 0.5, respectively.

Due to the characteristics of the solution space presented in Figure 4.37a, the minimum can be reliably found using a minimum searching algorithm. We use a Nelder-Mead simplex algorithm described in Lagarias et al. (1998) and implemented in Matlab^{TM}. It is essential to choose a starting point for l in the upper range of the expected values in order to avoid local minimum present for the poorly defined low range of l.

4.4.4.2 Determination of the Geometric Fracture Characteristics in a Fracture Network

The same approach is tested on the stress profile resulting from the interaction of multiple fractures presented in Fig. 4.36b. This profile is intersected by 8 fractures. We used the same assumptions as for the single fracture problem, i.e., the unknown parameters are i and l for each fracture. All other parameters are considered to be known. There are then 16 unknown parameters in the problem and obviously the solution space cannot be visualized easily.

We use the same minimum searching algorithm to try to find a reasonable estimate of i and l for each intersecting fracture. In this case, it will never be possible to obtain a perfect fit ($\phi = 0$) since fractures that do not intersect the borehole but still perturb the stress at the borehole are included in the model used to generate $\beta^{obs.}$. However, they are not included in the inverse models leading to the determination of $\beta^{comp.}$.

The profile of $\beta^{comp.}$ obtained for the combination of input parameters that produce a global minimum in the minimization function (eqn 4.12) is shown in Fig. 4.38 together with the profile of $\beta^{obs.}$.
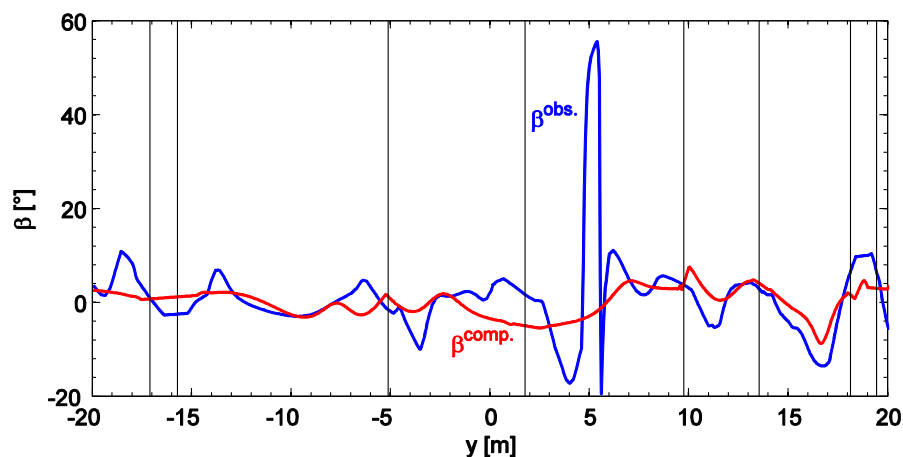
Fig. 4.38: Comparison of $\beta^{obs.}$ and $\beta^{comp.}$. The vertical black lines correspond to the location where the fractures intersect the profile.

The profiles of $\beta^{obs.}$ and $\beta^{comp.}$ in (Figure 4.38) show considerable differences. In particular, the large large perturbation in $\beta^{obs.}$ at y = 5, which is due to the proximity of the borehole to the stress concentration at the tip of a fracture, is not reproduced in the computed solution. The computed i and l values for the fracture don't match the actual fracture characteristics. This suggests that the solution space is not as well defined as for the case of a single fracture presented in Figure 4.37 and the problem is ill-defined.

4.4.4.3 Discussion

Natural fractures, if they slip, have a strong influence on the in-situ stress state of the rock mass. The characteristics of the stress perturbation associated with a fracture will depend upon its geometry as well as the slip. When considering a single fracture intersected by a vertical profile (e.g., a borehole), the intersection ratio (i) has a large influence on the perturbation in stress along the profile. The length of the fracture (l) does not modify the pattern of stress perturbation per se, but is linearly scaled to the range of influence. Within the limits of our modeling assumptions and our parameter analyses, variations of the stress and/or strength do not impact significantly the pattern of perturbation and its scaling. These findings suggest that it could be possible to derive fracture geometrical characteristics, particularly fracture length, if the pattern of the stress perturbation around a fracture is known (referred in this paper as the inverse problem).

The approach used to solve this inverse problem includes a least-squares estimation to evaluate the similarity of the computed stress profile with the observed stress profile and an optimization algorithm to find

the combination of parameters that minimized the misfit. This approach succeeded in extracting the geometrical characteristics of the fracture (i and l) for the simple case of a single fracture. However, in the case of a fracture network the proposed approach fails to find a satisfying solution. This is likely because fractures that do not intersect the profile can have a large influence on the stress perturbation, but cannot be captured in our models. Considering the other assumptions taken in our investigation using synthetic data (i.e. a 2D simplification and the fact that we consider stress magnitudes and strength characteristics to be known exactly), our results suggest that the approach will not be practicable with real data. A statistical approach that relates the wavelength distribution of the stress variability to the distribution of fracture length may be more successful in the case of fracture networks.

4.5 Conclusions and outlook

The modelling of the stress perturbations induced by fractures performed in Section 4.4 highlight the close relationship between these two elements and particularly how fracture length variations impact the wave length of the stress perturbation. However as discussed in Section 4.4.4.3, a deterministic approach to estimate fracture length from stress perturbation fails in a realistic and complex fracture network. This is due to the fact that fractures not intersecting the well will also influence the stress perturbation at the well and these perturbations cannot be accounted for and jeopardize the inversion approach that was applied.

Therefore, a statistical approach is considered to be a possible substitute for the deterministic approach attempted above. A probabilistic approach is expected to relate the statistical properties of the fracture network (mainly fracture length scaling relationships) to the stress perturbations characteristics. The results presented in Section 4.2 and 4.3 lay down the necessary basis for this work. Based on these results, robust methodology are available to characterize statistical characteristics and specifically scaling relationships for both fracture networks and stress heterogeneities.

These methodology will now be combined with synthetic and actual fracturing and stress heterogeneities data sets. Using the synthetic fracture networks created by Multiplicative Cascade process (Darcel et al. 2003b), we will create two and three dimensional geomechanical models and subject them to far field stresses or deformation at the model boundary. The stress heterogeneities in two dimensions will be calculated using Hybrid Finite Difference-Displacement Discontinuity Method developed by Jalali (2013). For three dimensional geotechnical simulations, we have not decided which available tool to choose. We expect to find a relation among the fracture network properties and stress heterogeneities along a one dimensional virtual borehole crossing the two dimensional network. If the fluid is injected into the fracture network, using a hydro-mechanical simulator, the slip on fracture planes allows us to quantify the induced seismicity by the relations between seismic moment and fault length Kanamori and Anderson (1975). These result will allow us to precise the nature of the relationship between the scaling parameters of fracture networks, stress heterogeneities and induced seismicity. These methodology will then be deployed on actual data set from deep geothermal borehole in order to improve our ability to characterize deep geothermal reservoir. The results of these developments will be present in the deliverable 8.3 of the IMAGE project.

4.6 References

Barton CA, Zoback MD (1992) Self-similar distribution and properties of macroscopic fractures at depth in crystalline rock in the Cajon Pass Scientific Drill Hole. J Geophys Res Solid Earth 97:5181–5200. doi: 10.1029/91JB01674

Boadu FK, Long LT (1994) The fractal character of fracture spacing and RQD. Int J Rock Mech Min Sci Geomech Abstr 31:127–134. doi: http://dx.doi.org/10.1016/0148-9062(94)92802-9

Bonnet E, Bour O, Odling NE, et al (2001) Scaling of fracture systems in geological media. Rev Geophys 39:347–383.

Bour O, Davy P, Darcel C, Odling NE (2002) A statistical scaling model for fracture network geometry, with validation on a multiscale mapping of a joint network (Hornelen Basin, Norway). J Geophys Res 107:2113.

Brown SR (1995) Measuring the dimension of Self-Affine Fractals: example of rough surfaces. In: Barton CC, La Pointe PR (eds) Fractals in the Earth Sciences. Plenum Press, New York,

Cannon MJ, Percival DB, Caccia DC, et al (1997) Evaluating scaled windowed variance methods for estimating the Hurst coefficient of time series. Phys Stat Mech Its Appl 241:606–626. doi: 10.1016/s0378-4371(97)00252-5

Crouch SL (1976) Solution of plane elasticity problems by the displacement discontinuity method. I. Infinite body solution. Int J Numer Meth Engng 10:301–343. doi: 10.1002/nme.1620100206

Darcel C, Bour O, Davy P (2003a) Stereological analysis of fractal fracture networks.

Darcel C, Bour O, Davy P, de Dreuzy JR (2003b) Connectivity properties of two-dimensional fracture networks with stochastic fractal correlation. Water Resour Res 39:n/a–n/a. doi: 10.1029/2002WR001628

Davies RB, Harte DS (1987) Tests for Hurst effect. Biometrika 74:95–101. doi: 10.1093/biomet/74.1.95

Davy P, Le Goc R, Darcel C, et al (2010) A likely universal model of fracture scaling and its consequence for crustal hydromechanics. J Geophys Res Solid Earth 115:n/a–n/a. doi: 10.1029/2009JB007043

Day-Lewis A, Zoback M, Hickman S (2010) Scale-invariant stress orientations and seismicity rates near the San Andreas Fault. Geophys Res Lett 37:L24304+. doi: 10.1029/2010gl045025

Enescu B, Ito K (2001) Some premonitory phenomena of the 1995 Hyogo-Ken Nanbu (Kobe) earthquake: seismicity, b-value and fractal dimension. Tectonophysics 338:297–314. doi: http://dx.doi.org/10.1016/S0040-1951(01)00085-3

Genter A, Evans K, Cuenot N, et al (2010) Contribution of the exploration of deep crystalline fractured reservoir of Soultz to the knowledge of enhanced geothermal systems (EGS). Comptes Rendus Geosci 342:502–516. doi: 10.1016/j.crte.2010.01.006

Hainzl S (2004) Seismicity patterns of earthquake swarms due to fluid intrusion and stress triggering. Geophys J Int 159:1090–1096.

Häring MO, Schanz U, Ladner F, Dyer BC (2008) Characterisation of the Basel 1 enhanced geothermal system. Geothermics 37:469–495. doi: 10.1016/j.geothermics.2008.06.002

Jalali M (2013) Thermo-Hydro-Mechanical Behavior of Conductive Fractures using a Hybrid Finite Difference – Displacement Discontinuity Method. University of Waterloo

Kanamori H, Anderson DL (1975) Theoretical basis of some empirical relations in seismology. Bull Seismol Soc Am 65:1073.

Lagarias J, Reeds J, Wright M, Wright P (1998) Convergence Properties of the Nelder-Mead Simplex Method in Low Dimensions. SIAM J Optim 9:112–147. doi: 10.1137/S1052623496303470

Percival DB (1992) Simulating Gaussian Random Processes with Specified Spectra. In: Page C, LePage R (eds) Computing Science and Statistics,Proceedings of the 22nd Symposium on the Interface. Springer, pp 534–538

Power WL, Tullis TE (1991) Euclidian and Fractal Models for the Description of Rock Surface Roughness. J Geophys Res 61:415–424.

Saupe D (1988) Algorithms for random fractals. In: Peitgen H-O, Saupe D (eds) The science of fractal images. Springer Verlag,

Smalley RF, Chatelain J-L, Turcotte DL, Prévot R (1987) A fractal approach to the clustering of earthquakes: Applications to the seismicity of the New Hebrides. Bull Seismol Soc Am 77:1368–1381.

Tafti TA, Sahimi M, Aminzadeh F, Sammis CG (2013) Use of microseismicity for determining the structure of the fracture network of large-scale porous media. Phys Rev E 87:32152. doi: 10.1103/PhysRevE.87.032152

Turcotte DL, Huang J (1995) Fractal distribution in geology, scale invariance, and deterministic chaos. In: Barton CC, La Pointe PR (eds) Fractals in the Earth Sciences. Plenum Press, New York,

Valley B (2007) The relation between natural fracturing and stress heterogeneities in deep-seated crystalline rocks at Soultz-sous-Forêts (France). Eidgenössische Technische Hochschule ETH Zürich, Nr. 17385

Valley B, Evans K (2010) Stress Heterogeneity in the Granite of the Soultz EGS Reservoir Inferred from Analysis of Wellbore Failure. In: Proceedings World Geothermal Congress 2010. Bali, Indonesia,

Valley B, Evans K (2009) Stress orientation to 5 km depth in the basement below Basel (Switzerland) from borehole failure analysis. Swiss J Geosci 102:467–480. doi: 10.1007/s00015-009-1335-z

Valley B, Evans KF (2014) Preliminary assessment of the scaling relationships of in-situ stress orientation variations indicated by wellbore failure data. In: Alejano LR, Perucho Á, Olalla C, Jimémez R (eds) EUROCK 2014: Rock Engineering and Rock Mechanics: Structures in and on Rock Masses. CRC Press,

Valley B, Evans KF (2007) Stress state at Soultz-sous-Forêts to 5 km depth from wellbore failure and hydraulic observations. In: Proceedings, 32nd workshop on geothermal reservoir engineering. pp 17481–17469

Valley B, Jalali MR, Ziegler M, Evans KF (2014) Constraining DFN characteristics for deep geothermal project considering the effects of fractures on stress variability. In: DFNE2014. Vancouver, Canada,

Velde B, Dubois J, Touchard G, Badri A (1990) Fractal analysis of fractures in rocks: the Cantor's Dust method. Tectonophysics 179:345–352.

Vicsek T (1992) Fractal growth phenomena. World Scientific

Wood ATA, Chan G (1994) Simulation of Stationary Gaussian Processes in [0, 1] d. J Comput Graph Stat 3:409–432. doi: 10.1080/10618600.1994.10474655

Ziegler M, Valley B, Evans K (2015) Characterisation of Natural Fractures and Fracture Zones of the Basel EGS Reservoir Inferred from Geophysical Logging of the Basel-1 Well.

5 Upfront predictions of natural fracture permeability for geothermal exploration

Jan ter Heege, Stefan Carpentier, Hans Veldkamp

Part of this work has been published as an extended abstract entitled "Fault permeability models for geothermal doublet designs" by J.H. ter Heege for the European Geothermal Congress 2016, held on 19-22 September 2016 in Strasbourg, France

5.1 Abstract

The occurrence and properties of natural faults and fractures in geothermal reservoirs are key in determining reservoir flow properties, and thereby controls the performance of geothermal doublets placed in fractured reservoirs or in the vicinity of fault zones. In this paper, an analytical model is presented that describes the 3D non-isotropic permeability of geothermal reservoirs where flow is controlled by faults and fractures. Typical fault architectures consisting of a fault core, a damage zone and surrounding intact reservoir matrix are taken into account in the permeability model. Fault scaling relations and experimental data is used to constrain permeability of each structural unit. The sensitivity of model predictions to orientations of sedimentary layers, damage zone fractures and fault core is analysed for typical fault populations and permeability contrasts. The model can be used to determine optimum orientation of geothermal doublets near major fault zones or in fractured reservoirs, taking into account the distribution and characteristics of faults, fractures and sedimentary layering. The model is applied to a potential geothermal play in a fractured Dinantian carbonate platform near Luttelgeest in the northern onshore regions of the Netherlands. Fault populations in the carbonate formation were analysed using 2D and 3D seismic data. Implications for optimizing the design of geothermal doublets placed in the Dinantian carbonate platform are given based on combining analysed fault populations, fault scaling relations, and existing data and models for permeability of reservoir, fractures and fault gouge. It is shown that the current analysis can be used to optimize geothermal doublets in geothermal reservoirs upfront, i.e. before exploitation has commenced when limited data on doublet performance is available.

5.2 Introduction

The occurrence and properties of natural faults in geothermal reservoirs are key in determining reservoir flow properties, and thereby the success of many geothermal projects (Hickman et al 1997; Fairly and Hinds 2004; Faulds et al. 2010; Moeck 2014). Accordingly, exploration for new geothermal sites will benefit from site-specific data on fault-related factors like damage zone fracture density, connectivity and permeability. In most cases, such data is lacking during geothermal exploration, but existing knowledge can be used to constrain typical fault zone architectures, spatial distribution of permeability and characteristics of damage zone fracture populations.

The characteristics of natural fault zones can vary widely depending on local geological and tectonic settings (Kim et al 2004; Wibberley et al 2008; Faulkner et al 2010). Site-specific characteristics of fault and fracture populations have been determined using seismic surveys, outcrop analogues, core material, and laboratory experiments (Odling et al 1999; Bonnet et al 2001; Torabi and Berg 2011). These studies have provided some generic fault scaling relations that can be used to constrain fault zone characteristics, such as damage zone width, fracture density and dominant fracture orientation. Accordingly, typical fault zone permeability models can be constructed even if site-specific (subsurface) data on fault zone characteristics is lacking.

The relationship between fluid flow and faulting has been studied extensively (Frank 1965; Sibson 1981; Caine et al 1996; Fisher and Knipe 2001). Most fault zones consists of a specific architecture with different structural units, i.e. a single or multiple fault cores and damage zones, surrounded by intact reservoir rock (Chester and Logan 1986; Wibberley et al 2008; Faulkner et al 2010). Permeability may vary considerably in each of these structural units, and the characteristic architecture of a fault zone will determine the permeability in and around fault zones (Barton et al 1995; Wibberley and Shimamoto 2003; Mitchell and Faulkner 2012).

Although many studies that model the permeability in fractured reservoirs or around fault zones address some aspects of fault architecture (Yielding et al 1997; Brown and Bruhn 1998; Odling et al 1999), few consider 3D permeability in all structural units. Moreover, one dominant fracture set with equally-spaced fractures is often assumed to describe fractured media such as damage zones (Pickup et al 1995; Lei et al 2015), hence ignoring relations between the orientation of main faults and damage zone fractures (Tchalenko 1970; Kim et al 2004) and spatial variation in fracture density (Mitchell and Faulkner 2012). Another major challenge for application to fault-controlled geothermal energy resources is the general lack of site-specific data on fault and fracture populations.

This study addresses these issues by (1) derivation of an analytical model for the bulk permeability of geothermal reservoirs where flow is controlled by faults and fractures, (2) incorporation of fault and fracture distributions and properties in the model that are derived from seismic data and used in combination with existing data and generic relations from literature, and (3) applying the model to a potential geothermal play to optimize geothermal doublets in geothermal reservoirs upfront.

Fault zones are modelled with a typical architecture consisting of 3 structural units, i.e. a fault core, a damage zone and surrounding intact reservoir matrix. Permeability is modelled using 3D permeability tensors that describe non-isotropic permeability in each of the structural units. Permeability of intact reservoir rock includes anisotropy due to sedimentary layering. Damage zone permeability is based on fracture density and orientation, and includes the effect of decreasing fracture density with increasing distance from the fault core. The permeability of the fault core can include anisotropy due to fabric in the fault gouge. Fault zone permeability can be described by combining permeability of the fault core, damage zone and intact reservoir including typical dimensions of each structural unit as well as distance and orientation between geothermal doublets.

The model is applied to a potential geothermal play in a fractured Dinantian carbonate platform near Luttelgeest in the northern onshore regions of the Netherlands (Lipsey et al 2016). Fault populations in the carbonate formation were analysed using a combination of (1) post-stack reprocessing of 2D and 3D seismic data, (2) generation of envelope, instantaneous phase and coherence attributes, and (3) autotracking of Dinantian reflectors and faults. Together with generic fault scaling relations, and existing data and models for permeability of reservoir, fractures and fault gouge, the fault population data is used to derive a model for bulk permeability.

The bulk permeability model can be used to analyse the geothermal power for a doublet system consisting of a surface heat exchanger, an injection well ("injector") and a production well ("producer") that is placed in the vicinity of a fault zone. Implications for the optimum design of geothermal doublet systems placed around fault zones are discussed. It is shown that produced geothermal power can be considerably enhanced if doublets are placed in optimum orientation with respect to existing damage zone fracture populations. Therefore, optimization of geothermal doublet designs in geothermal reservoirs that are crosscut by fault zones help de-risking geothermal exploration and exploitation.

5.3 Theory & models

5.3.1 Model for fault zone permeability

Fault zones are modelled with a typical architecture consisting of 3 structural units, i.e. a fault core, a damage zone and surrounding intact reservoir matrix (Figure 5.1).
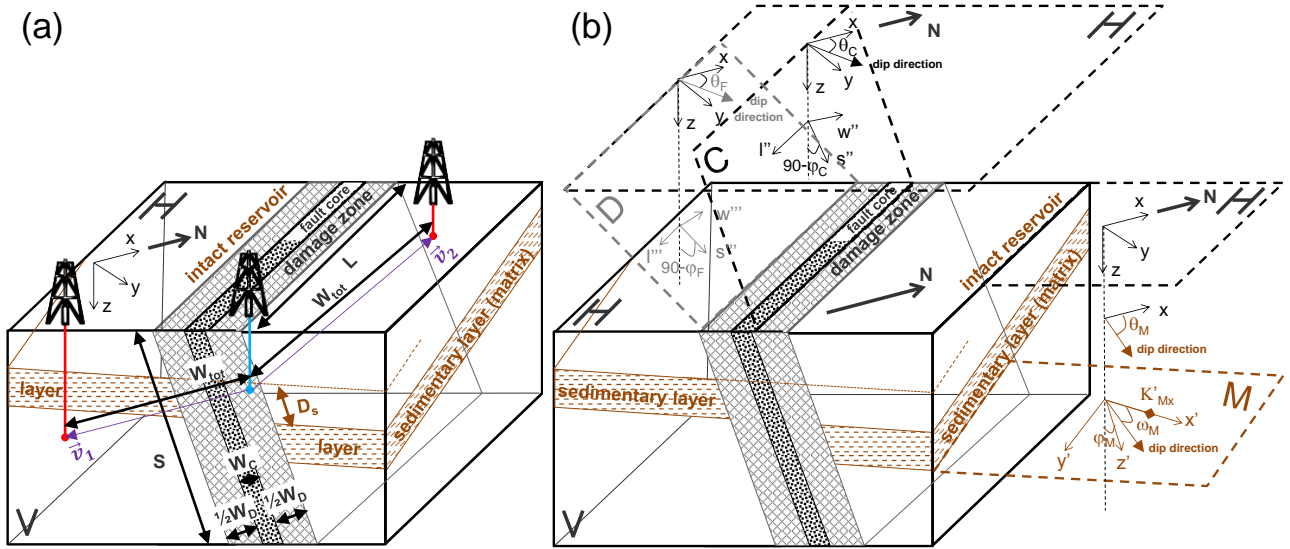
Figure 5.1. Schematic diagram of a simplified fault zone showing different structural units (i.e. intact reservoir matrix with sedimentary layers, damage zone and fault core), horizontal (H) and vertical (V) planes, and northern direction (N). (a) Dimensions used in the permeability model (L- length along fault strike, S- length along fault dip, D_S- displacement along fault dip, W_D- damage zone width, W_C- fault core width, W_{tot}- distance between injector and producer doublet wells, $\vec{v_x}$- orientation of geothermal doublet injector-producer). The geographical coordinate system (with axes x, y, z in northern, eastern and depth direction, respectively), and two possible doublet designs (described by vectors $\vec{v_1}$ and $\vec{v_2}$) are also indicated. (b) Different (right-handed) coordinate systems used to define 3D permeability tensors of the reservoir matrix (M with axes x', y' and z' parallel to the largest in-layer permeability, perpendicular to the largest in-layer permeability and parallel to the depth axis, respectively), damage zone (D with axes w''', l''' and s''' parallel to the normal vector, strike and slip direction of dominant damage zone fractures, respectively), and fault core (C with axes w'', l'' and s'' parallel to the normal strike and slip direction of the fault zone). The orientation of the principal permeabilities of fault zone, dominant damage zone fractures and reservoir layers (subscripts C, F, and M, respectively) in the geographical coordinate system are described by the angle between the largest principal permeability and dip direction in the sedimentary layers (ω_M), the dip directions (θ) and dips (φ).

Permeability around a single fault zone is modelled by combining permeability of the fault core, damage zone, and reservoir matrix. Anisotropic permeability in each of the structural units is described using 3D permeability tensors (K^*) that are defined in terms of 3 orthogonal principal permeabilities in different coordinate systems:

$$\boldsymbol{K}^* = \begin{pmatrix} K_{11}^* & 0 & 0 \\ 0 & K_{22}^* & 0 \\ 0 & 0 & K_{33}^* \end{pmatrix} \tag{5.1}$$

The asterisk in Eq. (5.1) is included to acknowledge that the principal permeabilities are defined using different Cartesian coordinate systems for the different structural units (following the right-hand rule for axes orientations). Permeability tensors are transformed between the different coordinate systems by tensor transformations using a rotation matrix $\boldsymbol{R}$ for a full Euler rotation based on the orientations of principal permeabilities relative to matrix layers, fault core and damage zone. The convention for definition Euler angles adopted by Rose (1957) is consistently

followed which involves (intrinsic) rotations about the original z-axis, the new y-axis and the new z-axis, respectively (see also Fjaer et al 2008).

The matrix permeability tensor ($K^* = K_M'$) is defined on the basis of sedimentary layers that may be present in the intact reservoir at an orientation described by the dip direction (θ_M) and dip (φ_M). The following orientations of principle permeabilities are assumed (c.f. Figure 5.1): (1) K_{M11}' is within the layers at an angle ω_M relative to θ_M, (2) K_{M22}' is within the layers perpendicular to K_{M11}', and (3) K_{M33}' is perpendicular to the layers in downward direction (i.e. parallel to the depth axis). It is assumed that K_{M11}' and K_{M22}' are perpendicular. Together, the principle permeabilities define a layer-based coordinate system. The matrix permeability tensor and layer-based coordinate system can account for effects of sedimentary structures such as cross-bedding (i.e. by specifying ω_M and K_{M11}'/K_{M22}') and permeability anisotropy due to bedding (i.e. by specifying K_{M11}'/K_{M33}').

The damage zone permeability tensor ($K^* = K_D''$) is defined on the basis of a dominant fracture set that may be present in the damage zone at an orientation described by the dip direction (θ_F) and dip (φ_F). The following orientations of principle permeabilities are assumed: (1) K_{F11}''' is parallel to the normal vector of fracture planes for the dominant fracture set, (2) K_{F22}''' is parallel to the layer strike, and (3) K_{F33}''' is parallel to the layer dip vector. Together, the principle permeabilities define a fracture-based coordinate system. The principle damage zone permeabilities are expressed as a combination of matrix permeability (K_M''', now in the fracture-based coordinate system) and damage zone fracture permeability (K_F'''). The damage zone permeability tensor and fracture-based coordinate system can account for effects of permeability anisotropy in the fractures (i.e. by specifying K_{F11}''', K_{M22}''' and K_{M33}'''), different fracture orientations (i.e. by specifying θ_F and φ_F), and different fracture densities. Damage zone permeability perpendicular to the fracture plane (K_{D11}''') is calculated using the harmonic mean of diagonal tensor components (K_{M11}''' and K_{F11}'''), while damage zone permeability parallel to the fracture plane (K_{D22}''' and K_{D33}''') is calculated by the arithmetic mean of K_{M22}''' and K_{F22}''' and K_{M33}''' and K_{F33}''', respectively. As off-diagonal tensor components of K_F''' are zero per definition, the off-diagonal components of K_D''' that govern cross-flow are based on K_M''' (e.g., Pickup et al., 1995):

$$K_{D11}''' = \left(\frac{F_w W_F}{K_{F11}'''} + \frac{\left(1 - F_w W_F\right)}{K_{M11}'''} \right)^{-1} \tag{5.2a}$$

$$K_{Dii}''' = F_w W_F K_{Fii}''' + \left(1 - F_w W_F\right) K_{Mii}''' \qquad \text{for } i = 2, 3 \tag{5.2b}$$

$$K_{Dij}''' = \left(1 - F_w W_F\right) K_{Mij}''' \qquad \text{for } i \neq j \tag{5.2d}$$

where the contribution of matrix and damage zone fractures to damage zone permeability is weighted using damage zone fracture width (W_F) and density of fractures in the damage zone (F_w). In this case, fracture width is defined as the distance perpendicular to the fracture plane that bounds the zone on both sides of the fracture where permeability equals K_F'''.

Fracture density decreases with increasing distance (w) from the center of the fault core (c.f. Mitchell and Faulkner, 2012):

$$F_w = F_{CD}\, exp\left(-\alpha_F\, \frac{2w}{W_D} \right) \qquad \text{with } 0 \leq w \leq W_D \tag{5.3}$$

where distance from the fault core is normalized to give fracture density $F_w = F_{CD}$ at the outer edge of the fault core ($w = 0$, c.f. Figure 5.1), and the constant α_F describes the decay in fracture density with distance from the fault core ($\alpha_F = W_D/2\beta_F$ which can be regarded as a dimensionless damage zone width, c.f. Mitchell and Faulkner 2012). In this case, a symmetrical damage zone on both

sides of the fault core is assumed (c.f. Figure **5.1**). The local permeability tensor components for the damage zone at any distance from the core-damage zone boundary can be found by substituting Eq. (5.3) in Eq. (5.2). The average damage zone permeability can be calculated by integrating local permeability tensor components over damage zone width:

$$\widetilde{K}_{Dij}^{'''} = \frac{2}{w_D} \int_0^{\frac{1}{2}W_D} K_{Dij}^{'''} dw \tag{5.4a}$$

$$\widetilde{K}_{D11}^{'''} = \frac{2}{w_D} \int_0^{\frac{1}{2}W_D} \frac{1}{ae^{bw}+c} dw = \frac{w}{c} - \frac{1}{bc} ln\left(ae^{bw}+c\right) \tag{5.4b}$$

$$\text{with} \quad a = F_{CD}W_F\left(K_{M11}^{'''} - K_{F11}^{'''}\right); \; b = -\frac{2\alpha_F}{W_D}; b \neq 0 \; ; \; c = K_{F11}^{'''}; \; c \neq 0$$

$$\widetilde{K}_{Dii}^{'''} = \frac{2}{w_D} \int_0^{\frac{1}{2}W_D} \left(F_w W_F K_{Fii}^{'''} + K_{Mii}^{'''} - F_w W_F K_{Mii}^{'''}\right) dw = aW_F K_{Fii}^{'''} + (1-a)W_F K_{Mii}^{'''} \tag{5.4c}$$

$$\text{with} \quad a = \frac{F_{CD}}{\alpha_F}\left(1 - e^{-\alpha_F}\right) \qquad \text{for } i = 2, 3$$

$$\widetilde{K}_{Dij}^{'''} = \frac{2}{w_D} \int_0^{\frac{1}{2}W_D} \left(1 - F_w W_F\right)K_{Mij}^{'''} dw = \left(1 + aW_F\right)K_{Mij}^{'''} \tag{5.4d}$$

$$\text{with} \quad a = \frac{F_{CD}}{\alpha_F} e^{-\alpha_F} \qquad \text{for } i \neq j$$

where tensor components are rewritten as combinations of integrals with known solutions with constants a, b and c (c.f. Gradsteyn and Rhyzik 1994).

The fault core permeability tensor ($K^* = K_C''$) is defined on the basis of the dominant fault zone orientation described by the dip direction (θ_C) and dip (φ_C) of the fault core. The following orientations of principle permeabilities are assumed: (1) K_{C11}'' is parallel to the normal of the main fault plane through the fault core, (2) K_{C22}''' is parallel to the strike of the main fault plane, and (3) K_{C33}''' is parallel to the dip vector of the main fault plane. Together, the principle permeabilities define a fault-based coordinate system. The fault core permeability tensor and fault-based coordinate system can account for effects of permeability anisotropy in the fault core (i.e. by specifying K_{C11}''', K_{C22}''' and K_{C33}''').

The principle bulk permeabilities are determined in the fault-based coordinate system (K_B'') by combining matrix permeability (K_M''), average damage zone permeability (K_D'') and fault core permeability (K_C''), averaged over the distance (W_{tot}) between the doublet injector and producer. Bulk permeability perpendicular to the fault core (K_{B11}') is calculated using the harmonic mean of diagonal tensor components K_{M11}'', K_{D11}'' and K_{C33}''. Bulk permeability parallel to the fracture plane (K_{B22}'' and K_{B33}''') is calculated by the arithmetic mean of K_{M22}'', K_{D22}'', K_{C22}'', and K_{M33}'', K_{D33}'', K_{C33}'', respectively. As off-diagonal tensor components of K_C'' are zero per definition, the off-diagonal components of K_B'' that govern cross-flow are based on K_M'' and K_D'':

$$K_{B11}^{''} = \left(\frac{\left(W_{tot} - W_D - W_C\right)}{W_{tot}K_{M11}^{''}} + \frac{W_D}{W_{tot}\widetilde{K}_{D11}^{''}} + \frac{W_C}{W_{tot}K_{C11}^{''}}\right)^{-1} \tag{5.5a}$$

$$K_{B22}^{''} = \frac{\left(W_{tot} - W_D - W_C\right)K_{M22}^{''}}{W_{tot}} + \frac{W_D \widetilde{K}_{D22}^{''}}{W_{tot}} + \frac{W_C K_{C22}^{''}}{W_{tot}} \tag{5.5b}$$

$$K_{B33}^{''} = \frac{(W_{tot} - W_D - W_C)K_{M33}^{''}}{W_{tot}} + \frac{W_D \tilde{K}_{D33}^{''}}{W_{tot}} + \frac{W_C K_{C33}^{''}}{W_{tot}} \tag{5.5c}$$

$$K_{B1j}^{''} = \left(\frac{(W_{tot} - W_D - W_C)}{W_{tot} K_{M1j}^{''}} + \frac{W_D}{W_{tot} \tilde{K}_{D1j}^{''}} \right)^{-1} \quad \text{for } j = 2, 3 \tag{5.5d}$$

$$K_{Bij}^{'''} = \frac{(W_{tot} - W_D - W_C)K_{Mij}^{'''}}{W_{tot}} + \frac{W_D \tilde{K}_{Dij}^{''}}{W_{tot}} \quad i \neq j; \; i = 2, 3 \tag{5.5e}$$

It should be noted that Eqs. (5.5) describe bulk permeability around a single fault zone, covering the fault core, damage zone and part of the intact reservoir matrix ($W_{tot} > W_D + W_C$). It therefore governs the contribution of all structural units to flow around the fault zone, assuming flow is uniform. The tensor for bulk permeability (K_B) is defined with the following orientations of principle permeabilities: (1) K_{B11} is South to North, (2) K_{B22} is West to East, and (3) K_{B33} is downward along depth. Together, the principle permeabilities define a geographical based coordinate system. Dip directions (θ_M, θ_C, θ_F) and dip angles (φ_M, φ_C, φ_F) are defined within the geographical coordinate system. K_B can be derived from $K_B^{''}$ by transformation between the fault-based and geographic coordinate system using a rotation matrix that is based on fault dip direction (θ_C) and dip angle (φ_C).

5.3.2 Model for bulk permeability in layered reservoirs with multiple fault and fracture populations

The fault zone model can be extended to account for structural or lithological differences between matrix layers by describing matrix permeability as a combination of permeability in multiple (N_M) parallel layers or lithological units (Pickup et al 1995):

$$\overline{K}_{Mij}^{'} = \frac{\sum_{n=1}^{N_M} K_{Mij}^{'} W_{Mn}}{\sum_{n=1}^{N_M} W_{Mn}} \quad \text{for } i, j = 1, 2 \tag{5.6a}$$

$$\overline{K}_{Mij}^{'} = \left[\frac{\sum_{n=1}^{N_M} \frac{W_{Mn}}{K_{Mij}^{'}}}{\sum_{n=1}^{N_M} W_{Mn}} \right]^{-1} \quad \text{for } i, j = 3 \tag{5.6b}$$

where each layer or lithological unit ($n = n_M$) can have an unique thickness (W_{Mn}) and orientation of the largest principle permeability with respect to the layer dip direction (ω_{Mn}, c.f. Figure **5**.**1**). Note that combination of layers or lithological units with different ω_{Mn} requires rotation of coordinate systems for each layer or lithological unit (n_M) to a common layer-based coordinate system using rotation matrix R_{Mn} based on angle ω_{Mn} (c.f. Figure **5**.**1**). Variation in ω_{Mn} results in an overall 3D matrix permeability tensor with both diagonal and off-diagonal components. This model extension is useful in case data is available on variation in interbedded low permeability layers or sedimentary structures such as cross-bedding between different layers or lithological units within the reservoir.

The description of damage zone permeability (Eqs. (5.2) can be extended to account for multiple (N_F) damage zone fracture sets:

$$\overline{K}_{Dij}^{''} = \sum_{n=1}^{N_F} K_{Dij}^{''} \qquad \text{with } \sum_{n=1}^{N_F} F_{wn} = F_w \tag{5.7}$$

where each fracture set ($n = n_F$) can have an unique fracture thickness (W_{Fn}), density (F_{wn}), dip direction (θ_{Fn}), dip (φ_{Fn}) and fracture permeability ($K_F^{'''}$, c.f. Eqs. (5.2). It is assumed that individual fracture sets consists of a series of parallel fractures and that the fracture density of all fractures combined decreases with increasing distance from the center of the fault core following Eq. (5.3). A transformation of the different fracture-based coordinate systems for each fracture set to a common coordinate system is required to combine the different fracture sets in the description of damage zone permeability. For convenience, the fault-based coordinate system is used as the common coordinate system, and rotation matrices R_{FCn} are used for the coordinate system transformations. Incorporation of multiple fracture sets is useful in case more than one dominant set controls permeability, which is frequently observed in fault damage zones (e.g., following Riedel orientations, Tchalenko 1970; Kim et al 2004).

The frequency distribution of fault properties and dimensions in a population of faults is often observed to follow power law or lognormal distributions (Odling et al 1999; Bonnet et al 2001; Torabi and Berg 2011). If a population of faults is analyzed for an area of observation (A_o) crosscutting a rock volume (V_r), the number of faults of size Z can be described by considering the density or cumulative density function (e.g., Bonnet et al 2001). If the distribution of fault sizes is characterized by a power law distribution, the number of faults of size Z (n_C) or the cumulative number of faults with size greater than Z (N_C) can be described by:

$$n_C(Z) = \alpha_Z Z^{-a_Z} \qquad \text{with } \alpha_Z = \frac{N_{Ctot}(a_Z - 1)}{A_o Z_{min}^{1-a}} \tag{5.8}$$

$$N_C(Z) = \int_Z^\infty n_C(Z) dZ = \beta_Z Z^{-a_Z + 1} \quad \text{with } \beta_Z = \frac{\alpha_Z}{a - 1} = \frac{N_{Ctot}}{A_o Z_{min}^{1-a}} \tag{5.9}$$

where, within the framework of the current model, Z can denote the fault length along strike (L) or along dip (S), or fault core width (W_C). N_{Ctot} is the total number of faults observed in A_o, and Z_{min} is the minimum fault size. Z_{min} can either be the actual minimum fault size that can be observed (controlled by the resolution of the fault size analysis method), or a theoretical lower limit derived from using the power law fit to extrapolate fault sizes beyond the lower limit in data (for example, the minimum size of faults that significantly contribute to bulk permeability). The adopted definition of constants α_Z and β_Z has the advantage that both types of distributions can be used to constrain their values, and that the constants have a physical meaning as they are determined by the overall fracture density (N_{Ctot}/A_{obs}) in the area. Note that generally α_Z and β_Z are used as constants derived from best fit of fault size distribution data to Eqs. (5.8) and (5.9). If the distribution of fault sizes is characterized by a lognormal distributions, n_C and N_C can be described by:

$$n_C(Z) = \frac{\alpha_Z}{Z\sigma\sqrt{2\pi}} exp\left(-\frac{[log Z - \mu]^2}{2\sigma^2}\right) \qquad \text{with } \alpha_Z = \frac{N_{Ctot}}{A_o} \tag{5-10}$$

$$N_C(Z) = \int_Z^\infty n_C(Z) dZ = \frac{1}{2}\beta_Z\left[1 + erf\left(\frac{log Z - \mu}{\sigma\sqrt{2}}\right)\right] \qquad \text{with } \beta_Z = \alpha_Z \tag{5-11}$$

The effect of multiple fault zones with distributed lengths (L and S, c.f. Figure **5**.**1**) on the bulk permeability in the rock volume ($V_r = \Delta X_r \Delta Y_r \Delta Z_r$) is accounted for by defining sub-volumes (V_n) representing average rock volumes occupied by individual fault zones. V_n is oriented parallel to fault strike (L) and dip vector (S), and covers the fault core and damage zone, i.e. $V_n = C_n L_n S_n W_n$ (with L_n, S_n, W_n representing average values for length along strike, length along dip and width, respectively). Constant C_n depends on the fault geometry, and may be chosen depending on the dimensions and detail of mapped fault geometries (e.g., $C_n = 1$ for rectangular fault volumes that cut through V_r, or $C_n = 1/6\pi$ for ellipsoidal fault volumes that are completely contained within V_r). If fault segments are fully mapped (for example using 3D seismics) an average V_n can be determined. If only 2D sections are available (for example from 2D seismic surveys or outcrops), a representative V_n need to be based on theoretical considerations of fault mechanics (c.f. Nicol et al 1996, Figure **5**.**2**), and need to account for sectioning effects (see for example the discussion in Berkowitz and Adler 1998; Bonnet et al 2001).

Fault zones are clustered according to their orientation so that each cluster contains a number of faults with different sizes but roughly similar orientations described by the dip direction (θ_{Cn}) and dip (φ_{Cn}). The clustering of faults is convenient as fault populations in rock formations generally show two or more preferred orientations, depending on deformation conditions at the time of faulting (Tchalenko 1970; Kim et al 2004). Each orientation cluster may have an unique lower (Z_{min}) and upper (Z_{max}) limit of fault sizes to acknowledge the dependence of fault sizes on fault hierarchy (i.e. populations of smaller faults may be associated with major fault zones with typical angular relations, Ouillon et al 1996; Kim et al 2004). The total number (N_{Cn}) and volume (V_{Cn}) of faults within each orientation cluster can vary and can be determined deterministically (for example based on seismic and outcrop data), or statistically by evaluating the integrals of Eqs. (5.9) and (5-11) for relevant limits Z_{min} and Z_{max}:

$$V_{Cn} = \sum_{n=1}^{N_{Cn}} V_n = C_n L_n S_n W_n \text{ (deterministic), or } V_{Cn} = \int_{Z_{min}}^{Z_{max}} n_C(Z) V_n(Z) dZ \text{ (statistic)} \quad (5.12)$$

Average permeability within each orientation cluster is approximated by volume averaging the contribution of faults within that cluster:

$$\widetilde{K}_{Bijn}^{''} = \sum_{n=1}^{N_{Cn}} \frac{V_n}{V_{Cn}} K_{Bij}^{''} \text{ (deterministic), or } \widetilde{K}_{Bijn}^{''} = \int_{Z_{min}}^{Z_{max}} \frac{V_n(Z)}{V_{Cn}} K_{Bij}^{''} dZ \text{ (statistic)} \quad (5.13)$$

with, in this case, bulk permeability ($K_B^{''}$) is calculated with $W_{tot} = W_D + W_C$ (c.f. Eqs. (5.5). Note that because faults with similar orientation are clustered no coordinate system transformation is required account for the contribution of individual faults in an orientation cluster. Bulk permeability in V_r is then calculated by volume averaging the permeability of each orientation cluster ($n = n_O$), and matrix permeability:

$$\overline{K}_{Bij} = \sum_{n=1}^{N_{On}} \left[\left(1 - \frac{V_{Cn}}{V_r} \right) K_{Mij} + \frac{V_{Cn}}{V_r} \widetilde{K}_{Bijn} \right] \quad (5.14)$$

where a coordinate system transformation from the fault-based to geographical coordinate system is performed for the permeability of each orientation cluster.

5.3.3 Permeability and geothermal potential for doublet systems in fractured reservoirs

The permeability models are used to analyze the permeability that controls flow in a doublet system consisting of a surface heat exchanger, an injection well ("injector") and a production well ("producer"). For a reservoir volume (V_r) with anisotropic permeability due to layering, faults and fractures, flow between the injector and producer will be dependent on the orientation of the doublet relative to layers, faults and fractures:

$$\left| K_{Bi} \right| = \left| K_{Bij} v_i \right| \tag{5.15}$$

where K_{Bi} and $|K_{Bi}|$ are the vector and bulk permeability in the direction given by v_i, and v_i is the unit vector indicating the orientation of the doublet system (i.e. direction of the injector to the producer, Figure **5.1**). Single phase, steady state, laminar (Darcy) flow of incompressible fluids in a porous medium can be expressed as $Q = K \nabla P / \mu$. For radial flow through reservoir volume $V_r = 2\pi W_{tot}$ at homogeneous pressure conditions ($\delta P/\delta x = \delta P/\delta y = \delta P/\delta x$), the volumetric flow rate Q_v for a vertical injector or producer are aligned along vector v_i can then be expressed as (Verruijt 1970; Dake, 1978):

$$Q_v = \frac{2\pi}{\mu} \left(ln\left[\frac{W_{tot}}{R_o} \right] + S \right)^{-1} \left(P_w - P_a \right) W_{Mtot} \left| K_{Bi} \right| \qquad \text{with } W_{Mtot} = \sum_{n=1}^{N_M} W_{Mn} \tag{5.16}$$

where μ is the fluid viscosity, R_o is the outer wellbore radius, S is a skin factor, P_w is the bottomhole flowing pressure at the well, and P_a is the aquifer pressure. Geothermal power is calculated using a similar methodology as outlined by Van Wees et al (2012) in which geothermal power (G_P, in Watt) is expressed as:

$$G_P = Q_m c_p \Delta T \tag{5.17}$$

where Q_m is the mass flow rate (in kg/s) which is considered constant throughout the doublet (i.e. the doublet is acting as a closed system), c_p is the specific heat capacity of the formation fluid (in J/kgK) and ΔT is the temperature drop at the heat exchanger. The mass flow rate can be calculated using Eq. (5.16) and the fluid density at the injector or producer ($Q_m = Q_v \rho_f$), which is a function of local bottomhole conditions at the wells (e.g., pressure, temperature and salinity). Accordingly, the gain or loss in geothermal power due to variations in doublet orientation (v_i) relative to layers, faults and fractures (G_{P1} with anisotropic permeability $|K_{Bi}| = K_{Bij} v_i$) compared to a base case (G_{P0} with isotropic matrix permeability $|K_{Bi}| = K_{iso} = (K_{M11} + K_{M22} + K_{M33})/3$) can be expressed as:

$$\frac{G_{P1}}{G_{P0}} = \frac{Q_{m1}}{Q_{m2}} = \frac{Q_{v1}}{Q_{v2}} = \frac{K_{Bij} v_i}{K_{iso}} \tag{5.18}$$

assuming bottomhole flowing pressure (P_w), fluid properties (c_p, ρ_f, μ) and fluid conditions (ΔT, P_a) are similar between the anisotropic permeability case (G_{P1}) and the base case (G_{P1}). Note that volumetric flow rate at surface pumps and heat exchanger can be derived by imposing a pressure balance on the doublet system. The pressure balance needs to account for factors including (1) flow in the aquifer, (2) near-well pressure variations (i.e. skin factors), (3) wellbore friction between the fluid and inner casings, and (4) gravitational forces. The temperature drop at the heat exchanger, required to calculate geothermal power (c.f. Eq. (5.17) can be derived by imposing an energy balance on the doublet system (Van Wees et al 2012).

5.4 Data compilation to constrain model parameters

5.4.1 Model dimensions and fault scaling laws

Limited data may be available in early phases of geothermal exploration and doublet planning, in particular in virgin areas prior to drilling. However, fault and fracture populations, orientations, and permeability have been analysed in studies of seismic surveys, outcrop analogues, core material, and laboratory experiments (Odling et al., 1999; Bonnet et al., 2001; Torabi and Berg, 2011). Data from these studies can be used to constrain model dimensions in case required data is not available. Here, some typical examples of available data are provided, including some statements on how the data can be used to constrain models dimensions (Figure 5.2).
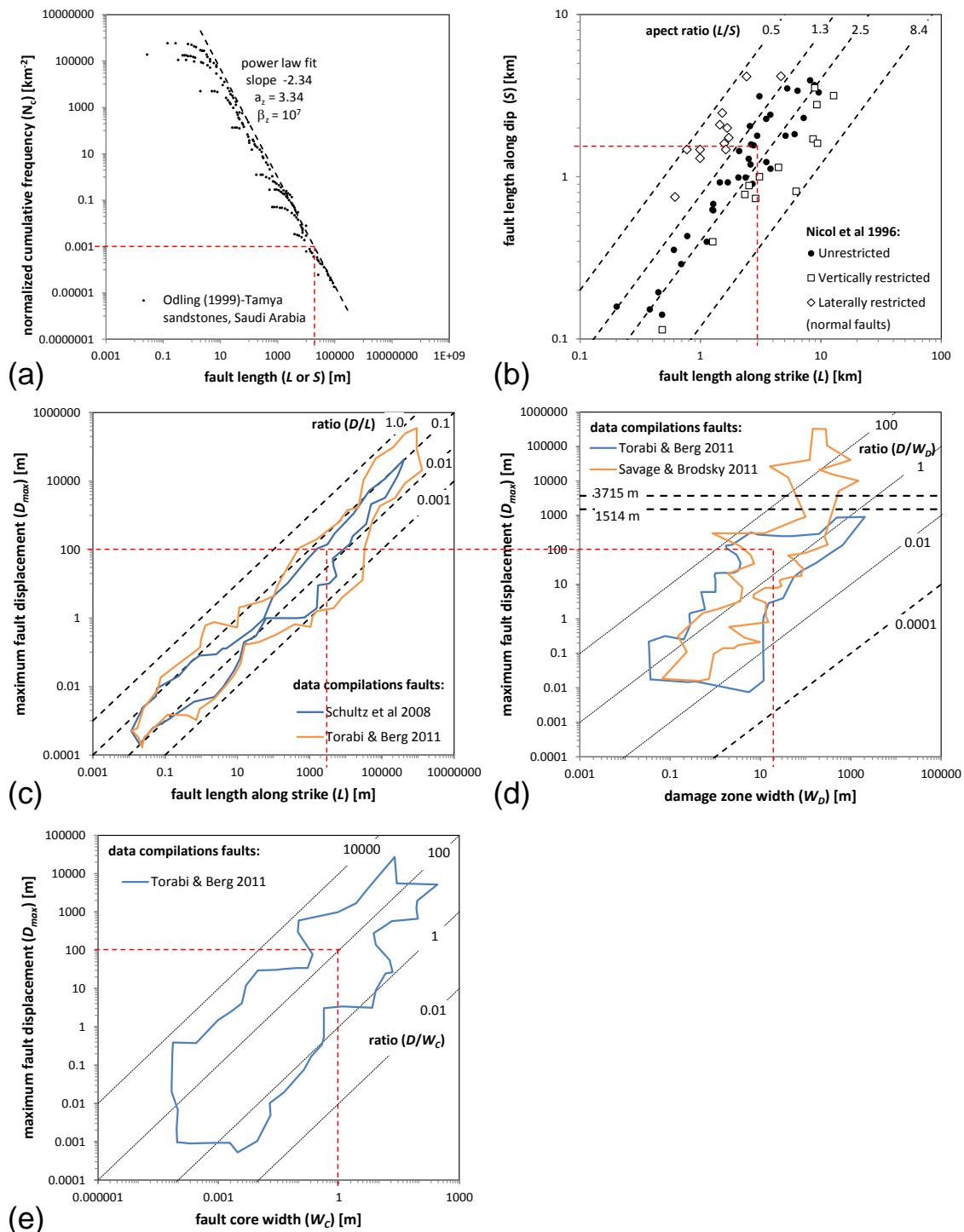
Figure 5.2 (*previous page*) Examples of data on the properties and dimensions of fault and fractures in populations analysed from outcrops and seismic surveys. (a) Normalized cumulative distribution of fault lengths for Cambrian–Ordovician sandstones in the Tayma region of NW Saudi Arabia from outcrop, aerial photographs and satellite images showing a lognormal distribution of lengths of individual datasets and an overall power law distribution for the combined datasets covering the full scale of observation (Odling et al 1999). A best fit of the data to a power law distribution can be used to determine α_Z and β_Z (Eqs. (**5.8**, (**5.9**). (b) Compilation of fault aspect ratios (*L/S*) for normal faults in different geological settings that are unrestricted average aspect ratios of 2.15), vertically restricted (aspect ratios > 2.5) or laterally restricted (aspect ratios <1.3, Nicol et al 1996). These data can be used to constrain V_n if the full geometry of fault surfaces is unknown (e.g., if data is limited to lengths *L* or *S* from 2D sections, c.f. Eqs. (**5.12**, 5.(**5.13**, (**5.14**). (c) Compilation of data relating maximum fault displacement (D_{max}) to fault length along strike (*L*) showing typical *D/L* ratios and fields covered by fault data compiled by Schultz et al (2008) and Torabi and Berg (2011). (d) Compilation of data relating D_{max} to damage zone width (W_D) showing typical D/W_D ratios and fields covered by fault data compiled by Schultz et al (2008) and Savage and Brodsky (2011). Bounds of D_{max} (1514 and 3715 m) are indicated where D/W_D ratios may increase compared to faults with lower D_{max} (Savage and Brodsky 2011). e) Compilation of data relating D_{max} to fault core width (W_C) showing typical D/W_C ratios and the field covered by fault data compiled by Torabi and Berg (2011). The D/W_D and D/W_C ratios can be used to constrain W_D and W_C required in Eqs. (**5.3**, 5.(**5.4** and (**5.5** which may otherwise be difficult to constrain, in particular for seismic data. An example is indicated in (a)-(e) of how average fault properties and dimensions are related for a fault with $D_{max} = 100$ m (red dashed lines).

5.4.2 Fault, fracture and reservoir permeability

Several interrelated factors control the permeability of fault zones, including (1) the stress state, (2) mineralogy, (3) structure, (4) deformation (i.e. strain, displacement, stress and strain rate), and (5) dimensions (i.e. length, width and slipped area). Compilations of existing data and models can be used to constrain the permeability for different structural units (Figure 5.3).

Figure 5.3 (*next page*) Examples of data on fracture density and permeability for fractured rock and fault gouges analysed in laboratory experiments and outcrops. (a) Typical decrease in density of macro- and microfractures (F_w) with distance from the centre of the fault core (*w*) for the Punchbowl Fault in the US (Savage and Brodsky 2011) and the Atacama Fault system in Chile (Mitchell and Faulkner 2009; 2012). Best fits of the data to a relation for exponential decay are shown for the Atacama Fault system (orange dashed lines) that can be used to determine the damage decay exponent ($n = 2\alpha_F/W_D$) and pre-exponential constant ($c = F_w$, c.f. Eq. (**5.3**). A best fit of the data to a relation for power law decay is shown for the Punchbowl Fault (blue dashed line, Savage and Brodsky 2011). (b) Typical data for *n* and *c* with increasing *D* for the Atacama Fault system and Punchbowl Fault showing a roughly power law relation between *n* and *D* (orange dashed lines, lower line is fit by Mitchell and Faulkner 2012, upper line is rough upper bound on all data). F_{CD} is roughly constant with values around 100 faults per meter for macrofractures and 16 faults per millimeter for microfractures. For macrofracture densities, *n* is determined using best fits for exponential decay for data in (a). The relations can be used to constrain $2\alpha_F/W_D$ and F_{CD} (and hence F_w, c.f. Eq. (**5.3**) on the basis of fault displacement as by the red dashed line in (e) for *D* = 100 m. (c) Compilation of data for the decrease in permeability (K_D) with increasing distance from the centre of the fault core (*w*) for the Atacama Fault system in Chile (orange symbols and lines) based on the relation between microfracture density and permeability from laboratory experiments on Westerly Granite from Mitchell and Faulkner 2012). The data and relations can be used to predict K_D-*w* relations for different fault displacements based on F_w-*w* relations (as indicated by the red curve for *D* = 100 m). (d) Compilation of data for the evolution of fault gouge permeability (K_C) with shear strain (γ) for quartz-clay mixtures (coloured symbols, Crawford et al 2008). A rough division of permeability regimes is indicated based on clay content of the fault gouge (coloured fields). Also indicated are predictions from a theoretical relation between shale gouge ratio (*SGR*) and *D* from Manzocchi et al 1999 (solid lines), assuming that all deformation is constrained to the fault core ($\gamma = D/W_C$) and that *SGR* is a measure for clay content in the fault core (c.f. Yielding 2002; Wibberly et al 2008). Note that, if indicated, upper lines are for $W_C = 0.001$ m and lower lines are for $W_C = 10$ m (c.f. Figure 5.2e, if not indicated, these lines overlap, i.e. there is no significant dependence of K_C on W_C). The compilation can be used together

with Figure 5.2e to constrain K_C if clay content of the fault gouge or *SGR* is analysed, and fault displacement is known.
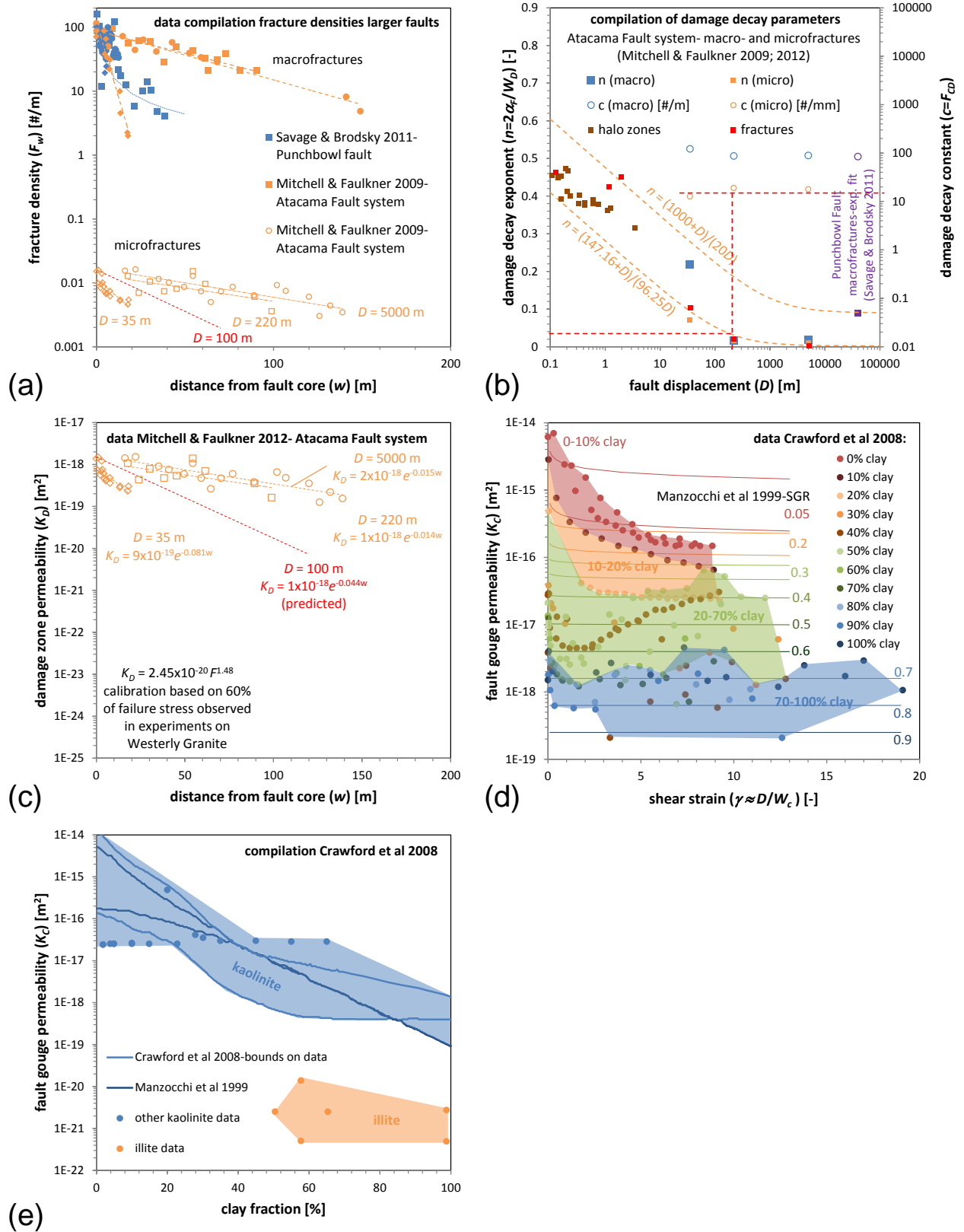

(a)

(b)

(c)

(d)

(e)

Figure 5.2 **and** Figure 5.3 **include an example of how typical relations and data compilations can be used to constrain other model parameters if available data is limited. For example, if only a 2D seismic section is available that shows a main fault with D_{max} = 100 m, the data compilations can be used to constrain most other model parameters (**
Table **5**.**1**).

Parameter	Unit	Reference	Value	Rock	Remarks (key reference)
D_{max}	m	assumed	100	S	derived from vertical sections
L	m	Figure 5.2e	3000	S	compilations (Schultz et al 2008; Torabi & Berg 2011)
S	m	Figure **5.2**b	1500	S	average for blind isolated normal faults (Nicol et al 1999)
W_D	m	Figure **5.2**d	20	S	compilations (Savage & Brodsky 2011; Torabi & Berg 2011
W_C	m	Figure **5.2**e	1	S	compilation (Torabi & Berg 2011)
W_F	m	assumed	0.001	-	from additional data or models (c.f. Bisdom et al. 2016)
W_{tot}	m	assumed	1000	-	distance between injector and producer
F_{CD}	#/m	Figure 5.3a	100	C	macrofractures, crystalline rock (Mitchell & Faulkner 2009)
$n=2\alpha_F/W_D$	-	Figure **5.3**b	0.03	C	microfractures, crystalline rock (Mitchell & Faulkner 2012)
$c = F_{CD}$	#/mm	Figure **5.3**b	16	C	microfractures, crystalline rock (Mitchell & Faulkner 2012)
N_c	#/km^2	Figure **5.2**a	0.001	S	sandstones (Odling et al. 1999)
K_{M11}'	mD	assumed	10	S	typical for tight sandstone reservoirs
K_{M22}'	mD	assumed	5	S	anisotropic permeability due to sedimentary structures
K_{M33}'	mD	assumed	1	S	anisotropic permeability due to sedimentary layering
K_{F11}'''	mD	assumed	1000	S	from additional data or models (c.f. Bisdom et al. 2016)
K_{F22}'''	mD	assumed	1000	S	from additional data or models (c.f. Bisdom et al. 2016)
K_{F33}'''	mD	assumed	1000	S	from additional data or models (c.f. Bisdom et al. 2016)
K_{C11}''	mD	Figure 5.3d	2000	S	D/W_c = 100 in this example, for 0-10% clay in gouge
K_{C22}''	mD	Figure 5.3d	2000	S	D/W_c = 100 in this example, for 0-10% clay in gouge
K_{C33}''	mD	Figure 5.3d	2000	S	D/W_c = 100 in this example, for 0-10% clay in gouge

Table 5.1 Typical model parameters for a fault with D_{max} = 100 m. Note that average parameters are given based on the data compilations (c.f. Figure 5.2, Figure 5.3) without considering differences in geological setting. Only microfracture densities are considered because they can be used to constrain permeability using the relation of Mitchell and Faulkner (2012) (c.f. Figure 5.3).

It should be emphasized that caution is warranted in applying data and relations to very different geological settings. Some data that are included in compilations may be site-specific, i.e. depending on local geological settings, and care must be taken in applying it to different settings. On the other hand, relations may be generic if they reflect physical processes that allow extrapolations beyond local conditions (Schultz et al 2008; Wibberley et al 2008; Faulkner et al 2010). Uncertainty in the prediction of model parameters may be reduced by applying relations and data that are most applicable to the geothermal reservoir under consideration, in particular concerning geological setting (e.g., lithology, faulting regime and local deformation conditions). In addition, the relations and data give ranges of predicted model parameters that can be used to perform sensitivity analysis and stochastic modelling with the aim to quantify uncertainties. The rationale behind this approach that generic relations based on compilations of data give added value to characterizing fault zones and fractures reservoirs compared to scenarios where fractures are not included or randomly distributed (Odling et al 1999; Savage and Brodsky 2011).

5.5 Sensitivity analysis to illustrate model performance

Model predictions are given for typical permeability contrasts and dimensions of intact reservoir, damage zone fractures and fault core (
Table **5.2**).

Parameter	Unit	Value
K_{M11}'	mD	100
K_{M22}'	mD	90
K_{M33}'	mD	10
K_{F11}'''	mD	1000
K_{F22}'''	mD	1000
K_{F33}'''	mD	1000
K_{C11}''	mD	2000
K_{C22}''	mD	2000
K_{C33}''	mD	2000
W_F	m	0.001
W_D	m	100
W_C	m	0.1
W_{tot}	m	1000
F_C	#/m	100

Table 5.2 Input parameters for model sensitivity analysis

Orientations of fault core, damage zone fractures and reservoir bedding or layering are varied to show the sensitivity of permeability to fault and fracture orientations for each of the structural units (Figure 5.4). The examples show values for bulk permeability, assuming that the doublet is oriented in S-N direction ($\vec{v} = [1,0,0]$, Figure 5.4a, b, c), and placed in the intact reservoir matrix outside the damage zone or in the damage zone. In Figure 5.4d, bulk permeability is given by color-coding for all possible orientations of a geothermal doublet. The variation in bulk permeability results from permeability anisotropy due to layering and density of damage zone fractures, and different orientations of the layers and fractures relative to the doublet.
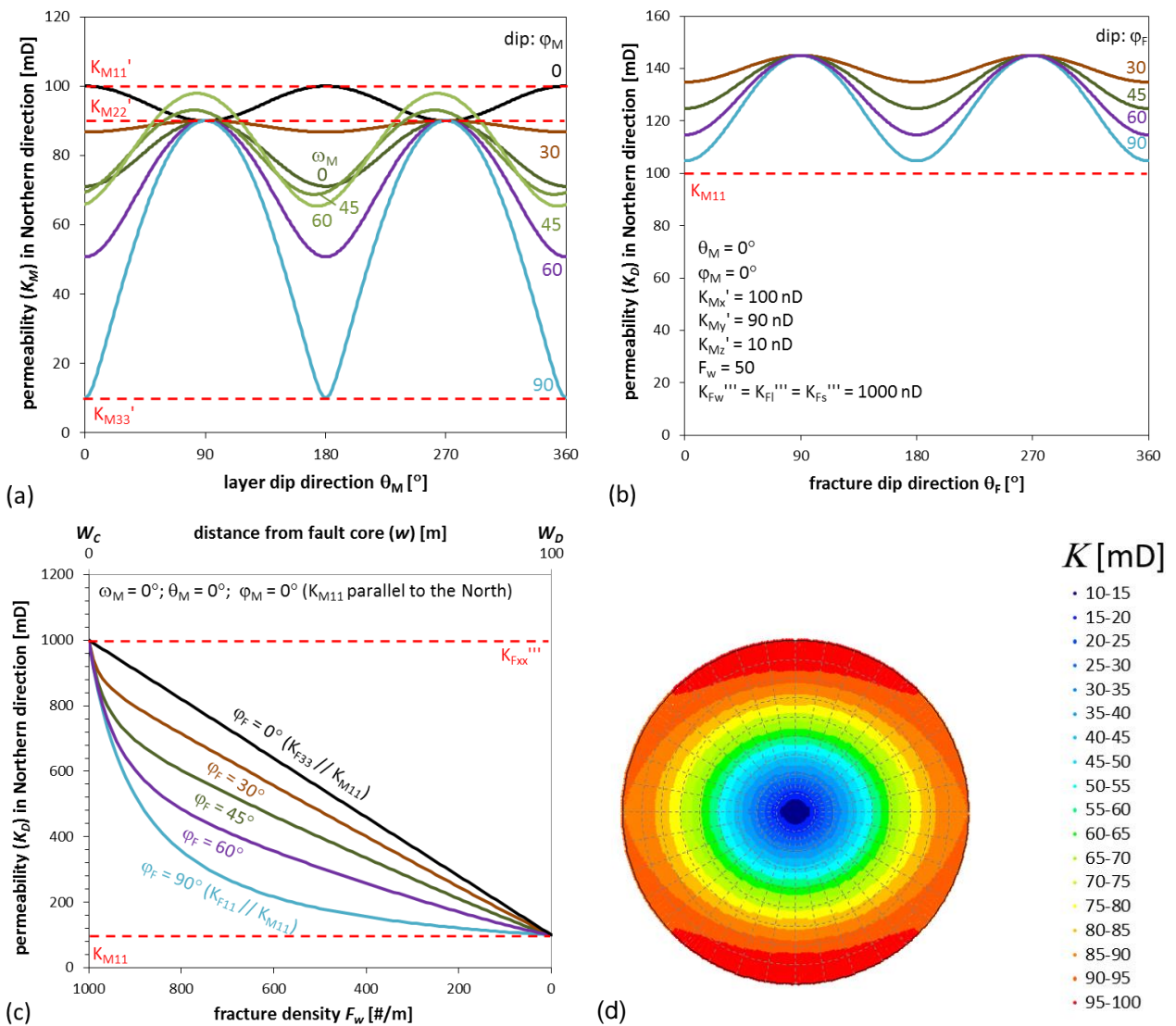
Figure 5.4 Variation of bulk permeability for a doublet oriented in S-N direction for: (a) different orientations of sedimentary layering in the reservoir (given by layer dip direction θ_M and dip angle φ_M) and largest principal matrix permeability within the matrix layers (ω_M), (b) different orientations of damage zone fractures (given by fracture dip direction θ_D and dip angle φ_D) and $F_w = 50$, (c) increasing distance from fault core (w) and associated decrease in fracture density (F_w, c.f. Eq. 5.6), (d) stereonet illustrating the variation of permeability along different directions (i.e. potential doublet orientations) in a geothermal reservoir with strong permeability anisotropy ($K_v/K_h \ll 1$, warmer colours indicate higher permeability). Model input parameters for the sensitivity analysis are given in Table 5.2.

5.6 Field example of fault populations in a potential geothermal play

The procedure for determining fault population data from field cases is illustrated using a potential geothermal play in a fractured Dinantian carbonate platform near Luttelgeest in the northern onshore regions of the Netherlands (Figure 5.5). Fault populations in the carbonate formation were analysed using 2D and 3D seismic data.
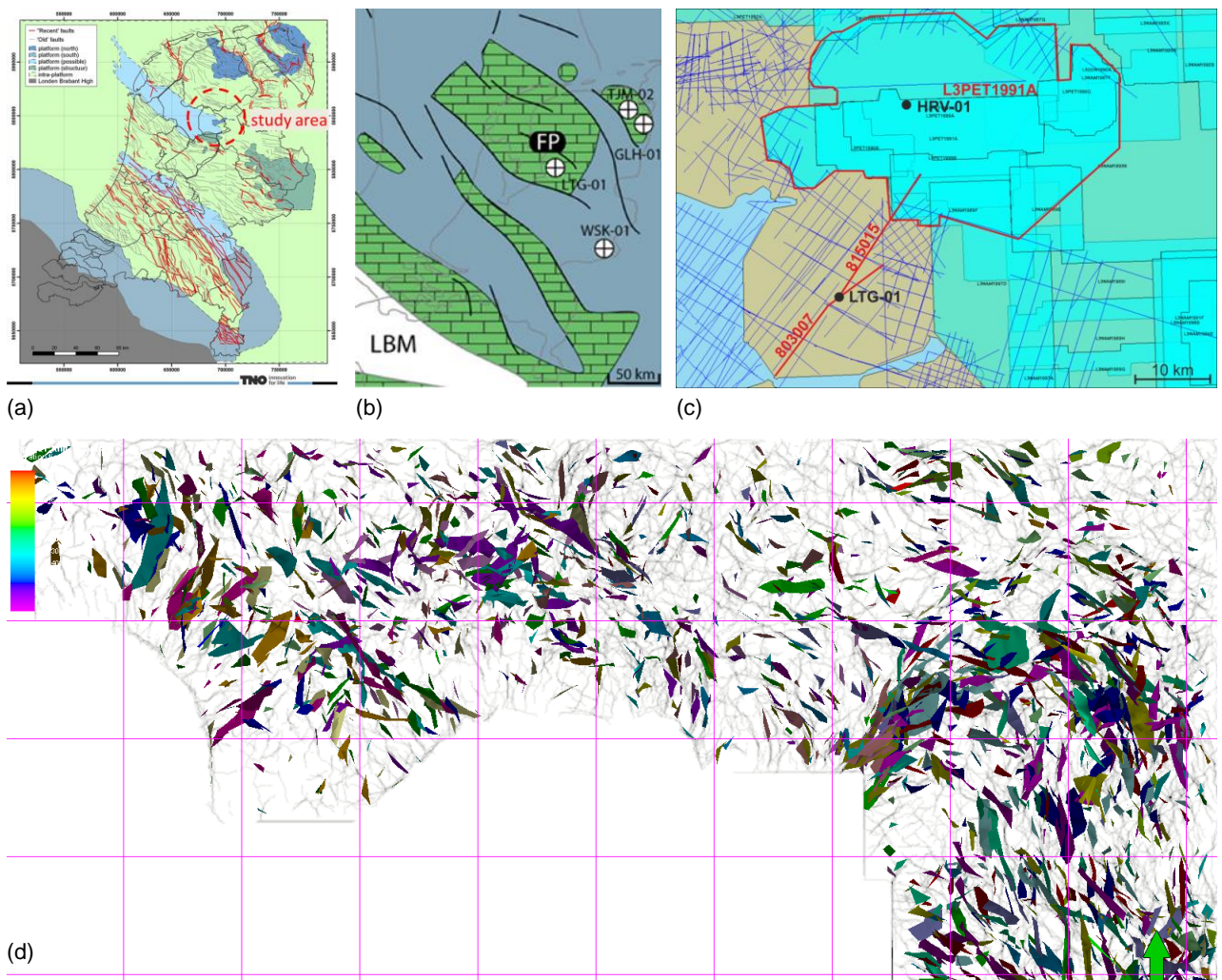

Figure 5.5 Potential geothermal play in a fractured Dinantian carbonate platform near Luttelgeest in the northern onshore regions of the Netherlands. (a) Location of the study area in the Netherlands showing specific geological features relevant to the play (b) paleogeographic map of the Netherlands during the Early Carboniferous (LBM- London-Brabant Massif, FP- Friesland Platform, Lipsey et al. 2016, adapted after Kombrink 2008), (c) 2D (blue and red lines) and 3D (red bounded areas) seismic data covering the platform of interest, (d) faults crosscutting the platform derived from seismic interpretation using a non-local means approach for reduction of seismic noise and an ant-tracking approach for imaging faults (c.f. Carpentier et al. 2016, colour coding indicates fault orientation).

Distributions of fault azimuths, dips and lengths are derived from the interpretation of 2D and 3D seismics (Figure 5-6). These distributions can be used to determine the preferred orientation of faults and scaling relations (c.f. (5.8)-(5-11), which together with an assessment of geothermal aquifer performance can be used to determine the optimum orientation and distance between the injector and producer in a doublet. The optimum orientation of the doublet will depend on the complex interplay between matrix, damage zone and fault core permeability. The optimum injector-producer distance need to take into account maximum flow performance as well as potential cold

water breakthrough. Accordingly, the fault data can be used to constrain the permeability models and subsequently serve as input for geothermal performance calculations (c.f. Van Wees et al. 2012) to determine optimum doublet designs. This will be shown in the results of WP8 of IMAGE
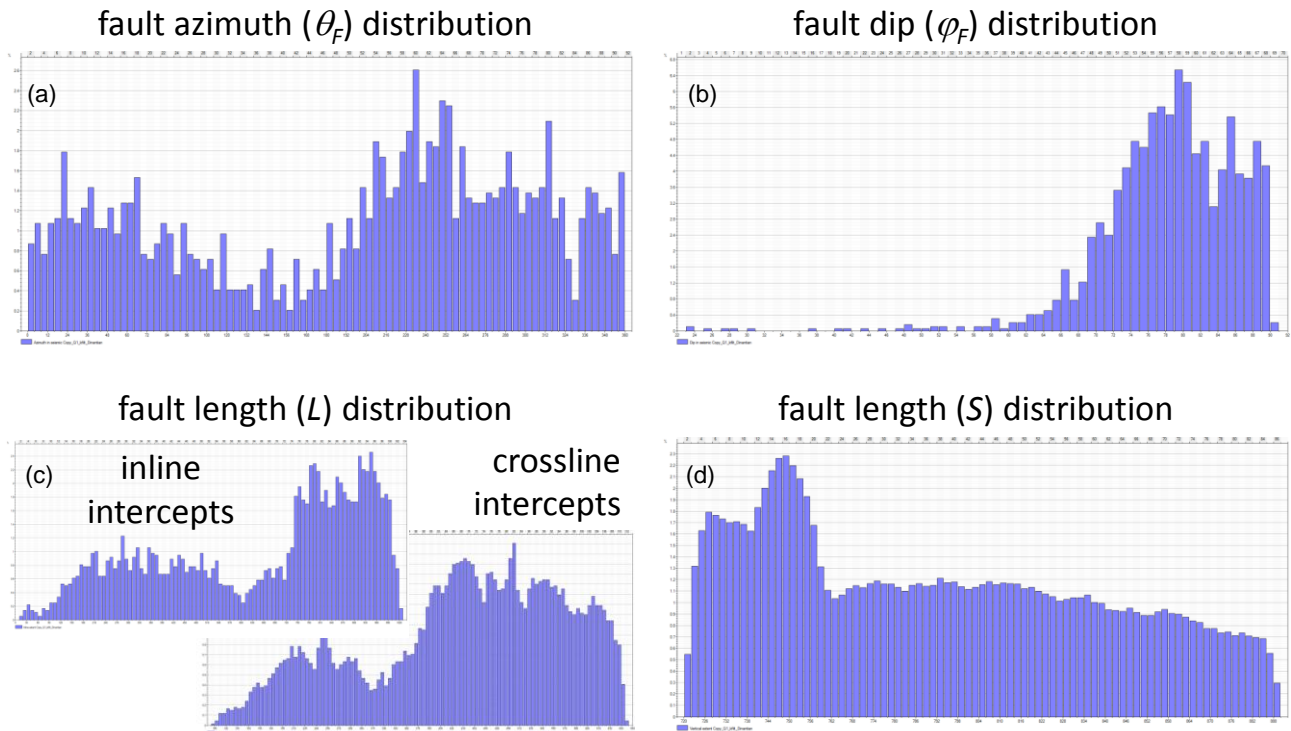
Figure 5-6 Fault size distributions derived from the 2D and 3D seismic data (c.f. Figure 5.5c, d). (a) Distribution of fault azimuth (θ_F) showing a preferred ENE-WSW fault strike, (b) distribution of fault dip (φ_F) showing a preferred dip between 76-81°, (c) distribution of number of intercepts between faults and seismic cross- or inlines that can be used to determine fault length (L) along the fault strike, (d) distribution of fault lengths (S).

5.7 Summary and conclusions

This study investigates the influence of fault and fracture populations on the permeability of geothermal reservoirs with multiple fault and fracture populations. The main research question addressed is:

What is the optimum design of a geothermal doublet in a reservoir with fault- and fracture-controlled permeability?

Some key challenges related to geothermal exploration are that (1) studies need to be based on limited data for geothermal exploration, (2) deep reservoirs with poorly constrained properties are targeted in the quest for high temperatures fluids, (3) there is a strong need for de-risking the business case of new play concepts that involve cost-intensive deep drilling. These challenges are addressed in this study by developing a modelling approach for determining optimum doublet designs.

The main work and conclusions can be summarized as follows:
- Analytical 3D permeability models for fractured reservoir are derived that incorporate fault and fracture populations and describes the permeability of fault zones using 3D permeability tensors for intact layered reservoir (matrix), damage zone and fault core.
- Together with a model for the potential of geothermal doublets, the permeability model can be used to calculate doublet performance for all injector-producer orientations. In this way, the optimum injector-producer orientation and distance can be determined.
- Compilations of (generic) data on fault dimensions and properties are presented. The data can be used to constrain model parameters if site-specific data from geological & geophysical characterization is lacking.
- The sensitivity of the model to the orientations of layers, fractures and faults as well as damage zone fracture density is analyzed. It shows that bulk permeability can vary considerably, mainly depending on (i) permeability anisotropy in the matrix, damage zone and fault core, (ii) the orientation of matrix layers and damage zone fractures, and (iii) the location relative to the fault core.
- Fault populations have been analyzed for a potential geothermal field case consisting of a Dinantian carbonate platform located near Luttelgeest in the northern onshore regions of the Netherlands. Fault sizes and orientations are determined based on 2D and 3D seismic interpretation using a non-local means approach for reduction of seismic noise and an ant-tracking approach for imaging faults. The analysis shows showing that faults have a preferred ENE-WSW fault strike and a preferred dip between 76-81°.
- Using generic models with typical input parameters it is shown that the approach can be used to optimize doublet designs in faulted and fractured geothermal reservoirs. Optimum doublet designs for the Dinantian carbonate platform field case will be analysed during the continuation of the IMAGE project.

References

Barton CA, Zoback MD, Moos D. 1995. Fluid flow along potentially active faults in crystalline rock. *Geology* 23:683.

Berkowitz B and Adler PM. 1998. Stereological analysis of fracture network structure in geological formations. *Journal of Geophysical Research: Solid Earth* 103(B7):15339-15360.

Bisdom K, Bertotti G, Nick HM. 2016. A geometrically based method for predicting stress-induced fracture aperture and flow in discrete fracture networks. AAPG Bulletin 100(7):1075-1097.

Bonnet E, Bour O, Odling NE, Davy P, Main I, Cowie P, Berkowitz B. 2001. Scaling of fracture systems in geological media. *Reviews of Geophysics* 39(3):347-383.

Brown SR and Bruhn RL. 1998. Fluid permeability of deformable fracture networks. *Journal of Geophysical Research: Solid Earth* 103(B2):2489-2500.

Caine JS, Evans JP, Forster CB. 1996. Fault zone architecture and permeability structure. *Geology* 24(11):1025-1028.

Carpentier, S.F., Steeghs, P., Boxem, B. 2016. Seismic reprocessing and attributes for geothermal exploration: a case study in Friesland, Netherlands, European Geothermal Congress 2016, held on 19-22 September 2016 in Strasbourg, France.

Chester FM and Logan JM. 1986. Implications for mechanical properties of brittle faults from observations of the Punchbowl fault zone, California. *Pure and Applied Geophysics* 124(1):79-106.

Crawford BR, Faulkner DR, Rutter EH. 2008. Strength, porosity, and permeability development during hydrostatic and shear loading of synthetic quartz-clay fault gouge. Journal of Geophysical Research: Solid Earth 113(B3).

Dake, L. 1978. Fundamentals of reservoir engineering. Elsevier, Heidelberg-London-New York.

Fairley JP and Hinds JJ. 2004. Rapid transport pathways for geothermal fluids in an active Great Basin fault zone. *Geology* 32(9):825-828.

Faulds, J., Coolbaugh, M., Bouchot, V., Moeck, I. and Oğuz, K. 2010. Characterizing Structural Controls of Geothermal Reservoirs in the Great Basin, USA, and Western Turkey: Developing Successful Exploration Strategies in Extended Terranes, *Proceedings World Geothermal Congress 2010*, Bali, Indonesia: 1-11.

Faulkner DR, Jackson CAL, Lunn RJ, Schlische RW, Shipton ZK, Wibberley CAJ, Withjack MO. 2010. A review of recent developments concerning the structure, mechanics and fluid flow properties of fault zones. *Journal of Structural Geology* 32(11):1557

Fisher QJ and Knipe RJ. 2001. The permeability of faults within siliciclastic petroleum reservoirs of the North Sea and Norwegian Continental Shelf. *Marine and Petroleum Geology* 18(10):1063-1081.

Fjaer, E., R.M. Holt, P. Horsrud, A.M. Raaen, and R. Risnes. 2008. Petroleum related rock mechanics. 2nd ed.: Elsevier.

Frank, F.C. 1965. On dilatancy in relation to seismic sources. *Reviews of Geophysics* 3: 485-503.

Gradshteĭn IS, Ryzhik IM, Jeffrey A. 1994. Table of integrals, series, and products. Academic Press

Hickman, S. H., Barton, C. A., Zoback, M.D., Morin, R., Sass, J., Benoit, R. 1997. In situ stress and fracture permeability along the Stillwater fault zone, Dixie Valley, Nevada. *Int. J. Rock Mech. and Min. Sci.*, 34, 3–4, Paper No. 126.

Kim, Y.-S., Peacock, D.C.P., Sanderson, D.J. 2004. Fault damage zones. *Journal of Structural Geology* 26: 503-517.

Kombrink H. 2008. The Carboniferous of the Netherlands and surrounding areas; a basin analysis. *Geologica Ultraiectina* 294, Utrecht University.

Lei G, Dong PC, Mo SY, Yang S, Wu ZS, Gai SH. 2015. Calculation of full permeability tensor for fractured anisotropic media. *Journal of Petroleum Exploration and Production Technology* 5(2):167-176.

Lipsey L, Pluymaekers M, Goldberg T, van Oversteeg K, Ghazaryan L, Cloetingh S, van Wees J. 2016. Numerical modelling of thermal convection in the Luttelgeest carbonate platform, the Netherlands. *Geothermics* 64:135-151

Nicol A, Watterson J, Walsh JJ, Childs C. 1996. The shapes, major axis orientations and displacement patterns of fault surfaces. *Journal of Structural Geology* 18(2–3):235-248.

Manzocchi T, Walsh JJ, Nell P, Yielding G. 1999. Fault transmissibility multipliers for flow simulation models. *Petroleum Geoscience* 5(1):53-63.

Mitchell TM and Faulkner DR. 2009. The nature and origin of off-fault damage surrounding strike-slip fault zones with a wide range of displacements: A field study from the Atacama fault system, northern Chile. *Journal of Structural Geology* 31(8): 802-816.

Mitchell TM and Faulkner DR. 2012. Towards quantifying the matrix permeability of fault damage zones in low porosity rocks. *Earth and Planetary Science Letters* 339–340: 24-31

Moeck IS. 2014. Catalog of geothermal play types based on geologic controls. *Renewable and Sustainable Energy Reviews* 37: 867-882.

Odling, N.E., P. Gillespie, B. Bourgine, C. Castaing, J.P. Chiles, N.P. Christensen, E. Fillion, A. Genter, C. Olsen, L. Thrane, R. Trice, E. Aarseth, J.J. Walsh, and J. Watterson. 1999. Variations in fracture system geometry and their implications for fluid flow in fractures hydrocarbon reservoirs. *Petroleum Geoscience* 5**:** 373-384.

Ouillion, G., Castaing, C., Sornette, D. 1996. Hierarchical geometry of faulting. *J. Geoph. Res. 101*: 5477-5487.

Pickup, G.E., Ringrose, P.S., Corbett, P.W.M., Jensen, J.L., Sorbie, K.S. 1995. Geology, geometry and effective flow. *Petroleum Geoscience 1*: 37-42.

Rose, M.E. 1957. Elementary Theory of Angular Momentum. John Wiley & Sons, New York.

Savage HM and Brodsky EE. 2011. Collateral damage: Evolution with displacement of fracture distribution and secondary fault strands in fault damage zones. Journal of Geophysical Research: Solid Earth 116(B3)

Schultz RA, Soliva R, Fossen H, Okubo CH, Reeves DM. 2008. Dependence of displacement–length scaling relations for fractures and deformation bands on the volumetric changes across them. *Journal of Structural Geology* 30(11):1405-1411.

Sibson, R.H. 1981. Fluid flow accompanying faulting: Field evidence and models. *Maurice Ewing Series 4 Earthquake prediction: An international review*: 593-603.

Tchalenko, J.S. 1970. Similarities between Shear Zones of Different Magnitudes. *Geological Society of America Bulletin 81*: 1625-1640.

Torabi A and Berg SS. 2011. Scaling of fault attributes: A review. *Marine and Petroleum Geology* 28(8):1444-1460.

Van Wees, J.D., Kronimus, A., Van Putten, M., Pluymaekers, M.P.D., Mijnlieff, H., Van Hooff, P., Obdam, A. and Kramers, L.: Geothermal aquifer performance assessment for direct heat production - Methodology and application to Rotliegend aquifers, *Netherlands Journal of Geosciences* 91, (2012), 651-665.

Verruijt, A. 1970. Theory of Groundwater Flow. Macmillan, London, 190 pp.

Wibberley CAJ and Shimamoto T. 2003. Internal structure and permeability of major strike-slip fault zones: the Median Tectonic Line in Mie Prefecture, Southwest Japan. *Journal of Structural Geology* 25(1):59-78

Wibberley CAJ, Yielding G, Di Toro G. 2008. Recent advances in the understanding of fault zone internal structure: a review. *Geological Society, London, Special Publications* 299(1):5-33

Yielding, G., Freeman, B., Needman, T. 1997. Quantitative fault seal prediction. *American Association of Petroleum Geologists Bulletin, 81*: 897–917.

Yielding G. 2002. Shale Gouge Ratio — calibration by geohistory. Norwegian Petroleum Society Special Publications 11: 1-15.

6 Predictive models approaches for temperature and fracture permeability

Lindsay Lipsey, Maarten Pluymaekers, Tatiana Goldberg, Katrien van Oversteeg, Lilya Ghazaryan, Sierd Cloetingh, Jan-Diederik van Wees

An extensive version of this work has been published as "Numerical modelling of thermal convection in the Luttelgeest carbonate platform, the Netherlands" geothermics, 64, November 2016, Pages 135–151, and has been included as appendix B.

Thermal anomalies in deep sedimentary layers and basement rock are largely controlled by convective fluid flow within zones of increased fracture permeability. Convection is of interest in geothermal energy, as upwelling hot fluid yields relatively shallow high-temperature anomalies. These are preferential targets for geothermal exploration. Convective fluid flow leaves a distinct pattern on the local geothermal gradient. The thermal effect is critically dependent on the pre-existing thermal gradient, thickness and permeability (e.g. Pasquale et al., 2013) (Lipsey et al., 2016).

Recent work on the temperature distribution in the Dutch subsurface revealed a thermal anomaly at 4-5 km depth at the Luttelgeest-01 well (LTG-01), which could be explained by thermal convection. Temperature measurements show a shift to higher temperatures at depths greater than 4000 m, corresponding to the Dinantian carbonate interval. The local thermal gradient strongly resembles the thermal signature that is believed to be characteristic of convective processes (Lipsey et al., 2016).

3D numerical models of thermal convection are used to reproduce the temperature pattern in Luttelgeest, in order to illuminate possible flow and thermal structures. The goal is to gain a better understanding of the interplay between geothermal anomalies, platform geometry and natural fracture permeability (Lipsey et al., 2016). The Luttelgeest anomaly is used as an example to show how predictive models can facilitate in exploration workflows to assess thermal variation and location of upwelling zones.

6.1 Evidence for convection

6.1.1 Well location

The LTG-01 well is located on the Luttelgeest carbonate platform, which is found on the Texel-Ijsselmeer structural high in the northern onshore Netherlands. This is a prominent NW-SE trending fault block of mid-Palaeozoic origin (Fig. 6.1) (Geluk et al., 2007). The southern boundary is made up of a steep fault system and the northern margin gradually transitions into the adjacent Friesland platform. The Luttelgeest carbonate platform is elongated in the E-W direction, with dimensions of approximately 14 km E-W and 8 km N-S (Lipsey et al., 2016). The seismic profile in Fig. 6.1 shows the relative position of the LTG-01 well, which appears to be situated on the edge of the platform, or platform margin. This is in agreement with other seismic studies of the Luttelgeest platform (e.g. van Hulten and Poty, 2008).
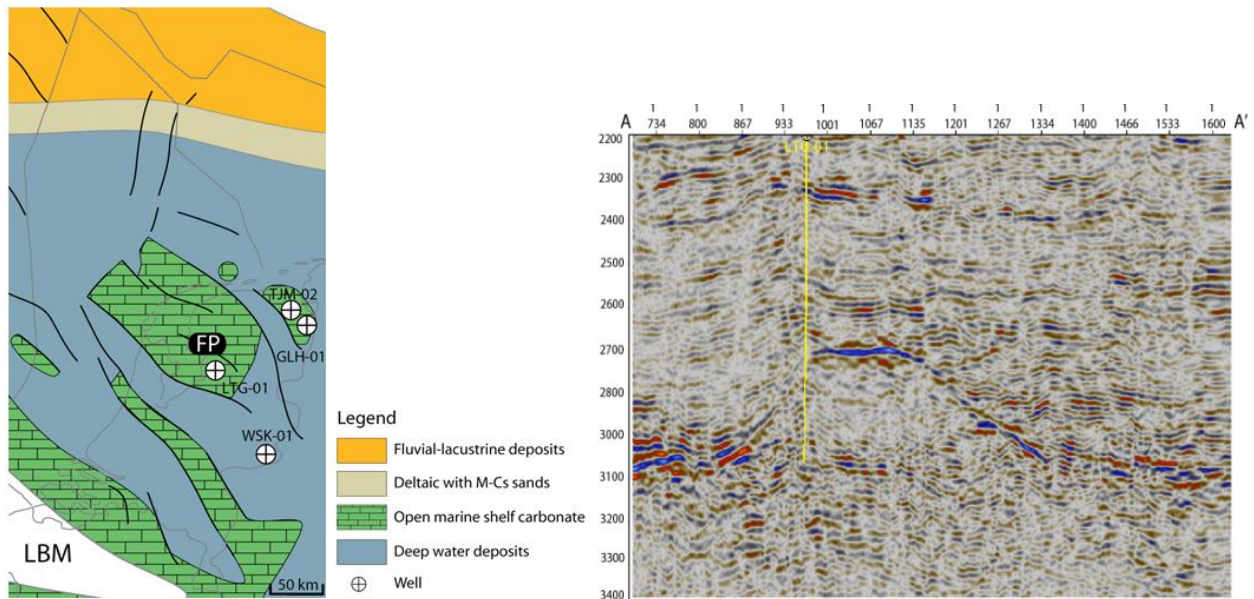
Figure 6.1. Location of LTG-01 well (left) and the seismic section across LTG-01 and the Luttelgeest platform (right). The LTG-01 well is indicated in yellow. Note the location of the well along the platform margin. LBM: London-Brabant Massif; FP: Friesland Platform (Lipsey et al., 2016).

6.1.2 Temperature

Bonté et al. (2012) provides the most recent up-to-date coherent temperature dataset for the Netherlands. In total, the dataset includes 1293 corrected bottom-hole temperature measurements (BHT) distributed over 454 wells and yields an average gradient of 31.3 °C km^{-1} with a mean surface temperature of 10.1 °C (Fig. 4.2). However, there is a sudden shift in the data towards high temperatures at depths greater than 4 km, as indicated by the dashed line in Fig. 6.2a (Lipsey et al., 2016).

For a better understanding of subsurface temperatures, Bonté et al. (2012) use this dataset to calibrate 3D thermal models for the complete Dutch subsurface. The comparison between the model and the values within a 10km radius of the LTG-01 well is shown in Fig. 6.2b (Bonté et al., 2012).

The dataset for LTG-01 yields a temperature gradient of 39 °C km^{-1} though contains several intervals of anomalous values. Within the platform, the gradient is nearly 10 °C km^{-1} lower than the Dutch average, whereas above the platform the gradient is roughly 20 °C km^{-1} higher. Such a decrease in the temperature gradient through the platform is typical of a convective signature resulting from hot upwelling fluid (Guillou-Frottier et al., 2013) (Lipsey et al., 2016).
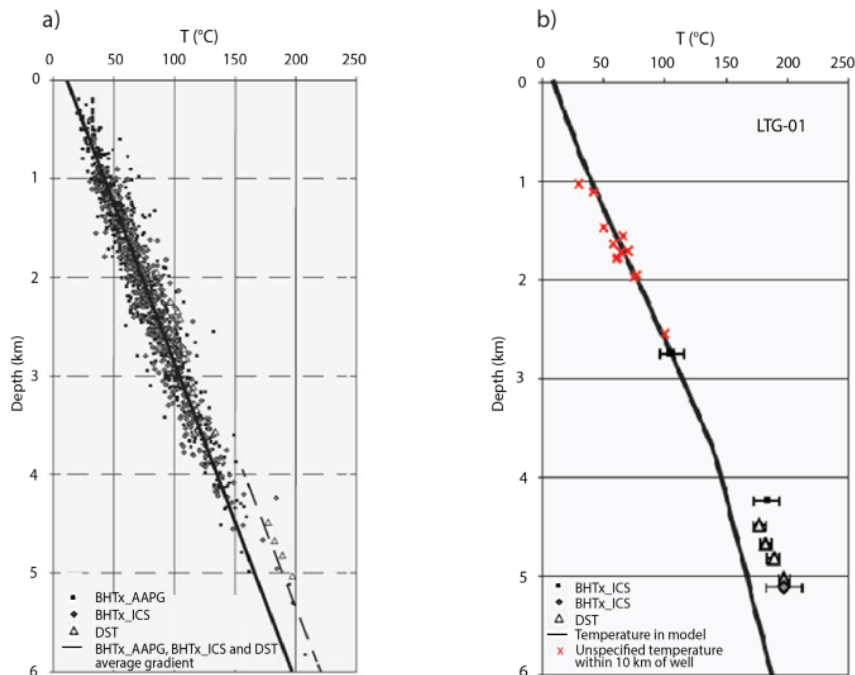
Figure 6.2. Temperature vs. depth for the Dutch subsurface. (a) DST and corrected BHT dataset. Dashed black line represents the trend for deeper temperatures. (b) Comparison between the values used as calibration and the modelled temperature for LTG-01. See legend for explanation of symbols (adapted after Bonté et al., 2012).

6.1.3 Permeability assessment

Permeability was calculated by TOTAL from wireline pressure tests and reported in the composite log (report accessible from www.nlog.nl). The permeability values range from 10 to 598 mD (10^{-14} to $6 \cdot 10^{-13}$ m^2), however several measurements were registered as fair or questionable (Lipsey et al., 2016). Van Oversteeg et al. (2014) calculated the permeability and transmissivity based on mud losses and proposed that there is an interval with fracture permeability between 4550 to 5150 m. For a reservoir thickness of 600 m, an overall permeability of $6 \cdot 10^{-14}$ m^2 was calculated (Van Oversteeg, 2014). This value is in accordance with the permeability range inferred from pressure measurements, but should be taken with caution as the permeability is not equally distributed throughout the entire interval of 600m. For example, between 4800 and 4975 m there is no evidence of permeability. An overview of the permeability assessment is presented in Table 6.1 (Lipsey et al., 2016).

Table 6.1. Overview of results from permeability assessment.

Source/method	Depth interval	Permeability
Composite well log	Some intervals of increased permeability	
Wireline Pressures	4535 – 4647 m	$10^{-14} – 6 \cdot 10^{-13}$ m^2
Rock samples	4378 – 4473 m	$2 \cdot 10^{-16} – 9 \cdot 10^{-15}$ m^2
Mud losses	600 m	$> 10^{-12}$ m^2

6.2 Methods

6.2.1 Equations

The numerical study of thermal convection in permeable and porous media involves the coupling of heat transfer and fluid flow equations that incorporate realistic fluid and rock properties. In a Eulerian reference framework, the heat equation is written as

$$\rho c \frac{\partial T}{\partial t} = \nabla \cdot (\lambda \cdot \nabla T) - \vec{v} \cdot \nabla T \qquad [6.1]$$

See Table 6.2 for nomenclature. The advective velocity can also be a result of fluid flow inside pores or fractures which can strongly affect the thermal distribution (e.g. Guillou-Frottier et al., 2013; Cherubini et al., 2014). The fluid velocity is resolved from solving the Darcy flow equation:

$$c_h \frac{\partial P}{\partial t} = \nabla \cdot \left(\frac{k}{\mu} \left(\nabla P + \frac{(\rho_f - \rho_0)}{\rho_0} g \nabla z \right) \right) + Q \qquad [6.2]$$

See Table 2 for nomenclature. Through solving the pressure field in equation [6.2], the velocities can be determined as

$$\vec{v_f} = \frac{k}{\mu} \left(\nabla P + \frac{(\rho_f - \rho_0)}{\rho_0} g \nabla z \right) \qquad [6.3]$$

And can be incorporated in equation [1] by adopting:

$$\vec{v} = \varphi \frac{\rho_f c_f}{\rho c} \vec{v_f} \qquad [6.4]$$

Temperature dependent density and fluid dynamic viscosity have been used. For the details of the equations, refer to Lipsey et al. (2016).

6.2.2 Geometry and boundary conditions

Three-dimensional coupled fluid and heat transport models are simulated using a numerical solver developed in a Java programming language. Temperature at the top of the model is 10 °C and 244 °C at the bottom reflecting a linear thermal gradient of 39 °C km^{-1}. All boundaries of the platform are impermeable, defining a closed system with no sources or sinks for the fluid. Lateral boundaries are thermally insulating. Rock thermal properties are assumed to be uniform for the entire model.

Experiments begin with an initial perturbation to the conductive temperature field by injecting cold fluid into the platform. During computation, the initial conductive field evolves towards steady-state convection within a few thousand years, therefore simulations run for 500k years.

6.2.3 Model scenarios

Two platform geometries are tested. The first geometry, referred to as model 1, is characterized by a flat platform base, where the thickness of the inner platform is 800 m. In the second geometrical configuration (model 2) the shape of the platform top remains the same, however the base of the platform is curved upwards. In order to keep the thickness of the inner platform at 800 m, the thickness of the margins is increased by 400 m, extending down to 5600 m depth at the platform margin. Fig. 6.3 provides an overview of the model geometries (Lipsey et al., 2016).
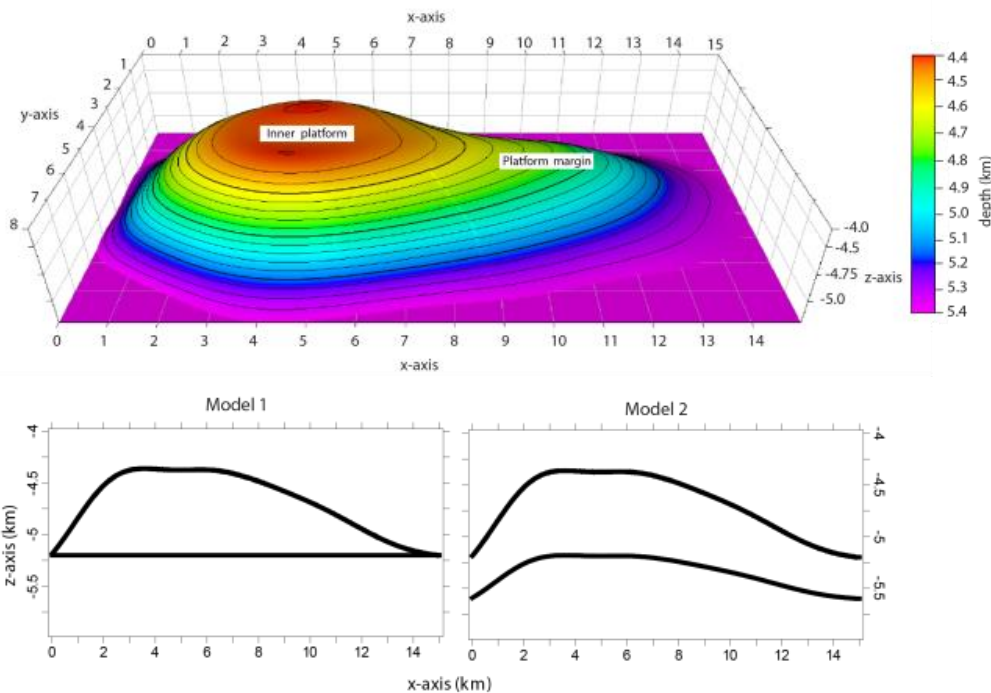
Figure 6.3. Geometry of the platform. Inner platform and platform margin indicated. Platform is at a depth of 4.4 – 5.2 km. Bottom: cross sections showing the different geometries in model 1 and model 2 (Lipsey et al., 2016).

6.3 Results

The results for a permeability of $2 \cdot 10^{-14}$ m^2 (subscript a) and $6 \cdot 10^{-14}$ m^2 (subscript b), which are applied to both geometric scenarios (models 1a,1b, 2a,2b), are presented here. For a full detail description of the model results, refer to Lipsey et al., 2016.

Model 1a relaxes into a steady-state eight cell convection pattern, characterized by four dominant upwelling plumes. Model 1b relaxes into a more complex convection pattern, characterized by four elongate polyhedral shapes. The upwelling plumes are concentrated in the thickest part of the platform in both model 1a and 1b (Fig. 6.4) .

Models 2a and 2b, where the base geometry of the platform changes from flat to upward curving, steady-state convection is reached sooner. Model 2a relaxes into a structure that is a combination of circular and elongated shaped upwellings, whereas model 2b is dominated by a more circular upwelling pattern with an increased number of convection cells (Fig. 6.5).
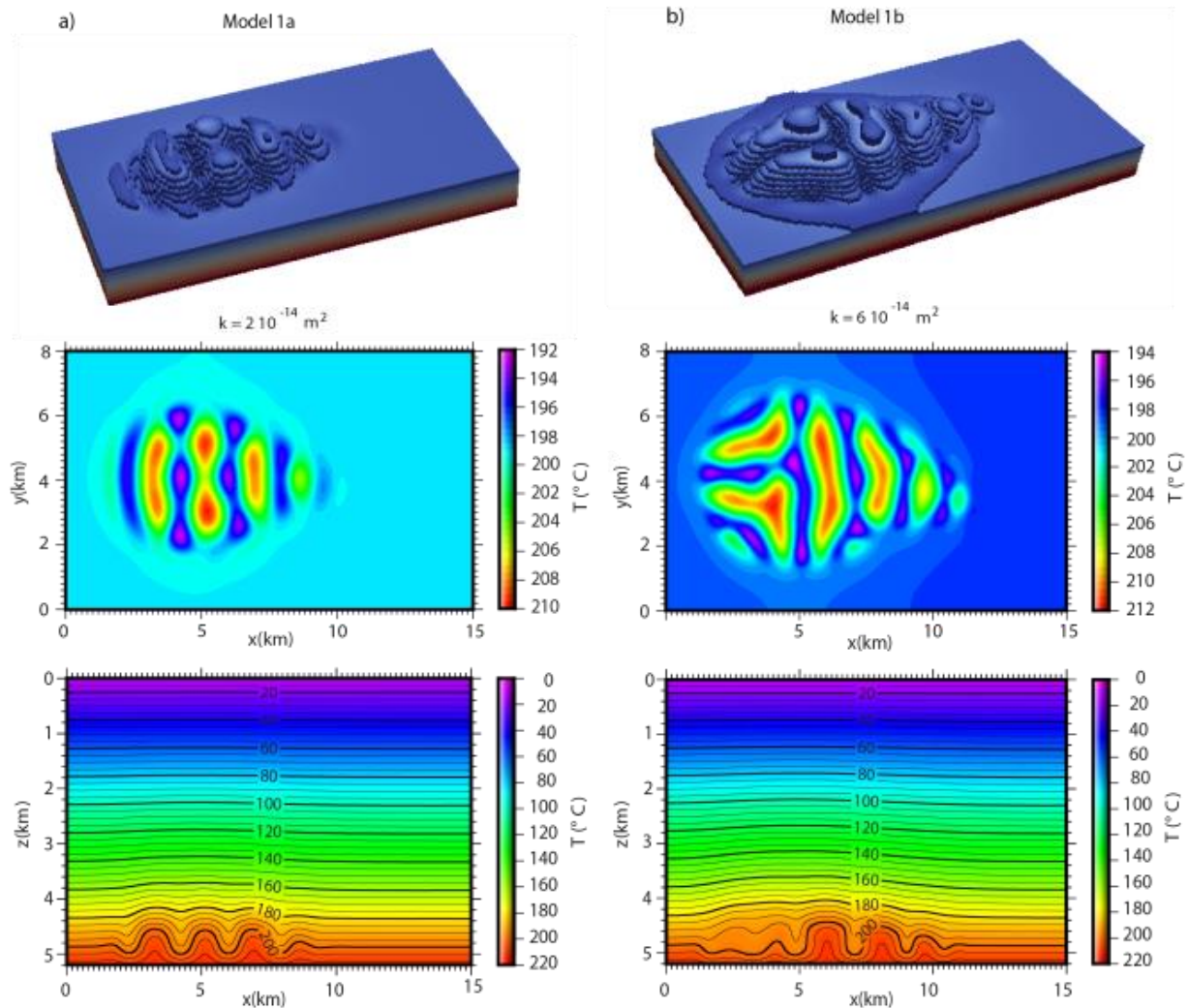
Figure 6.4. Results for model 1a and 1b. Top: 3D view of the modelled temperature field at the top of the platform. Middle: Temperature on horizontal plane z=4.8km. Bottom: Cross section at y=4km (Lipsey et al., 2016).
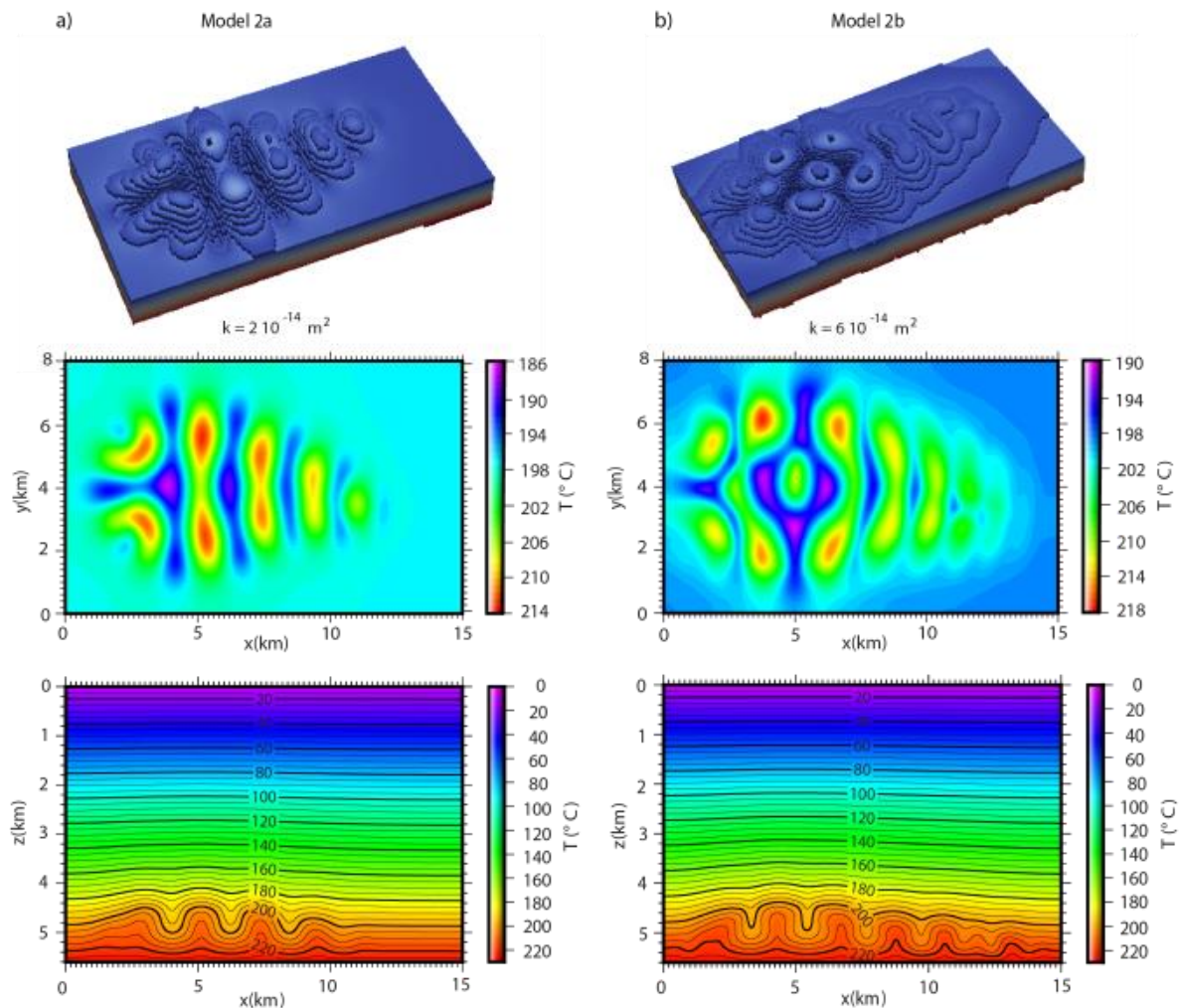
Figure 6.5. Results for model 2a and 2b. Top: 3D view of the modelled temperature field at the top of the platform. Middle: Temperature on horizontal plane z=4.8km. Bottom: Cross section at y=4km (Lipsey et al., 2016).

Fig. 6.6 shows how convective fluid flow effects the temperature field in models 1 and 2. The measured temperature values from within the platform in well LTG-01 have been added for reference. Geothermal gradients have been measured along the axis of three points in each model: downwelling, mixing zone and upwelling (Lipsey et al., 2016).

The gradient is steepest along the axes of upwelling, which results in relatively low gradients through the platform. The gradient is as low as 13°C km^{-1} in model 2b, where the platform has both a large permeability and thickness. As models have matching thermal boundary conditions, the temperature oscillates around the same temperature (200 °C) at mid-depth.

While the temperature data set from the LTG-01 well does suggest that the average gradient is elevated with respect to the Dutch average gradient of 31 °C km-1 , it appears that applying a gradient of 39 °C km^{-1} causes an over enhancement of temperatures once convection stabilizes within the carbonate platform reservoir. We therefore adjust the boundary conditions such that the gradient is no longer elevated. The result is shown in Fig. 6.7. The temperature enhancement relative to the conductive profile is similar to the previous models. As the geothermal gradient is now lower, the maximum temperatures attained within regions of upwelling are lower, ranging from 182 °C in model 1a to 192 °C in model 2b. These temperatures are more comparable with the measured temperature values at the LTG-01 well.
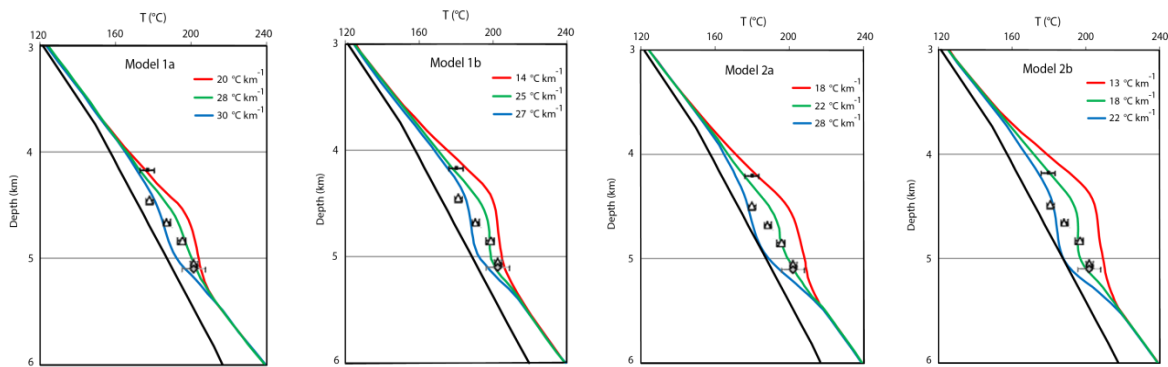
Figure 6.6. Modelled profiles along three axes: upwelling (red), mixing zone (green) and downwelling (blue). Measured temperature data from LTG-01 included for comparison. Black curve represents measured geothermal gradient (Lipsey et al., 2016).
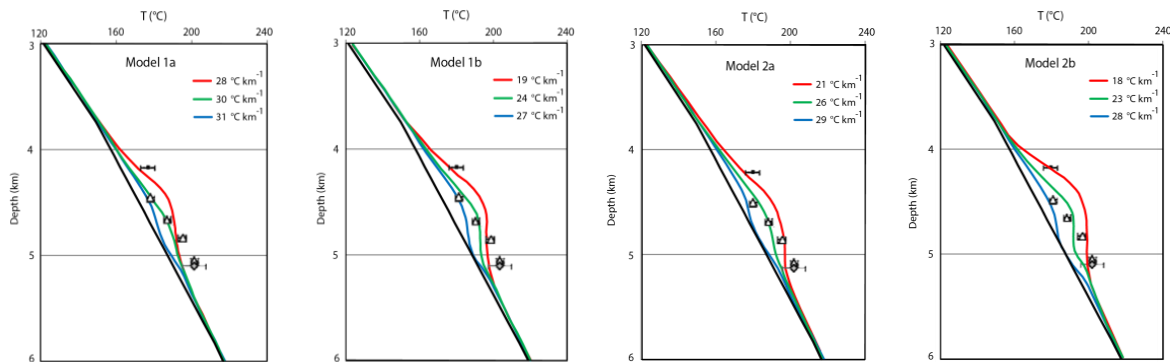

Figure 6.7. Modelled profiles for a non-elevated gradient. See Fig. 6.6 for explanation of curves.

6.4 Conclusions

The Dinantian carbonates encountered at LTG-01 well in the Netherlands contains intervals of relatively high fracture permeability showing potential as a geothermal reservoir. Temperature measurements indicate variations in subsurface temperature that could be indicative of convection. This is important, as convection creates areas where the temperature is anomalously high at shallow depths.

Numerical models show that the spacing of convective upwellings, and therefore spacing of thermal anomalies, can be predicted theoretically by knowing the platform thickness and permeability. The strong spatial variability of thermal anomalies in convective fractured aquifers at large depth can have a strong effect on exploration opportunity and risk of prospective areas. Numerical models can facilitate in exploration workflows to assess thermal variation and location of upwelling zones.

6.5 References

Bonté, D., Van Wees, J.-D., and Verweij, J. M.: Subsurface temperature of the onshore Netherlands: new temperature dataset and modelling, Geol. Mijnbouw-N. J. G., 91, 491–515, 2012.

Geluk, M.C., Dusar, M., and de Vos, W.: Pre-Silesian, in: Geology of the Netherlands, Royal Netherlands Academy of Arts and Sciences, Amsterdam, the Netherlands, 27–42, 2007.

Guillou-Frottier, L., Carré, C., Bourgine, B., Bouchot, V., and Genter, A.: Structure of hydrothermal convection in the Upper Rhine Graben as inferred from corrected temperature data and basin-scale numerical models, J. of Volcanol. Geoth. Res., 256, 29–49, 2013.

Kombrink, H.: Tectonics and sedimentation in the Northwest European Carboniferous Basin, in: The Carboniferous of the Netherlands and surrounding areas; a basin analysis, PhD Thesis, Universiteit Utrecht, 21 – 46, 2008.

Lipsey, L., Pluymaekers, M., Goldberg, T., van Oversteeg, K., Ghazaryan, L., Cloetingh, S., and van Wees, J.D.: Numerical modelling of thermal convection in the Luttelgeest carbonate platform, the Netherlands, Geothermics, 64, 135-151, 2016.

Pasquale, V., Chiozzi, P., and Verdoya, M.: Evidence for thermal convection in the deep carbonate aquifer of the eastern sector of the Po Plain, Italy, Tectonophysics, 594, 1–12, 2013.

Van Hulten, F.F.N., and Poty, E.: Geological factors controlling Early Carboniferous carbonate platform development in the Netherlands, Geol. J., 43, 175–196, 2008.

Van Oversteeg, K., Lipsey, L.C., Pluymaekers, M., van Wees, J.-D., Fokker, P.A., and Spiers, C.J.: Fracture Permeability Assessment in Deeply Buried Carbonates and Implications for Enhanced Geothermal Systems: Inferences from a Detailed Well Study at Luttelgeest-01, The Netherlands, in Proceedings Thirty-Eighth Workshop on Geothermal Reservoir Engineering, Stanford University, Stanford, California, 2014.

7 Synthesis and outlook

7.1 Stress models

The contemporary stress field in the basement/sedimentary systems of key importance for safe and sustainable subsurface operations and reservoir engineering such as required for geothermal operations. The stress state is amongst other factors used to :

- Determine the criticality of faults within reservoirs and hence knowledge of the stress state is an important component for the research of potential for induced seismicity and likelihood of fluid path ways in fractures related to active faulting
- optimize well designs in view of the drilling process, well bore stability and optimal performance in view of stimulation potential

7.1.1 multi-stage stress models

The widely scattered distribution of stress data records (both magnitude and orientation) requires a large-scale regional model to simulate the stress state in the volume. Yet, the simulated stress state is meant for a local application in a reservoir sized area. However, usually no stress data records are available within the area of the reservoir previous to any exploration activity. Hence the only available stress data are most likely in a large distance to the actual area of interest.

IMAGE has developed a strategy to overcome this scale-gap with a multistage geomechanical modelling, which is detailed in an open access publication (**Error! Reference source not found.**), which is included as appendix, and has been outlined in chapter 2. The method includes a multi-stage 3-D geomechanical–numerical modelling approach, which provides a cost efficient, reliable, and fast way to generate and evaluate the criticality of the stress state in a small target area where, in general, no stress data for model calibration are available. The approach uses a large-scale root model which is calibrated on available stress data and a small-scale branch model which is calibrated on the root model. We exemplify this in a two-stage approach in the German Molasse Basin around the municipality of Munich.

Furthermore, the discussion of reliability of the model results clearly shows (1) that variations are large and (2) that they are mainly introduced by the uncertain material properties and missing SHmax magnitude data. At this stage, the model's quality depends on the amount and quality of available input data and not on the modelling technique itself. Any further improvements in the model's resolution and applied techniques will not lead to an increase in reliability. This can only be achieved by more high-quality data for calibration.

7.1.2 Regional stress models for faulted areas

Modelling of regional stresses deals with large dimensions (hundreds to tens of thousands of square kilometres at surface per tens to hundreds of kilometres height). When such large scales are considered, the modelled rock masses are cut by major fault zones that affect the overall mechanical behaviour. Fault zones must be taken into account in the modelling, especially if numerous ones are encountered in the studied region. Besides, fault zones (FZs) themselves are affected by the tectonic regime, and studying their mechanical response might be of interest depending on the context of the study (flow-paths creation, seismogenic potential …).

In conventionally used finite element methods (e.g. previous section), it is a major challenge to incorporate large numbers of fault zones (>50) capable of reproducing spatial heterogeneity in stress response related to the faulting and rheological heterogenieity at faults. The Distinct Element Method offers a relevant tool to handle mechanically active discontinuities. With the DEM, deformable blocks interact one with another through joints. The DEM thus offers the possibility to:
- explicitly account for discontinuities and their impact on blocks,
- use complex mechanical laws for the joints, and thus study their response to tectonic efforts.

In chapter 3, we demonstrate the use of the DEM method for calculating regional stress in the structurally complex upper rhine graben area.

As far as the DEM is concerned, three limitations should be considered:
- joints are planar surfaces, and cannot reproduce the large scale irregular profiles of fault zones. The smaller scales irregularities can be considered through the constitutive equations (e.g., dilatancy).
- meshing algorithms lack optimization, and high-resolution meshes cannot be obtained. As a result, dense sedimentary sequences cannot be modelled.
- to model joints stopping within the rock mass (i.e., non-persistent), user must create a joint cutting through the rock mass (i.e., persistent), then affect heterogeneous mechanical parameters: realistic parameters on the area where joint actually exists, and very stiff parameters elsewhere to simulate the rock mass continuity. This is not that much of a limitation, but must be highlighted here since it requires additional work compared to more direct methods.

The strong advantage of the DEM resides in its explicit handling of mechanically active discontinuities. Along these joints, blocks can slide, rotate or even detach one from another. Also, specific constitutive equations governing the joints behaviour must be given. These equations exist in a wide range of complexity (purely elastic, Coulomb slip, Coulomb slip with dynamic and static friction, peak-residual) and can be adapted to describe specific behaviours through customizing facilities.

We recommend using the DEM whenever at least one of those situations is encountered:
- highly segmented regions,
- necessity to account for large displacements and rotations along fault zones (e.g., full normal or thrusting mechanisms),
- complex constitutive equations for fault zones.

7.2 Physical linkage between power-law scaling relations for fractures inferred for observed stress heterogeneity, b-value of induced seismicity and fracture scaling using data-constrained models

In order to design and assess the performance of Enhanced Geothermal Systems (EGS), a geological model of the target rock mass is required. This geological model should be representative of the whole reservoir with a realistic distribution of geological features. Of particular importance is the assessment of fracture geometries and properties which are relevant to geothermal development, including size, aperture etc.

Power law scaling has been widely utilized to characterize Discrete Fracture Network (DFN) attributes such as length, spatial distribution, aperture etc.. The scale invariance of power law distributions facilitates the construction of a geological model at different scales. In addition to DFNs, stress heterogeneities and induced seismicity have been observed to follow well-defined scaling relationships. The possible relation among these three scaling relationships might enable us to improve the way we characterize fracture

network and to better anticipate the occurrence of induced seismicity during the reservoir stimulation and exploitation.

Chapter 4 investigates the relationships from different perspectives. The modelling of the stress perturbations induced by fractures performed in Section 4.4 highlight the close relationship between these two elements and particularly how fracture length variations impact the wave length of the stress perturbation. However as discussed in Section 4.4.4.3, a deterministic approach to estimate fracture length from stress perturbation fails in a realistic and complex fracture network. This is due to the fact that fractures not intersecting the well will also influence the stress perturbation at the well and these perturbations cannot be accounted for and jeopardize the inversion approach that was applied.

Therefore, a statistical approach is considered to be a possible substitute for the deterministic approach attempted above. A probabilistic approach is expected to relate the statistical properties of the fracture network (mainly fracture length scaling relationships) to the stress perturbations characteristics. The results presented in Section 4.2 and 4.3 lay down the necessary basis for this work. Based on these results, robust methodology are available to characterize statistical characteristics and specifically scaling relationships for both fracture networks and stress heterogeneities.

Thes methodologies are currently being combined with synthetic and actual fracturing and stress heterogeneities data sets. Using the synthetic fracture networks we will create two and three dimensional geomechanical models and subject them to far field stresses or deformation at the model boundary.We expect to find a relation among the fracture network properties and stress heterogeneities along a one dimensional virtual borehole crossing the two dimensional network. If the fluid is injected into the fracture network, using a hydro-mechanical simulator, the slip on fracture planes allows us to quantify the induced seismicity by the relations between seismic moment and fault length. These result will allow us to precise the nature of the relationship between the scaling parameters of fracture networks, stress heterogeneities and induced seismicity. These methodology will then be deployed on actual data set from deep geothermal borehole in order to improve our ability to characterize deep geothermal reservoir. The results of these developments will be presented in future deliverables of WP8 of the IMAGE project.

7.3 Upfront predictions of natural fracture permeability for geothermal exploration

An analytical model was presented in chapter 5 that describes the 3D non-isotropic permeability of geothermal reservoirs where flow is controlled by faults and fractures.

The 3D permeability models for fractured reservoir incorporate fault and fracture populations and describes the permeability of fault zones using 3D permeability tensors for intact layered reservoir (matrix), damage zone and fault core.

Together with a model for the potential of geothermal doublets, the permeability model can be used to calculate doublet performance for all injector-producer orientations. In this way, the optimum injector-producer orientation and distance can be determined.

Compilations of (generic) data on fault dimensions and properties have been presented, and can be used to constrain model parameters if site-specific data from geological & geophysical characterization is lacking.

The sensitivity of the model to the orientations of layers, fractures and faults as well as damage zone fracture density has been analyzed. It shows that bulk permeability can vary considerably, mainly depending on (i) permeability anisotropy in the matrix, damage zone and fault core, (ii) the orientation of matrix layers and damage zone fractures, and (iii) the location relative to the fault core.

For a site demonstration, fault populations have been analyzed for a potential geothermal field case consisting of a Dinantian carbonate platform located near Luttelgeest in the northern onshore regions of the Netherlands. Fault sizes and orientations have been determined based on 2D and 3D seismic interpretation using a non-local means approach for reduction of seismic noise and an ant-tracking approach for imaging faults, which has been developed in WP7 and WP8. The analysis shows showing that faults have a preferred ENE-WSW fault strike and a preferred dip between 76-81°.

Using generic models with typical input parameters it is shown that the approach can be used to optimize doublet designs in faulted and fractured geothermal reservoirs. Optimum doublet designs for the Dinantian carbonate platform field case will be analysed during the continuation of the IMAGE project.

7.4 Predictive models approaches for temperature and fracture permeability

Thermal anomalies in deep sedimentary layers and basement rock are largely controlled by convective fluid flow within zones of increased fracture permeability. Convection is of interest in geothermal energy, as upwelling hot fluid yields relatively shallow high-temperature anomalies. These are preferential targets for geothermal exploration. Convective fluid flow leaves a distinct pattern on the local geothermal gradient. The thermal effect is critically dependent on the pre-existing thermal gradient, thickness and permeability.

Chapter 6 highlighted the use 3D numerical models for thermal convection capable of predicting thermal anomalies in relation to the full 3D complexity of a fractured reservoir. These models serve to gain a better understanding of the interplay between geothermal anomalies, reservoir geometry at large depth and natural fracture permeability therein.

The model has been used to Recent analysed the possible relationship of a thermal anomaly at 4-5 km depth encountered at the Luttelgeest-01 well (LTG-01) in a Dinantian carbonate platform, which could be explained by thermal convection. The models are successful in reproducing the temperature pattern and shed light on possible convective flow interpretations, including implications for fracture permeability.

Numerical models show that the spacing of convective upwellings, and therefore spacing of thermal anomalies, can be predicted theoretically by knowing the platform thickness and fracture permeability. The strong spatial variability of thermal anomalies in convective fractured aquifers at large depth can have a strong effect on exploration opportunity and risk of prospective areas. Numerical models can facilitate in exploration workflows to assess thermal variation and location of upwelling zones. The characteristics effects of convection in terms of predicting thermal anomalies as a function of relatively thick low permeability basement/sedimentary sequences can be adopted in a simplified numerical approach for practical use in regional and local models. This approach is explained in further detail in Deliverable D8.3 and will be further developed in the continuation of IMAGE.

Appendix A   Ziegler et al., 2016

Appendix B   Lipsey et al., 2016

A multi-stage 3-D stress field modelling approach exemplified in the Bavarian Molasse Basin

Moritz O. Ziegler[1,2], **Oliver Heidbach**[2], **John Reinecker**[3], **Anna M. Przybycin**[4], and **Magdalena Scheck-Wenderoth**[1,5]

[1]Helmholtz Centre Potsdam, German Research Centre for Geosciences, Telegrafenberg, 14473 Potsdam, Germany
[2]University of Potsdam, Institute of Earth and Environmental Science, Karl-Liebknecht-Str. 24–25, 14476 Potsdam, Germany
[3]GeoThermal Engineering GmbH, Baischstrasse 8, 76133 Karlsruhe, Germany
[4]Bundesanstalt für Gewässerkunde, Am Mainzer Tor 1, 56068 Koblenz, Germany
[5]RWTH Aachen University, Department of Geology, Geochemistry of Petroleum and Coal, Templergraben 55,
52056 Aachen, Germany

Correspondence to: Moritz O. Ziegler (mziegler@gfz-potsdam.de)

Abstract. The knowledge of the contemporary in situ stress state is a key issue for safe and sustainable subsurface engineering. However, information on the orientation and magnitudes of the stress state is limited and often not available for the areas of interest. Therefore 3-D geomechanical–numerical modelling is used to estimate the in situ stress state and the distance of faults from failure for application in subsurface engineering. The main challenge in this approach is to bridge the gap in scale between the widely scattered data used for calibration of the model and the high resolution in the target area required for the application. We present a multi-stage 3-D geomechanical–numerical approach which provides a state-of-the-art model of the stress field for a reservoir-scale area from widely scattered data records. Therefore, we first use a large-scale regional model which is calibrated by available stress data and provides the full 3-D stress tensor at discrete points in the entire model volume. The modelled stress state is used subsequently for the calibration of a smaller-scale model located within the large-scale model in an area without any observed stress data records. We exemplify this approach with two-stages for the area around Munich in the German Molasse Basin. As an example of application, we estimate the scalar values for slip tendency and fracture potential from the model results as measures for the criticality of fault reactivation in the reservoir-scale model. The modelling results show that variations due to uncertainties in the input data are mainly introduced by the uncertain material properties and missing $S_{H_{max}}$ magnitude estimates needed for a more reliable model calibration. This leads to the conclusion that at this stage the model's reliability depends only on the amount and quality of available stress information rather than on the modelling technique itself or on local details of the model geometry. Any improvements in modelling and increases in model reliability can only be achieved using more high-quality data for calibration.

1 Introduction

The contemporary in situ upper crustal stress field is of key importance for our understanding of geodynamic processes such as natural and induced seismicity (Häring et al., 2008; Gaucher et al., 2015; Scholz, 2002; Heidbach and Ben-Avraham, 2007; Townend and Zoback, 2004; Zang et al., 2014). The stress field also provides critical a priori information for safe and sustainable underground engineering such as wellbore planning and stability, reservoir management, tunnelling, mining, and underground waste storage (Altmann et al., 2014; Cornet et al., 1997; Fuchs and Müller, 2001; Moeck and Backers, 2011; Tingay et al., 2008; Zang et al., 2013; Ziegler et al., 2015; Zoback, 2010). The quantification of the criticality of the in situ stress state in terms of fault reactivation in advance of any underground treatment is essential for identifying areas of low criticality for safe and efficient utilization of the subsurface (Hornbach et al.,

2015; Zoback et al., 1985; Häring et al., 2008; Kohl and Mégel, 2007). In particular, the enhancement of permeability through hydraulic fracturing should be achieved without reactivation of sealing faults or inducing seismic events of economic concern (Deichmann and Ernst, 2009; Yoon et al., 2015; Zoback et al., 1985; Townend and Zoback, 2000).

The main focus of current research is to quantify stress changes due to anthropogenic underground usage (McClure and Horne, 2014; Jeanne et al., 2014; Orlecka-Sikora, 2010; Gaucher et al., 2015; Magri et al., 2013). Induced changes of the 3-D stress state in geo-reservoirs are simulated with thermo-hydro-mechanical (THM) models since the treatment of the underground, e.g. the rate of injected fluid or the amount of mass removal, is well known (Kohl and Mégel, 2007; Gaucher et al., 2015; Van Wees et al., 2014; Jeanne et al., 2014; Cacace et al., 2013; Rutqvist et al., 2013; Magri et al., 2013). However, to assess whether the subsurface engineering pushes the system into a critical stress state in terms of absolute values, knowledge of the contemporary in situ stress, i.e. the undisturbed stress state, is essential (Hergert et al., 2015; Häring et al., 2008).

The 3-D in situ stress state can be described with a symmetric tensor of second degree with six independent components (Jaeger et al., 2007; Zang and Stephansson, 2010). Assuming that the vertical stress S_v is one of the principal stresses in the upper crust, the number of independent unknowns reduces to four (Zoback, 2010). In the principal axis system these are the orientation of one of the two principal horizontal stresses, i.e. the maximum and minimum horizontal stress, $S_{H_{max}}$ and $S_{h_{min}}$, as well as the magnitudes S_v, $S_{H_{max}}$ and $S_{h_{min}}$ (Zoback, 2010; Schmitt et al., 2012). Thus, the orientation of this so-called reduced-stress tensor is described by the $S_{H_{max}}$ orientation, which is systematically compiled by the World Stress Map (WSM) project (Heidbach et al., 2010, 2008; Sperner et al., 2003; Zoback, 1992).

Figure 1 shows a stress map with a typical density of $S_{H_{max}}$ orientation data records with 172 reliable data records for the $82\,000\,km^2$ large part of the Alpine Foreland Molasse (Reiter et al., 2015; Reinecker et al., 2010; Heidbach and Reinecker, 2013). This results in an average data density of 0.21 data records per $100\,km^2$, which is the typical claim size for exploration. In general, the orientation of the stress field does not change with depth in the upper crust (Rajabi et al., 2016; Pierdominici and Heidbach, 2012; Heidbach et al., 2007). Laterally the stress field in the Alpine Molasse rotates only gently anticlockwise from east to west (Reinecker et al., 2010). Thus, the available stress orientation data allows the determination of the orientation of the reduced-stress tensor to a relatively high degree of reliability (Heidbach et al., 2007; Ziegler et al., 2016; Reiter et al., 2015).

More important for assessing criticality is the estimation of the differential stress between the magnitudes of the largest and smallest principal stresses and their changes during stimulation and production. The S_v magnitude can be derived from the vertical-density distribution. In contrast to this, the

horizontal stress magnitudes originate from geological history and ongoing tectonic evolution and cannot be determined directly from rock properties (Brown and Hoek, 1978; Zang et al., 2012; Zang and Stephansson, 2010). Furthermore, the increase of horizontal stress magnitude with depth is often described with a linear gradient, which is only justified when rock strength and density do not change significantly with depth (Brudy et al., 1997; Lund and Zoback, 1999). In sedimentary basins this linear increase cannot always be assumed. Competent layers, e.g. from the Malm and Muschelkalk, alternate with weaker layers with high clay content such as Dogger and Keuper and result in a sudden deviation of the stresses from a linear trend across these layers (Warpinski, 1989; Hergert et al., 2015; Cornet and Röckel, 2012; Gunzburger and Cornet, 2007; Zang et al., 2012). Moreover, the density of stress magnitude data records is, in general, up to 2 magnitudes lower than that of the orientation data (Fig. 1).

To summarize, our knowledge of the 3-D in situ stress state is based on sparsely distributed and incomplete information. Only the orientation of the reduced-stress tensor and, to a lesser extent, information about the stress regime are relatively well estimated from stress indicators. The crustal in situ stress magnitudes are underdetermined, since they vary laterally and vertically. To determine the full stress tensor for every point in a volume, a 3-D geomechanical–numerical model workflow that uses the available stress information for model-independent constraints for calibration is essential. Moreover, at reservoir scale, often no stress information is available for model calibration (Fig. 1). Thus, it is necessary to enlarge the model area until sufficient stress data are within the model volume. In the Bavarian Molasse Basin, which we use as an example, this enlargement of the model area leads to an increase in model size from a $10 \times 10\,km^2$ reservoir-sized model to $70 \times 70\,km^2$ regional model (Fig. 1). Considering a constant resolution, this enlargement would lead to a higher number of model degrees of freedom by a factor of 50. In most cases of THM reservoir modelling, this is beyond feasibility due to the time required for iterations and limitations in computation power. One option for avoiding a high degree of freedom is to refine the structure only in the area of interest (Jeanne et al., 2014; Westerhaus et al., 2008) (Fig. 2a). However, this becomes challenging when local structures have to be integrated. An alternative option is to use nested modelling, which is applied in various scientific disciplines such as meteorology, climate simulations, and the simulation of seismic cycles (Warner and Hsu, 2000; Cacas et al., 2001; Giorgi et al., 1998; Hergert and Heidbach, 2011). Essentially, a nested modelling approach can be (1) a local high-resolution grid inside a coarse grid where the variables are matched at the boundaries (Fig. 2b) (Oey and Chen, 1992) or (2) a multi-stage approach of two or more individual models which increase their resolution within the same area or subarea (Warner and Hsu, 2000) (Fig. 2c). In contrast to the previously named nested
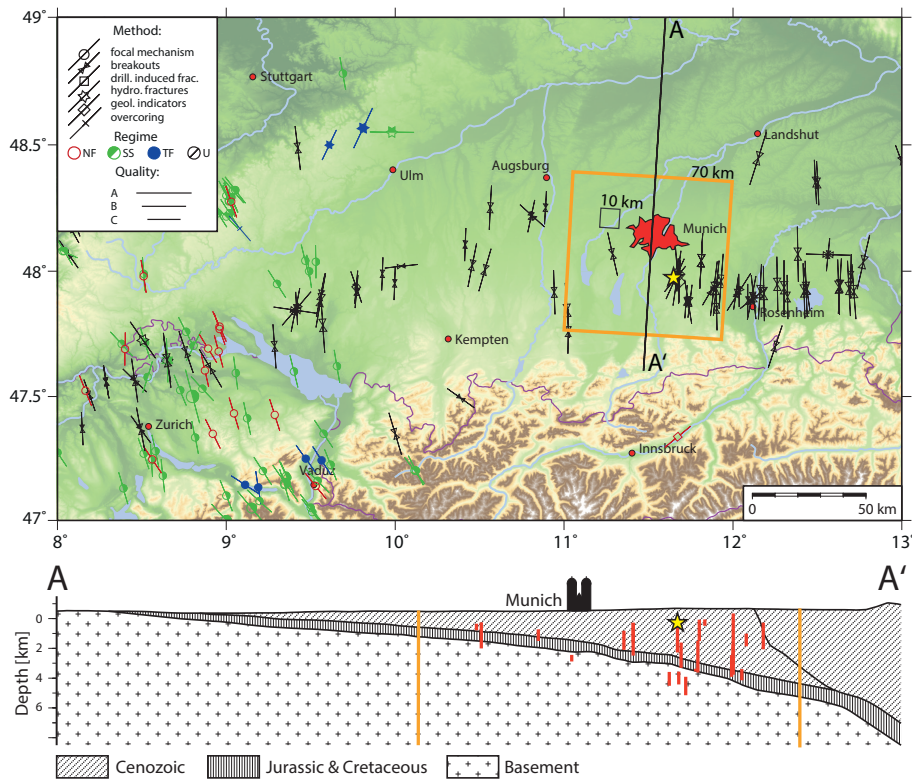
Figure 1. Stress map of the Bavarian Molasse with 172 A-C quality data records based on the World Stress Map database release 2008 (Heidbach et al., 2008, 2010) and additional data from Reiter et al. (2015) and Heidbach and Reinecker (2013). Lines show the $S_{H_{max}}$ orientation with line length proportional to WSM data quality (Heidbach et al., 2010). Colour coding of the data shows the stress regime with red for normal faulting (NF), green for strike-slip (SS), blue for thrust faulting (TF), and black if the regime is unknown (U). The star marks the location of the Sauerlach project where information on the $S_{h_{min}}$ magnitude is available (Seithel et al., 2015). The orange box shows the lateral boundaries of the 3-D geomechanical–numerical model area ($70 \times 70\,\mathrm{km}^2$) and the small black box indicates the typical dimensions of a reservoir model ($10 \times 10\,\mathrm{km}^2$). The cross section A-A' (based on Przybycin, 2015) shows a 1 : 2.5 exaggeration of the area with red lines being the borehole sections and stress indicators within the model area.
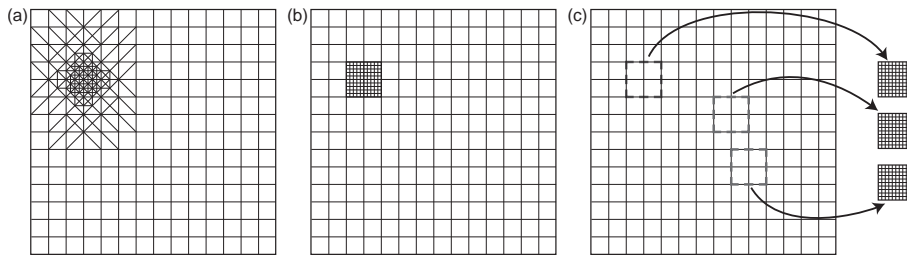
Figure 2. Different types of modelling approaches. **(a)** A refined mesh in the area of interest is expensive and inefficient due to the large number of elements required for the discretization of the gradient in resolution. Furthermore, it requires a complete remesh and re-evaluation in case of any change in the geometry or input data. **(b)** A local model nested within a regional model matches the variables at the boundary. A complete remesh and re-evaluation is required in case of geometry or input data changes. **(c)** A multi-stage approach has the easiest mesh generation since the differently sized models are generated independently. Furthermore, several reservoir models can be based on the same regional model.

approaches, the multi-stage procedure is most favourable in terms of required workload (fast and simple mesh generation) and quality of results (high spatial resolution in the area of interest). Furthermore, it may serve several individual reservoir model locations within the regional-area model volume (Fig. 2c). However, so far this procedure has not been applied in 3-D geomechanical–numerical modelling of the crustal stress field.

In this paper we demonstrate the applicability of the multi-stage nesting workflow for the 3-D geomechanical modelling of the stress tensor. We exemplify our approach with a 3-D model of the Greater Munich area in the northern Alpine Molasse Basin and a generic reservoir model (Fig. 1). We demonstrate the conceptual advantages of the multi-stage approach as a detailed, yet fast workflow for exploration from planning to exploitation. Furthermore, we quantify the impact of the uncertainties of the model parameters and the limited amount of calibration data on the model results and discuss the reliability of the 3-D geomechanical–numerical modelling.

2 Geological setting

The northern Alpine Molasse Basin is a typical asymmetric foreland basin which extends over 1000 km from Lake Geneva in the west to Lower Austria in the east (Bachmann et al., 1987). Its widest N–S extent is 130 km in southern Germany (Lemcke, 1988). The basin mainly consists of Tertiary sediments on top of Mesozoic successions and a Variscan basement with Permo-Carboniferous troughs (Lemcke, 1988; Bachmann et al., 1987). In the Foreland Molasse these sediments dip towards the south where a maximum thickness of approximately 6000 m is reached in front of and beneath the Alpine mountain chain and the Folded Molasse (Fig. 1) (Bachmann et al., 1987). Due to the Molasse Basin's close link to the Alpine orogeny (Schmid et al., 2008) most of the main faults in the Bavarian Foreland Molasse are steeply dipping ($> 60°$) and strike at least subparallel to the Alpine front approximately E–W (Reinecker et al., 2010; Bachmann et al., 1987; Lemcke, 1988). They are considered mostly inactive at the moment (Reinecker et al., 2010; Bachmann et al., 1987; Lemcke, 1988).

For our model geometry we use the upper 9 km of the 3-D structural model of the northern Alpine Foreland Basin by Przybycin (2015), which covers the entire German part of the Molasse Basin. It provides 12 stratigraphical units in total with a focus on the Malm and Purbeck, two target horizons for geothermal exploration (Lemcke, 1988; Bachmann et al., 1982; Fritzer et al., 2012). The lateral resolution of the structural model (1×1.7 km^2) is sufficient to provide the geometry for the generation of our regional-scale model of the Greater Munich area. The structure is based on freely available data on the depth and thicknesses of stratigraphic units from wells and seismic lines as well as 3-D gravity mod-

elling as a further constraint (Przybycin, 2015). The part of the structural model used for the geomechanical model has a size of 70×70 km^2 and is referred to as the root model. It includes the sediments in the Molasse Basin in their entire vertical extent. The bottom of the model is situated at a depth of 9 km entirely within the upper crust. The generic reservoir model located within the root model volume is called a branch model. It has a size of 10×10 km^2 with more detailed structural information, e.g. provided by a 3-D seismic survey.

3 In situ stress data

3.1 Orientation of $S_{H_{\max}}$

Within the root model area (Fig. 1, orange box) 18 reliable $S_{H_{\max}}$ orientation data records are located, while there are none in the branch model area (Fig. 1, black box). These data are exclusively from borehole measurements using drilling-induced tensile fractures (Aadnoy, 1990) and borehole breakouts (Bell and Gough, 1979; Bell, 1996) as indicators for the $S_{H_{\max}}$ orientation (Reinecker et al., 2010). In 15 wells in the model area, borehole breakouts are found with a combined length of 7.7 km. In 3 wells drilling-induced fractures are found with a combined length of 0.3 km. The stress indicators are found mainly between the surface and a depth of 2–3 km even though some are located at greater depth (Fig. 1). No significant stress rotation or perturbation with depth is observed in the available data (Reinecker et al., 2010; Heidbach et al., 2016). The quality of the data is exceptionally good according to the WSM quality ranking (Heidbach et al., 2010; Sperner et al., 2003; Zoback, 1992) with eight A-quality data records (i.e. an uncertainty of $\pm 15°$), six B-quality data records (± 15–$20°$), and four C-quality data records (± 20–$25°$). Under the assumption that S_v is a principal stress component, the reduced 3-D stress tensor within the model area has a mean $S_{H_{\max}}$ orientation of $1.7° \pm 19.2°$ which is approximately perpendicular to the Alpine front (Fig. 1).

3.2 Stress magnitudes

The magnitude of S_v can be estimated with a relatively high reliability from the thickness of the different overlying units (z) in the structural model provided by Przybycin (2015), the density of the corresponding rock material (ρ_{rock}, Table 1) and the gravitational acceleration (g) given by

$$S_v = \sigma_{zz} = \rho_{\mathrm{rock}} g z. \tag{1}$$

However, information on the horizontal stress magnitudes is sparse even within the root model area. The magnitude of $S_{h_{\min}}$ is usually derived from hydraulic fracturing (Haimson and Fairhurst, 1969; Hubbert and Willis, 1972), but such data are not available publicly for the Bavarian Molasse Basin. Alternatively, leak-off tests (LOTs), which rely on a cheaper

Table 1. The stratigraphic units, their discretization, and according rock properties, which are present in the root and branch models. Units which are only preserved in parts of the root model are marked with *.

Unit(s)	Root model: vertical layers	Branch model: number of elements	Density [kg m^{-3}]	E-module [GPa]	Poisson ratio
Molasse	6	–	2375[a,b]	15[c]	0.29[c]
Upper Molasse	–	1.1×10^6	2375[a,b]	15[c]	0.29[c]
Aquitanian	–	2.3×10^6	2495[d]	32.5[d]	0.21[d]
Chattian	–	7.6×10^6	2758[e]	39[d]	0.23[d]
Cretaceous	3*	–	2647[a,b]	22.5[b]	0.25[b]
Malm δ-Purbeck	8	6.3×10^6	2667[d,e]	40[b]	0.25[b]
Malm $\alpha - \gamma$	6	2.2×10^6	2460[d]	30[b,c]	0.29[b,c]
Pre-Malm	4*	–	2680[a,b]	20[c]	0.25[c]
Crust	6	2.2×10^6	2850[a]	45[c]	0.24[c]

[a] Przybycin (2015), [b] Koch (2009), [c] Hergert et al. (2015), [d] Lama and Vutukuri (1978), [e] Koch and Clauser (2006)

and faster method, are more frequently used for the estimation of $S_{h_{\min}}$. They provide information on the break-down pressure of the tested formation, which is then used as an approximation for the $S_{h_{\min}}$ magnitude (Haimson and Fairhurst, 1969; Bell, 1990; Zang et al., 2012). Further information on the $S_{h_{\min}}$ magnitude can be derived from a formation integrity test (FIT). It does not fracture the rock but provides a minimum pressure value at which the rock is stable, which in turn provides a lower bound for the $S_{h_{\min}}$ magnitude (Zoback et al., 2003). Even though no hydraulic fracturing was done in the model area a LOT has been conducted in the Unterhaching Gt 1/1a borehole which is used for calibration (T. Fritzer, personal communication, 2016). Furthermore, several FITs have been performed in the borehole Sauerlach (Fig. 1) that is in the root model area (Seithel et al., 2015). In contrast to the LOTs FITs are not used for calibration since the difference between the FIT pressure and the actual magnitude of $S_{h_{\min}}$ is not known. However, during one of the FITs in the Sauerlach borehole bore fluid was lost into the formation (T. Fritzer, personal communication, 2016). Hence a leak-off occurred and this FIT is treated as a LOT and used for the model calibration.

The direct estimation of the $S_{H_{\max}}$ magnitude would only be possible with overcoring measurements (Hast, 1969; Sjöberg et al., 2003). In addition, reasonable values for the $S_{H_{\max}}$ magnitude can be derived on the basis of the frictional equilibrium theory (Zoback et al., 2003) or physics-based relations for which reliability is largely dependent on the quality of the $S_{h_{\min}}$ magnitude estimation (Zoback, 2010; Cornet, 2015). Seithel et al. (2015) use the friction equilibrium approach and derive a single $S_{H_{\max}}$ magnitude between 112 and 116 MPa at a depth of 4 km. We use an $S_{H_{\max}}$ magnitude of 112 MPa in Sauerlach for the calibration even though the uncertainties introduced by the derivation are high. The impact of these high uncertainties on the model results is discussed later on.

3.3 Stress regime

In areas with a low number of magnitude stress data records, the stress regime provides information on the relative magnitudes of S_v, $S_{H_{\max}}$, and $S_{h_{\min}}$. The stress regime is mainly derived from focal mechanisms of seismic events and, to a small extent, from geological indicators or hydraulic fracturing experiments (Zoback, 1992; Sperner et al., 2003). In the Swiss part of the northern Alpine Molasse Basin a strike-slip ($S_{H_{\max}} > S_v > S_{h_{\min}}$) and, to a smaller extent, extensional ($S_v > S_{H_{\max}} > S_{h_{\min}}$) stress regime is mainly observed (Heidbach and Reinecker, 2013). However, in the Bavarian Molasse Basin north of the Alpine front, no natural seismicity has been recorded (Grünthal, 2011; Grünthal and Wahlström, 2012) to derive the stress regime from focal mechanisms.

Information from structural geology observing steeply dipping faults in the Bavarian Molasse Basin (Bachmann et al., 1987; Lemcke, 1988) indicates an extensional tectonic faulting regime (Anderson, 1905, 1951). In contrast to this Illies and Greiner (1978); Lemcke (1988), and Reinecker et al. (2010) propose a compressional ($S_{H_{\max}} > S_{h_{\min}} > S_v$) or strike-slip stress regime in the Molasse Basin. Seithel et al. (2015) also propose a strike-slip stress regime at a depth of 4 km for the Sauerlach project according to their analysis based on the frictional equilibrium theory. However, without further estimations of the stress magnitudes in other depth sections and locations, the regional tectonic stress regime setting is subject to large uncertainties.

4 Model workflow

4.1 Model set-up

Both the regional-scale root model and the reservoir-scale branch model are based on the same modelling assumptions. Assuming that accelerations other than gravity can be neglected, the models solve the partial differential equation

of the equilibrium of forces. Furthermore, we assume a linear elastic rheology and solve for absolute stresses (no pore pressure). The general model procedure follows the technical workflow explained in detail by Hergert et al. (2015) and Reiter and Heidbach (2014).

The root model extends $70 \times 70 \times 10\,\mathrm{km}^3$ in the entire Greater Munich area (Fig. 1). It consists of six different stratigraphic layers (Table 1) based on the 3-D structural model by Przybycin (2015). The generic branch model of a potential geothermal site has a size of $10 \times 10 \times 10\,\mathrm{km}^3$ and includes six different stratigraphic units (Table 1). For both models the boundaries are oriented perpendicular and parallel to the orientation of $S_{H_{\max}}$ and $S_{h_{\min}}$ respectively (Fig. 1). Both models are populated with the Young's modulus, the Poisson ratio and the density according to the stratigraphic units (Table 1).

An exact fit of the overburden S_v is achieved by applying gravity, provided that the density of the stratigraphic units is correctly chosen. We implement an equilibrated initial stress state close to lithostatic ($S_{H_{\max}} \approx S_{h_{\min}} \approx S_v$). Dirichlet boundary conditions (i.e. displacements) are applied to the sidewalls of the model to create horizontal differential stresses. The boundary conditions are adjusted in a way that the modelled magnitude of $S_{H_{\max}}$ and $S_{h_{\min}}$ at the calibration points fit the observed magnitudes.

Due to the complex topology of the stratigraphy and inhomogeneous rock properties of the different units the finite element method (FEM) that allows unstructured meshes is used to solve the partial differential equation of the equilibrium of forces at discrete points. Thus, both models are discretized into finite element meshes. The root model is constructed with approximately 10^6 hexahedral elements resulting in approximately 400 m of horizontal and between 15 and 700 m of vertical resolution (Fig. 3). A vertically refined resolution is created in the units of interest for geothermal exploration, namely the Malm and Purbeck formation. The Cretaceous and the Triassic (pre-Malm) are only preserved in parts of the root model. Compared to the root model a significantly finer resolution with a total of 21×10^6 tetrahedral elements is chosen in the branch model. The edge length of the elements varies between 10 and 160 m with the coarsest resolution located at the bottom and the edges of the model and the highest resolution in the Purbeck and Malm units of interest for geothermal exploration (Fig. 3).

4.2 Model calibration procedure and two-stage approach

The calibration of the root model with stress magnitude data is achieved by applying two Dirichlet boundary conditions, each on one of the perpendicular sidewalls of the model (Fig. 4, left row). A single $S_{h_{\min}}$ magnitude data record can be exactly modelled by a certain combination of two boundary conditions. More precisely an unlimited combination of two boundary conditions exist to achieve an exact fit of a single
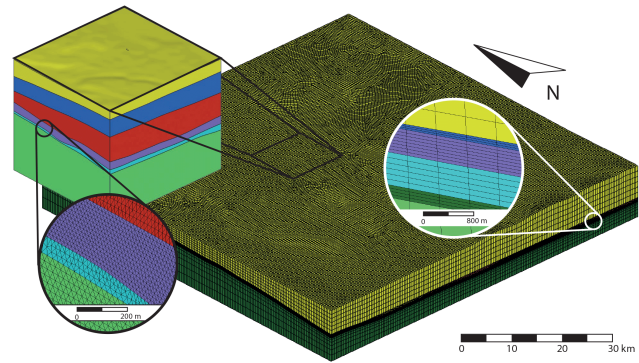

Figure 3. The root and branch model discretized with 10^6 hexahedral and 21×10^6 tetrahedral elements respectively. Please note that to improve visibility the discretization of the branch model is only displayed within the magnified inset. Both magnified regions show the Malm $\alpha - \gamma$ (turquoise) and Malm $\delta - \zeta$ and Purbeck (purple) units, which are the predominant target units for geothermal exploration in the Bavarian Molasse Basin.

$S_{h_{\min}}$ magnitude calibration point. This unlimited number of combinations of displacement boundary conditions is a linear function of the E–W and N–S displacements and is displayed as a linear slope in Fig. 4a with displacement in N–S direction on the x axis and displacement in E–W direction on the y axis. Due to the assumed linear elastic model rheology, each combination of east–west and north–south displacement that lies on the slope leads to an exactly calibrated model (Fig. 4a).

If several $S_{h_{\min}}$ magnitudes are available for calibration, each of them can be exactly reproduced by an unlimited number of combinations of displacement boundary conditions. However, to achieve a calibration which works for all of the observed $S_{h_{\min}}$ magnitudes, a single "best-fit" slope is derived from the linear slopes for the individual calibration points using a linear regression (Fig. 4b) (Reiter and Heidbach, 2014). Each combination of displacement boundary conditions specified by this slope results in a best-fit model for all of the considered calibration points.

The same procedure is applied for the calibration of $S_{H_{\max}}$ magnitudes so that eventually a best-fit slope for both the $S_{H_{\max}}$ and $S_{h_{\min}}$ magnitude stress data records used for calibration are available (Fig. 4c). Displacement boundary conditions defined by the point where these two best-fit slopes intersect are used to compute the best-fit model that reproduces the $S_{H_{\max}}$ and $S_{h_{\min}}$ stress data records best (Fig. 4c) (Reiter and Heidbach, 2014).

Application of this calibration procedure is fast and simple since the best-fit boundary conditions can be found by combining two linear slopes based on the calibration data and the displacement boundary conditions. Therefore, to find the best-fit boundary conditions only three different models with arbitrary displacement boundary conditions are required (Fig. 5a). The modelled $S_{H_{\max}}$ and $S_{h_{\min}}$ magnitudes at the
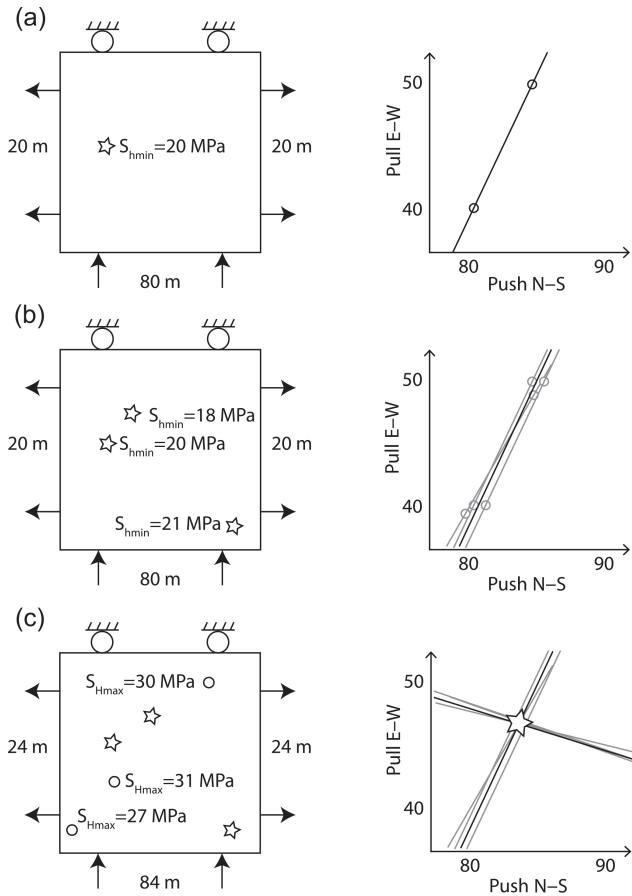
Figure 4. Left: exemplified schematic models with the data records used for calibration (star: $S_{h\min}$ magnitude, circle: $S_{H\max}$ magnitude). Right: linear slopes that display the magnitudes of possible combinations of displacement boundary conditions applied normal to the E–W (y axis) and N–S (x axis) sidewalls of the model. For each data record an individual slope defines the possible combinations of boundary conditions to fit the model to this calibration data record. **(a)** A single $S_{h\min}$ magnitude can be calibrated by an unlimited number of combinations of boundary conditions which are on a linear slope. **(b)** Several $S_{h\min}$ magnitudes usually cannot be calibrated to an exact fit. However, a linear regression of all the linear slopes derived for the calibration of each individual data record provides a best-fit slope. This slope defines combinations of best-fit boundary conditions that fit the data records used for calibration equally well. **(c)** Several $S_{h\min}$ and $S_{H\max}$ magnitude data records used for calibration results for each $S_{h\min}$ and $S_{H\max}$ in a linear slope of combinations of best-fit boundary conditions. At the intersection of these two slopes the best-fit boundary conditions (indicated by a star) are found for the calibration of $S_{H\max}$ and $S_{h\min}$ together.

location of calibration points in each of the three models are compared to the actually observed data records (Fig. 5b, c). A linear regression with two unknown variables leads to the best-fit slopes for the combination of boundary conditions to model the $S_{H\max}$ and $S_{h\min}$ magnitude (Fig. 5d). At the intersection of the two slopes, the boundary conditions for the best-fit model can be derived (Fig. 5d).

It is assumed that the stress data records used for the calibration are the result of the far-field stress state and its interaction with structural features such as local density and/or strength contrasts represented within the root model. If the measurements were, e.g. the result of an unknown or unimplemented local active fault, the results of the calibration would not be reliable. Thus, in general, the data used for calibration should be representative for a large volume of the individual lithological layer.

Under this assumption the best-fit model simulates the stress state at discrete points in the entire model volume. Hence, information on the stress state is now also available in areas of the root model where previously no observables on the stress state were available. This means that in the branch model, which does not include any observed stress data records, simulated information on the stress state is also now available from the root model and can be used to calibrate the branch model (Fig. 5d, f).

Since the branch model is calibrated in the same way as the root model (but with a simulated stress state from the root model as calibration points instead of observed stress data records), a large number of potential calibration points with $S_{h\min}$ and $S_{H\max}$ magnitudes are available. The $S_{H\max}$ and $S_{h\min}$ magnitudes at each calibration point can be modelled individually in the branch model by combinations of boundary conditions, each described by a linear slope (Fig. 4a). For all $S_{H\max}$ and $S_{h\min}$ magnitudes a best-fit slope is derived, based on the individual linear slopes (Fig. 4b). Two best-fit slopes describe the combinations of boundary conditions which model the $S_{H\max}$ and $S_{h\min}$ magnitudes best. The intersection of these two best-fit slopes defines the boundary conditions, which are used to compute the best-fit branch model (Fig. 4c). This calibration procedure is performed analogously to that of the root model (Fig. 5e–h).

For a successful transfer of the stress state from the root to the branch model, it is critical that the stress state used for the calibration of the branch model is obtained at discrete points of the root model and not in its volume. Otherwise the stress state extracted from the root model is potentially biased due to interpolations from discrete points into the volume, which are performed by the visualization software. Since the large number of possible calibration points can be chosen arbitrarily, their locations need to be considered. We recommend using calibration points close to the border of the branch model but outside the zone prone to boundary effects. Calibration points from the root model in the centre of the branch model are a contradiction of the two-stage approach which aims at finding local stress changes due to high-resolution structural features that are only present in the branch model. Due to the lack of any other stress data in the branch model area, the calibration procedure imposes the root model's basic stress state on the branch model, which prevents such local stress perturbations. Hence, this necessary imposition should be re-
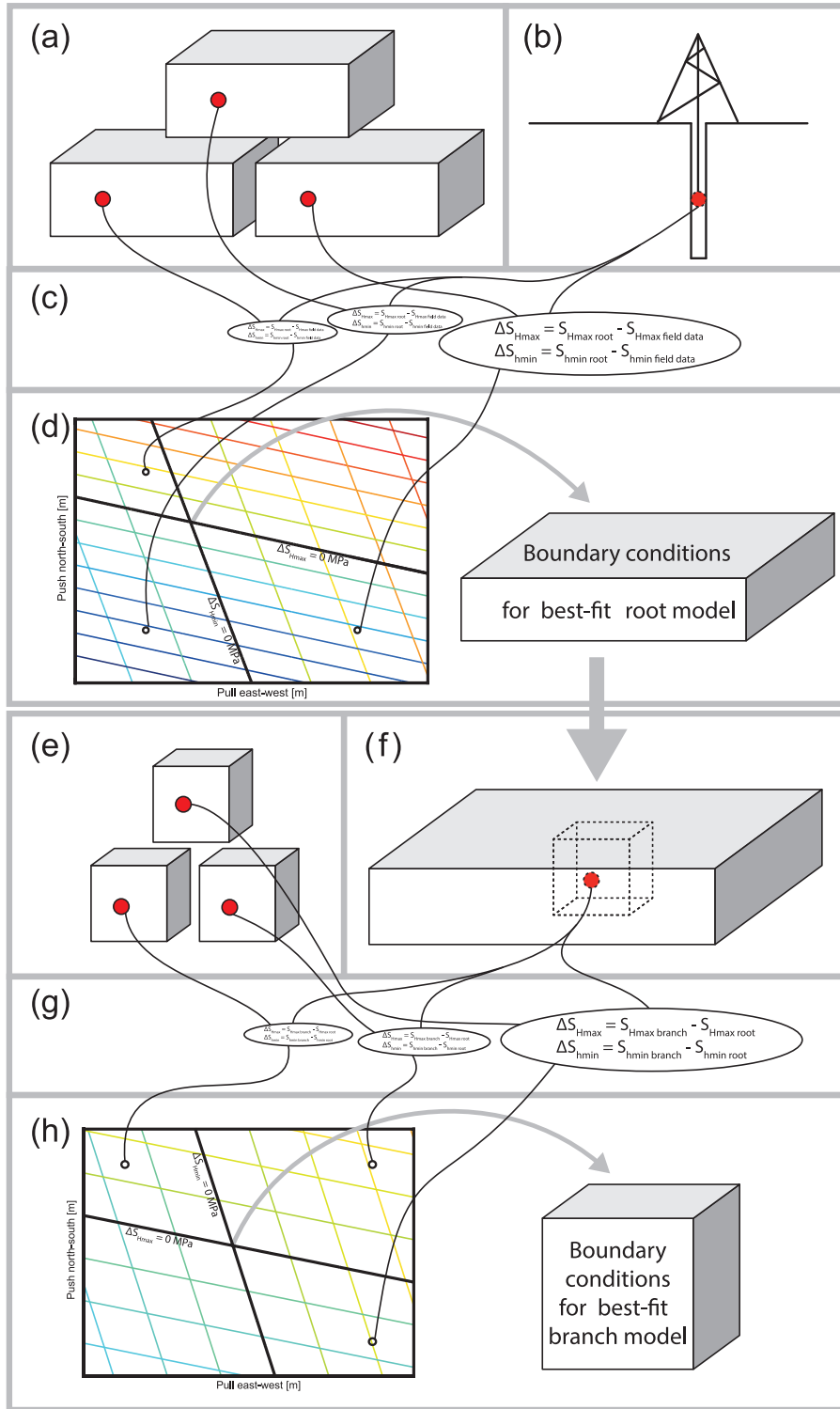
Figure 5. The calibration workflow for the root and branch model. **(a)** Three models with different Dirichlet boundary conditions provide stress data comparison values for a calibration with **(b)** observed magnitude stress data. The deviation of the modelled from the observed stress state of each of the three scenarios **(c)** is used in a linear regression to derive the boundary conditions to compute the best-fit root model **(d)**. **(e)** Three different branch models provide stress data comparison values for a calibration with magnitude data from the best-fit root model **(f)**. The deviation of the modelled stress state to that provided from the root model for each of the three scenarios **(g)** is used in a linear regression to derive the boundary conditions required to compute the best-fit branch model **(h)**.

duced to the boundaries of the branch model that are not used for interpretation. Furthermore, the calibration points should be evenly distributed along the branch model boundary and represented in all stratigraphic units to account for different material properties. Special attention needs to be paid to units which are either only present in the root or the branch model or have a significantly different geometry or rock properties in the two models.

5 Model results

In the following two sections we present the results of two model scenarios for the root model that fit equally well the observed stress data, but with different stress regimes (Fig. 6). For the branch model we present our results on one scenario that can be considered our best-fit model (Fig. 7).

5.1 Root model

The best-fit root model of the stress state at discrete points in the Greater Munich area is calibrated using $S_{h_{\min}}$ magnitudes from the two LOTs and one $S_{H_{\max}}$ magnitude described in detail in the stress data in Sect. 3.2. The best-fit model has a good fit to the two $S_{h_{\min}}$ calibration data points and an almost perfect fit for the single $S_{H_{\max}}$ calibration point. Deviations between observed and modelled data are on average 0.4 MPa for the two $S_{h_{\min}}$ calibration points and 0.04 MPa for the single $S_{H_{\max}}$ calibration point.

Figure 8 shows the best-fit model results along the Sauerlach borehole profile along with the FIT data of Seithel et al. (2015). The black line shows the vertical stress magnitude with depth, which depends only on the chosen rock density. The blue line is the $S_{h_{\min}}$ magnitude, which is larger than all FIT values at all depth sections. The blue star represents the magnitude and depth of the $S_{h_{\min}}$ magnitude inferred from a FIT with leak-off. The red line is the $S_{H_{\max}}$ magnitude in the best-fit model while the dashed line represents $S_{H_{\max}}$ in another model scenario. The red star marks the depth and magnitude of $S_{H_{\max}}$ in the best-fit model. The shaded areas show the modelled magnitudes for model scenarios, which use $S_{H_{\max}}$ magnitudes between 92 and 118 MPa in a depth of 4 km below the Sauerlach site for calibration. This demonstrates that the single $S_{H_{\max}}$ magnitude derived in conjunction with the ambiguity of the stress regime opens up a wide range of model scenarios which all equally well fit the $S_{h_{\min}}$ data. Even though a compressional regime can be excluded by the available data in Sauerlach, no indication exists of whether $S_{H_{\max}} > S_v$ or $S_{H_{\max}} < S_v$. That means that the prevalence of a normal faulting or a strike-slip stress regime is possible. To account for this variability, several different scenarios have been computed, two of which are compared in Fig. 6. Note that the only difference between these scenarios is the $S_{H_{\max}}$ magnitude value used for the root model calibration (Fig. 6a

96 MPa, Fig. 6b 112 MPa); the fit to the $S_{h_{\min}}$ data from the LOTs is equally good (Fig. 6).

In Fig. 6 we show a number of scalar stress values derived from the modelled 3-D stress tensor on cross sections and within stratigraphic units for the aforementioned two model scenarios. The figure shows that the values vary depending on the stratigraphic units horizontally and laterally. More importantly, the results from the two model scenarios which fit the model-independent calibration data equally well are quite different. The first row of Fig. 6 shows the variability of the stress regime using a continuous scale, the so-called regime stress ratio (RSR) from Simpson (1997). Close to the surface a strike-slip regime dominates with compressional components in some areas. With increasing depths this changes to a prevailing extensional regime. Moreover, some changes from strike-slip to extensional and back to strike-slip can be observed. They are not a smooth linear trend but are highly dependent on the lithology.

The second row of Fig. 6 displays the horizontal stress anisotropy as a stress magnitude ratio of $S_{H_{\max}}/S_{h_{\min}}$ on a N–S and E–W cross section through the two model scenarios of the root model. It is clearly visible that the ratio varies significantly with depth and between the model scenarios. The southward-dipping Malm and Purbeck units have stress ratios of up to 0.15 higher than the basement layer and overlying sediments respectively.

The last row in Fig. 6 shows the differential stress in the middle of the Malm unit. Both model scenarios show higher differential stresses in the south where the Malm units are deeper than in the north. The largest N–S difference is 7 MPa in model scenario (a) in contrast to 12 MPa in model scenario (b), even though the relative pattern of the differential stresses in the Malm unit is quite similar in both model scenarios. This pattern highlights the main trend of an increasing differential stress towards the south. At the same time significant changes of the differential stress within less than 10 km of up to 1 MPa are predicted.

5.2 Branch model

In this section we show the model results of the branch model (Fig. 7) that uses the stress data derived from the root model scenario displayed in the right row of Fig. 6. In order to visualize the criticality of the reservoir, we use two scalar values which are computed from the modelled 3-D stress state. The first one is the fracture potential (FP) of intact rock volume (Connolly and Cosgrove, 1999). It is computed as

$$\text{FP} = \frac{\text{actual maximum shear stress}}{\text{acceptable shear stress}} \tag{2}$$

$$= \frac{0.5(S1 - S3)}{C\cos(\Phi) + 0.5(S1 + S3)\sin(\Phi)}, \tag{3}$$

with $S1$ and $S3$ as the maximum and minimum principal stress, C as the cohesion, and Φ as the friction angle. As a second scalar value, slip tendency (ST) is computed on faults

(a)   **(b)**
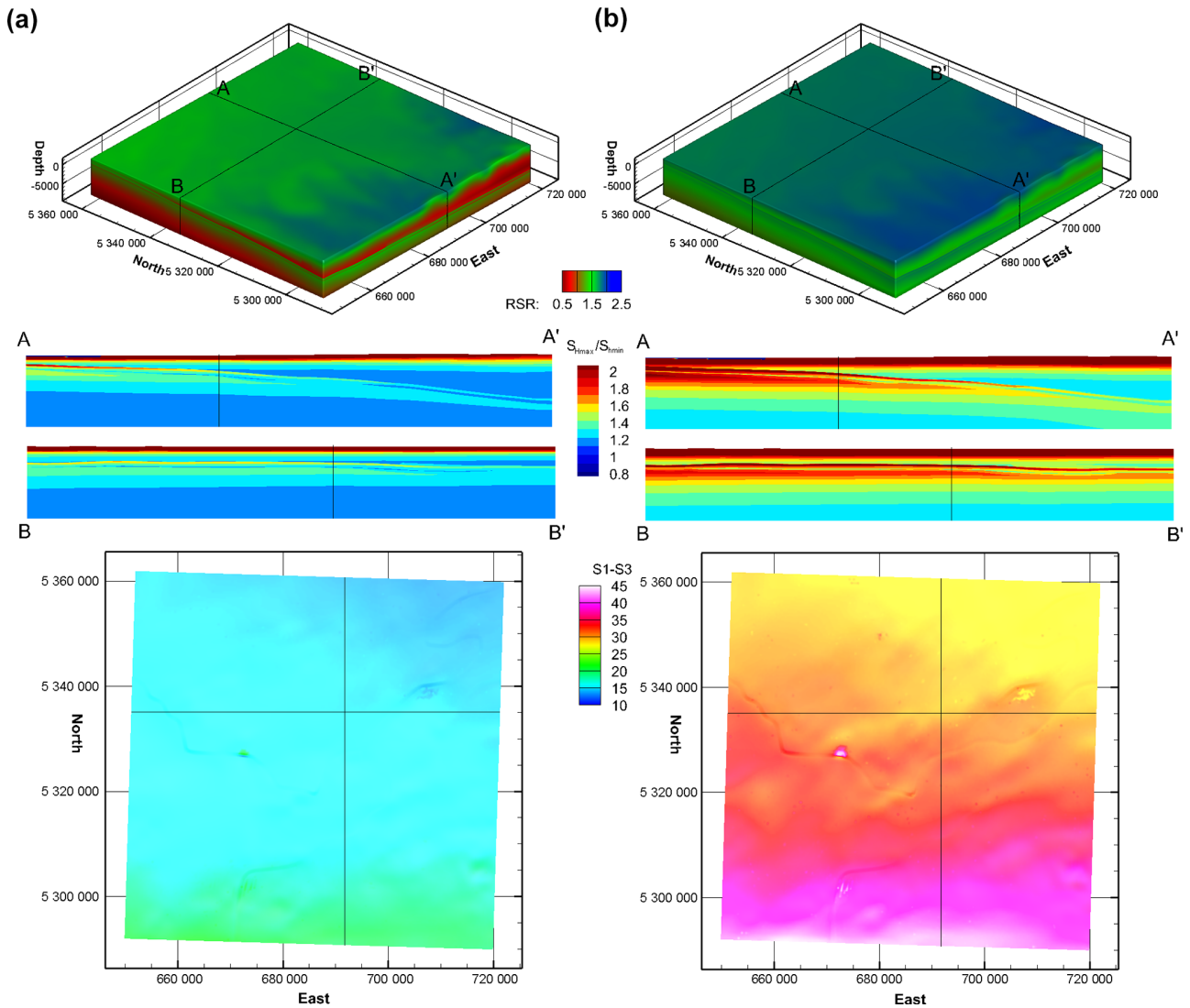

Figure 6. Results of the best-fit root model (b) and an alternative scenario that fits the $S_{h_{min}}$ values equally well, but is calibrated against a lower $S_{H_{max}}$ value (a). The overall difference that results from the different $S_{H_{max}}$ values used for the calibration is expressed in the continuous scale of the regime stress ratio (RSR), which is between 0.5 (normal faulting regime), 1.5 (strike-slip), and 2.5 (thrust faulting regime) (Simpson, 1997) in the model volume. The horizontal stress anisotropy expressed in the ratio of $S_{H_{max}}/S_{h_{min}}$ is shown on two cross sections which intersect below Munich. The differential stress (difference between the maximum and minimum principal stress, lowermost panel) is mapped on a surface which is vertically centred in the Malm $\alpha - \gamma$ units.

(Morris et al., 1996). It is a measure of the criticality of faults which is illustrated as a scalar value for the distance to failure derived from the stress tensor with values between 0 (safe) and 1 (failure). Slip tendency is computed for faults or fault segments of a certain orientation and is defined as

$$\mathrm{ST} = \frac{\frac{\tau_{max} C}{\sigma_n}}{\mu} = \frac{\frac{\tau_{max} C}{\sigma_n}}{\tan(\Phi)}, \tag{4}$$

with the maximum shear stress τ_{max}, the normal stress σ_n, the friction angle $\Phi = \arctan(\mu)$, and the friction coefficient μ. The application of these two values is shown in the branch model with generic faults in Fig. 7.

The high dependence of slip tendency on the orientation, friction, and cohesion of the fault is displayed in Fig. 7. A high variability of slip tendency between 0.05 and 0.3 is observed on the generic faults. This variability is induced by the 3-D stress tensor and the curved fault surfaces. Furthermore, due to differently assumed friction and cohesion of the rocks, the Malm δ – Purbeck units have a clearly smaller value of slip tendency compared to the Chattian units in the hanging wall and the Malm $\alpha - \gamma$ in the footwall. The fracture potential in the basement generally lies between 0.1 and 0.2, which is quite low, hence it requires high pressure for hy-
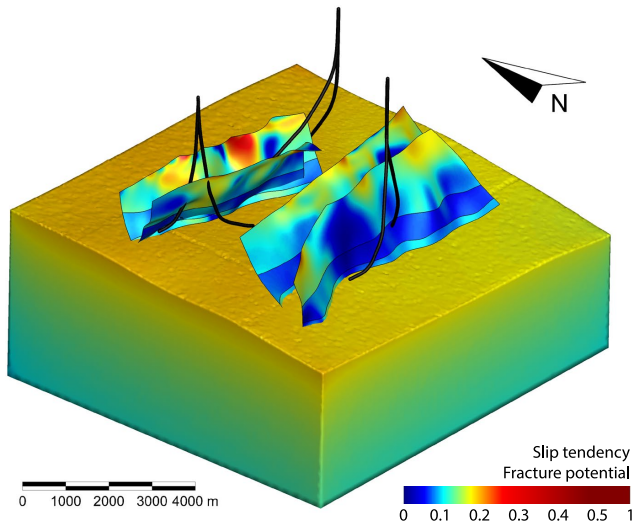
Figure 7. The generic branch model results are shown by means of slip tendency (ST) values (Morris et al., 1996) mapped on generic faults in the Chattian, Purbeck, and Malm units and by means of the fracture potential (FP) (Connolly and Cosgrove, 1999) displayed for the model volume of the basement. Both values vary from zero to one indicating low and high criticality. Note, that the colour map of these values is non-linear. The results clearly indicate that the generic faults are far away from failure with the largest value of ST of 0.3. The low FP values (max. 0.38) give an estimate on how much fluid pressure would be needed to fracture the intact rock in a stimulation experiment to enhance the permeability.

Figure 8. Stratigraphy and model result of the root model along the borehole of the geothermal project in Sauerlach. Lines show the results of the best-fit root model: blue for the $S_{h_{\min}}$ magnitude, black for the vertical stress S_{v}, and red for the $S_{H_{\max}}$ magnitude. The blue dots are formation integrity tests (FITs), which are a lower boundary for the magnitude of $S_{h_{\min}}$ and not used for calibration, the blue star represents the suspected LOT, the red star shows the $S_{H_{\max}}$ magnitude of 112 MPa used for calibration (Seithel et al., 2015). Shaded areas in the same colour around the lines show the range of model scenarios that fit equally well to the model-independent constraints. The dotted red line shows the $S_{H_{\max}}$ magnitude for the model scenario in Fig. 6a.

draulic fracturing operations to enhance the permeability of the fracture network.

Information provided by the branch model is used in an early pre-drilling stage of a project to assess whether the initial conditions of the reservoir and its criticality allow safe production; i.e. both slip tendency and fracture potential have low values as in Fig. 7. Before the drilling of the borehole begins the planning of the drill paths can be optimized. Especially if intersections with faults are required, their paths can be monitored and adapted in a way that they circumnavigate fault segments which have a higher value of slip tendency, meaning that this fault segment is more favourably oriented for a potential failure compared to other fault segments. In Fig. 7 areas with cool colours are preferred for intersections of boreholes with faults compared to areas with hot colours. In Fig. 7 the Malm δ – Purbeck unit is mostly blueish coloured which indicates the lowest slip tendency values. Hence these are the best units for the intersection of boreholes with faults. An intersection with the northernmost fault in the red areas should be avoided.
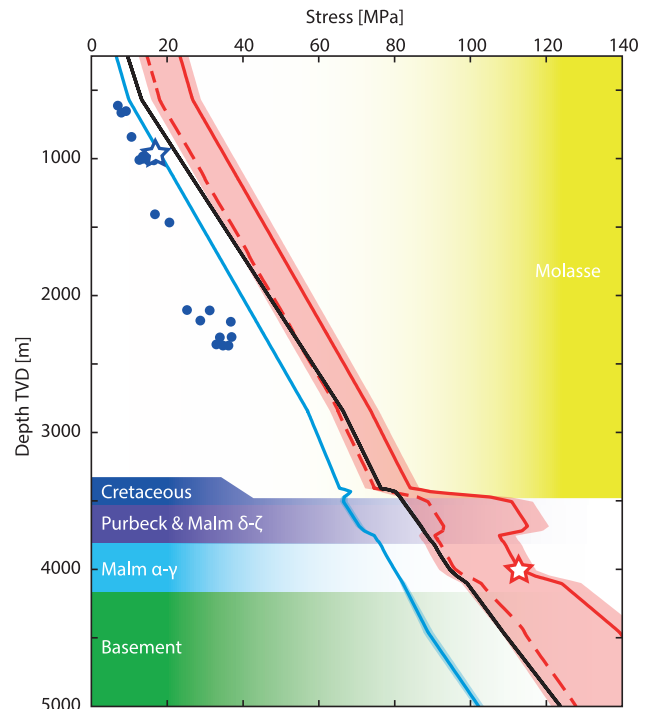
6 Reliability of the model results

One of the key points in geomechanical modelling is the reliability of the model results in terms of the predicted processes and the presented multi-stage simulation of the in situ stress field. As already mentioned in the result Sect. 5 the calibration procedure introduces uncertainties due to the low number of data points as well as their relatively large uncertainties. Further uncertainties are introduced by the model input, e.g. calibration data, rock properties, and structure. Hence, the reliability of the model depends on the uncertainties of the input data used for the model. To quantify the model's reliability we use the already presented scalar value slip tendency (Morris et al., 1996), for which variability is introduced by the uncertainties in different input data.

We compute the slip tendency for model scenarios which use the extreme values of the input parameters range of uncertainties. The model's linear elastic behaviour allows the individual quantification of the impact of different model pa-

rameter uncertainties on the model's reliability. Therefore we compute several model scenarios in which sequentially only a single parameter is changed to an extreme value. This enables us to derive the individual impact of different parameters and quantify the most important ones. The results of the slip tendency for each model scenario are subsequently compared to the best-fit slip tendency values from the best-fit model (Table 2). The variations of slip tendency introduced by the different independent parameters are added together, which leads to an expected maximum variability in slip tendency of ± 0.57.

The two main sources for the variability of slip tendency can be identified as the model-independent data for the $S_{H_{max}}$ magnitude used for the model calibration and the rock properties density, Young's modulus, and Poisson ratio (Table 2). A high variability of slip tendency of 0.14 is introduced by uncertainties in the $S_{H_{max}}$ magnitude. Since the $S_{H_{max}}$ magnitude is derived under several assumptions, a wide range of possible $S_{H_{max}}$ magnitudes is used for the calibration of the slip tendency model scenarios. Due to the fact that only limited knowledge and measurements of the rock properties are available a wide range of values are possible and they introduce a high variability of 0.18 in slip tendency.

Slip tendency proves to be quite robust (± 0.01) to the small uncertainties in the $S_{h_{min}}$ magnitude under the assumption that the available data used for calibration is a valid proxy for the entire model (Table 2). Likewise only small variations in slip tendency are introduced by changes of $\pm 10°$ in the fault strike (± 0.02) and dip (± 0.03). The cohesion and friction angle act as more sensitive parameters (each ± 0.07). Finally the two-stage calibration procedure itself introduces some moderate deviations (± 0.05) with a large number of calibration points and their individual locations used in the branch model.

7 Discussion

The objective of this work was to demonstrate the multi-stage approach for a high-resolution 3-D geomechanical–numerical modelling workflow assessing the criticality in reservoirs. In contrast to a single model, which includes both stress data records for calibration and high-resolution representation of a local reservoir structure, we use two models of different sizes. The regional-scale root model is calibrated on stress data records and provides the stress state for the calibration of the reservoir-scale branch model. This approach provides a cost-efficient, quick, and reliable state-of-the-art calibration of geomechanical–numerical models of the contemporary 3-D in situ stress field across scales. It is used to assess the criticality of reservoirs which can be quantified by scalar values such as slip tendency. If detailed information on the fracture behaviour of the rock are known, more elaborate fracture criteria than Mohr-Coulomb (e.g. Sulem, 2007; Zang and Stephansson, 2010) can be applied to analyse the

Table 2. The expected maximum variations in slip tendency (ST) introduced by the uncertainties of the model parameters. This comparison is made at 40 locations in the Malm $\alpha-\gamma$ and Purbeck target units and an arithmetic mean is computed for each model parameter.

Source of uncertainty		Δ_{max} ST
Rock properties		0.18
Calibration	$S_{H_{max}}$	0.14
	$S_{h_{min}}$	0.01
Analysis	Strike $\pm 10°$	0.02
	Dip $\pm 10°$	0.03
	Cohesion ± 5 MPa	0.07
	Friction angle $\pm 10°$	0.07
Two-stage calibration		0.05
Total variations		0.57

model results. Furthermore, the approach provides the initial stress state for local application such as in THM models.

7.1 Workflow

A single model with the same functionality as the two models in the multi-stage approach needs to account for the required high resolution in the reservoir area and the large model extent to include data for calibration. These two requirements are not contradictory per se but prolong the process of mesh generation, e.g. by needing to harmonize a regional-scale low-resolution and local-scale high-resolution structural model in the area of overlap. Furthermore, the manageability of the model (e.g. logical size) and the available time for computation (number of elements) in most instances requires a variable resolution which is refined only in the target area. Such a change in element size in a single model is possible but the mesh generation is cumbersome and needs a high number of elements. For a THM simulation of production and (re)injection, incrementation over time significantly increases the computation time for each single element. Furthermore, in a single large model, only a very small area is of interest, hence large areas are simulated to no purpose while at the same time the logical size, computation time, and effort are increased.

If a multi-stage approach with two models is applied, each model has its own fixed resolution with no required variation in element size (Fig. 2c). This significantly speeds up and simplifies the process of model generation since neither the structural models need to be harmonized nor a large difference in elements size needs to be implemented. Regarding the same resolution in the target area, the time required for computation decreases, but not as much as the logical size of the models, which improves the model's manageability. A geomechanical root model can also provide the stress state for a THM branch model which helps to save computation

time by focussing the time-consuming THM simulation on the actual area of interest. Calibration data records for the additionally required scalar values on the pore pressure or temperature are provided in the literature or by dedicated models, e.g. Przybycin et al. (2015).

In addition the application of two models opens further possibilities for improved and safer exploration and drilling. Structural features and stress magnitude measurements recorded during advanced exploration or even initial drillings can be implemented into the model workflow due to the simplified mesh regeneration. Even a change in the target area within the root model can be more easily implemented in the workflow since only a new branch model is required. The calibration of the root model can be updated with new stress data records as soon as they become available. Finally, a large calibrated root model may include several target areas and can be reused and applied for more than one project.

7.2 Calibration

The two models in the presented two-stage approach are calibrated with different Dirichlet boundary conditions applied to an initial stress state. This approach follows the modelling procedure using isotropic elastic materials described by e.g. Reiter and Heidbach (2014), Hergert et al. (2015), and Gunzburger and Magnenet (2014). Almost identical results can be achieved by the application of according orthotropic elastic material and gravity loading only (Cornet and Magnenet, 2016). For deep lithosphere and asthenosphere models elasto-plastic materials with the application of gravity but no further boundary conditions can be applied and yield similar results (Maury et al., 2014).

Our root model is calibrated with data records which display the stress state as a result of the geologic history and tectonic evolution. In the presented region the stress field is very homogeneous but in other regions significant local lateral variations exist and need to be accounted for. This can be accomplished for example by lateral variations of the material properties or faults. It is crucial to ensure that the data used for the calibration is representative for the regional material and geometry in the root model.

The branch model, however, is calibrated on the stress state simulated in the root model. Both calibration procedures are not limited in the number of calibration points and a weighting of the calibration points according to reliability can be easily realized. An extension of the two-stage approach to include three (or even more) models of different sizes is possible. Furthermore, the calibration procedure allows running several alternating models with different calibration data or differently weighted calibration points as well as variations in rock properties to quantify model-specific variations. This ability was used to quantify the reliability of the model's results. It is also useful for future attempts at statistically determining uncertainties in the model's results.

Even without any additional computations, a first-order assessment of the impact of individual data records on the model calibration can be made by assessing changes in the boundary conditions. Therefore the best-fit boundary conditions derived with and without certain data records are compared. Such a data record could be a newly performed hydraulic fracturing experiment which provides an additional $S_{h_{\min}}$ magnitude data record. The variation of the derived boundary conditions induced by such a new data record provides a first idea of the variation of the stress state. Although, this feature cannot be used as a replacement for computations it helps to identify whether the newly included calibration point yields a significantly different stress state which requires a reassessment of the situation or if the changes are minor and the exploration can be continued as planned.

The models showed in this work do not include any implicit faults and no strain partitioning is assumed. The calibration of a model including faults and fault-specific behaviour, e.g. strain weakening or hardening or long-term relaxation of the gauge material, is possible as well if sufficient information on the fault properties are available. However, due to the non-linearities introduced by active faults the calibration process requires a regression analysis of a higher degree, hence several more test scenarios. This is beyond the scope of this work.

7.3 Model independent reliability

Apparently the model's reliability is mainly affected by the lack and high uncertainty of $S_{H_{\max}}$ magnitude data. The large influence of the $S_{H_{\max}}$ magnitude is shown by two different models for viable $S_{H_{\max}}$ magnitudes in Fig. 6. A feasible method to narrow down the $S_{H_{\max}}$ variability is to enhance the knowledge of the Andersonian stress regime, e.g. by gathering information on earthquake focal mechanism data (if available) or the crack orientation induced by leak-off tests or hydraulic fracturing (Haimson and Fairhurst, 1969; Hubbert and Willis, 1972; Zang and Stephansson, 2010). Such information is most likely available in the model area but not publicly accessible. Furthermore, an array of many expensive deep overcoring measurements (several per borehole) could provide valuable information on the stress state and $S_{H_{\max}}$ in particular (Hast, 1969; Sjöberg et al., 2003).

The uncertainties related to the material properties are another large factor that limits the model's reliability. This can be mitigated at least partly by using data from extensive databases (e.g. Bär et al., 2015; Lama and Vutukuri, 1978; Koch, 2009) or by converting seismic velocities which are founded on empirical relations (Mavko et al., 2009). Finally, averaging mean values from several laboratory tests of rock samples from the area and lithologic formations of interest are the safest but most expensive ways to retrieve reliable information of rock properties.

The uncertainties in the strike and dip of faults have a comparably small share in the reliability of the model while be-

ing challenging to mitigate due to the general uncertainties in the interpretation of 3-D subsurface structures. The fault parameters cohesion and friction angle which are even more difficult to determine compared to the orientation reduce the model's reliability to a slightly higher degree compared to strike and dip. Increasing the model's reliability through a better understanding of these parameters is possible but requires a detailed understanding of the great variability of in situ fault zone behaviour and extent at depth.

Statistical methods to quantify uncertainties in the subsurface geometry exist for purely static structural models (Wellmann, 2013; Wellmann and Regenauer-Lieb, 2012). However, the computation time required to extend this approach to a 3-D geomechanical–numerical modelling approach and the ensuing analysis is beyond the scope of this work. A further investigation should be conducted as a sequel to the work by Bond et al. (2015) in a generic approach including geomechanical–numerical modelling.

7.4 Model dependent reliability

This model focusses on the stress tensor in the uppermost part of the crust and its extent is accordingly chosen. Deep-seated processes at depths larger than 9 km are, therefore, not represented in the model. However, as shown by Maury et al. (2014), the lateral variations in the differential stress in the depths are small compared to variations introduced by the uncertain material properties and magnitude of $S_{H_{max}}$ in our model. Furthermore the influence of deep structures such as the Moho geometry is minor, as shown by Reiter and Heidbach (2014) or Hergert et al. (2011).

The model does not include any faults. The inclusion of faults makes sense in situations where detailed information on fault geometry, extent, and parameters are available and a significant impact of the faults on the regional stress field or (re)activation is expected. However, in this example, the available stress data suggests that no faults with a major impact are located neither within the root model nor the branch model area. Therefore the variations introduced by omitting faults is assumed to be small.

Variations of the model results are also introduced by the multi-stage calibration approach itself and cannot be mitigated due to both models 3-D stress state with lateral and vertical variations. The model's calibration, however, depends on the variations of only two independent boundary conditions. Additionally, small variations may be introduced by the model assumptions. However, these variations can be disregarded in the light of the major reasons for variations due to the small amount of stress magnitude data and rock properties. Table 2 clearly shows that any further advances in modelling are not efficient as long as the amount and quality of input data ($S_{H_{max}}$, rock properties) is not increased.

8 Application in geoengineering

Hydrocarbon reservoirs are currently exploited on a minor level in the Alpine Foreland (Lemcke, 1988; Sachsenhofer et al., 2006) and some of the former reservoirs are used for oil and gas storage (Sedlacek, 2009). However, hydrothermal reservoirs of economic interest for district heating or power generation are available (Lemcke, 1988; Bachmann et al., 1982; Fritzer et al., 2012). These reservoirs are situated in highly karstified limestones of the Late Jurassic which are locally referred to as Malm formations (Lemcke, 1988). As of 2016 those deep reservoirs have already been exploited by 21 municipal geothermal power plants and district heating projects of which Aschheim, Dürrnhaar, Erding, Freiham, Garching, Holzkirchen, Ismaning, Oberhaching, Poing, Riem, Sauerlach, and Unterschleißheim are in the root model area (Bundesverband Geothermie, 2016). Borehole data from these projects could be easily implemented in the calibration of the root model and would increase its reliability if they became publicly available.

Within the root model perimeter, several geothermal projects are currently at the planning stage, namely Bernried, Gräfelfing/Planegg, Königsdorf, Markt Schwaben, Puchheim/Germering, Raststätte Höhenrain, Starnberg, Weilheim/Wielenbach, and Wolfratshausen (Bundesverband Geothermie, 2016). In addition the municipal energy supplier of Munich (SWM) plans to install an extensive geothermally driven district heating grid for the entire city (Stadtwerke München GmbH, 2012). Therefore, a 3-D seismic survey was conducted in the entire southern part of Munich in winter 2015/16 (Bundesverband Geothermie, 2015). The presented root model provides data for a first-order assessment of the in situ stress state at the exact locations of these planned geothermal projects. Furthermore, it provides calibration data for local-/reservoir-scale models based on high-resolution 3-D seismic surveys which simulate the stress state, its criticality, and the possibility of subsidence due to the production and reinjection of fluid and heat.

Furthermore, the two-stage approach could be extended to a three-stage approach which incorporates a global model of the entire Bavarian Molasse Basin. More data for calibration, as well as more potential applications, might be available in such an enhanced area. Thereby the regional or global root model could be established as a community model which provides the stress state for further applications and/or local models for planned projects.

9 Conclusions

In this work we present a multi-stage 3-D geomechanical–numerical modelling approach, which provides a cost-efficient, reliable, and fast way to generate and evaluate the criticality of the stress state in a small target area where,

in general, no stress data for model calibration are available. The approach uses a large-scale root model which is calibrated on available stress data and a small-scale branch model which is calibrated on the root model. We exemplify this in a two-stage approach in the German Molasse Basin around the municipality of Munich. The discussion of reliability of the model results clearly shows (1) that variations are large and (2) that they are mainly introduced by the uncertain material properties and missing $S_{H_{\max}}$ magnitude data. At this stage, the model's quality depends on the amount and quality of available input data and not on the modelling technique itself. Any further improvements in the model's resolution and applied techniques will not lead to an increase in reliability. This can only be achieved by more high-quality data for calibration.

10 Data availability

The stress orientation data used for model set-up and calibration is available from Reiter et al. (2016) and Heidbach et al. (2016).

References

Aadnoy, B. S.: Inversion technique to determine the in-situ stress field from fracturing data, J. Petrol. Sci. Eng., 4, 127–141, doi:10.1016/0920-4105(90)90021-T, 1990.

Altmann, J., Müller, B., Müller, T., Heidbach, O., Tingay, M., and Weißhardt, A.: Pore pressure stress coupling in 3D and consequences for reservoir stress states and fault reactivation, Geothermics, 52, 195–204, doi:10.1016/j.geothermics.2014.01.004, 2014.

Anderson, E.: The dynamics of faulting, Transactions of the Edinburgh Geological Society, 8, 387–402, 1905.

Anderson, E.: The dynamics of faulting, Oliver and Boyd, Edinburgh, 2 edn., 1951.

Bachmann, G., Müller, M., and Weggen, K.: Evolution of the Molasse Basin (Germany, Switzerland), Tectonophysics, 137, 77–92, doi:10.1016/0040-1951(87)90315-5, 1987.

Bachmann, G. H., Dohr, G., and Mueller, M.: Exploration in a classic thrust belt and its foreland: Bavarian Alps, Germany, AAPG Bulletin, 66, 2529–2542, 1982.

Bär, K., Reinsch, T., Sippel, J., Freymark, J., Mielke, P., Strom, A., and Wiesner, P.: Internationale Datenbank petrophysikalischer Kennwerte – Grundlage zur Reservoircharakterisierung, in: Der Geothermiekongress 2015, Bundesverband Geothermie, 2015.

Bell, J.: In situ stresses in sedimentary rocks (Part 1): Measurement Techniques, Geoscience Canada, 23, 85–100, 1996.

Bell, J. and Gough, D.: Northeast-southwest compressive stress in Alberta – evidence from oil wells, Earth Planet. Sc. Lett., 45, 475–482, doi:10.1016/0012-821X(79)90146-8, 1979.

Bell, J. S.: Investigating stress regimes in sedimentary basins using information from oil industry wireline logs and drilling records, in: Geological Applications of Wireline Logs, vol. 48, pp. 305–325, Geological Society Special Publication, doi:10.1144/GSL.SP.1990.048.01.26, 1990.

Bond, C., Johnson, G., and Ellis, J.: Structural model creation: the impact of data type and creative space on geological reasoning and interpretation, Geological Society, London, Special Publications, 421, SP421–4, doi:10.1144/SP421.4, 2015.

Brown, E. E. and Hoek, E.: Trends in relationships between measured in-situ stresses and depth, International Journal of Rock Mechanics and Mining Sciences & Geomechanics Abstracts, 15, 211–215, doi:10.1016/0148-9062(78)91227-5, 1978.

Brudy, M., Zoback, M. D., Fuchs, K., Rummel, F., and Baumgärtner, J.: Estimation of the complete stress tensor to 8 km depth in the KTB scientific drill holes: Implications for crustal strength, J. Geophys. Res., 102, 18453, doi:10.1029/96JB02942, 1997.

Bundesverband Geothermie: Stadtwerke München: Seismologische Untersuchungen im Großraum München, available at: http://www.geothermie.de/news-anzeigen/2015/08/27/stadtwerke-munchen-seismologische-untersuchungen-im-grossraum-munchen.html (last access: June 2016), 2015.

Bundesverband Geothermie: Tiefe Geothermie in Deutschland, available at: http://www.geothermie.de/fileadmin/useruploads/wissenswelt/Projekte/Projektliste_Tiefe_Geothermie_2016.pdf (last access: June 2016), 2016.

Cacace, M., Blöcher, G., Watanabe, N., Moeck, I., Börsing, N., Scheck-Wenderoth, M., Kolditz, O., and Huenges, E.: Modelling of fractured carbonate reservoirs: outline of a novel technique via a case study from the Molasse Basin, southern Bavaria, Germany, Environ. Earth Sci., 70, 3585–3602, doi:10.1007/s12665-013-2402-3, 2013.

Cacas, M., Daniel, J., and Letouzey, J.: Nested geological modelling of naturally fractured reservoirs, Petrol. Geosci., 7, 43–52, doi:10.1144/petgeo.7.S.S43, 2001.

Connolly, P. and Cosgrove, J.: Prediction of static and dynamic fluid pathways within and around dilational jogs, Geological Society, London, Special Publications, 155, 105–121, doi:10.1144/GSL.SP.1999.155.01.09, 1999.

Cornet, F. and Magnenet, V.: A non-tectonic origin for the present day stress field in the sedimentary Paris Basin, EGU General Assembly Conference Abstracts, 18, 1939, 2016.

Cornet, F., Helm, J., Poitrenaud, H., and Etchecopar, A.: Seismic and aseismic slips induced by large-scale fluid injections, in:

Seismicity Associated with Mines, Reservoirs and Fluid Injections, 563–583, Springer, doi:10.1007/978-3-0348-8814-1_12, 1997.

Cornet, F. H.: Elements of Crustal Geomechanics, Cambridge University Press, 2015.

Cornet, F. H. and Röckel, T.: Vertical stress profiles and the significance of "stress decoupling", Tectonophysics, 581, 193–205, doi:10.1016/j.tecto.2012.01.020, 2012.

Deichmann, N. and Ernst, J.: Earthquake focal mechanisms of the induced seismicity in 2006 and 2007 below Basel (Switzerland), Swiss J. Geosci., 102, 457–466, doi:10.1007/s00015-009-1336-y, 2009.

Farr, T. G., Rosen, P. A., Caro, E., Crippen, R., Duren, R., Hensley, S., Kobrick, M., Paller, M., Rodriguez, E., Roth, L., Seal, D., Shaffer, S., Shimada, J., Umland, J., Werner, M., Oskin, M., Burbank, D., and Alsdorf, D.: The shuttle radar topography mission, Rev. Geophys., 45, 1–33, doi:10.1029/2005RG000183, 2007.

Fritzer, T., Settles, E., and Dorsch, K.: Bayerischer Geothermieatlas, Tech. rep., Bayerisches Staatsministerium für Wirtschaft, Infrastruktur, Verkehr und Technologie, München, 2012.

Fuchs, K. and Müller, B.: World stress map of the Earth: A key to tectonic processes and technological applications, Naturwissenschaften, 88, 357–371, doi:10.1007/s001140100253, 2001.

Gaucher, E., Schoenball, M., Heidbach, O., Zang, A., Fokker, P. A., van Wees, J.-D., and Kohl, T.: Induced seismicity in geothermal reservoirs: A review of forecasting approaches, Renewable and Sustainable Energy Reviews, 52, 1473–1490, doi:10.1016/j.rser.2015.08.026, 2015.

Giorgi, F., Mearns, L. O., Shields, C., and McDaniel, L.: Regional nested model simulations of present day and 2× CO2 climate over the central plains of the US, Climatic Change, 40, 457–493, doi:10.1023/A:1005384803949, 1998.

Grünthal, G.: Earthquakes, intensity, Encyclopedia of Solid Earth Geophysics, 237–242, 2011.

Grünthal, G. and Wahlström, R.: The European-Mediterranean earthquake catalogue (EMEC) for the last millennium, J. Seismol., 16, 535–570, doi:10.1007/s10950-012-9302-y, 2012.

Gunzburger, Y. and Cornet, F. H.: Rheological characterization of a sedimentary formation from a stress profile inversion, Geophys. J. Int., 168, 402–418, doi:10.1111/j.1365-246X.2006.03140.x, 2007.

Gunzburger, Y. and Magnenet, V.: Stress inversion and basement-cover stress transmission across weak layers in the Paris basin, France, Tectonophysics, 617, 44–57, doi:10.1016/j.tecto.2014.01.016, 2014.

Haimson, B. and Fairhurst, C.: In-situ stress determination at great depth by means of hydraulic fracturing, in: The 11th US Symposium on Rock Mechanics (USRMS), American Rock Mechanics Association, 1969.

Häring, M. O., Schanz, U., Ladner, F., and Dyer, B. C.: Characterisation of the Basel 1 enhanced geothermal system, Geothermics, 37, 469–495, doi:10.1016/j.geothermics.2008.06.002, 2008.

Hast, N.: The state of stress in the upper part of the earth's crust, Tectonophysics, 8, 169–211, doi:10.1016/0040-1951(69)90097-3, 1969.

Heidbach, O. and Ben-Avraham, Z.: Stress evolution and seismic hazard of the Dead Sea Fault System, Earth Planet. Sc. Lett., 257, 299–312, doi:10.1016/j.epsl.2007.02.042, 2007.

Heidbach, O. and Reinecker, J.: Analyse des rezenten Spannungsfeldes der Nordschweiz, Nagra Arb. Ber. NAB 12-05, Nagra, Wettingen, 2013.

Heidbach, O., Reinecker, J., Tingay, M., Müller, B., Sperner, B., Fuchs, K., and Wenzel, F.: Plate boundary forces are not enough: Second- and third-order stress patterns highlighted in the World Stress Map database, Tectonics, 26, 1–19, doi:10.1029/2007TC002133, 2007.

Heidbach, O., Tingay, M., Barth, A., Reinecker, J., Kurfeß, D., and Müller, B.: The 2008 release of the World Stress Map, doi:10.1594/GFZ.WSM.Rel2008, 2008.

Heidbach, O., Tingay, M., Barth, A., Reinecker, J., Kurfeß, D., and Müller, B.: Global crustal stress pattern based on the World Stress Map database release 2008, Tectonophysics, 482, 3–15, doi:10.1016/j.tecto.2009.07.023, 2010.

Heidbach, O., Rajabi, M., Reiter, K., Ziegler, M., and the WSM Team: World Stress Map Database Release 2016, GFZ Data Services, doi:10.5880/WSM.2016.001, 2016.

Hergert, T. and Heidbach, O.: Geomechanical model of the Marmara Sea region-II. 3-D contemporary background stress field, Geophys. J. Int., 185, 1090–1102, doi:10.1111/j.1365-246X.2011.04992.x, 2011.

Hergert, T., Heidbach, O., Bécel, A., and Laigle, M.: Geomechanical model of the Marmara Sea region – I. 3-D contemporary kinematics, Geophys. J. Int., 185, 1073–1089, doi:10.1111/j.1365-246X.2011.04991.x, 2011.

Hergert, T., Heidbach, O., Reiter, K., Giger, S. B., and Marschall, P.: Stress field sensitivity analysis in a sedimentary sequence of the Alpine foreland, northern Switzerland, Solid Earth, 6, 533–552, doi:10.5194/se-6-533-2015, 2015.

Hornbach, M. J., DeShon, H. R., Ellsworth, W. L., Stump, B. W., Hayward, C., Frohlich, C., Oldham, H. R., Olson, J. E., Magnani, M. B., Brokaw, C., and Luetgert, J. H.: Causal factors for seismicity near Azle, Texas., Nature Communications, 6, 6728, doi:10.1038/ncomms7728, 2015.

Hubbert, M. K. and Willis, D. G.: M 18: Underground Waste Management and Environmental Implications, chap. Mechanics of Hydraulic Fracturing, 239–257, AAPG Special Volumes, 1972.

Illies, J. H. and Greiner, G.: Rhinegraben and the Alpine system, Geol. Soc. Am. Bull., 89, 770–782, doi:10.1130/0016-7606(1978)89<770:RATAS>2.0.CO;2, 1978.

Jaeger, J., Cook, N., and Zimmerman, R.: Fundamentals of Rock Mechanics, Blackwell Publishing Ltd., Malden Oxford Carlton, 4th edn., 2007.

Jeanne, P., Rutqvist, J., Dobson, P. F., Walters, M., Hartline, C., and Garcia, J.: The impacts of mechanical stress transfers caused by hydromechanical and thermal processes on fault stability during hydraulic stimulation in a deep geothermal reservoir, International Journal of Rock Mechanics and Mining Sciences, 72, 149–163, doi:10.1016/j.ijrmms.2014.09.005, 2014.

Koch, A.: Erstellung statistisch abgesicherter thermischer und hydraulischer Gesteinseigenschaften für den flachen und tiefen Untergrund in Deutschland Phase 2 – Westliches Nordrhein-Westfalen und bayerisches Molassebecken, Tech. rep., RWTH Aaachen, 2009.

Koch, A. and Clauser, C.: Erstellung statistisch abgesicherter thermischer und hydraulischer Gesteinseigenschaften für den flachen und tiefen Untergrund in Deutschland Phase 1 – Westliche Mo-

lasse und nördlich angrenzendes Süddeutsches Schichtstufen-land RWTH Aachen, RWTH Aachen, 234 pp., 2006.

Kohl, T. and Mégel, T.: Predictive modeling of reservoir response to hydraulic stimulations at the European EGS site Soultz-sous-Forêts, International Journal of Rock Mechanics and Mining Sciences, 44, 1118–1131, doi:10.1016/j.ijrmms.2007.07.022, 2007.

Lama, R. D. and Vutukuri, V. S.: Handbook on mechanical properties of rocks – Testing Techniques and Results – Volume II, Trans Tech Publications, Clausthal, 1 edn., 1978.

Lemcke, K.: Geologie von Bayern I. –Das bayerische Alpenvor-land vor der Eiszeit – Erdgeschichte – Bau – Bodenschätze, E. Schweizerbart'sche Verlagsbuchhandlung (Nägele u. Ober-miller), Stuttgart, 1 edn., 1988.

Lund, B. and Zoback, M.: Orientation and magnitude of in situ stress to 6.5 km depth in the Baltic Shield, International Journal of Rock Mechanics and Mining Sciences, 36, 169–190, doi:10.1016/S0148-9062(98)00183-1, 1999.

Magri, F., Tillner, E., Wang, W., Watanabe, N., Zimmermann, G., and Kempka, T.: 3D hydro-mechanical scenario analysis to evaluate changes of the recent stress field as a result of geological CO_2 storage, Energy Procedia, 40, 375–383, doi:10.1016/j.egypro.2013.08.043, 2013.

Maury, J., Cornet, F. H., and Cara, M.: Influence of the lithosphere-asthenosphere boundary on the stress field northwest of the Alps, Geophys. J. Int., 199, 1006–1017, doi:10.1093/gji/ggu289, 2014.

Mavko, G., Mukerji, T., and Dvorkin, J.: The Rock Physics Hand-book, Cambridge University Press, New York, 2nd edn., 2009.

McClure, M. W. and Horne, R. N.: An investigation of stimulation mechanisms in Enhanced Geothermal Systems, International Journal of Rock Mechanics and Mining Sciences, 72, 242–260, doi:10.1016/j.ijrmms.2014.07.011, 2014.

Moeck, I. and Backers, T.: Fault reactivation potential as a critical factor during reservoir stimulation, First Break, 29, 73–80, doi:10.3997/1365-2397.2011014, 2011.

Morris, A., Ferrill, D. A., and Henderson, D. B.: Slip-tendency analysis and fault reactivation, Geology, 24, 275, doi:10.1130/0091-7613(1996)024<0275:STAAFR>2.3.CO;2, 1996.

Oey, L.-Y. and Chen, P.: A nested-grid ocean model: With application to the simulation of meanders and eddies in the Norwegian Coastal Current, J. Geophys. Res.-Oceans, 97, 20063–20086, doi:10.1029/92JC01991, 1992.

Orlecka-Sikora, B.: The role of static stress transfer in mining in-duced seismic events occurrence, a case study of the Rudna mine in the Legnica-Glogow Copper District in Poland, Geophys. J. Int., 182, 1087–1095, doi:10.1111/j.1365-246X.2010.04672.x, 2010.

Pierdominici, S. and Heidbach, O.: Stress field of Italy – Mean stress orientation at different depths and wave-length of the stress pattern, Tectonophysics, 532–535, 301–311, doi:10.1016/j.tecto.2012.02.018, 2012.

Przybycin, A. M.: Lithospheric-scale 3D structural and thermal modelling and the assessment of the origin of thermal anomalies in the European North Alpine Foreland Basin, Ph.D. thesis, Freie Universität Berlin, 2015.

Przybycin, A. M., Scheck-Wenderoth, M., and Schneider, M.: The 3D conductive thermal field of the North Alpine Foreland Basin: influence of the deep structure and the adjacent European Alps, Geothermal Energy, 3, 17, doi:10.1186/s40517-015-0038-0, 2015.

Rajabi, M., Tingay, M., King, R., and Heidbach, O.: Present-day stress orientation in the Clarence-Moreton Basin of New South Wales, Australia: A new high density dataset reveals local stress rotations, Basin Research, doi:10.1111/bre.12175, 2016.

Reinecker, J., Tingay, M., Müller, B., and Heidbach, O.: Present-day stress orientation in the Molasse Basin, Tectonophysics, 482, 129–138, doi:10.1016/j.tecto.2009.07.021, 2010.

Reiter, K. and Heidbach, O.: 3-D geomechanical-numerical model of the contemporary crustal stress state in the Alberta Basin (Canada), Solid Earth, 5, 1123–1149, doi:10.5194/se-5-1123-2014, 2014.

Reiter, K., Heidbach, O., Reinecker, J., Müller, B., and Röckel, T.: Spannungskarte Deutschland 2015, Erdöl Erdgas Kohle, 131, 437–442, 2015.

Reiter, K., Heidbach, O., Müller, B., Reinecker, J., and Röckl, T.: Spannungskarte Deutschland 2016, GFZ Data Services, doi:10.5880/WSM.Germany2016, 2016.

Rutqvist, J., Dobson, P. F., Garcia, J., Hartline, C., Jeanne, P., Old-enburg, C. M., Vasco, D. W., and Walters, M.: The Northwest Geysers EGS Demonstration Project, California: Pre-stimulation Modeling and Interpretation of the Stimulation, Mathematical Geosciences, 47, 3–29, doi:10.1007/s11004-013-9493-y, 2013.

Sachsenhofer, R., Gratzer, R., Tschelaut, W., and Bechtel, A.: Char-acterisation of non-producible oil in Eocene reservoir sandstones (Bad Hall Nord field, Alpine foreland basin, Austria), Mar. Petrol. Geol., 23, 1–15, doi:10.1016/j.marpetgeo.2005.07.002, 2006.

Schmid, S. M., Bernoulli, D., Fügenschuh, B., Matenco, L., Schefer, S., Schuster, R., Tischler, M., and Ustaszewski, K.: The Alpine-Carpathian-Dinaridic orogenic system: correlation and evolution of tectonic units, Swiss J. Geosci., 101, 139–183, doi:10.1007/s00015-008-1247-3, 2008.

Schmitt, D. R., Currie, C. A., and Zhang, L.: Crustal stress determination from boreholes and rock cores: Fundamental principles, Tectonophysics, 580, 1–26, doi:10.1016/j.tecto.2012.08.029, 2012.

Scholz, C. H.: The mechanics of earthquakes and faulting, Cambridge University Press, 2002.

Sedlacek, R.: Untertage-Gasspeicherung in Deutschland – Under-ground Gas Storage in Germany, Erdöl Erdgas Kohle, 125, 412–426, 2009.

Seithel, R., Steiner, U., Müller, B., Hecht, C., and Kohl, T.: Local stress anomaly in the Bavarian Molasse Basin, Geothermal Energy, 3, 4, doi:10.1186/s40517-014-0023-z, 2015.

Simpson, R. W.: Quantifying Anderson's fault types, J. Geophys. Res.-Solid Earth (1978–2012), 102, 17909–17919, doi:10.1029/97JB01274, 1997.

Sjöberg, J., Christiansson, R., and Hudson, J.: ISRM suggested methods for rock stress estimation – Part 2: overcoring methods, International Journal of Rock Mechanics and Mining Sciences, 40, 999–1010, doi:10.1016/j.ijrmms.2003.07.012, 2003.

Sperner, B., Muller, B., Heidbach, O., Delvaux, D., Rei-necker, J., and Fuchs, K.: Tectonic stress in the Earth's crust: advances in the World Stress Map project, Geological Society, London, Special Publications, 212, 101–116, doi:10.1144/GSL.SP.2003.212.01.07, 2003.

Stadtwerke München: SWM Vision: Fernwärmeversorgung bis 2040 zu 100 % aus erneuerbaren Energien, 2012.

Sulem, J.: Stress orientation evaluated from strain localisation analysis in Aigion Fault, Tectonophysics, 442, 3–13, doi:10.1016/j.tecto.2007.03.005, 2007.

Tingay, M., Heidbach, O., Davies, R., and Swarbrick, R.: Triggering of the Lusi mud eruption: Earthquake versus drilling initiation, Geology, 36, 639–642, doi:10.1130/G24697A.1, 2008.

Townend, J. and Zoback, M.: Regional tectonic stress near the San Andreas fault in central and southern California, Geophys. Res. Lett., 31, 1–5, doi:10.1029/2003GL018918, 2004.

Townend, J. and Zoback, M. D.: How faulting keeps the crust strong, Geology, 28, 399–402, doi:10.1130/0091-7613(2000)28<399:HFKTCS>2.0.CO;2, 2000.

Van Wees, J., Buijze, L., Van Thienen-Visser, K., Nepveu, M., Wassing, B., Orlic, B., and Fokker, P.: Geomechanics response and induced seismicity during gas field depletion in the Netherlands, Geothermics, 52, 206–219, doi:10.1016/j.geothermics.2014.05.004, 2014.

Warner, T. T. and Hsu, H.-M.: Nested-model simulation of moist convection: The impact of coarse-grid parameterized convection on fine-grid resolved convection, Mon. Weather Rev., 128, 2211–2231, doi:10.1175/1520-0493(2000)128<2211:NMSOMC>2.0.CO;2, 2000.

Warpinski, N.: Determining the minimum in situ stress from hydraulic fracturing through perforations, in: International Journal of Rock Mechanics and Mining Sciences & Geomechanics Abstracts, vol. 26, 523–531, Elsevier, doi:10.1016/0148-9062(89)91430-7, 1989.

Wellmann, J. F.: Information Theory for Correlation Analysis and Estimation of Uncertainty Reduction in Maps and Models, Entropy, 15, 1464–1485, doi:10.3390/e15041464, 2013.

Wellmann, J. F. and Regenauer-Lieb, K.: Uncertainties have a meaning: Information entropy as a quality measure for 3-D geological models, Tectonophysics, 526, 207–216, doi:10.1016/j.tecto.2011.05.001, 2012.

Wessel, P., Smith, W. H. F., Scharroo, R., Luis, J., and Wobbe, F.: Generic Mapping Tools: Improved Version Released, Eos, Transactions American Geophysical Union, 94, 409–410, doi:10.1002/2013EO450001, 2013.

Westerhaus, M., Altmann, J., and Heidbach, O.: Using topographic signatures to classify internally and externally driven tilt anomalies at Merapi Volcano, Java, Indonesia, Geophys. Res. Lett., 35, doi:10.1029/2007GL032262, 2008.

Yoon, J. S., Zimmermann, G., and Zang, A.: Discrete element modeling of cyclic rate fluid injection at multiple locations in naturally fractured reservoirs, International Journal of Rock Mechanics and Mining Sciences, 74, 15–23, doi:10.1016/j.ijrmms.2014.12.003, 2015.

Zang, A. and Stephansson, O.: Stress Field of the Earth's Crust, Springer Netherlands, Dordrecht, doi:10.1007/978-1-4020-8444-7, 2010.

Zang, A., Stephansson, O., Heidbach, O., and Janouschkowetz, S.: World Stress Map Database as a Resource for Rock Mechanics and Rock Engineering, Geotechnical and Geological Engineering, 30, 625–646, doi:10.1007/s10706-012-9505-6, 2012.

Zang, a., Yoon, J. S., Stephansson, O., and Heidbach, O.: Fatigue hydraulic fracturing by cyclic reservoir treatment enhances permeability and reduces induced seismicity, Geophys. J. Int., 195, 1282–1287, doi:10.1093/gji/ggt301, 2013.

Zang, A., Oye, V., Jousset, P., Deichmann, N., Gritto, R., McGarr, A., Majer, E., and Bruhn, D.: Analysis of induced seismicity in geothermal reservoirs – An overview, Geothermics, 52, 6–21, doi:10.1016/j.geothermics.2014.06.005, 2014.

Ziegler, M., Reiter, K., Heidbach, O., Zang, A., Kwiatek, G., Stromeyer, D., Dahm, T., Dresen, G., and Hofmann, G.: Mining-Induced Stress Transfer and Its Relation to a M_w 1.9 Seismic Event in an Ultra-deep South African Gold Mine, Pure Appl. Geophys., 172, 2557–2570, doi:10.1007/s00024-015-1033-x, 2015.

Ziegler, M., Rajabi, M., Heidbach, O., Hersir, G. P., Ágústsson, K., Árnadóttir, S., and Zang, A.: The Stress Pattern of Iceland, Tectonophysics, 674, 101–113, doi:10.1016/j.tecto.2016.02.008, 2016.

Zoback, M.: Reservoir Geomechanics, Cambridge University Press, Cambridge, 2010.

Zoback, M., Barton, C., Brudy, M., Castillo, D., Finkbeiner, T., Grollimund, B., Moos, D., Peska, P., Ward, C., and Wiprut, D.: Determination of stress orientation and magnitude in deep wells, International Journal of Rock Mechanics and Mining Sciences, 40, 1049–1076, doi:10.1016/j.ijrmms.2003.07.001, 2003.

Zoback, M. D., Moos, D., Mastin, L., and Anderson, R. N.: Well bore breakouts and in situ stress, J. Geophys. Res.-Solid Earth, 90, 5523–5530, doi:10.1029/JB090iB07p05523, 1985.

Zoback, M. L.: First- and second-order patterns of stress in the lithosphere: The World Stress Map Project, J. Geophys. Res., 97, 11703, doi:10.1029/92JB00132, 1992.
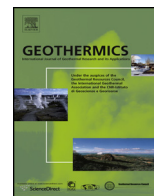
Numerical modelling of thermal convection in the Luttelgeest carbonate platform, the Netherlands

Lindsay Lipsey [a,b,*], Maarten Pluymaekers [b], Tatiana Goldberg [b], Katrien van Oversteeg [a,b], Lilya Ghazaryan [b], Sierd Cloetingh [a], Jan-Diederik van Wees [a,b]

[a] Faculty of Geosciences, Utrecht University, PO Box 80.021, 3508 TA Utrecht, The Netherlands
[b] TNO, PO Box 80015, 3508 TA Utrecht, The Netherlands

ARTICLE INFO

ABSTRACT

The presence of convective fluid flow in permeable layers can create zones of anomalously high temperature which can be exploited for geothermal energy. Temperature measurements from the Luttelgeest-01 (LTG-01) well in the northern onshore region of the Netherlands indicate variations in the thermal regime that could be indicative of convection. This thermal anomaly coincides with a 800 m interval of Dinantian carbonates showing signs of increased fracture permeability of $6 \ 10^{-14} \ m^2$.

In this study, we reproduce the thermal gradient at LTG-01 using 3D numerical models in order to better understand the interplay between natural fracture permeability and temperature patterns. Numerical models of thermal convection are used to illustrate the role of permeability on the timing of convection onset, convection structure development and resulting temperature patterns.

Rayleigh number calculations indicate that convective flow is realistic within the Luttelgeest carbonate platform. The degree and pattern of convection depends strongly on the platform geometry and thickness, permeability structure and geothermal gradient of the convective zone. The spacing of convective upwellings and their thermal anomalies can be well predicted by numerical models that provide evidence for significant convection-driven thermal anomalies. Numerical models can facilitate in exploration workflows to assess thermal variation and location of upwelling zones.

1. Introduction

Thermal anomalies in deep sedimentary layers and basement rock are largely controlled by convective fluid flow within permeable zones. Convection is of particular interest in geothermal energy, as the up flow of hot fluids yields relatively shallow high-temperature anomalies, which are preferential targets for geothermal exploration. In fact, numerical studies show that convective fluid flow leaves a distinct pattern on the local geothermal gradient. The thermal effect is critically dependent on the pre-existing thermal gradient, thickness and permeability (e.g. Pasquale et al., 2013).

Owing to oil and gas exploration, the accessibility of subsurface temperature data has assisted in our understanding of temperature patterns. Analyses have revealed significant thermal anomalies located in graben systems and sedimentary basins, several of which

* Corresponding author at: Faculty of Geosciences, Utrecht University, PO Box 80.021, 3508 TA Utrecht, The Netherlands.
E-mail address: l.c.lipsey@uu.nl (L. Lipsey).

were interpreted to be the result of thermal convection (Garibaldi et al., 2010; Bonté et al., 2012; Pasquale et al., 2013; Guillou-Frottier et al., 2013). These studies have used a combination of numerical tools to link deep temperatures, geological structures and fluid flow. Guillou-Frottier et al. (2013) use 2D numerical models to reproduce thermal features observed in the Upper Rhine Graben in fractured granitic basement and thick sedimentary layers at shallow depth. The models help to understand how convective cells establish and show that these anomalously hot zones can only be explained by fluid circulation (Baillieux et al., 2013). At larger depth, Pasquale et al. (2013) argue that a thick carbonate unit in the Po Plain may host thermal convection, which would explain the lower geothermal gradient within the carbonate layer and the higher gradient in the overlying layers. This particular thermal signature is thought to be characteristic of convection processes. They quantified the potential for thermal convection by performing Rayleigh number analyses and calculate the minimum thermal gradient that is required for convection based on permeability and thickness.

While both reservoir and basin scale modelling have been used to address thermal features characteristic of convective fluid flow, to date there have been no 3D numerical modelling studies which
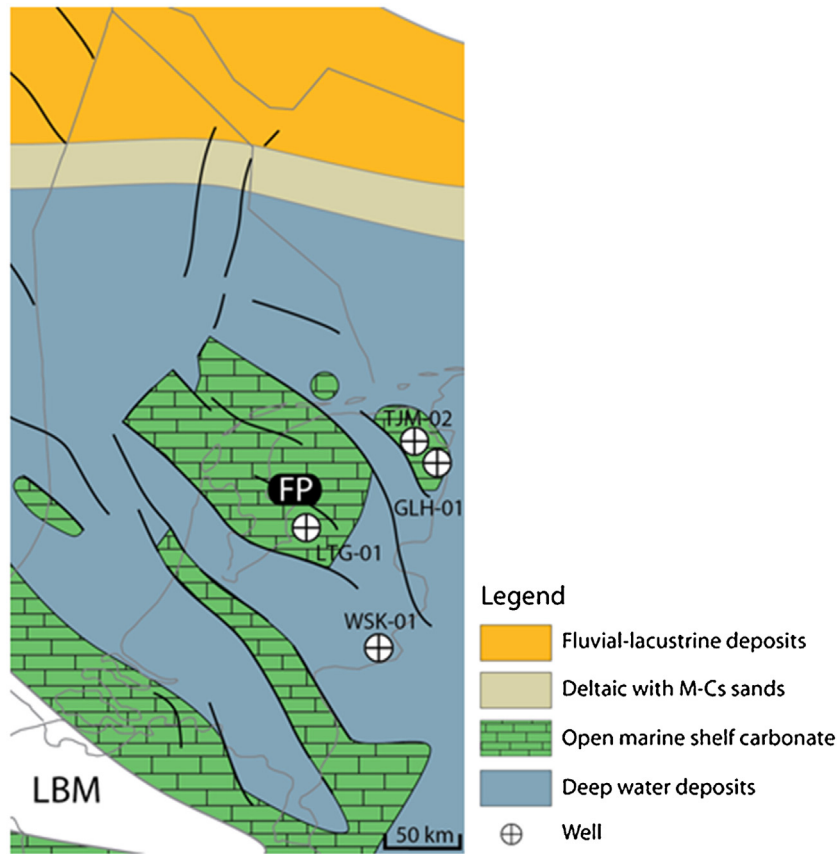
Fig. 1. Paleogeographic map of the Netherlands during the Early Carboniferous. LBM: London-Brabant Massif; FP: Friesland Platform. (Adapted after Kombrink, 2008).

focus on deep carbonate reservoirs in detail. In the Netherlands, renewed interest in deeper formations has led to the drilling of several deep wells. Recent work on the temperature distribution in the Dutch subsurface revealed a thermal anomaly at 4–5 km depth at one of the deep wells, Luttelgeest-01 (LTG-01), which could be explained by thermal convection. Temperature measurements show a shift to higher temperatures at depths greater than 4000 m, corresponding to the Dinantian carbonate interval. The local thermal gradient strongly resembles the thermal signature that is believed to be characteristic of convective processes.

The aim of the study is to reproduce the temperature pattern at Luttelgeest through 3D numerical models of thermal convection in order to elucidate possible flow and thermal structures. This is done to better understand the interplay between geothermal anomalies, platform geometry and natural permeability. Numerical experiments are used to test the effect of platform geometry and the permeability structure on the development of thermal convection and resulting temperature patterns.

First we introduce the geological setting of the Luttelgeest platform, and subsequently present the evidence for convection from temperature data, permeability measurements on cores and determine the minimum permeability required for convection using the Rayleigh number analysis. Determining whether convection is possible is important for predicting and understanding the likely distribution of geothermal resources in deep carbonate layers. Following this, we use site-specific fluid and rock properties to perform numerical simulations of thermal convection. Results from numerical simulations are used to illustrate the type of behaviour that may occur, in terms of flow paths and temperature patterns. The numerical simulations allow for a better understanding of the nature and evolution of convective flow.
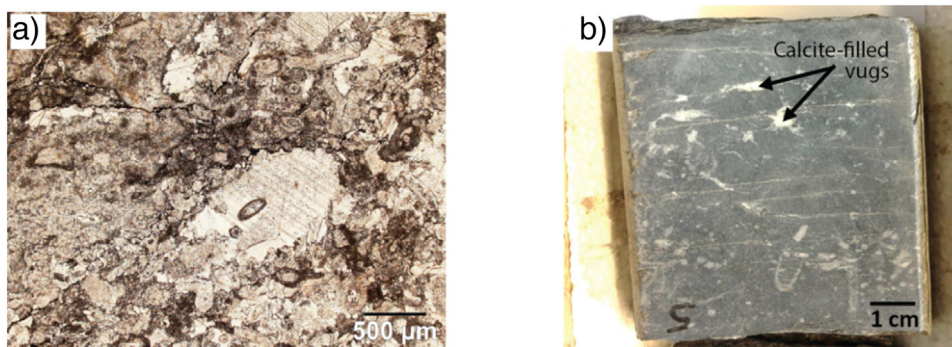

Fig. 2. (a) Thin section from a sample at depth 4376 m. Bioclastic packstone. Note abraded and fragmented crinoid plate in the center and sutured stylolites with insoluble residue in black. Plane poloarized light. (b) Sample from the core of Dinantian carbonate interval (depth 4376 m). Note the vugs filled with sparitic calcite.
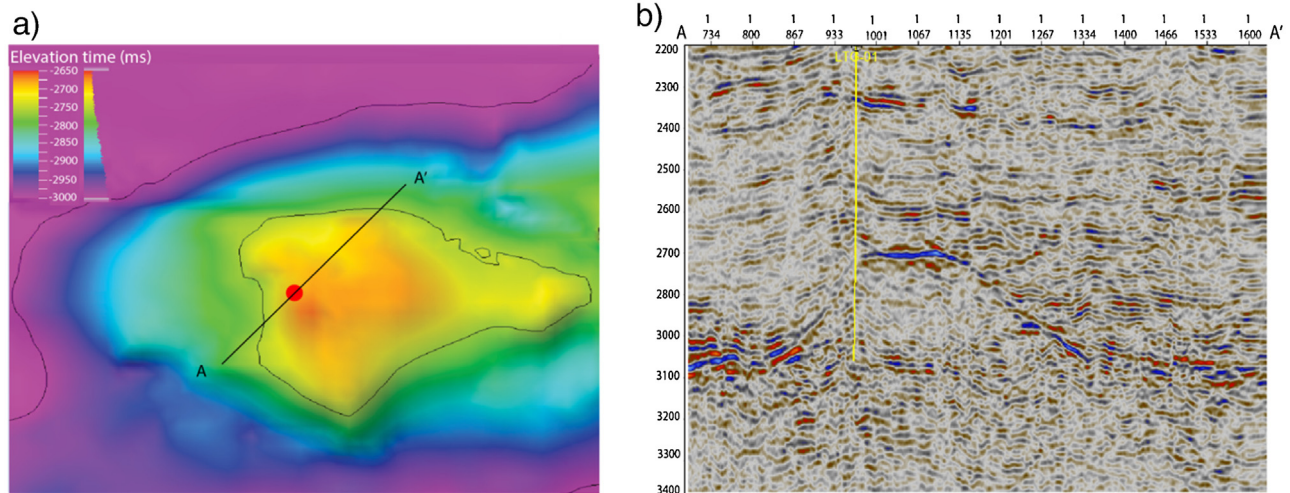
Fig. 3. (a) Top view of the Luttelgeest platform. The LTG-01 well is indicated in red. (b) Seismic section A–A'. The LTG-01 well is indicated in yellow. Note the location of the well along the margin of the platform.

2. Geology

2.1. Geological setting

In Carboniferous times the Netherlands and surrounding areas were part of a large intra-cratonic basin known as the Northwest European Carboniferous Basin (NWECB) (Kombrink et al., 2010). The basin is delineated by the Mid north Sea High to the north and the London-Brabant Massif to the south. It formed in response to renewed back-arc extension in the Rhenohercynian basin, which occurred following the Caledonian orogeny during mid-Devonian times. This initiated the formation of a series of linked NW-SE trending fault blocks. During the Dinantian the Netherlands part of the NWECB experienced a tensional regime, resulting in a horst-and-graben complex (Kombrink et al., 2010) (Kombrink, 2008) (Fig. 1).

Differential subsidence of this horst-and-graben topography strongly influenced sedimentation and facies distribution during the Carboniferous (Kombrink et al., 2010). While fluvial systems dominated the Mid North Sea High, horst blocks effectively shielded large regions further south from siliclastic influx (Van Hulten, 2012). This created an ideal environment for widespread carbonate platform development on hanging-wall blocks during the Dinantian. Late Visean sea level lowering left platforms locally subaerially exposed, inducing significant leaching and karstification. Ultimately, Namurian sea-level transgression caused the platforms to become gradually flooded (Geluk et al., 2007).

The present day stress regime in the Netherlands is extensional with maximum horizontal stress oriented NW-SE (De Jager, 2007). Many structural elements show a characteristic rhomboid pattern of intersecting fault trends. The dominant family of faults trend NW-SE and formed during the mid-Devonian and Early Carboniferous. The trend was reactivated during the Early Permian in response to Late-Variscan wrench faulting and thermal uplift. A conjugate set of NNE-SSW faults developed regionally (De Jager, 2007). Rift basins and platforms appear to share a similar fault pattern, despite having significant differences in structural development (Van Hulten, 2012). The high degree of fault parallelism suggests that faults were repeatedly reactivated under different stress regimes throughout the Netherlands geologic history (Kombrink et al., 2010).

Dinantian carbonates in the Dutch subsurface have varying geometries and show a large range of reservoir quality. These variances reflect differences in tectonic setting, sea level and burial/diagenesis history between areas. A high variability in carbonate sedimentology means that the mechanical properties of carbonate platforms are expected to be heterogeneous and affect the characteristics of fractures. Diagenesis results from a series of processes that develop in response to the availability of fluids and reactants within a given tectonostratigraphic framework. The resultant porosity/permeability architecture develops in response to these depositional events (Goldscheider et al., 2010).

The framework of the Dinantian carbonates in the central part of the NWECB is poorly constrained. With the Upper Carboniferous generally regarded as the lower limit of the economic fairway, there is a scarcity of wells that penetrate the base of the Carboniferous (Van Hulten, 2012). The wells that do are clustered along the NWECB margins. Seismic reflections are often hard to distinguish, making seismic interpretation and contouring of Dinantian structures difficult.

2.2. Local geology at Luttelgeest

The LTG-01 well is located on the Luttelgeest carbonate platform which is found on the Texel-Ijsselmeer structural high, a prominent NW-SE trending fault block of mid-Palaeozoic origin (Fig. 1) (Geluk et al., 2007). The southern boundary is made up of a steep fault system, while the northern margin gradually transitions into the adjacent Friesland platform. The Luttelgeest carbonate platform is elongated in the E-W direction, with dimensions of approximately 14 km E-W and 8 km N-S.

The LTG-01 well was drilled to a total depth of 5162 m. The Dinantian carbonates span the depth interval between 4355 and 5123 m, being in total 768 m thick. The LTG-01 core taken in the Dinantian interval comprises massive dark-grey limestones rich in millimetre sized bioclasts, that commonly contain fractures and vugs filled with early sparitic calcite (Fig. 2). The most abundant microfacies association is bioclastic packstone with abundant crinoids and fragments of echinoids, calcareous algae, foraminifera and brachiopods, as seen in the thin section in Fig. 2a. In the lower 120 m, dolomite is intercalated with limestone. Two depositional environments can be recognized from analysing the core and log. The first is a relatively open environment under moderately agitated conditions below the effective wave base, most likely representing the carbonate platform break. The second is a moderate to high-energy subtidal environment above wave base but in conditions of relatively slow sedimentation which usually occur in the inner platform.
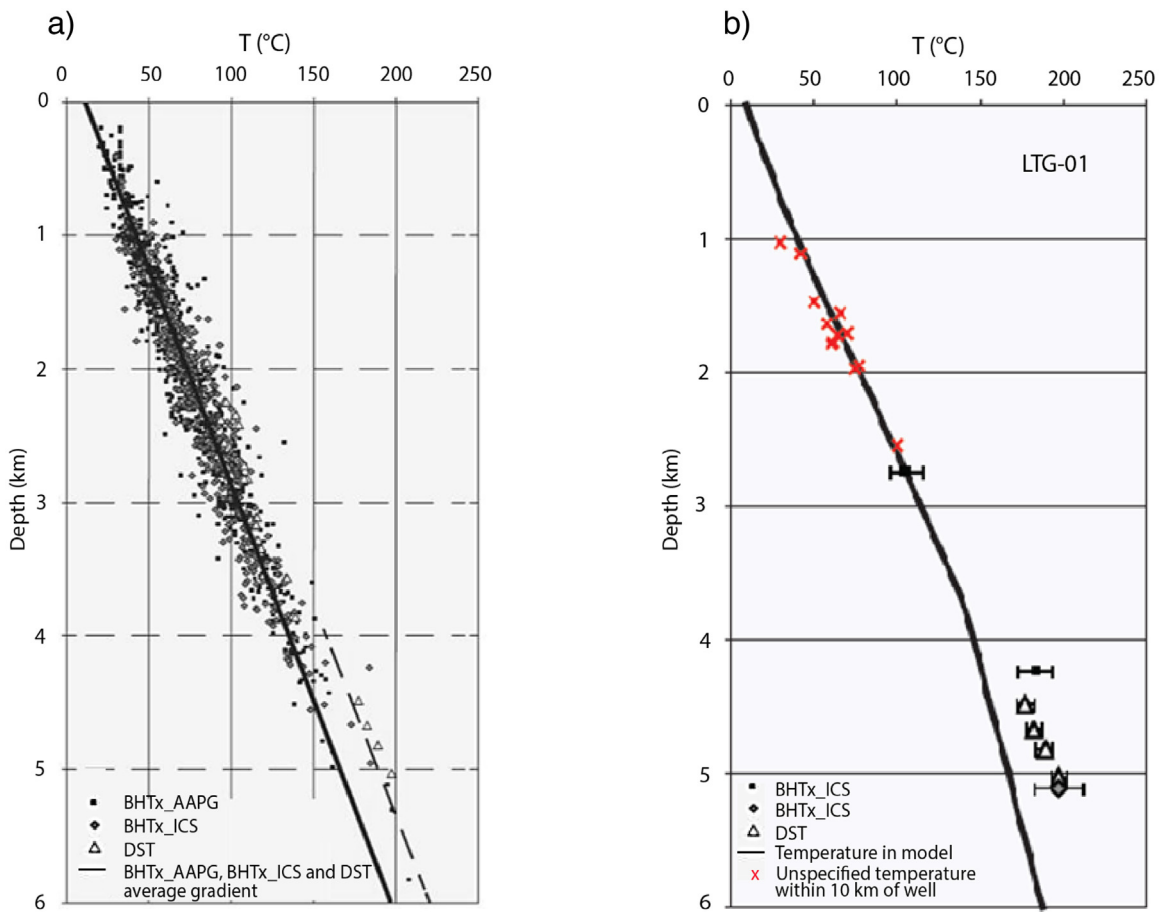
Fig. 4. Temperature vs. depth for the Dutch subsurface. (a) DST and corrected BHT dataset. Dashed black line represents the trend for deeper temperatures. (b) Comparison between the values used as calibration and the modelled temperature for LTG-01. See legend for explanation of symbols (adapted after Bonté et al., 2012).

Various processes during deposition affect the overall geometry of carbonate platforms. A general distinction can be made of platform geometry by considering sedimentological domains including platform interior, margin and slope (Boro et al., 2013). The seismic profile in Fig. 3b shows the relative position of the LTG-01 well, which appears to be situated on the edge of the platform, or platform margin. This is in agreement with other seismic studies of the Luttelgeest platform (e.g. Van Hulten and Poty, 2008).

3. Evidence for convection

The potential for convection in the Luttelgeest platform is evaluated by looking at evidence of convection in temperature data, permeability measurements on cores and by using the Rayleigh number analysis to determine the minimum permeability at which convection could occur in the Luttelgeest platform.

3.1. Temperature

The Netherlands is covered by more than 5000 oil and gas exploration wells, providing valuable information on the thermal state of the Dutch subsurface. Bonté et al. (2012) provides the most recent up-to-date coherent temperature dataset for the Netherlands, adding to it a number of recently drilled wells including LTG-01. In total, the dataset includes 1293 corrected bottom-hole temperature (BHT) measurements distributed over 454 wells and yields an average gradient of 31.3 °C km^{-1} with a mean surface temperature of 10.1 °C (Fig. 4a). There is, however, a sudden shift in the data towards high temperatures at depths greater than 4 km, as indicated by the dashed line in Fig. 4a. These anomalous high val-

ues at great depth correspond to the following deep wells: LTG-01, TJM-02, WSK-01 and GLH-01 (See Fig. 1 for locations).

For a better understanding of subsurface temperatures, Bonté et al. (2012) use this up-to-date temperature dataset to calibrate 3D thermal models for the complete Dutch subsurface. Models use a tectonic heat flow method that is based on the varying petrophysical parameters and the transient effects of vertical tectonic motions. The modelling method takes into account not only the well itself, but the closest values around the well in order to calibrate the model (Bonté et al., 2012).

The comparison between the model and the values within a 10 km radius of the LTG-01 well is shown in Fig. 4b (Bonté et al., 2012). The complete dataset for LTG-01 yields a temperature gradient of 39 °C km^{-1}, though contains several intervals of anomalous values. Most notably, within the platform the gradient is nearly 10 °C km^{-1} lower than the Dutch average, whereas above the platform the gradient is roughly 20 °C km^{-1} higher.

The first observation is that between 1 and 4 km, the results show a good fit of the temperature model with the calibration data. In the Noordoospolder area, the low conductivity overlying Silesian shale and coal is thick. The Silesian has an insulating effect, resulting in lower temperatures at the top of the Silesian and higher than average temperatures at the base. In LTG-01 well, the Silesian is reached at 1776 m. The insulating effect is represented by the steep gradient extending down to 3800 m. This is in agreement with the close proximity wells (indicated in red in Fig. 4b).

Another important observation is the major misfit of temperatures deeper than 4 km, which are all higher than the modelled temperatures. There are several different mechanisms that could explain the local thermal configuration, including basal heat flow
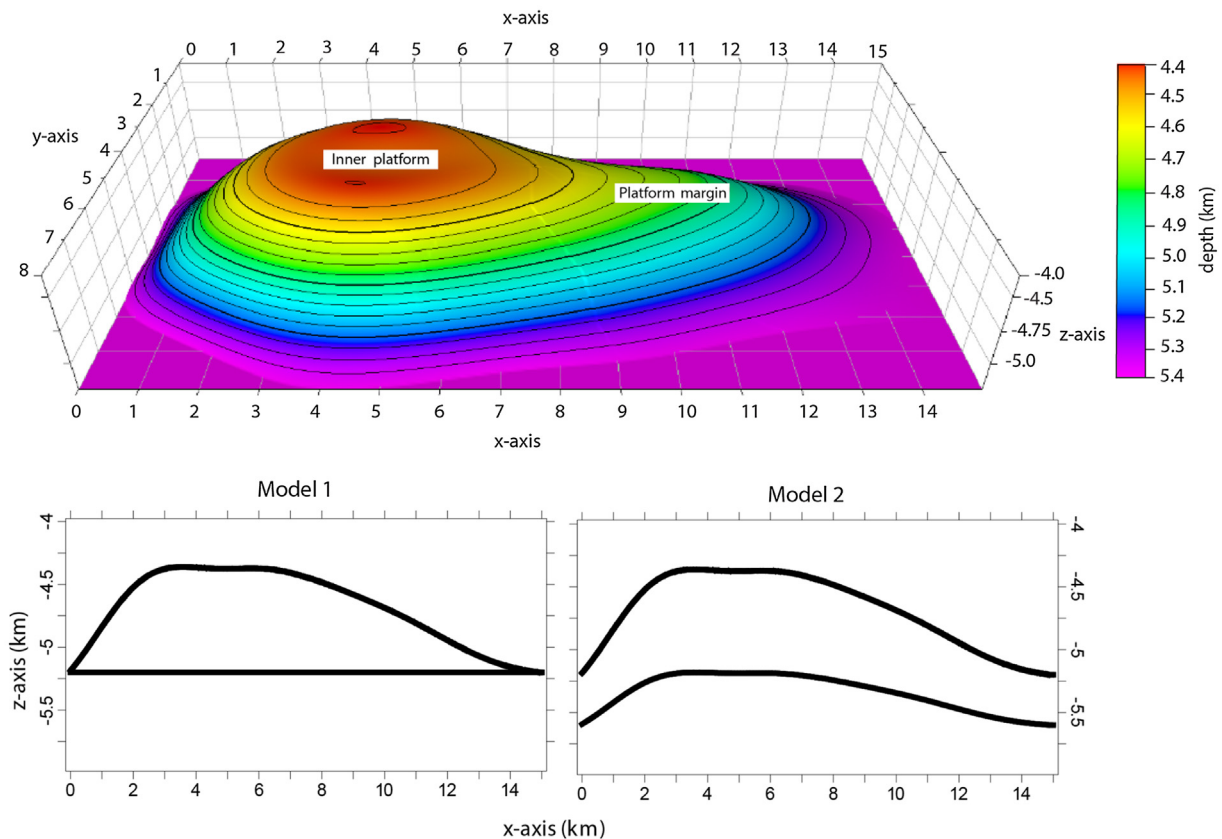
Fig. 5. Geometry of platform. Inner platform and platform margin indicated. Platform is at a depth of 4.4–5.2 km. Bottom: cross sections showing the different geometries in model 1 and model 2.

variation, thermal conductivity contrasts or additional heat generation. For example, higher conductivity may result in heat refraction effects, whereas a thick sedimentary cover may cause an increase in temperatures due to a lower thermal conductivity, known as thermal blanketing. Thermal blanketing effect is well recognized in studies (e.g. Ziegler et al., 1998; Van Wees and Beekman, 2000). Additionally, variation in basal heat flow can cause regional variations in the surface heat flux. A high heat generating body such as a granite intrusion may also cause additional heat generation thereby enhancing the surface heat flow (e.g. Cloetingh et al., 2010).

The conductive model by Bonté et al. (2012) does not give the predicted conductivity structure. Bonté et al. (2012) addresses several different explanations for the thermal anomaly. At the base of their model, the heat flow of the basin fill gives a value of 53 mWm^{-2}. This value is too low to be able to reach the high temperatures required by using coherent thermal conductivity values in the Carboniferous (around 1.7). However, it cannot be ruled out that perhaps the Carboniferous conductivity is high, which could give a refraction effect of the geotherm as seen in the Luttelgeest model. There are simply not enough conductivity measurements to rule it out. Furthermore, while the presence of local heat structures could cause thermal variations spatially, it would not cause a vertical differentiation of the gradient. Further, there have been no recent heat sources nor tectonic processes.

If the model is to fit the measured data from LTG-01, the geothermal gradient would need to increase between 3 and 4 km, and then decrease between 4 and 5 km through the carbonate platform (Fig. 4b). Such a decrease in the temperature gradient is typical of a convective signature resulting from hot upwelling fluid (Guillou-Frottier et al., 2013). In this study, we investigate the possibility that the thermal anomaly at Luttelgeest is due to the occurrence of convective heat transfer in the deep carbonate platform. Thermal convection can cause small-scale thermal anomalies, provided permeability is sufficient.

3.2. Permeability assessment

Permeability was calculated by TOTAL from wirelines pressure tests and reported in the composite log (report accessible from www.nlog.nl)The permeability values range from 10 to 598 mD (10^{-14} to $6\,10^{-13}$ m^2), however several measurements were registered as fair or questionable. Van Oversteeg et al. (2014) calculated the permeability and transmissivity based on mud losses and proposed that there is an interval with fracture permeability between 4550–5150 m. For a reservoir thickness of 600 m, an overall permeability of $6\,10^{-14}$ m^2 was calculated (Van Oversteeg et al., 2014). This value is in accordance with the permeability range inferred from pressure measurements, but should be taken with caution as the permeability is not equally distributed throughout the entire interval of 600 m. For example, between 4800 and 4975 m there is no evidence of permeability.

An overview of the permeability assessment is presented in Table 1. The cuttings description of the composite log states that no visible porosity was encountered. According to Van Hulten and Poty (2008), only a few fracture zones were encountered on bore hole imaging. Van Hulten and Poty (2008) propose that the two fracture zones corresponding with high gamma ray peaks indicate karstified horizons. However, the fact that fracture zones have high gamma ray peaks likely implies argillaceous, clay-rich fracture sedimentation. Furthermore, areas of potential permeability increase can be derived from wireline logs by comparing the neutron porosity and density logs. High neutron porosity and low density indicate areas with increased/present porosity that can be translated to permeability. In fact, several mud losses are encountered in the

Table 1
Overview of results from the permeability assessment of the Dinantian carbonate interval from LTG-01 well.

Source/method	Depth interval	Permeability
Composite well log	Several intervals show signs of increased permeability	
Wireline Pressures	4535–4647 m (100 m)	10–598 mD (10^{-14}–6 10^{-13} m^2)
Rock samples	4378–4473 m (100 m)	0.2–9.6 mD (2 10^{-16}–9 10^{-15} m^2)
Mud loss calculations	600 m	>1D (10^{-12} m^2)

Table 2
Nomenclature for model equations.

Symbol	Name	Unit
Ra	Rayleigh number	–
Ra*	Critical Rayleigh number	–
k	Permeability	m^2 or mD
k$_{min}$	Minimum permeability for convection	m^2
α	Volumetric thermal expansion coefficient	$°C^{-1}$
ρ	Bulk Density of porous rock	kg m^{-3}
ρ_f	Fluid density	kg m^{-3}
ρ_0	Reference density	–
C	Bulk Specific heat capacity of porous rock	J kg^{-1} K^{-1}
C$_f$	Specific heat capacity of fluid	J kg^{-1} K^{-1}
C$_h$	Bulk hydraulic storage capacity of porous rock	m^3 Pa^{-1}
g	Gravitational acceleration	m/s^2
H	Total thickness of the aquifer	m
T	Temperature	$°C$
t	Time	s
P	Pressure	Pa
ΔT	Temperature difference across layer	$°C$
μ	Fluid viscosity	Pa s
λ	Thermal conductivity	W m^{-1} K
Q	Source term	m^3 s^{-1}

well; one at 4450 m, six between 4575 and 4700 m, one at 4775 m and two between 4975 m and 5025 m, which points to permeability streaks that are probably related to fractures. The combination of neutron porosity and density indicates porous intervals around 4500 m, between 4570 and 4600 m, and between 4770 and 4800 m.

3.3. Permeability from Rayleigh number analysis

Assuming that thermal convection is able to explain the abnormally low thermal gradient within the Luttelgeest platform at well LTG-01, the rationale of Horton and Rogers (1945) and Lapwood (1948) can be followed to find the minimum required permeability values for convection. The Rayleigh number is a non-dimensional number that includes characteristics of the porous medium, thermodynamic properties of the fluid and a vertical temperature difference. In a homogeneous, isotropic porous medium saturated by a single-phase fluid, the Rayleigh number is defined as

$$\text{Ra} = \frac{k\alpha\rho^2 c_p g H \Delta T}{\mu\lambda} \tag{1}$$

See Table 2 for nomenclature. The critical Rayleigh number for onset of convection is calculated from linearized governing equations (Lord Rayleigh, 1916). If Ra is above the threshold value of the system, known as the critical Rayleigh number (Ra*), convection is expected to occur. For a horizontal, homogeneous isotropic porous medium bounded from above and below by fixed temperature conditions, Ra* is $4\pi^2$.

Using Ra*, Eq. (1) can be rewritten to constrain the minimum required permeability (k$_{min}$):

$$K_{min} = \frac{Ra^*\mu\lambda_e}{(\rho C_p)\,\rho g\alpha\Delta T H} \tag{2}$$

For the parameter values, site specific values from LTG-01 well are used for the temperature difference and the height of the convective layer. Furthermore, temperature dependent relationships are used for density and fluid dynamic viscosity, as provided by

Holzbecher (1998) (see Section 4.2). By means of the Rayleigh number analysis using the temperature range of the carbonate platform (182–213 °C) and a thickness of 800 m, the theoretical minimum permeability for convection is 1.9 10^{-14} m^2.

While the theoretical Rayleigh number analysis can be a useful tool in determining the conditions necessary for the onset of convection, it does ignore several important factors, such as the heterogeneous nature of fluid and rock properties of the reservoir (Nield and Bejan, 2013). In addition, the critical Rayleigh number applies to a specific set of conditions, including initial and boundary conditions and the geometry of the layer. This study assumes the carbonate platform is uniformly heated from below and is a perfect conductor. Changing the lower thermal boundary condition may result in smaller values for Ra* (Bjørlykke et al., 1988).

Moreover, conductive heat transfer along the sides of the platform is likely to play a role in the overall physical state and stability of the convective system. Murphy (1979) highlighted on the fact that heat transfer between fluid in the permeable layer and surrounding rock is exceptionally stable. Tournier et al., (2000) demonstrated that this blanketing effect of thermal gradients across vertical walls by conduction might result in delayed onset of convection. Though the conjectures of both Murphy (1979) and Tournier et al. (2000) were related to studies on the onset of convection in vertical fault planes, the concept can be applied to any confined, fluid saturated medium where convective fluid flow is occurring. Thus, assuming that only convective heat transfer is occurring in the system is a significant simplification to the model.

4. Methods

4.1. Governing equations

The numerical study of thermal convection in permeable and porous media involves the coupling of heat transfer and fluid flow equations that incorporate realistic fluid and rock properties. In a Eulerian reference framework, the heat equation is written as

$$\rho c \frac{\partial T}{\partial t} = \nabla \cdot (\lambda \cdot \nabla T) - \vec{v} \cdot \nabla T \tag{3}$$

See Table 2 for nomenclature. The advective velocity can also be a result of fluid flow inside pores or fractures which can strongly affect the thermal distribution (e.g. Guillou-Frottier et al., 2013; Cherubini et al., 2014). The fluid velocity is resolved from solving the Darcy flow equation:

$$c_h \frac{\partial P}{\partial t} = \nabla \cdot \left(\frac{k}{\mu} \left(\nabla P + \frac{(\rho_f - \rho_0)}{\rho_0} g\nabla z \right) \right) + Q \tag{4}$$

See Table 2 for nomenclature. Through solving the pressure field in Eq. (4), the velocities can be determined as

$$\to v_f = \frac{k}{\mu} \left(\nabla P + \frac{(\rho_f - \rho_0)}{\rho_0} g\nabla z \right) \tag{5}$$

And can be incorporated in (Eq. (3)) by adopting:

$$\vec{v} = \varphi \frac{\rho_f c_f}{\rho c} \to v_f \tag{6}$$

4.2. Petrophysical and fluid properties

The following properties are considered temperature dependent and have been defined here. Laws are based on experimental data measured on pure water between 100 and 300 °C (Holzbecher, 1998). Under single-phase conditions, the following polynomial trend has been chosen for temperature dependent density

$$\rho = 1758.4 + 10^{-3}T - \left(4.8434 \times 10^{-3} + T\left(1.0907 \times 10^{-5} - 9.8467 \times 10^{-9}T\right)\right) \quad (7)$$

where T is in K and ρ in kg m^{-3}. For the relationship between temperature and fluid dynamic viscosity, the law adapted by Rabinowicz et al. (1998) is used:

$$\mu = 2.4141 \times 10^{-5} \times 10^{\frac{247.8}{T-140}} \quad (8)$$

where T is in K and μ in kg m^{-1} s^{-1}.

4.3. Geometry and boundary conditions

Three-dimensional coupled fluid and heat transport models are simulated using a numerical solver developed in a Java programming language. The equations are solved in a 3D cellular model. A 3D model of the platform was constructed with grid resolution of 100×100 m in the x and y directions and 10 m in the z direction at platform depth level and xx m in the z direction elsewhere A sensitivity analysis was performed only within platform, using a larger mesh size ($200 \times 200 \times 10$ m) as well as a smaller one ($50 \times 50 \times 10$ m). There is no discrepancy in the temperature nor the convection cell width between the different mesh sizes. The top of the platform is at a depth of 4.4 km and base at 5.2 km, resulting in a thickness of 800 m. The model domain extends from the surface to below the base of the platform down to a depth of 6 km. The platform extends 14 km and 8 km in the x and y directions, respectively. This results in a total 896,000 for the 100 m resolution model and 224,000 and 358,4000 grid cells for the 200 and 50 m resolution models, respectively. Temperature at the top of the model is 10 °C and 244 °C at the bottom reflecting a linear thermal gradient of 39 °C km^{-1}. This gradient is chosen based on the calculated average gradient from the LTG-01 temperature data. All boundaries of the platform are impermeable, defining a closed system with no sources or sinks for the fluid. Lateral boundaries are thermally insulating. Rock thermal properties are assumed to be uniform for the entire model.

Experiments begin with an initial perturbation to the conductive temperature field by injecting cold fluid into the platform. If the system is unstable (Ra < Ra*), a perturbation to the diffusive regime will grow and instability will occur, generating convection cells (Weatherill et al., 2004). An instability in a real system could be caused, for example, by lateral contrasts in the temperature gradient, for example caused vertical tectonic movement. A sensitivity analysis was carried out with regard to the location of perturbation and its magnitude relative to the background temperature. While convection cells do initially develop from the location of perturbation, at pseudo steady-state the system evolves into the same convection cell pattern with matching wavelengths, regardless of the location of perturbation. During computation, the initial conductive field evolves towards steady-state convection within a few thousand years, therefore simulations run for 500 k years.

The prediction of convective flow patterns necessitates the use of 3D numerical modelling to allow for a more accurate specification of platform geometry, which has a significant control on convection cell development. Indeed, simple 2D models of thermal convection show that. The introduction of a third dimension results in a complex polyhedral structure which cannot develop in 2D. Two-dimensional models represent an oversimplification, marked by convective instabilities which occur in the form of longitudinal square rolls, but are still commonly used in numerical
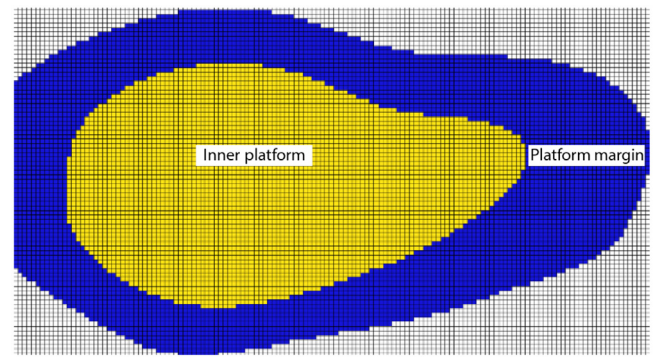

Fig. 6. Top view of the platform showing the permeability differentiation between platform margin and inner platform areas. The platform margin is assigned a higher permeability. See Table 4 for permeability values.

studies, despite several studies demonstrating that 2D and 3D models of convection can produce significantly different results with flow velocities of 2D models one order of magnitude lower than in the 3D case (e.g. Kühn et al., 2006). This study presents convective patterns which result from 3D numerical models of thermal convection.

4.4. Model scenarios

We begin with several convective flow simulations using a constant, homogeneous permeability. In doing so, two platform geometries are tested. The first geometry, referred to as model 1, is characterized by a flat platform base, where the thickness of the inner platform is 800 m. In the second geometrical configuration (model 2) the shape of the platform top remains the same, however the base of the platform is curved upwards. In order to keep the thickness of the inner platform at 800 m, the thickness of the margins is increased by 400 m, extending down to 5600 m depth at the platform margin. Fig. 5 provides an overview of the model geometries.

In carbonate platforms it is common for fractures to be less common in the inner platform and prominent in the outer platform to rim/slope area as seen in international analogues such as the Tengiz and Kashgan platforms in Kazakhstan (Collins et al., 2006; Kenter et al., 2002). Therefore, in the second set of convective flow simulations we investigate the effect of the permeability structure on convective flow. The margins of the platform have increased permeability, while the inner platform region is assigned a lower permeability. Fig. 6 depicts the differentiation between the inner platform and the platform margin. We also present two cases which address the effect of an anisotropic permeability field.

5. Results

5.1. Platform geometry sensitivity

A system is said to be in steady state convection once a constant fluid velocity is reached. The convection cell width is assessed by measuring the distance between each thermal high and its closest neighbor and halving it. As discussed in Section 3.3, the theoretical minimum permeability required for convection is 1.9 10^{-14} m^2. A range of permeability values are tested in numerical simulations, and by doing so we find the modelled minimum permeability is 1.7 10^{-14} m^2. Here the results for two permeability values are presented, 2 10^{-14} m^2 (subscript a) and 6 10^{-14} m^2 (subscript b), which are taken uniform over the platform and applied to both geometric scenarios (models 1a,1b, 2a,2b). An overview of the scenarios and the results is provided in Table 3.

Table 3
Numerical model results at end of simulation for models 1 and 2. T is the maximum temperature obtained along the axes of upwelling. Tc is the temperature without convection. T–Tc is the overall temperature enhancement relative to the conductive profile.

	Permeability (m^2)	T ($^\circ$C) at 4.4 km	T–Tc ($^\circ$C) at 4.4 km	Cell width (km)	Fluid velocity (m yr^{-1})
1a	2 10^{-14}	192	11	1.1	1.3
1b	6 10^{-14}	197	16	1.0	1.9
2a	2 10^{-14}	196	15	1.3	1.8
2b	6 10^{-14}	203	22	1.3	2.6

5.1.1. Convection cell structure

Results show that the development and number of convection cells is very much a time dependent process. The first sign of convective motion appears after 8k years in the form of longitudinal rolls forming from the location of perturbation. Longitudinal rolls fill the domain, increasing in width until eventually transforming into a more complex polyhedral structure within 50k years in all models. The system gradually develops into a distinct convective patter with alternating up-flows and down-flows, reaching steady-state convection after approximately 180k years in model 1a and 160k in model 1b.

Model 1a relaxes into a steady-state 8 cell convection pattern (Fig. 7a). This structure is characterized by four dominant upwelling plumes: two circular plumes in the thickest part of the platform, and two elongated plumes closer to the platform margin. The average convection cell width is 1.1 km. In cross-section view the upwellings are represented by significant uplift in the isotherms, all of comparable magnitude. Model 1b relaxes into a marginally more complex steady-state convection pattern (Fig. 7b). As in model 1a, the upwelling plumes are concentrated in the thickest part of the platform. The structure is characterized by four elongate polyhedral shapes. The average convection cell width is 1 km. The fluid circulates at an average velocity of 1.3 m yr^{-1} and 1.9 m yr^{-1} in model 1a and 1b, respectively. These values are in agreement with other studies on thermal convection in permeable basement and sedimentary layers (e.g. Guillou-Frottier et al., 2013; Schilling et al., 2013; Sheldon et al., 2012).

In models 2a and 2b, the base geometry of the platform changes from flat to upward curving, tracing the same shape as the top of the platform. The thickness at the margins is increased by 400 m in order to keep a constant thickness of 800 m in the platform interior. The development of convection cells follows that of model 1, where the first sign of convective motion takes the form of longitudinal rolls before 10k years. Steady-state convection is reached earlier, at 140k and 150k years in 2a and 2b, respectively. Model 2a relaxes into a steady-state structure that is a combination of circular and elongated shaped upwellings (Fig. 8a), whereas model 2b is dominated by a more circular upwelling pattern with an increased number of convection cells (Fig. 8b). Both models have an average cell width of 1.3 km. The fluid velocity at steady-state is approximately 1.8 m yr^{-1} and 2.6 m yr^{-1} in model 2a and 2b, respectively.

5.1.2. Temperature

The circulation of fluid has a major impact on the geothermal gradient and temperature patterns. Fig. 9 shows how convective fluid flow effects the temperature field in models 1 and 2, depending on the geometry and permeability of the platform. The measured temperature values from within the platform in well LTG-01 have been added for reference. Geothermal gradients have been taken along the axis of three points in each model: downwelling, mixing zone and upwelling. This represents how the shape of the gradient differs depending on the direction of fluid circulation, be it upwards or downwards.

At the top of the platform, large positive temperature anomalies are produced in areas of upwelling, whereas negative anomalies are present in zones of down-flow. In models 1a and 1b, the tempera-

ture peaks at around 192 $^\circ$C and 197 $^\circ$C in the center of upwelling areas, while the temperature is only 186 $^\circ$C and 189 $^\circ$C in zones of down-flow, respectively (Fig. 9a-b) In models 2a and 2b, the temperature is elevated to 196 $^\circ$C and 203 $^\circ$C in upwellings and reduced to 176 $^\circ$C and 181 $^\circ$C in down-flows (Fig. 9c–d).

The next observation is the overall shape of the geothermal gradients. Along the axes of upwelling, the gradient is steepest which results in relatively low gradients through the platform. The gradient is as low as 13 $^\circ$C km^{-1} in model 2b, where the platform has both a large permeability and thickness. Consequently, the largest temperature enhancement (22 $^\circ$C) at the top of the platform is also present in model 2b. Along the axes of downwelling, convective fluid flow causes the geothermal gradient to lower by 10–15 $^\circ$C km^{-1}. In models 1a and 1b, the average geothermal gradient within the platform is 28 $^\circ$C km^{-1} and 25 $^\circ$C km^{-1}, respectively. By changing the base geometry from flat to curved, the average geothermal gradient decreases to 22 $^\circ$C km^{-1} and 18 $^\circ$C km^{-1} in models 2a and 2b. As models have matching thermal boundary conditions, the temperature oscillates around the same temperature (200 $^\circ$C) at mid-depth.

The final observation is the fit of the modelled geothermal gradients with measured temperature values from well LTG-01. Looking at the overall trend of the modelled temperatures, it appears, with exception to the gradient along the axes of downwelling, that the models overestimate temperatures in the top and intermediate depth levels of the platform. The modelled and measured temperatures are comparable, but it is not a superimposed fit. While the temperature data set from the LTG-01 well does suggest that the average gradient is elevated with respect to the Dutch average gradient of 31 $^\circ$C km^{-1}, it appears that applying a gradient of 39 $^\circ$C km^{-1} causes an over enhancement of temperatures once convection stabilizes within the carbonate platform reservoir.

We therefore adjust the boundary conditions such that the gradient is no longer elevated, taking a closer look at the local nature of the thermal anomaly within the platform (Fig. 10). The permeability has also been scaled, as the minimum permeability required for convection is now higher due to the decrease in ΔT. (see Eq. (2)). This correction to permeability can be performed as the permeability is within the same order of magnitude. The temperature enhancement relative to the conductive profile is similar to the previous models. As the geothermal gradient is now lower, the maximum temperatures attained within regions of upwelling are lower, ranging from 182 $^\circ$C in model 1a to 192 $^\circ$C in model 2b. Not only are these temperatures more comparable with the measured temperature values, but the modelled geothermal gradients along axes of upwelling are also a better fit with the measured gradient at LTG-01 well.

5.2. Permeability structure sensitivity

In the second series of numerical experiments denoted as model 3, we test how different mechanisms and processes affect the development of convection by investigating the sensitivity of the permeability structure (refer to Fig. 6 for permeability setup). An overview of the cases that are tested is provided in Table 4. Results
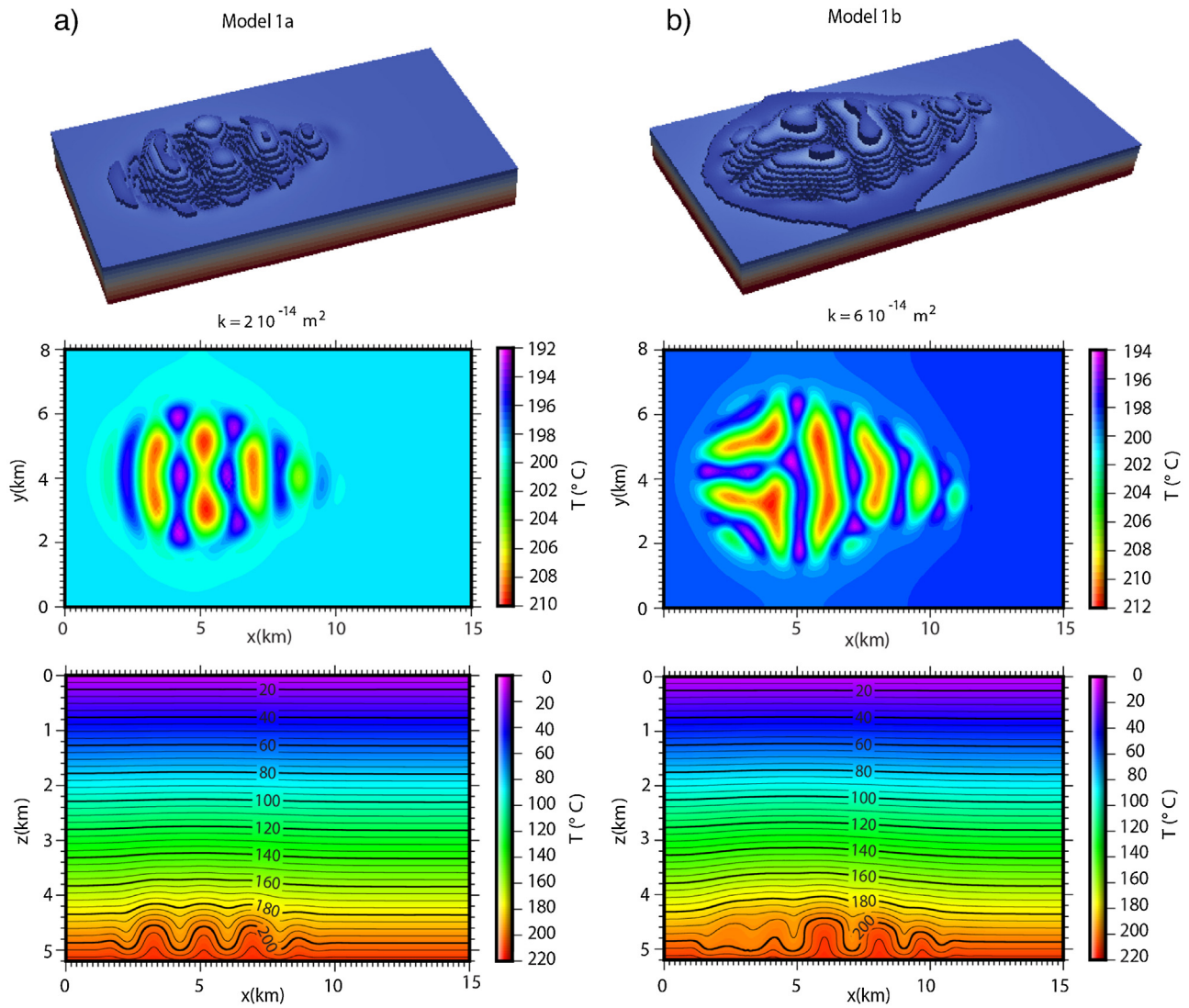
Fig. 7. (a) Results for model 1a. (b) Results for model 1b. Top: 3D view of the modelled temperature field at the top of the platform (4.4 km). Vertical exaggeration = 2. Middle: Temperature on the horizontal plane at z = 4.8 km. Note different temperature scale between (a) and (b). Bottom: Cross section at y = 4 km.

are presented in Fig. 11. The structure of convection is discussed first, followed by a summary of the resultant temperature fields.

The first permeability structure tested, model 3a, is one dominated by a permeability of $6\ 10^{-14}\ m^2$ in the margin and $1\ 10^{-14}\ m^2$ in the inner platform. Note that the inner platform permeability is below the permeability threshold for convection. Therefore, flow is constricted to the platform margin. Interesting to note is that the initial convection structure takes on the form of longitudinal rolls throughout the entire platform. However, with time flow dissipates in the inner platform as the fluid at depth is surrounded by less permeable rock and unable to facilitate flow. The steady-state structure

is dominated by a circular upwelling platform within the platform edges. Again we see that the largest upwellings are concentrated in the thickest marginal area.

By increasing the inner platform permeability above the threshold to a value of $2\ 10^{-14}\ m^2$ and keeping the margin permeability at $6\ 10^{-14}\ m^2$ there is a slight modification in the steady-state convection cell structure. An elongated shaped upwelling appears in the inner platform, however the largest upwellings remain concentrated in the platform margins. The temperature enhancement in both are similar (model 3a–b in Fig. 11). The next two cases (model 3c–d in Fig. 11) test the effect of introducing

Table 4
An overview of the four cases used in the permeability structure sensitivity tests. Kx,y is the permeability in the horizontal direction. Kz is the permeability in the vertical direction. T is the maximum temperature obtained along the axes of upwelling. Tc is the temperature without convection. T–Tc is the overall temperature enhancement relative to the conductive profile.

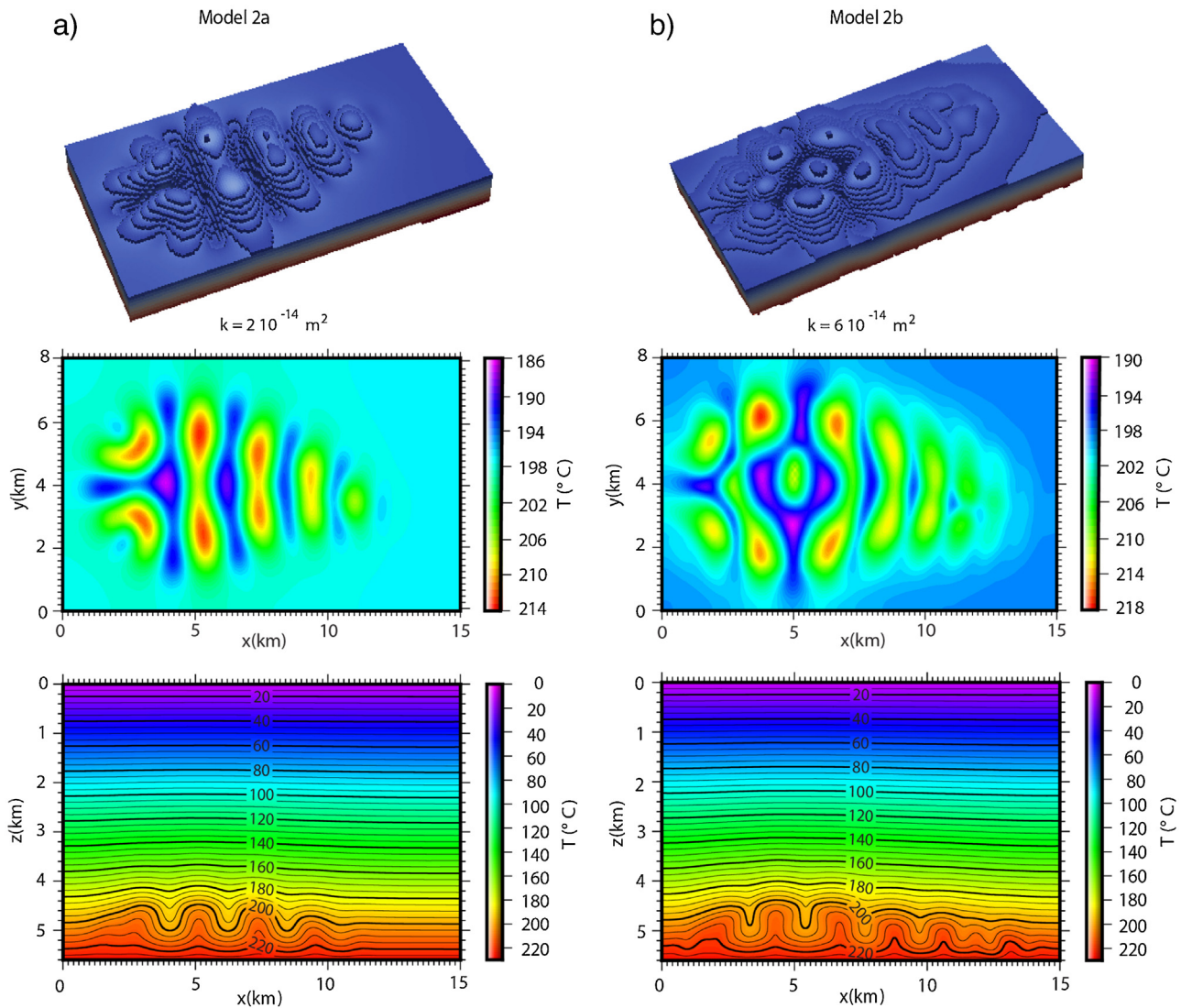| Model	Inner platform		Platform margin		T (°C) at 4.4 km	T−Tc (°C) at 4.4 km
	Kx,y	Kz	Kx,y	Kz		
3a	10	10	60	60	190	9
3b	20	20	60	60	194	13
3c	15	60	30	60	188	7
3d	20	100	60	100	196	15

Fig. 8. (a) Results for model 2a. (b) Results for model 2b. Top: 3D view of the modelled temperature field at the top of the platform (4.4 km). Vertical exaggeration = 2. Middle: Temperature on the horizontal plane at z = 4.8 km. Note different temperature scale between (a) and (b). Bottom: Cross section at y = 4 km.

an anisotropic permeability field. As in the first two cases, the platform margin is given a higher permeability than the inner platform, however now the vertical permeability is increased with respect to horizontal. As the vertical permeability is increased, the width of the convection cells decreases. Thus an increase in anisotropy causes upwellings to become more numerous, as they take on a more complex polyhedral shape (model 3d in Fig. 11).

As in models 1 and 2, the geothermal gradients have been measured along three axes (a downwelling, mixing zone and upwelling) (Fig. 12). The first observation is that the modelled temperature values have a better fit with the measured data. Whereas in models 1 and 2 the temperatures are overestimated in the top to middle platform, in model 3 there is a close fit with the measured data particularly within mixing zones. The temperature enhancement within regions of upwelling is lower than in models 1 and 2, ranging from 7 °C in model 3c to 15 °C in model 3d. The lowest gradient is therefore observed in model 3d of 18 °C km^{-1}, which is still noticeably larger than the 13 °C km^{-1} gradient in model 2b. The average geothermal gradient within the platform is 28 °C km^{-1} and 26 °C km^{-1} in models 3a and 3c, and lower values of 25 °C km^{-1} and 23 °C km^{-1} in models 3b and 3d, respectively.

While model 3 does have a better fit with the measured data, the modelled geothermal gradients remain elevated above the platform and at the base of the model due to the set boundary conditions. Therefore following the procedure in models 1 and 2, the boundary conditions are adjusted so that gradient is no longer elevated. Results are presented in Fig. 13. As seen in models 1 and 2, the temperature enhancement at the top of the platform relative to the conductive profile is comparable. The geothermal gradient along axes of upwelling range from 25 °C km^{-1} in model 3a to 18 °C km^{-1} in model 3b. The fit with measured data extends to the base of the platform (at depths greater than 5.2 km), where there is no significant elevation in the geothermal gradients with respect to the measured gradient (black curve). For example, the gradient along the axis of mixing zone in model 3b in Fig. 13 is roughly 10 °C km^{-1} lower than the average Dutch gradient, matching the dataset for the Dinantian carbonates in well LTG-01.

6. Discussion

Three-dimensional numerical models of thermal convection have shown that temperature anomalies of more than 15 °C, consistent with measured data, can easily develop within permeable
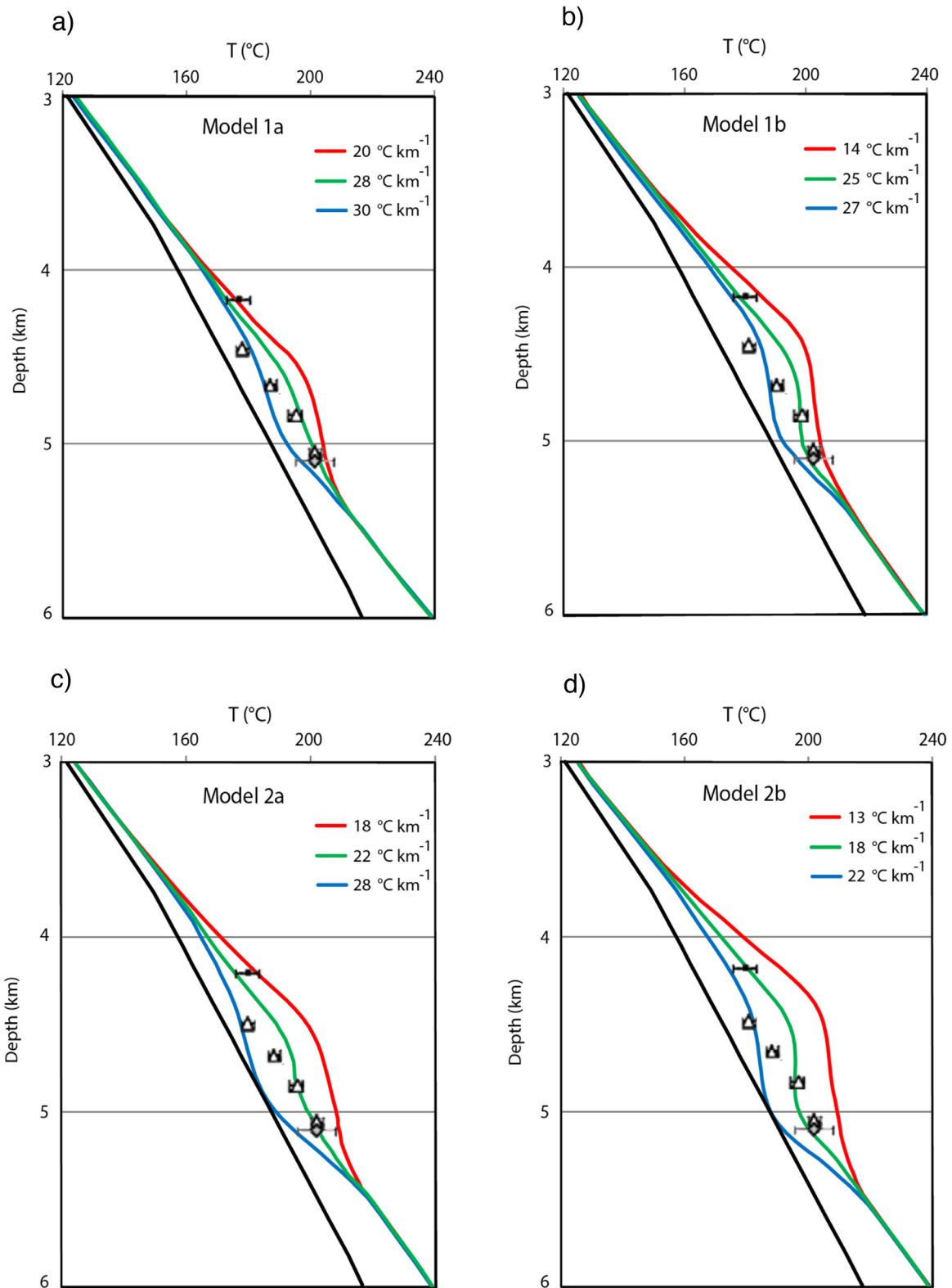
Fig. 9. Modelled temperature-depth profiles along three axes: upwelling (red curve), mixing zone (green curve) and downwelling (blue curve) in models 1 and 2. Measured temperature data from LTG-01 has been included for comparison. Black curve represents measured geothermal gradient. See Fig. 4 for explanation of symbols. (For interpretation of the references to colour in this figure legend, the reader is referred to the web version of this article.)

zones in the Luttelgeest platform. This study argues that the vertical variation of thermal gradient observed within the Luttelgeest carbonate platform cannot be justified by thermal conductivity changes with depth alone, but rather it is evidence of thermal convection.

The Luttelgeest carbonate platform is characterized by intervals of increased fracture permeability, as suggested by wireline
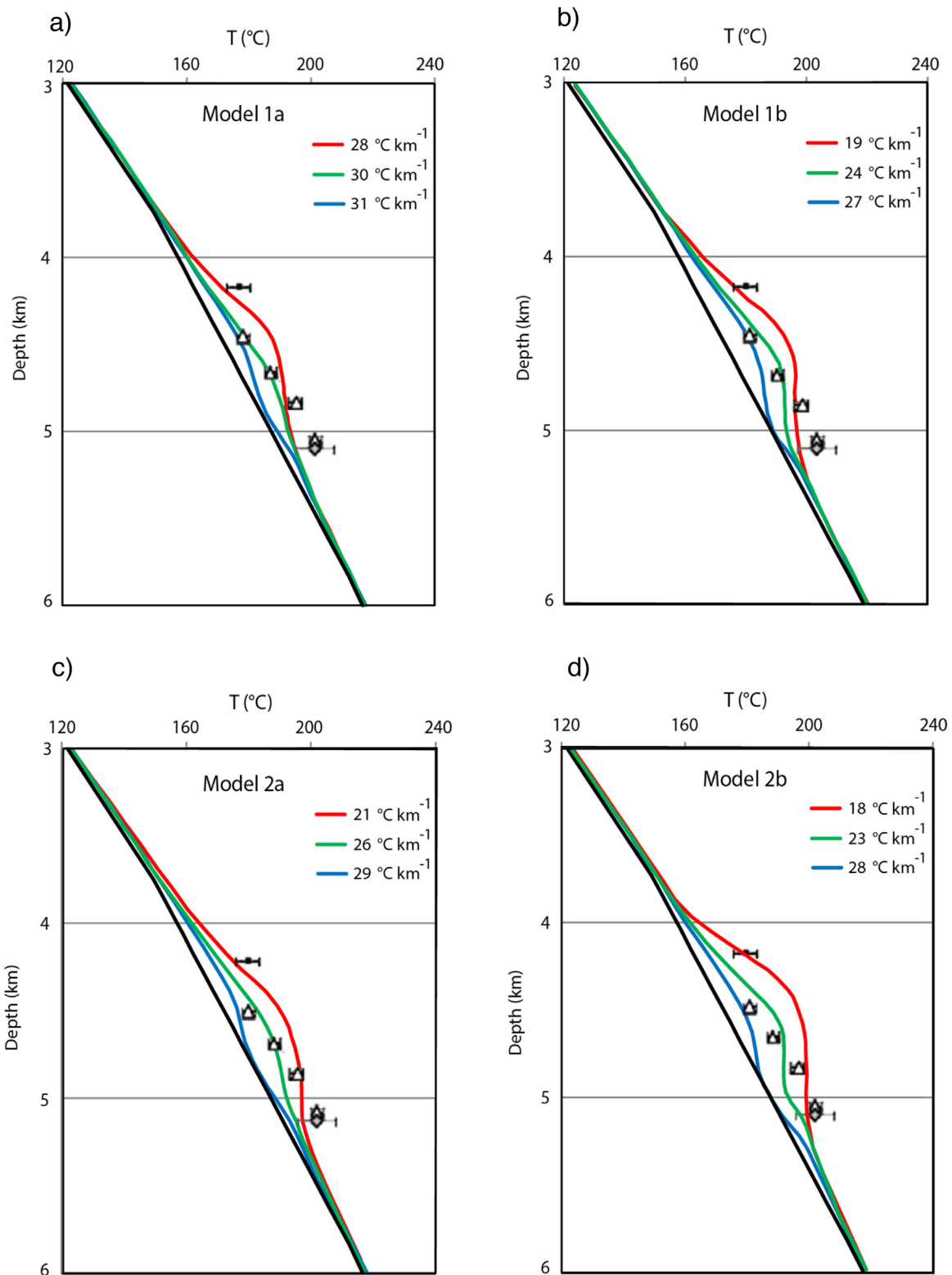
Fig. 10. Modelled temperature-depth profiles along three axes: upwelling (red curve), mixing zone (green curve) and downwelling (blue curve) in models 1 and 2 for a non-elevated gradient. Measured temperature data from LTG-01 has been included for comparison. Black curve represents measured geothermal gradient. See Fig. 4 for explanation of symbols. (For interpretation of the references to colour in this figure legend, the reader is referred to the web version of this article.)

pressure measurements, intervals of high gamma ray and neu-
tron density separation in wireline logs, analysis of mud losses
and observations from core samples. Van Oversteeg et al. (2014)
proposes that there is a 600 m interval of increased fracture per-
meability of 6 10^{-14} m^2 between 4150 and 5150 m. However,

permeability is not equally distributed throughout the entire plat-
form.

The minimum permeability calculations from the Rayleigh
number analysis confirms the potential for free convection. A
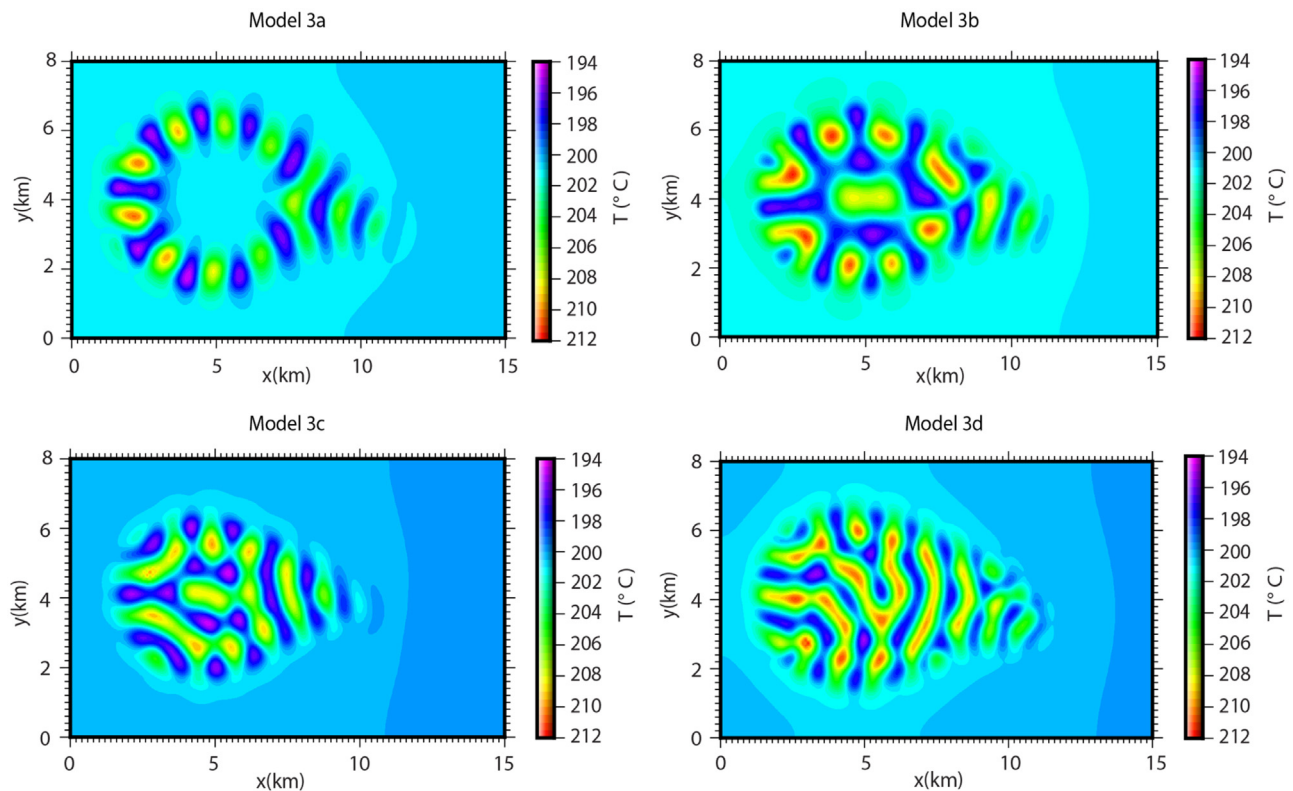minimum permeability of 1.9 10^{-14} m^2 is consistent with the per-

Fig. 11. Temperature on the horizontal plane at z = 4.8 km showing the effect of the permeability structure on convective patterns. For description of each model, see Table 4.

meability calculations derived from the well log and core samples. Compared to other studies, this value is rather large. Pasquale et al. (2013) found for a deep carbonate aquifer of the eastern sector of the Po Plain the minimum permeability to be 3.0 10^{-15} m^2. However, the reservoir considered in this study is significantly thicker (5 km), while the Luttelgeest platform only has a thickness of 800 m. Guillou-Frottier et al. (2013) considers a permeability in the order of 10^{-15} when studying the effect of permeability on convective patterns in the Soultz-sous-Forets region. Again, the layers in question are substantially thicker than this study (4 km). Furthermore, as noted in the permeability assessment, it is likely that there are smaller intervals of increased fracture permeability where the flow is concentrated, for example between 4550 and 5150 m (see Section 3.2). The permeability is also likely to be higher on the margins of the platform than in the inner platform region. The data from Luttelgeest shows that the permeability may be as high as 1 10^{-13} m^2. At this depth interval, a permeability value this large only requires a reservoir thickness of 150 m to facilitate flow.

Numerical model results highlight some important aspects of convection in the Luttelgeest carbonate platform. First, the modelled minimum permeability for convection is 1.7 10^{-14} m^2, which is remarkably close to the theoretical value considering the number of assumptions in the analysis (i.e. ignores the heterogeneous nature of fluid and rock properties and the salinity effects on water density and viscosity). Second, the development of convection cells is a time-dependent process. Convection cells grow from the location of instability at a rate depending on the system Rayleigh number. Third, the preferred initial form consists of multiple longitudinal rolls until 40–50k years, at which point a new structural mode is preferred. At steady-state, the shape of upwellings vary between circular and elongate. The structural development during transition to steady-state differs depending on the system permeability and reservoir thickness. Fourth, permeability heterogeneity controls the onset of convection and instabilities. The shape and

location of convection cells in real reservoirs are likely controlled by geometric features such as faults and undulations in the top and bottom surfaces of the reservoir. In fact, three-dimensional convective patterns and preferred convective wavelengths are highly sensitive to lateral dimensions of the permeable zone, and thus three-dimensional numerical modelling reveals new fluid patterns that are not observable in two dimensions, such as the occurrence of hexagonal type convection patterns and complex 3D polyhedral shapes.

In summary, the models which take into account the geometric features of the platform and a realistic permeability structure can explain the thermal anomaly at LTG-01. Using a geometrical configuration based on evidence from seismic studies of Luttelgeest allows for the model to incorporate the effect of the platform slope on thermal developments. Carbonate platforms are heterogeneous in nature, as they form on different scales and in different geometries. This is because platforms form under a variety of sedimentological conditions. The platform margin and platform interior often differ in permeability structure, with the margins of the platform being more heterogeneous in nature and with dissolution enlarged fractures (Boro et al., 2013). Karstification tends to be more effective on the platform rims, and fracture networks tend to be more pronounced on platform edges (eg. Boro et al., 2013). As seen in models 2a and 2b, zones of upwelling favour the combination of platform margin and areas of sufficient thickness. In fact, thermal features are predominately controlled by thickness and the permeability structure of permeable zones. Anomalies are more developed where the permeable carbonate platform is sufficiently thick.

The temperature enhancement that occurs in convective upwellings is critically dependent on the aquifer thickness, permeability structure and geothermal gradient (see Tables 3 and 4). The numerical results indicate that a temperature as high as 203 °C could be reached at 4.4 km depth for a reservoir which has a
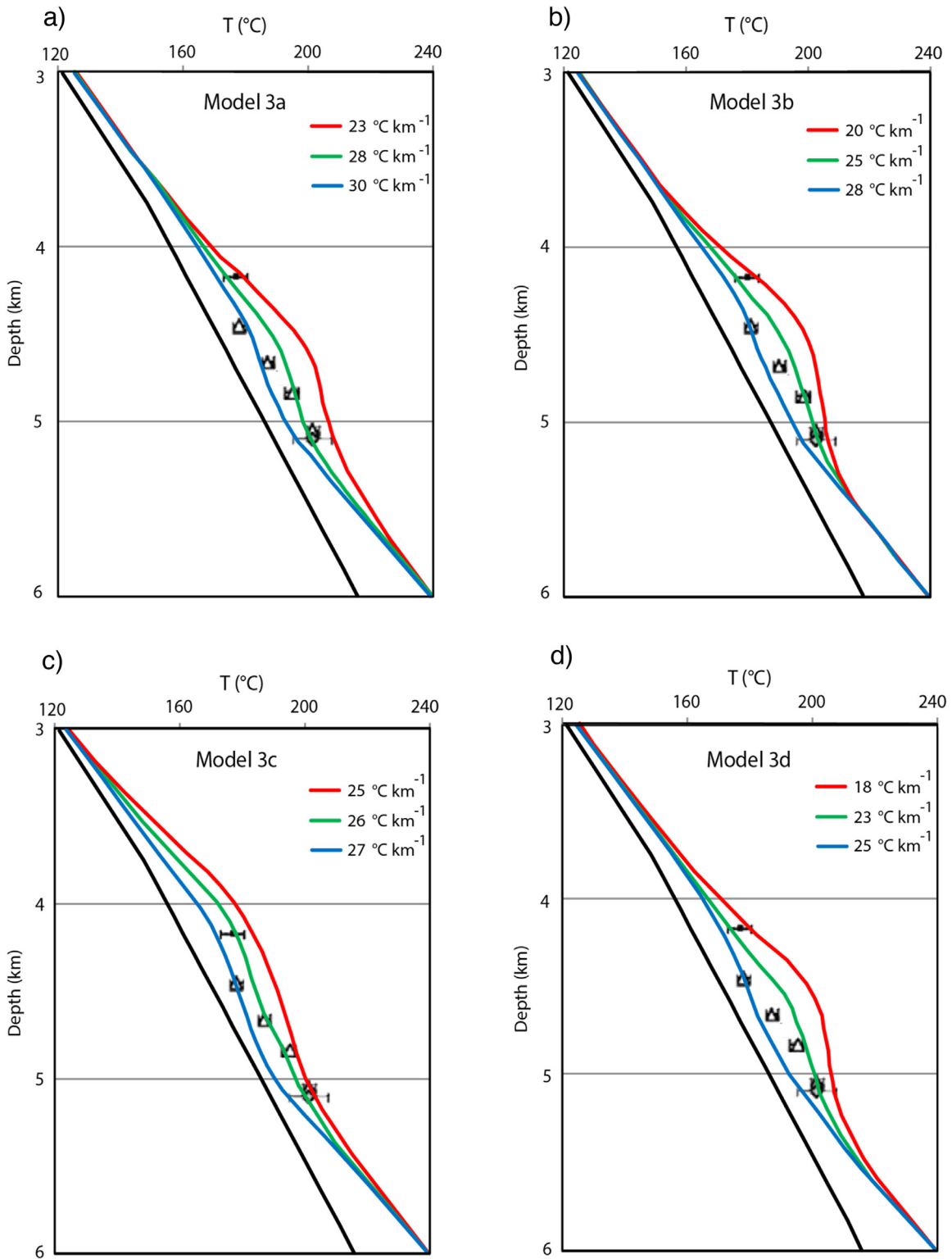
Fig. 12. Modelled temperature-depth profiles along three axes: upwelling (red curve), mixing zone (green curve) and downwelling (blue curve) for model 3. Measured data from LTG-01 has been included for comparison. Black curve represents measured geothermal gradient. See Fig. 4 for explanation of symbols. (For interpretation of the references to colour in this figure legend, the reader is referred to the web version of this article.)

geothermal gradient of $39\,°C\,km^{-1}$, a permeability of $6\,10^{-14}\,m^2$, an inner platform thickness of 800 m and platform margins extending down to 5.6 km (model 2b). This contrasts the situation in model 1a, where the permeability is $3\,10^{-14}\,m^2$ and the platform margin is thinner, resulting in a temperature of $192\,°C$ at the top of upwelling regions. The temperature enhancement in convective

upwellings can range from $7\,°C$ in model 3c to $22\,°C$ in model 2b. Even when the geothermal gradient is lowered, the overall temperature enhancement relative to the conductive profile can be as large as 15–$20\,°C$.

At first look at the measured temperature data, one might think that there are strong differences in heat flow in the Netherlands,
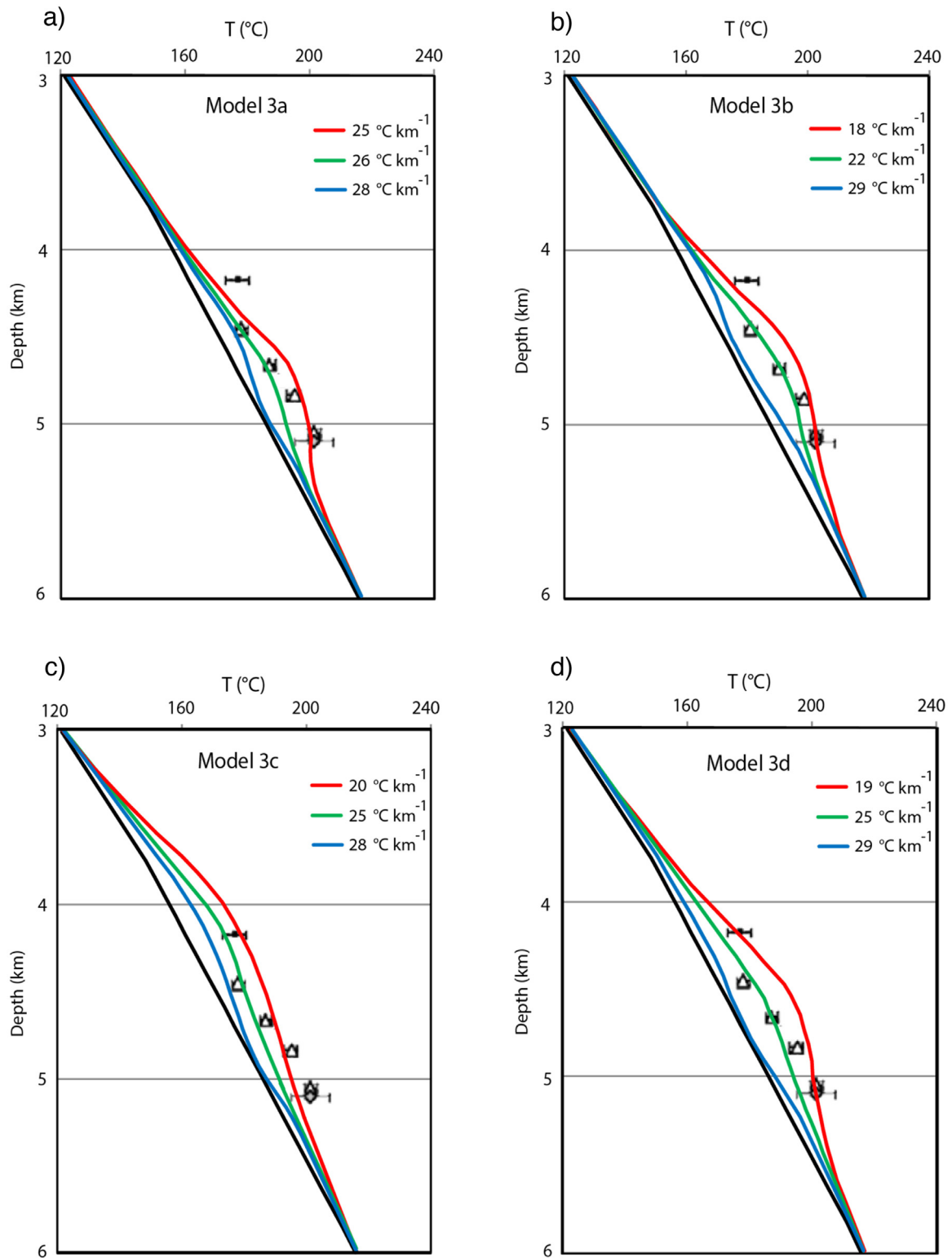
Fig. 13. Modelled temperature-depth profiles along three axes: upwelling (red curve), mixing zone (green curve) and downwelling (blue curve) for model 3 with a non-elevated gradient. Measured data from LTG-01 has been included for comparison. Black curve represents measured geothermal gradient. See Fig. 4 for explanation of symbols. (For interpretation of the references to colour in this figure legend, the reader is referred to the web version of this article.)

but models with a non-elevated temperature gradient show that this is not necessarily true (Figs. 12 and 13). Indeed, models 1 and 2, which consider a homogeneous permeability structure, overestimate the temperature within the Luttelgeest platform and result in elevated geothermal gradients both above and below the carbonate platform (Fig. 9). Even when the boundary conditions are changed

and a lower geothermal gradient is applied (Fig. 10), the modelled gradients either overestimate the temperature (red curve) or the shape of the gradient through the platform is not a good fit (green curve). Model 3, which incorporates the heterogeneous nature of permeability in the inner platform and margin, provides a better fit (i.e. green curve in Fig. 13b). In fact, model 3 in Fig. 13 shows that at

large, the thermal gradient is not elevated at Luttelgeest, but rather it is locally elevated within the carbonate platform due to thermal convection.

7. Inferences for geothermal applications

The recent development of Enhanced geothermal systems (EGS) has enabled the utilization of medium-enthalpy reservoirs located in deep sedimentary basins (Limberger et al., 2014). Whereas most EGS projects worldwide have been exploiting granitic or sandstone reservoirs, the focus in the Netherlands is on deep carbonate formations. Deep carbonate platforms can be ideal locations for both thermal water use for direct heating and for electricity generation, by means of doublet systems consisting of an injection and production well (Goldscheider et al., 2010). However, geothermal installations in these reservoirs are characterized by high exploration risk if zones of increased permeability are missed. Detailed geological, geophysical and hydrogeological research is vital for reservoir assessment (Cloetingh et al., 2010; Goldscheider et al., 2010).

As the Netherlands is situated in a low to medium enthalpy environment, so far geothermal projects have exploited shallow formations (2–3 km) for direct heating purposes. To date no electricity has been generated from geothermal resources. For conversion to electricity, subsurface temperature and fluid flow conditions are critical parameters, as they control the thermal power and efficiency of electricity generation (DiPippo, 2007). As detailed in Section 3.1, the surface temperature in the Netherlands has an annual average of 10 °C and a geothermal gradient between 25 and 40 °C km^{-1}, with an average of 31 °C km^{-1}. This means that a minimum of 4–5 km must be drilled in order to reach sufficiently high temperatures for electricity production. At greater depths, porosity and permeability tend to decrease, and transmissivity becomes a challenge. In addition to increased risk of the investment, this implies that the aquifer may need hydraulic simulation before the well can be used, which adds to the cost and complexity of the investment.

If permeability is defined by a natural fracture network, as inferred for the Luttelgeest carbonate platform, hydraulic fracturing can be used to increase the connectivity between fractures within the fractured reservoir itself, as well as the connectivity of the fractured reservoir with injection and production wells. Injection of fluids at high pressure reduces the effective normal stress and may result in tensile fracking of the reservoir rock, thereby creating pathways for fluid flow. Pluymaekers et al. (2013) shows that fracking of a reference reservoir with a default permeability of 4 mD (4 10^{-15} m^2) and a thickness of 200 m can produce very high flow rates, suitable for production of electricity. The permeability values found at Luttelgeest and inferred by this study indicate that permeability can be one order of magnitude higher, illustrating that the Luttelgeest platform may have physical potential for the development of EGS. In future, the Luttelgeest platform can be used as an example reservoir to test a tensile hydraulic stimulation strategy. The levelised cost of energy (LCOE) can be calculated in future studies based on a techno-economic performance assessment (e.g. Van Wees et al., 2012).

8. Conclusion

The Dinantian carbonates encountered at the LTG-01 well in the Netherlands contains intervals of relatively high fracture permeability showing potential as a geothermal reservoir for electricity production. Temperature measurements indicate variations in subsurface temperature that could be indicative of convection. This is important, as convection creates areas where the temperature is anomalously high at shallow depths. For the purpose of geothermal energy exploration, it is of interest to know whether or not convection can occur in a particular reservoir, where convection cells are likely to develop and the temperature enhancements in the convective upwellings.

This study investigates the potential for thermal convection in the Luttelgeest carbonate platform We reproduce the thermal gradient at LTG-01 well using 3D numerical models of thermal convection. Numerical experiments test the effect of platform geometry and the permeability structure on the development of thermal convection and resulting temperature patterns.

Convective upwellings can create significant temperature enhancements relative to the conductive profile and in agreement with the observations in the Luttelgeest carbonate platform. This enhancement is critically dependent on the platform geometry and permeability structure. Both anisotropic permeability and the differentiation between margin and inner platform permeability play an important role in the distribution of heat due to convective fluid flow. Furthermore, numerical models show that the spacing of convective upwellings, and therefore spacing of thermal anomalies, can be predicted theoretically by knowing the platform thickness and permeability. The strong spatial variability of thermal anomalies in convective fractured aquifers at large depth can have a strong effect on exploration opportunity and risk of prospective areas. Numerical models can facilitate in exploration workflows to assess thermal variation and location of upwelling zones.

References

Baillieux, P., Schill, E., Edel, J.B., Mauri, G., 2013. Localization of temperature anomalies in the Upper Rhine Graben: insights from geophysics and neotectonic activity. Int. Geol. Rev. 55 (14), 1744–1762.

Bjørlykke, K., Mo, A., Palm, E., 1988. Modelling of thermal convection in sedimentary basins and its relevance to diagenetic reactions. Mar. Petrol. Geol. 5, 338–351.

Bonté, D., Van Wees, J.-D., Verweij, J.M., 2012. Subsurface temperature of the onshore Netherlands: new temperature dataset and modelling. Geol. Mijnbouw-N. J. G. 91, 491–515.

Boro, H., Bertotti, G., Hardebol, N.J., 2013. Distributed fracturing affecting isolated carbonate platforms, the latemar platform natural laboratory (Dolomites, North Italy). Mar. Petrol. Geol. 40, 69–84.

Cherubini, Y., Cacace, M., Scheck-Wenderoth, M., Noack, V., 2014. Influence of major fault zones on 3-D coupled fluid heat transport for the Brandenburg region (NE German Basin). Geotherm. Energy Sci. 2, 1–20.

Cloetingh, S., van Wees, J.D., Ziegler, P.A., Lenkey, L., Beekman, F., Tesauro, M., Förster, A., Norden, B., Kaban, M., Hardebol, N., Bonté, D., Genter, A., Guillou-Frottier, L., Ter Voorde, M., Sokoutis, D., Willingshofer, E., Cornu, T., Worum, G., 2010. Lithosphere tectonics and thermos-mechanical properties: an integrated modelling approach for Enhanced Geothermal Systems exploration in Europe. Earth-Sci. Rev. 102, 159–206.

Collins, J.F., Kenter, J.A.M., Harris, P.M., Kuanysheva, G., Fischer, D.J., Steffen, K.L., 2006. Facies and reservoir-quality variations in the late Visean to Bashkirian outer platform, rim, and flank of the Tengiz buildup, Precaspian Basin, Kazakhstan, in: giant hydrocarbon reservoirs of the world: from rocks to reservoir characterization and modelling. SEPM Spec 88, 55–95.

De Jager, J., 2007. Geological development. In: Geology of the Netherlands. Royal Netherlands Academy of Arts and Sciences, Amsterdam, the Netherlands, pp. 5–26.

DiPippo, R., 2007. Ideal thermal efficiency for geothermal binary plants. Geothermics 36, 276–285.

Garibaldi, C., Guillou-Frottier, L., Lardeaux, J.M., Bouchot, V., 2010. Combination of numerical tools to link deep temperatures, geological structures and fluid flow in sedimentary basins: application to the thermal anomalies of the provence basin (South-East France). In: Proceedings World Geothermal Congress 2010, The International Geothermal Association, Bali, Indonesia.

Geluk, M.C., Dusar, M., de Vos, W., 2007. Pre-silesiam. In: Geology of the Netherlands. Royal Netherlands Academy of Arts and Sciences, Amsterdam, the Netherlands, pp. 27–42.

Goldscheider, N., Mádl-Szönyi, J., Eröss, A., Schill, E., 2010. Review: thermal water resources in carbonate rock aquifers. Hydrogeol. J. 18, 1303–1318.

Guillou-Frottier, L., Carré, C., Bourgine, B., Bouchot, V., Genter, A., 2013. Structure of hydrothermal convection in the Upper Rhine Graben as inferred from corrected temperature data and basin-scale numerical models. J. Volcanol. Geotherm. Res. 256, 29–49.

Holzbecher, E.O., 1998. Modeling Density-driven Flow in Porous Media: Principles, Numerics, and Software. Springer, Berlin, Germany, ISBN 3-540-63677-3.

Horton, C, Rogers, F., 1945. Convection currents in porous medium. J. Appl. Phys. 16 (6), 367–370.

Kühn, M., Dobert, F., Gessner, K., 2006. Numerical investigation of the effect of heterogeneous permeability distributions on free convection in the hydrothermal system at Mount Isa, Australia. Earth Planet. Sc. Lett. 244, 655–671.

Kenter, J.A.M., van Hoeflaken, F., Bahamonde, J., Bracco Gartner, G.L., Keim, L., Besems, R.E., 2002. Anatomy and lithofacies of an intact and seismic-scale Carboniferous carbonate platform (Asturias, NW Spain): analogues of hydrocarbon reservoirs in the Pricaspian Basin (Kazakhstan). SEPM Spec 74, 181–203.

Kombrink, H., Van Lochem, H., Van der Zwan, K.J., 2010. Seismic interpretation of Dinantian carbonate platforms in the Netherlands; implications for the palaeogeographical and structural development of the Northwest European Carboniferous Basin. J. Geol. Soc. 167, 99–108.

Kombrink, H., 2008. Tectonics and sedimentation in the northwest european carboniferous basin. In: The Carboniferous of the Netherlands and Surrounding Areas; a Basin Analysis, PhD Thesis. Universiteit Utrecht, pp. 21–46.

Lapwood, E., 1948. Convection in a porous medium. Proc. Camb. Phil. Soc. 44, 508–521.

Limberger, J., Calcagno, P., Manzella, A., Trumpy, E., Boxem, T., Pluymaekers, M.P.D., Van Wees, J.-D., 2014. Assessing the prospective resource base for enhanced geothermal systems in Europe. Geotherm. Energy Sci. 2, 1–15.

Lord Rayleigh, O.M.F.R.S., 1916. On convection currents in a horizontal layer of fluid, when the higher temperature is on the underside. Philos. Mag. Ser. 6 (32), 529–546.

Murphy, H.D., 1979. Convective Instabilities in Vertical Fractures and Faults. J. Geophys. Res. 1 (B11), 6121–6130.

Nield, D.A., Bejan, A., 2013. Convection in Porous Media. Springer, Berlin, Germany, ISBN 978-1-4514-5540-0.

Pasquale, V., Chiozzi, P., Verdoya, M., 2013. Evidence for thermal convection in the deep carbonate aquifer of the eastern sector of the Po Plain, Italy. Tectonophysics 594, 1–12.

Pluymaekers, M.P.D., Van Wees, J.D., Hoedeman, G.C., Fokker, P.A., 2013. Different Stimulation Strategies to Enhance the Performance of Subsurface Heat Exchangers Based on Tensile Fractures, Presented at Sustainable Earth Sciences Conference (SES) , European Association of Geoscientists and Engineers (EAGE), Pau, France.

Rabinowicz, M., Boulegue, J., Genthon, P., 1998. Two- and three-dimensional modelling of hydrothermal convection in the sedimented Middle Valley segment, Juan de Fuca Ridge. J. Geophys. Res. 103, 24045–24065.

Schilling, O., Sheldon, H.A., Reid, L.B., Corbel, S., 2013. Hydrothermal models of the Perth metropolitan area, Western Australia: implications for geothermal energy. Hydrogeol. J. 21, 605–621.

Sheldon, H.A., Florio, B., Trefry, M.G., Reid, L.B., Ricard, L.P., Ameed, K., Ghori, R., 2012. The potential for convection and implications for geothermal energy in the Perth Basin, Western Australia. Hydrogeol. J. 20, 1251–1268.

Tournier, C., Genthon, P., Rabinowicz, M., 2000. The onset of natural convection in vertical fault planes: consequences for the thermal regime in crystalline basements and for heat recovery experiments. Geophys. J. Int. 140, 500–508.

Van Hulten, F.F.N., Poty, E., 2008. Geological factors controlling Early Carboniferous carbonate platform development in the Netherlands. Geol. J. 43, 175–196.

Van Hulten, F.F.N., 2012. Devono-carboniferous carbonate platform systems of the Netherlands. Geol. Belg. 15, 284–296.

Van Oversteeg, K., Lipsey, L.C., Pluymaekers, M., van Wees, J.-D., Fokker, P.A., Spiers, C.J., 2014. Fracture Permeability Assessment in Deeply Buried Carbonates and Implications for Enhanced Geothermal Systems: Inferences from a Detailed Well Study at Luttelgeest-01, The Netherlands , Proceedings Thirty-Eighth Workshop on Geothermal Reservoir Engineering, Stanford University, Stanford, California.

Van Wees, J.D., Beekman, F., 2000. Lithosphere rheology during intraplate basin extension and inversion, inferences from automated modeling of four basins in western Europe. Tectonophysics 320, 219–242.

Van Wees, J.D., Kronimus, A., van Putten, M., Pluymakers, M.P.D., Mijnlief, H., van Hoof, P., Obdam, A., Kramers, L., 2012. Geothermal aquifer performance assessment for direct heat production—methodology and application to Rotliegend aquifers. Neth. J. Geosci. 91 (4), 651–665.

Weatherill, D., Simmons, C.T., Voss, C.I., Robinson, N.I., 2004. Testing density-dependent groundwater models: two-dimensional steady state unstable convection in infinite, finite and inclined porous layers. Adv. Water Resour. 27, 547–562.

Ziegler, P.A., van Wees, J.D., Cloetingh, S., 1998. Mechanical controls on collision-related compressional intraplate deformation. Tectonophysics 300, 103–129.